The construction of phthalocyanine- carbon nanoparticle conjugates for applications in photodynamic therapy and non-linear optics

A thesis submitted in fulfilment of the requirements for the degree of

DOCTOR OF PHILOSOPHY

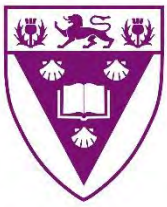

RHODES UNIVERSITY

Where leaders learn

By

REFILWE MATSHITSE

February 2021

My son (Aldo)
and
siblings (Mammuso and Aubrey Matshitse)

Late parents and grandparents

Kubu Kubu Ntsha Marota

in the words of

Maya Engelou

Out of the huts of history's shame, I rise
Up from a past that's rooted in pain, I rise
I'm a black ocean, leaping and wide,
Welling and swelling I bear in the tide.
Leaving behind nights of terror and fear, I rise
Into a daybreak that's wondrously clear, I rise
Bringing the gifts that my ancestors gave,
I am the dream and the hope of the slave.
I rise, I rise, I rise.

سبحان الله وبحمده سبحان الله العظيم

I would like to express my sincere gratitude to Distinguished Professor T. Nyokong for the opportunity to pursue my PhD degree under her supervision. Her mentorship and support throughout the programme equipped me with valuable academic and life skills that have carried me throughout my study. She allowed me to realise my potential, curve my path, be diligent, never dwell on negativity, to keep going and never give up. She gave me the opportunity to travel to Japan (Shinshu University) on research for a period of three months, this exposure strengthened my Phd study. Gratitude to Profs Koboyashi, Kimura and Osawa for welcoming me in their laboratory and equipping me with skills on how to synthesise silicon Pcs, store and purify detonation nanodiamonds. Special gratitude to Drs. M. Managa and N. Nwaji for their patience, relentless support in my research. Prof J. Mac, P. Ngoy, K. Lobb Drs E. Sekhosana, O. Achadu, T. Tshiwawa, Ms Centane and Y. Openda for collaborative work. Prof Earl Prinsloo for photodynamic therapy studies, Shirley and Marvin for TEM microscope. Dr J. Britton and Mr F. Chindeka for keeping every instrument in the CNI operational. Ms G. Cobus for her diligence in running the CNI and simplifying administrative work for S22 students. A special appreciation to my son for giving me a sense of purpose and the determination My sister M. Matshitse for her support throughout my study. My late Dad for his limitless selflessness and for teaching me the value of education. Mom for instilling hard work, resilience and independence. To friends Drs M. Shumba, I Bears, F. Dziike, P. Sén, B. Mutuma, T. Musyoka, Mr and Mrs M. Maloka, Mr and Mrs Motsoeneng, Ms L. Saad, J. Yasini, Sheikhs Salim, Hiddrissa , Fuáad and especially Ahmed for their prayers, patience and support throughout my study. Gratitude to National Research Fund (NRF) for the financial support.

The syntheses and characterization of symmetric and asymmetric Pcs functionalized at the peripheral position and sometimes positively charged are reported. The Pcs had either H_2, zinc or silicon as central metals and have pyridyloxy, benzothiozole phenoxy, and respective cationic analogues as ring substituents. The Pcs were linked to carbon based nanoparticles such as graphene quantum dots, carbon dots, and detonation nanodiamonds (DNDs) via an ester, amide bond and/or π - π stacking.

The physicochemical characteristics of the Pcs were assessed when alone and when in a conjugated system. Both symmetrically and asymmetrically substituted benzothiozole Pcs when quaternised displayed higher triplet and singlet oxygen quantum yields than their unquaternised counterparts.

Linkage to carbon nanoparticles (especially to detonation nanodiamonds) had an increasing effect on triplet and singlet oxygen quantum yield. However, a general decrease in singlet oxygen quantum yield on linkage to doped detonation nanodiamonds was associated with the screening effect of DNDs. Heteroatom doped DNDs-Pc nanohybrids have less singlet oxygen than Pcs alone due to molecular structural stability associated with strain that is relatively reduced upon linking Pcs

The *In vitro* dark cytotoxicity and photodynamic therapy of selected Pc complexes and conjugates against MCF-7 cells was tested. All studied Pc complexes and conjugates showed minimum dark toxicity making them applicable for PDT. When Pc complexes are alone, there is less phototoxicity with >22% cell viability at concentrations ≤ 50 µg/mL relative to conjugates with <22% cell viability at concentrations ≤ 50 µg/mL. There was no direct relationship between PDT and singlet oxygen quantum yields. Nonlinear optical characteristics of complexes was improved upon conjugation of DNDs. Absorbance, input energy, percentage loading, central metal, substituent of Pc and nature of interaction (covalent, noncovalent) are amongst some of the factors that influence nonlinear absorption properties of materials used in this study. All materials followed reverse saturable absorption through two photon absorption mechanism at the excitation wavelength of 532 nm. Aggregates reduce excited state lifetime and B_{eff} under high concentrations/absorbance. A direct relationship between absorbance and B_{eff} of DNDs nanoconjugated systems at low

concentrations result in increased optical limiting characteristics of materials. The findings from this work show the importance of linking (nonlinear optics and photodynamic therapy) and doping (photodynamic therapy) photosensitisers such as phthalocyanines and sometimes boron dipyrromethenes onto carbon based nanoparticles for the enhanced characteristics in variable applications.

Table of Contents

^{1}H NMR	Proton nuclear magnetic resonance
ADMA	Tetrasodium α,α -(anthracene-9,10- diyl) dimethylmalonate
$CDCl_3$	Deuterated chloroform
CDs	Carbon dots
CNPs	Carbon nanoparticles
DBU	1,8-Diazabicyclo[5.4.0]undec-7-ene
DCC	Dicyclohexylcarbodiimide
DLS	Dynamic light scattering
DMEM	Dulbecco's modified eagle's medium
DMF	Dimethylformamide
DMSO	Dimethylsulfoxide
DMSO-d_6	Deuterated dimethylsulfoxide
DNDs	Detonation nanodiamonds
DPBF	Diphenylisobenzofuran
DPBS	Dulbecco's modified phosphate buffer saline
FT–IR	Fourier Transform Infrared
GQDs	Graphene quantum dots
HOMO	Highest occupied molecular orbital
IRF	Instrument response function
ISC	intersystem crossing
LUMO	Lowest unoccupied molecular orbital
MALDI	Matrix–assisted Laser desorption/Ionization

MCF 7	Michigan cancer foundation 7
MPc	Metallophthalocyanine
MS	Mass spectrometer
Nd–YAG	Neodymium–doped yttrium aluminum Garnet
NPs	Nanoparticles
PACT	Photodynamic antimicrobial chemotherapy
Pc	Phthalocyanine
PDT	Photodynamic therapy
PS	Photosensitiser
PTT	Photothermal therapy
ROS	reactive oxygen species
SEM	Scanning electron microscope
Std	Standard
TCSPC	Time-correlated single photon counting
TEM	Transmission electron microscope
UV–Vis	Ultraviolet–Visible
XPS	X–ray Photoelectron spectroscopy
XRD	X–ray diffractometer

α	non-peripheral position
β	peripheral position
ε	molar extinction coefficient
λ	wavelength
τ_0	fluorescence radiative lifetime
τ_F	fluorescence lifetime
τ_T	triplet state lifetime
Φ_F	fluorescence quantum yield
Φ_T	triplet state quantum yield
Φ_Δ	singlet oxygen quantum yield
A/abs	absorbance
S_0	singlet ground state
S_1	singlet excited state
t	time
T_1	triplet excited state
$h\upsilon$ light	(h =Planck's constant; v = frequency of a photon of light)

Chapter 1

CHAPTER 1

1. Introduction

1.1. Phthalocyanines (Pcs)

1.1.1. Structure

Phthalocyanines (Pcs) also known as tetrabenzotetraaza porphyrin, are a special class of tetra pyrrole macrocyclic compounds having similar structure as naturally occurring porphyrin shown in **Figure 1.1 (a)** with an addition of four nitrogen atoms in the meso-position as shown in **Figure 1.1 (b) [1, 2]**.

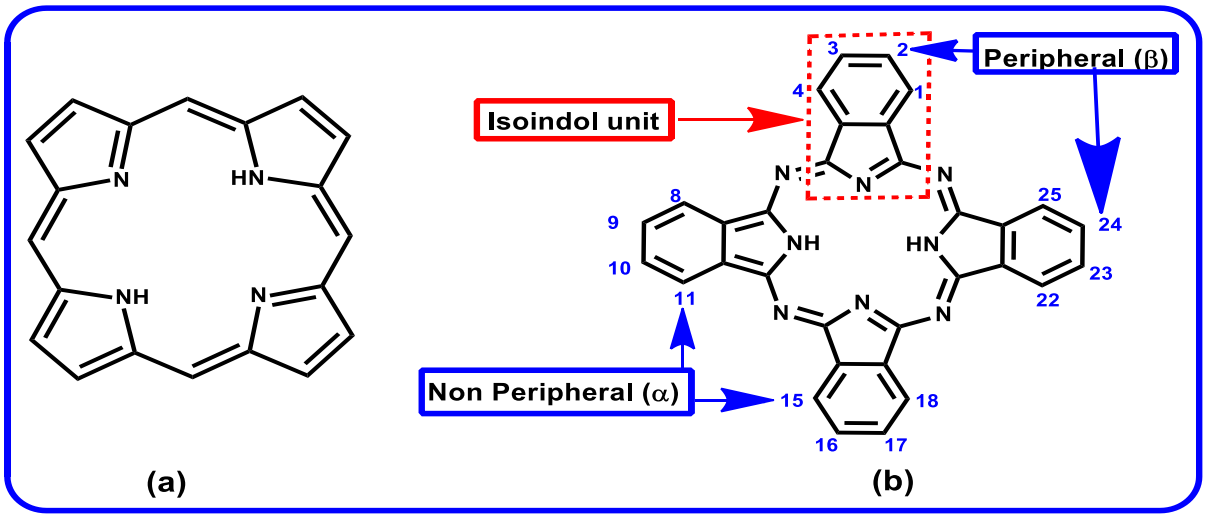

Figure 1.1: (a) Porphyrin (b) Molecular structure of phthalocyanine showing isoindoline unit and α, β substituent positions on the macrocycle.

Phthalocyanines are made up of four iminoisoindoline units in **Figure 1.1 (b)**. The carbon atoms of Pcs are numbered according to the IUPAC system as shown in **Figure 1.1 (b)**. Properties of Pc derivatives can be tuned by either varying the central metal atom **[3]** and substituents: position, number, charge and the number of charges **[4, 5]**. Ligand binding to the phthalocyanine ring at positions 2, 3, 9, 10, 16, 17, 23, 24, is referred to as peripheral substitution while at positions 1, 4, 8, 11, 15, 18, 22, 25, is referred to as non-peripheral substitution. The position of substitution onto the macrocycle structure alters spectroscopic

characteristics of a Pc **[6, 7]**. Introduction of non-peripheral (α) and peripheral (β) substituents reduces aggregation and enhances solubility of the phthalocyanine **[6, 7]**. All the Pcs used in the study were peripherally substituted. Pcs are used as traditional dyes and pigments, industrial catalytic systems, photosensitizers for photodynamic therapy (PDT) of cancer, materials for electrophotography, ink-jet printing, semiconductors, chemical sensors, electrochromic devices, functional polymers and liquid crystals **[6-8]** to mention a few.

1.1.2. Synthesis

Pcs can be synthesised from ortho-phthalic acid derivatives such as anhydrides, imides, amides and nitriles using phthalamide, phthalic acid, phthalic anhydride, o-cyanobenzamide, o-dibromobenzene, diiminosoindole and phthalonitrile as examples shown in **Figure 1.2**, but phthalonitrile (1,2-dicyanobenzene) derivatives are commonly used to synthesise the Pc in the laboratories **[7, 9]**. In this study both phthalonitrile and diiminosoindole precursors were used depending on the choice of central metal in the cavity the macrocycle.

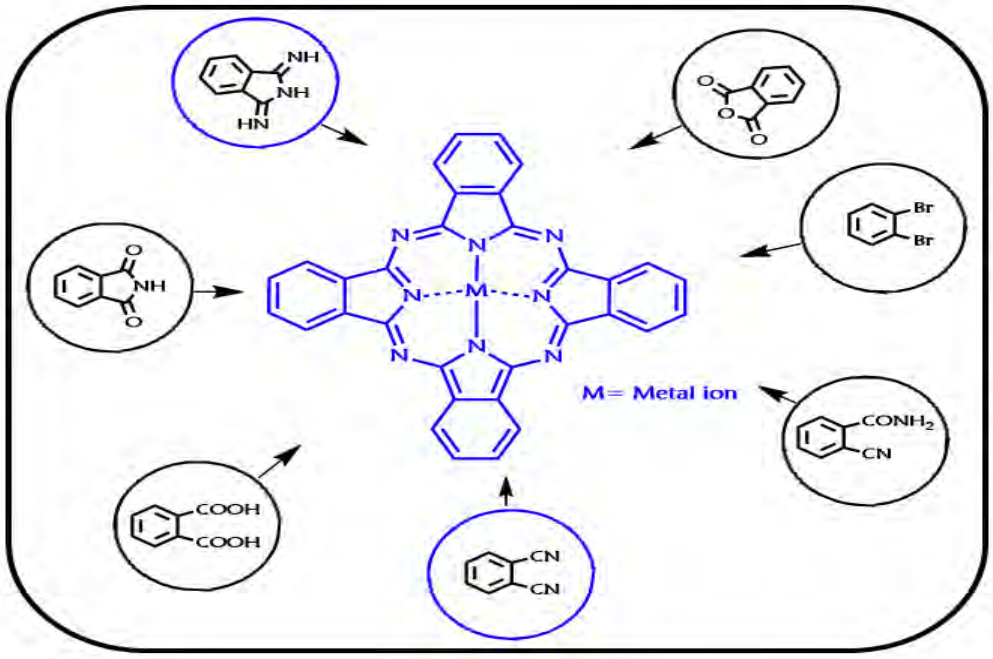

Figure 1.2: Precursor molecules used in constructing metallophthalocyanine

Asymmetrically substituted Pcs can be synthesised from methods such as sub-phthalocyanine, crossed polymer and statistical condensation **[10]**. However, the statistical reaction of two differently substituted phthalonitriles or 1,3-diiminoisoindolines **[11, 12]** is a commonly used method to prepare asymmetrically substituted Pcs. The method involves a combination of phthalonitriles in ratio of 3:1 or 9:1 (A:B) or higher depending on reactivity of phthalonitriles which usually affords a mixture of six compounds but favours the formation of asymmetrical Pc (A_3B) shown **Scheme 1.1 [10]**. In this study, asymmetric Pcs synthesised using the statistical condensation method were applied in PDT.

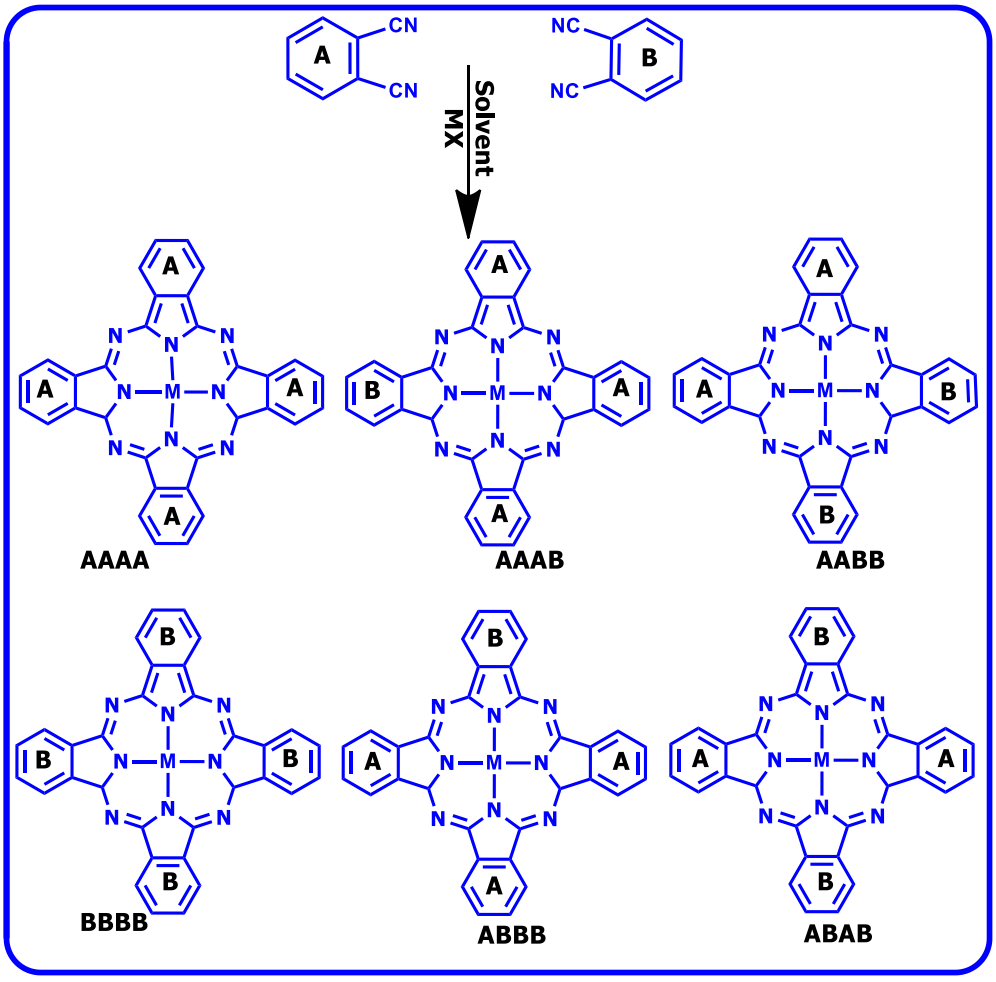

Scheme 1.1: Statistical condensation method for synthesis of asymmetric Pcs, MX= metal salt.

The cyclization mechanism of phthalocyanines is not yet fully understood. However, several intermediates formed during the synthesis have been isolated and identified **[13]**. Based on the products that were isolated, a mechanism has been proposed of how these complexes are formed. 1, 5-Diazabicyclo [4. 3. 0] non-5-ene (DBN) and 1, 8-diazabicyclo [5. 4. 0] undec-7-ene (DBU) are strong non-nucleophilic bases which are used as organic catalysts that acts as proton acceptors **(Scheme 1.2)**. Alkoxide ion (RO^-) is a result of the removal of proton by DBU from alcohol solvent (ROH). DBU is the catalyst base used in this study for tetramization of Pc.

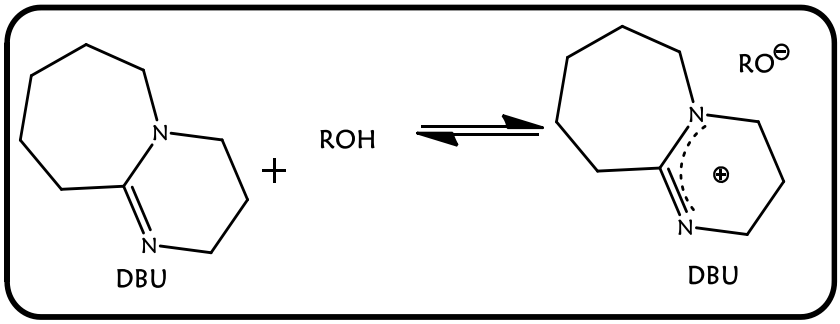

Scheme 1.2: Mechanism of DBU as a proton acceptor **[13]**. ROH is for alcohol solvent.

Phthalocyanine cyclization shown in **Scheme 1.3,** is a three step procedure that entails:

Step (i) Nucleophilic attack of the alkoxide ion on the phthalonitrile to reduce it to imine intermediate (*X*).

Step (ii) This is followed by addition-elimination to form a 1-alkoxy-3-iminoisoindolenine intermediate (*Y*).

Step (iii) In the last stage, the phthalocyanine molecule is formed by oxidation of the intermediate product.

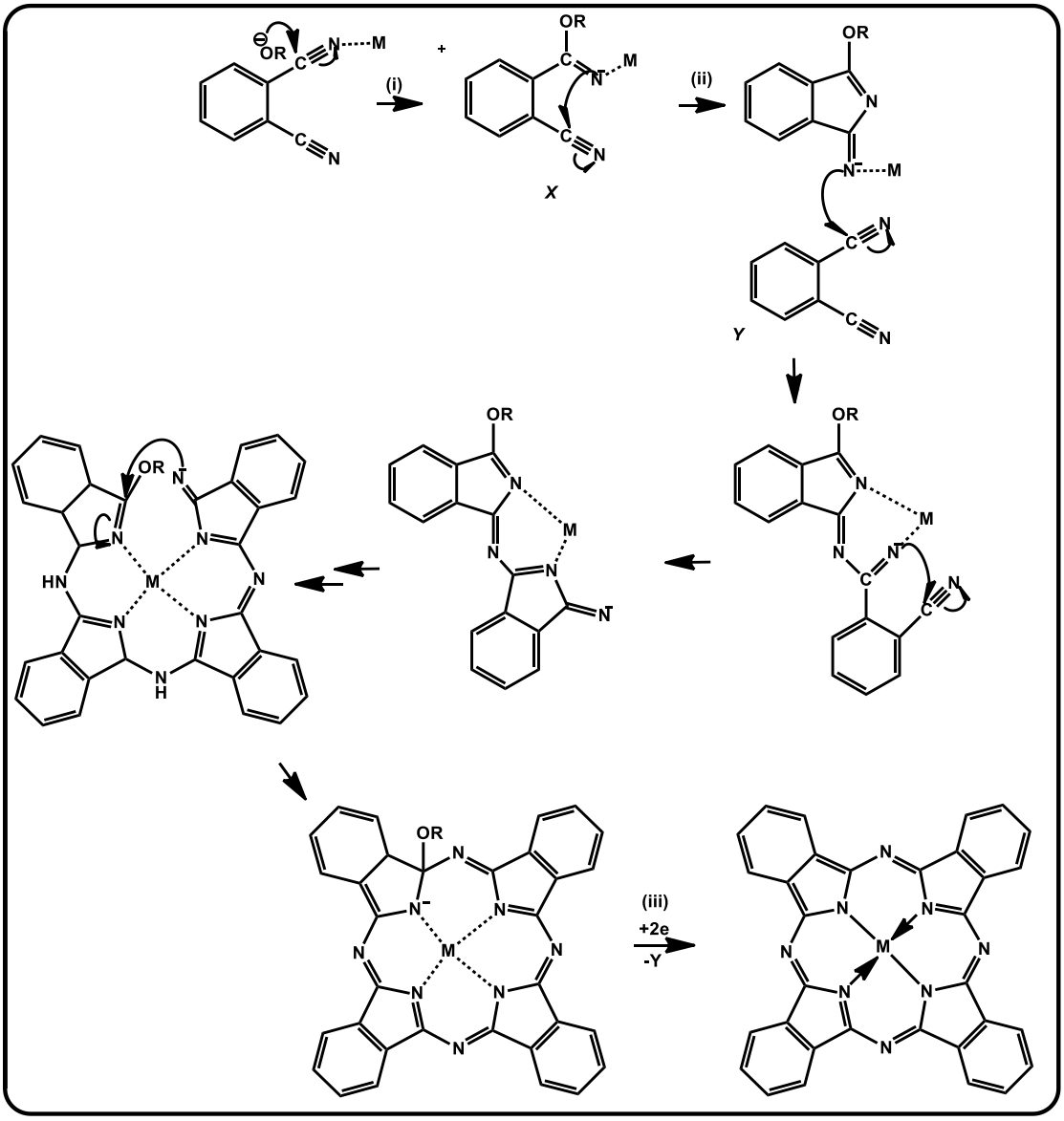

Scheme 1.3: Mechanism of cyclization of Pc from 1,2-dicyanobenzene **[13].**

1.1.3. Electronic absorption characteristics of Pc

Absorption spectral peaks of Pc in the near infrared (670 - 1000 nm) and the ultraviolet (325 - 370 nm) regions of the spectrum correspond to Q and B-bands, respectively **[14]**. **Figure 1.3** shows a broad B band with less intensity due to peak overlap of B_1 and B_2 **[15]**. Solvent, symmetry, substituents and central metal are amongst some of the factors that affect electronic absorption spectrum of the macrocycle **[9, 16-18]**.

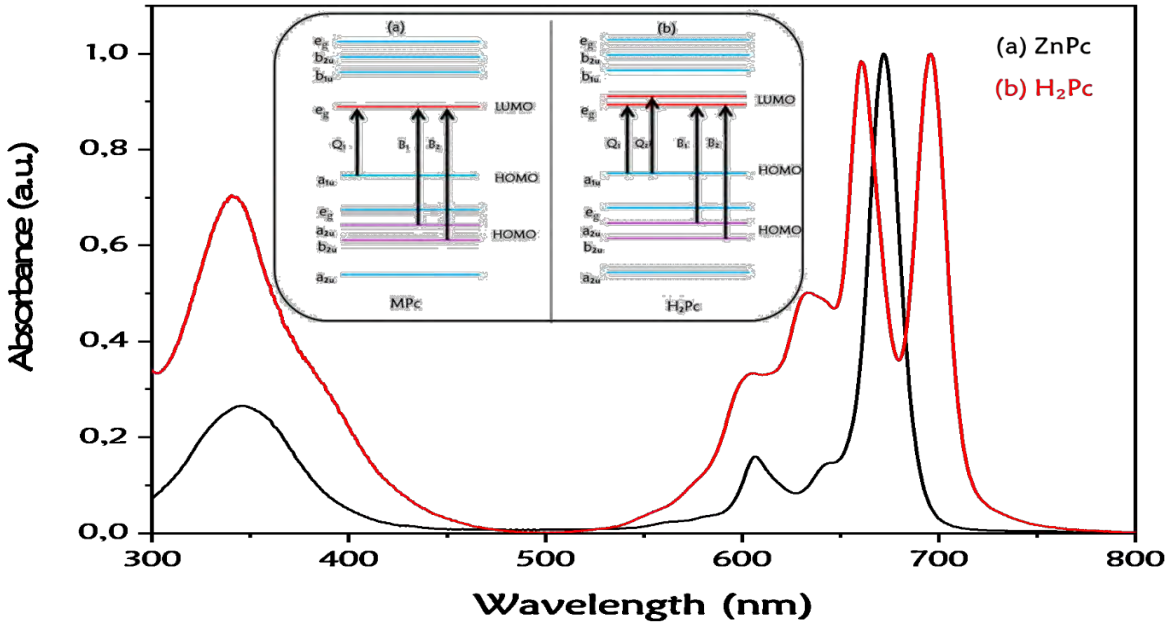

Figure 1.3: Electronic ground state absorption spectra of (a) metallated (ZnPc), (b) unmetallated Pc (H_2Pc) and respective ground state electronic transition between molecular orbital energy levels (insert) showing the origin of Q and B bands

In metallated Pcs, the single intense Q band is associated with D_{4h} symmetry due to π - π* transitions from the a_{1u} of the highest occupied molecular orbital (HOMO) to e_g of lowest unoccupied molecular orbital (LUMO) in **Figure 1.3 [10, 19, 20]**. A split Q band in unmetallated Pc is a result of the D_{2h} reduced symmetry associated with transitions from a_{1u} (HOMO) to the non-degenerate b_{2g} and b_{3g} (LUMO) in **Figure 1.3 (b) [10, 21]**.

1.1.4. Aggregation

Aggregation of Pcs has a great impact on their optical properties **[22]**. There are two types of aggregation in Pcs which occur through face-to-face (H-aggregation) and of edge-to-edge (J-aggregation) π - π interaction shown in **Figure 1.4** to be associated with blue and red shift of the Q band, respectively. H aggregation is more common. Aggregation reduces photoactivity of Pcs. Central metal ions with axial ligation increase solubility, reduce aggregation and

change the electronic structure of the molecule **[21, 22]**, the choice of a central metal affects physicochemical characteristics of the macrocycle **[23, 24]**.

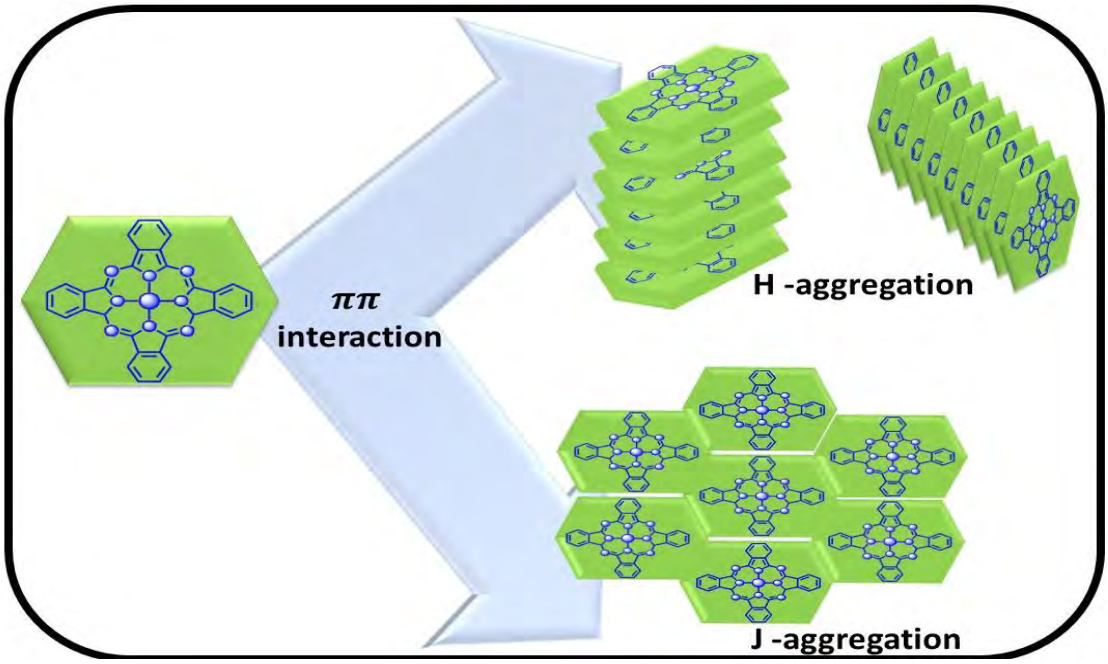

Figure 1.4: π - π interaction can occur through H or J type aggregation.

In summary, careful consideration on the choice of substituent, position of substituent and central metal (axial ligation) is important in order to reduce aggregation and improve spectroscopic characteristics of Pc macrocycle **[22, 25, 26]**. Thus, all Pcs employed in this work were substituted on the periphery of the macrocycle, unmetalated and metalated with central metals (such as $(Si(OH)_2$ with axial ligation or Zn(II)).

1.1.5. Pcs used in this work

Table 1.1 shows Pcs which will be used. Complexes **1**, **3, 4 - 7** have been published before **[5, 24, 27-37]**, **2** was purchased, the rest are new.

Table 1.1: Pcs used in this study

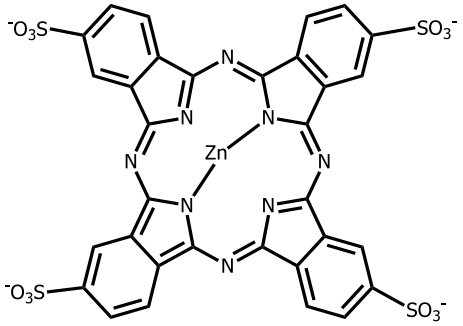	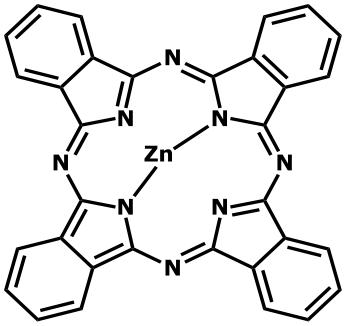
1	**2**
[25-29, 35]	**(Purchased)**
1-GQDs (π - π)	**2-GQDs (π - π)**
Physicocochemical	Physicochemical
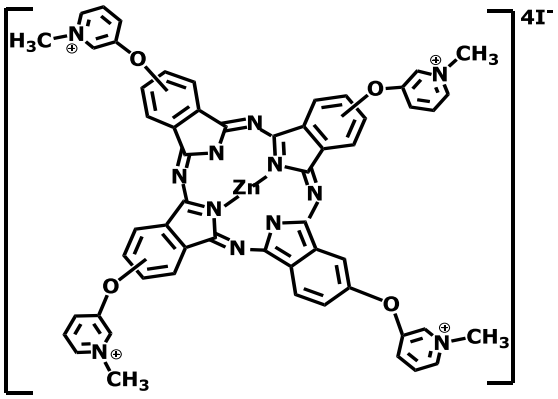	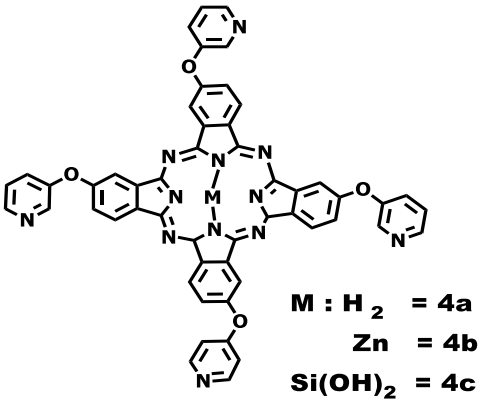
3	**4**
[5, 30, 31]	**[5, 36, 37]**
3-GQDs, 3-CDs and 3-DNDs (π - π)	**4a, 4b-DNDs (π - π) and 4c-DNDs(ester)**
Physicochemical and *In vitro* PDT	Photophysics and NLO

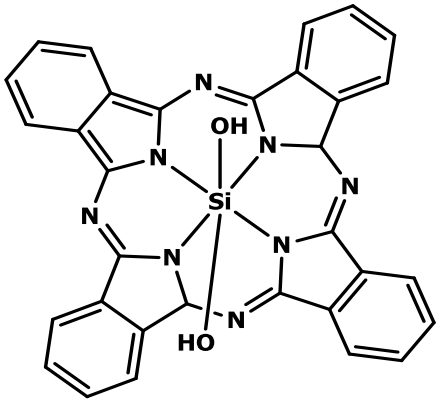

5

[24]

5-DNDs (ester)

Photophysics and NLO

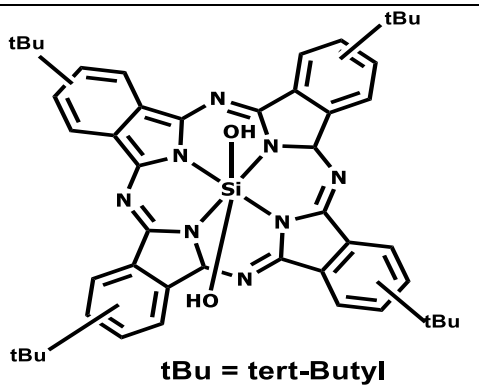

tBu = tert-Butyl

6

[32]

6-DNDs (ester)

Photophysics and NLO

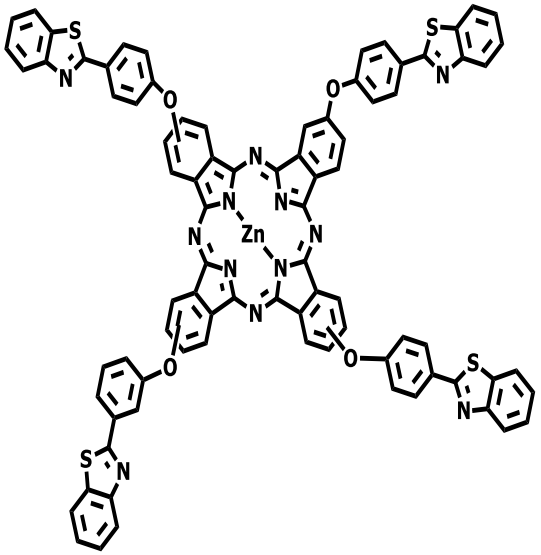

7

[33, 34]

Physicochemical and *In vitro* PDT

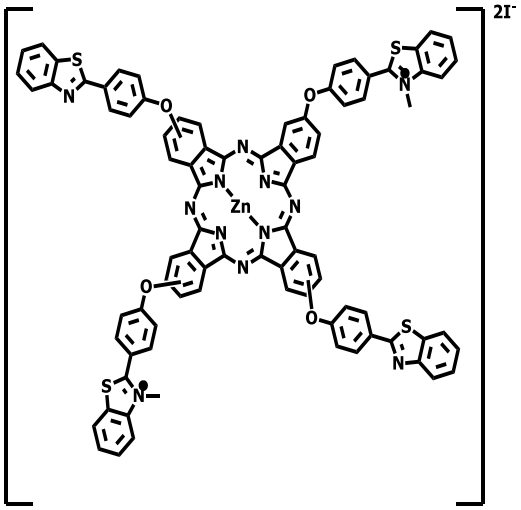

8

(New)

Physicochemical and *In vitro* PDT

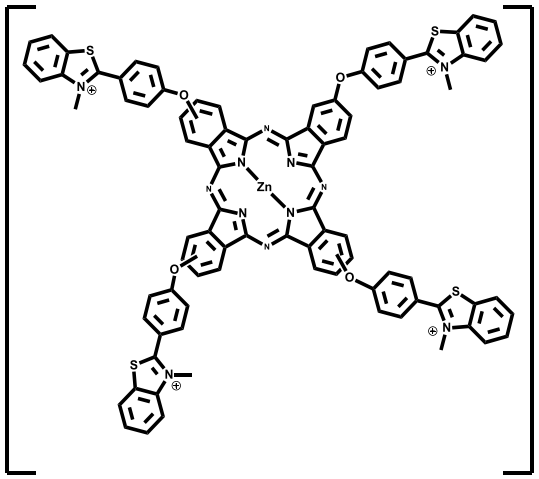

9

(New)

9-B@DNDs (π - π)

Physicochemical and *In vitro* PDT

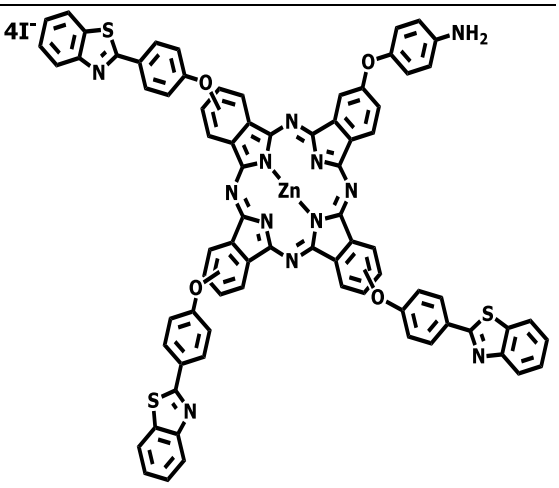

10

(New)

10-B, P, N and N&S @ DNDs (amide)

Physicochemical and *In vitro* PDT

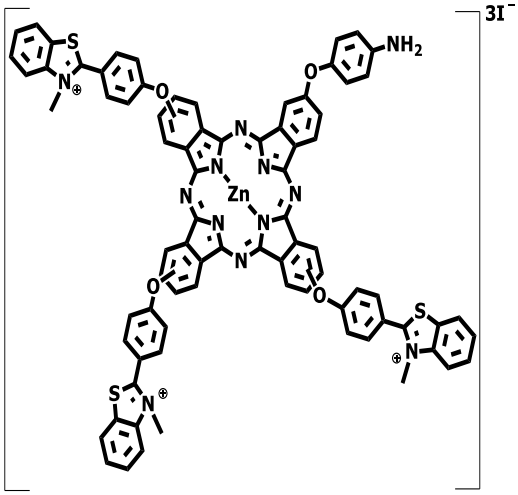

11

(New)

11-B@DNDs (amide)

Physicochemical and *In vitro* PDT

- Complexes **1**, **2**, **4b, 7** will be compared for effect of substituents, on the photophysicochemical properties. Central metal is Zn.

- **7** and **10,** and **8**, and **11** will be compared for the effect of symmetry on photophysical and PDT activity. Central metal is Zn.

- Complex **7**, **8** and **9** will be compared for the effect of charges on photophysical and PDT activity. Central metal is Zn.

- Complex **3** will be compared for the effect of different carbon nanomaterials on the photophysicochemical properties and PDT activity. Central metal is Zn

- Complex **10** will be studied for the effect of doping on DNDs. Central metal is Zn

- Complexes **4c**, **5**, **6** will be compared for effect of substituent on the photophysics and nonlinear optical properties. Central metal is $Si(OH)_2$.

- Complex **4a**, **4b** and **4c** will be compared for the effect of central metals on photophysical and nonlinear characteristics. (Central metals varied)

1.2. Boron dipyrromethenes (BODIPY)

Boron dipyrromethenes (4,4'-difluoro-4-bora-3a,4a-diaza-s-indacenes BODIPY) dyes are a class of planar heterocyclic, fluorescent dyes **[38, 39]**. The central six-membered ring of the BODIPY moiety is almost coplanar with the adjacent pyrrole rings **[40]**. The meso (position 8), α (positions 3 and 5), β (positions 1, 2, 6 and 7) and boron centre (position 4) in **Figure 1.5**, indicate eight reactive positions of BODIPY core that can be used to modulate its optical properties **[39, 41]**.

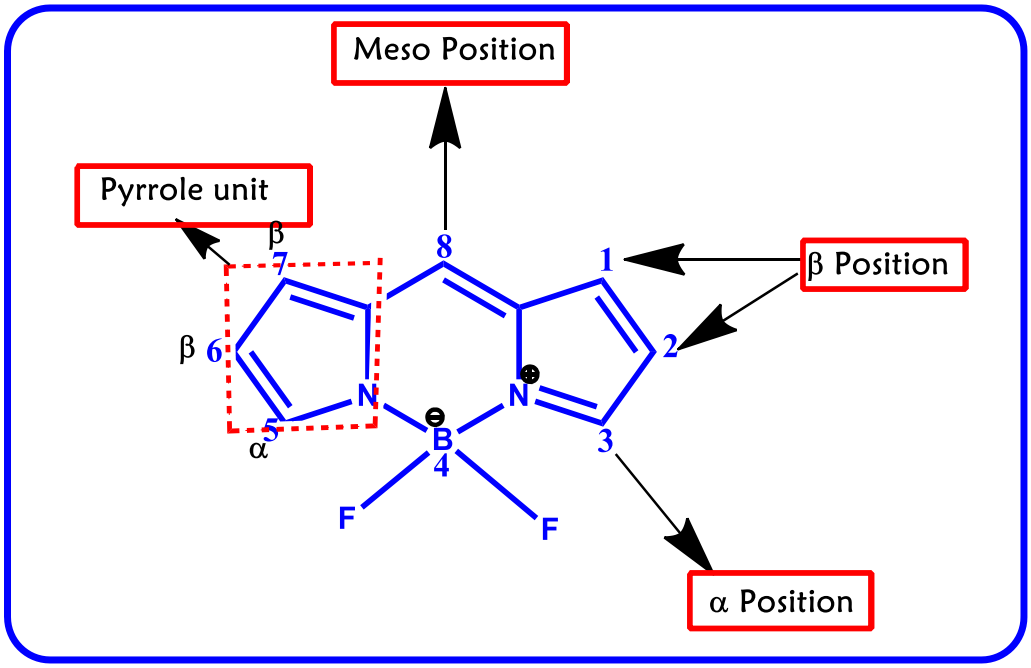

Figure 1.5: Molecular structure of BODIPY dye showing pyrrole unit and meso, β, α substituent positions on the macrocycle.

Slightly polarized heteroatoms on BODIPY dye allows for nucleophilic and electrophilic reaction sites of the molecule **[42]**. Therefore, modification in the BODIPY dye structure through substitution at the meso, peripheral (β) and non-peripheral (α) position of the molecule allows for halogenation and metalation in order to enhance physicochemical characteristics of the dye for application in photodynamic therapy (PDT) **[40, 43-47]**. Improved singlet oxygen generation properties of halogenated styryl-substituted BODIPY have been previously reported **[38, 46]**. Hence, halogenated BODIPY dye is used in this study. Hybrids of BODIPYs with phthalocyanines are very few, and have been shown to have high singlet oxygen quantum yields **[48-53]**. There has been a literature report on physicochemical characteristics of a hybrid structure containing three photosensitising agents such as BODIPY, MPc and graphene quantum dots (GQDs) **[48]**. In this study, physicochemical properties of a composite containing BODIPY, positively charged MPc and detonated nanodiamonds (DNDs) as a platform for potential use in PDT will be investigated.

In this study, the physicochemical and *In vitro* PDT studies of Pc complexes are studied in the presence of 3,5-di-p-benzyloxystyryl BODIPY dye (**Figure 1.6)** and DNDs. The BODIPY employed has been reported **[54]**.

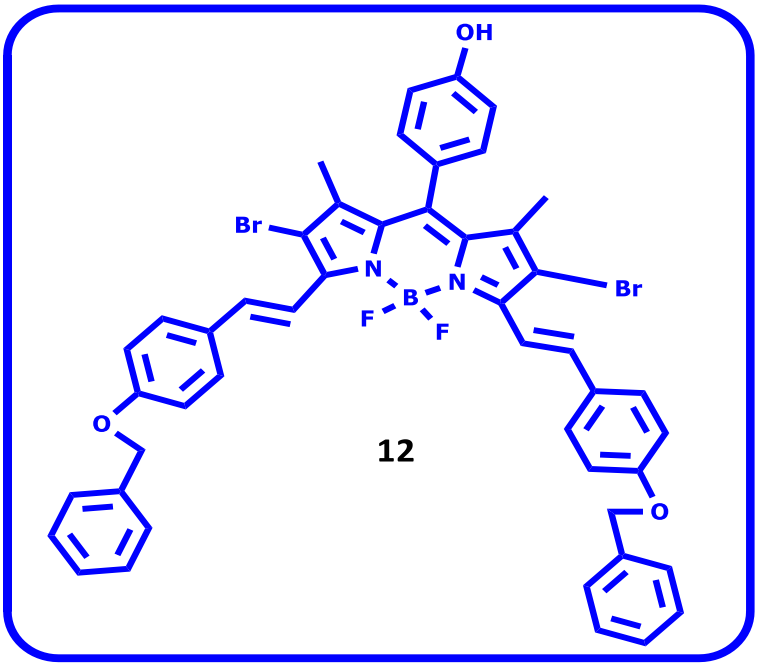

Figure 1.6: Structure of 3,5-di-p-benzyloxystyryl BODIPY **(12) [54]**.

1.3. Carbon nanomaterials

1.3.1. Structure

Large surface energy and stability of carbon nanomaterials are the major reasons they are being vastly researched **[55-58]**. Hence, zero-dimensional carbon allotropes GQDs, CDs and DNDs will be used in this thesis, **Table 1.2.** Modifications of carbon materials with heteroatoms (N, S, S&N, B, etc.) **[59-61]** and inorganic/organic dyes (Pc, BODIPY, etc.) **[60, 62, 63]** have been reported to improve solubility and physicochemical properties. Thus, the choice of heteroatom dopant greatly influences physical characteristics and applicability of the nanomaterial.

Table 1.2: A List of carbon nanoparticles (CNPs) used in this study

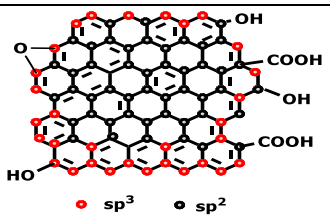

Graphene Quantum dots (GQDs): Physicochemical and *In vitro* PDT

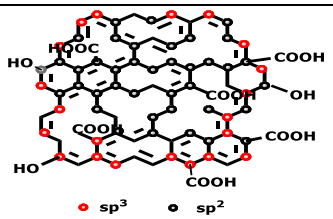

Carbon nanodots (CDs): Physicochemical and *In vitro* PDT

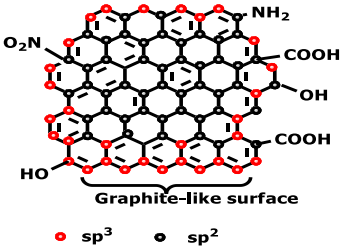

Detonation nanodiamonds (DNDs): Physicochemical and *In vitro* PDT and NLO

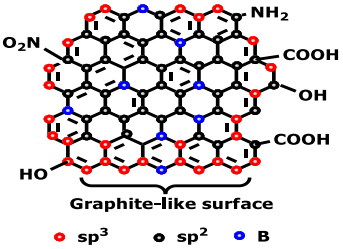

Boron@Detonation nanodiamonds (B@DNDs): Physicochemical and *In vitro* PDT

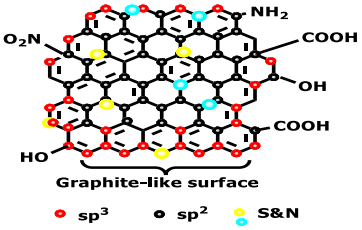

Sulfur and nitrogen@Detonation nanodiamonds (S&N@DNDs): Physicochemical and *In vitro* PDT

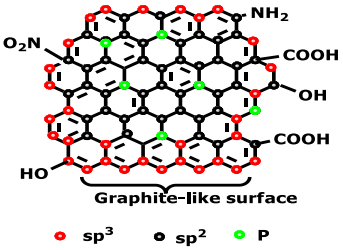

Phosphorus@Detonation nanodiamonds (P@DNDs): Physicochemical and *In vitro* PDT

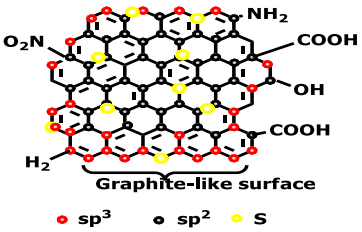

Sulfur @Detonation nanodiamonds (S@DNDs): Physicochemical and *In vitro* PDT

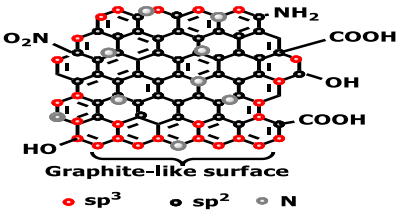

Nitrogen@Detonation nanodiamonds (N@DNDs): Physicochemical and *In vitro* PDT

Graphene quantum dots (GQDs) and carbon nanodots (CDs) are characterized by planar structures that consists of delocalized π electrons of graphene which enables strong π–π interactions with other π-conjugated aromatic molecules **[56, 57]**. Structurally, the carbon backbone of pristine GQDs and CDs is made up of sp^2/sp^3 hybridized nanographene that is edge-terminated with functional groups (e.g. hydroxyl, carbonyl, and carboxyl) **[64-66]**. The presence of carboxyl and hydroxyl functional groups on GQDs surface and edges enable partial solubility, covalent attachment, electrostatic interactions, and hydrogen bonding with other suitable moieties **[67].** In this study, GQDs and CDs will be linked to Pcs by π - π or covalent interaction.

DNDs have tetrahedral network structures, and comprise of a diamond core (sp^3), a middle core (sp^2+x) and a graphitized outer layer (sp^2) that is often partially oxidized **[68]**. In their pristine state, DNDs contain several functional groups present on the surface including amine, amide, alcohol, carbonyl, and carboxyl **[69, 70]**. These functional groups facilitate the linking of DNDs to other molecules. They are π - π or covalently linked to Pcs in this work. Properties of DNDs are dictated by the surface functionalities, diamond core or a combination of both **[71-75]**. Molecular structures and stability of DNDs doped with various heteroatoms (boron, nitrogen, oxygen, sulfur) will be calculated using theoretical simulations **[59, 76].** Doping DNDs with respective heteroatoms result in change in orientation of symmetry and stability **[59]**.

1.3.2. Synthesis

Methods utilised in fabricating various structures of carbon nanomaterials have a great impact on structural and chemical properties of the fabricated nanomaterials **[64, 77-79]**. These methods can be subdivided into two groups (top-down and bottom-up approach) as shown in **Figure 1.7**.

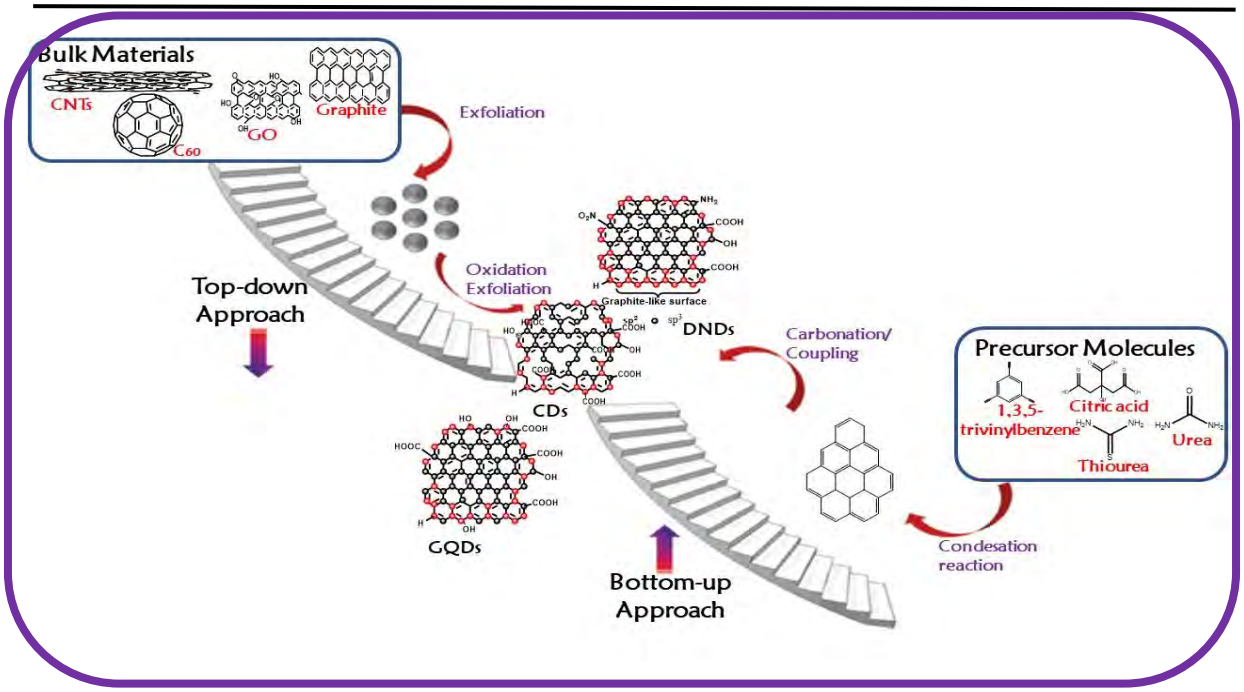

Figure 1.7: Synthetic approaches for carbon nanomaterial: Top-down and Bottom-up approach

1.3.2.1. Top-down Approach

Fabricating graphene quantum dots (GQDs), carbon nanaodots (CDs) and detonation nanodiamonds (DNDs) using the top-down approach can be achieved from carbon materials such as fullerenes **[64, 78, 79]** graphene **[80]**, graphene oxide **[81-83]**, carbon nanotubes **[84, 85]**, carbon fibres **[86]**, natural coal **[87]**, carbon black **[88]**, block co-polymer graphite electrodes **[89]** and metal organic frameworks (MOFs)-derived mesoporous carbon **[90]**. The mechanisms upon which these carbon allotropes are fabricated can occur through cutting down of a bulky carbon based materials via chemical or physical methods such as acid oxidation **[86, 87]**, chemical exfoliation **[86, 88, 91],** hydrothermal **[84]** or solvothermal method **[82]**, electrochemical oxidation **[80, 85]**, ultrasonic-assisted **[92]** or microwave-assisted **[81, 83]**, chemical vapor deposition (CVD) **[89]** and laser ablation **[93]**. The top-down approach is used in this thesis to fabricate GQDs and CDs (Hummers method) while DNDs were purchased.

1.3.2.2. Bottom-up Approach

The bottom-up approach involves uncontrollable synthesis or carbonization from suitable small organic molecules such as citric acid, polymers, urea, thiourea, etc **[60]**. The synthesis of graphene quantum dots using this approach occurs through carbonization method from small molecules or polymers by dehydration and further carbonization **[64, 78, 79]**. The uncontrollable synthesis is not reproducible, and the exact mechanism upon which this approach is not clear.

1.3.3. Electronic ground state absorbance

Broad peaks of GQDs, CDs and DNDs observed in the ground state absorption spectra in **Figure 1.8(a) – (c)**, are associated with π–π* transition of aromatic sp^2 domains **[94]**. Changes in sizes **[95, 96]** and functional groups **[61, 97]** on the nanoparticles results in alterations in the band gap and red or blue shift in absorbance.

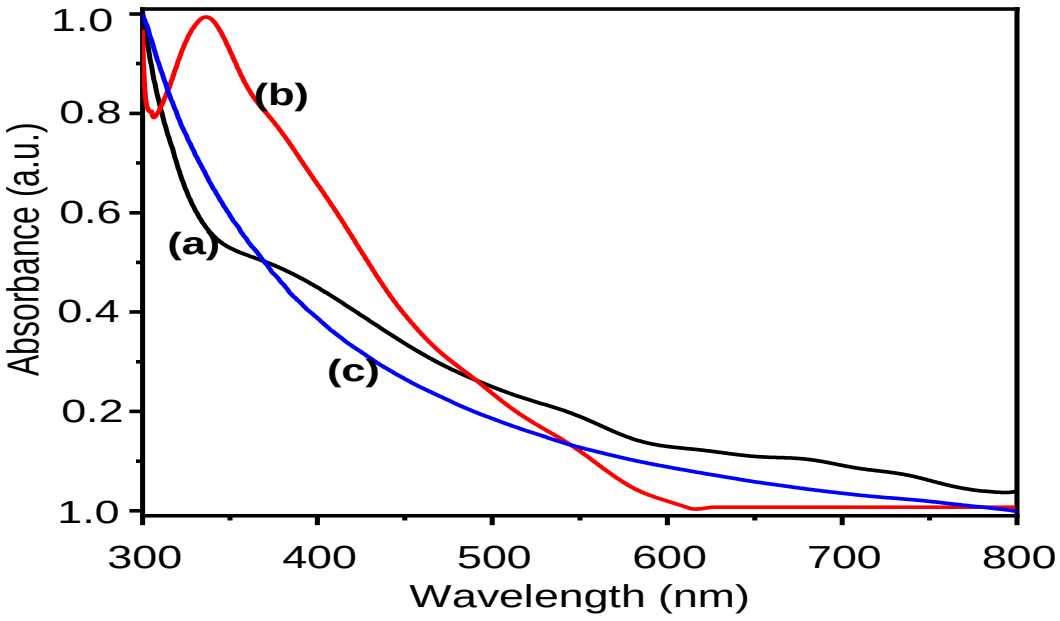

Figure 1.8: Absorption spectra of (a) GQDs, (b) CDs and (c) DNDs in DMSO

1.4. Nanohybrids

A combination of individual photosensitisers such as carbon nanomaterials (GQDs, CDs and DNDs), phthalocyanines (H_2Pc, ZnPc, $Si(OH)_2Pc$) and/or BODIPy dye results in nanohybrids with improved characteristics comprising of dual synergistic effect from the individual components. **Table 1.3** represents the hybrids employed in this work. All are new except **3**-GQDs **[60, 98, 99]**. Complexes **7** and **8** were not studied with nanomaterials.

Table 1.3 Physicochemical characteristics of dyed carbon nanohybirds constructed in this study for application in PDT and NLO

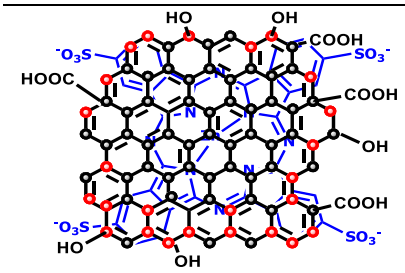	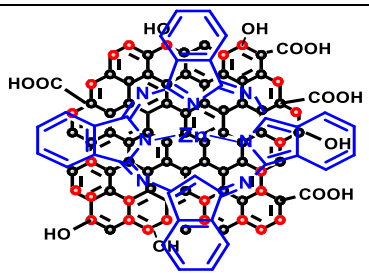
New	**New**
1-GQDs (π - π)	**2-GQDs (π - π)**
Physicochemical	Physicochemical
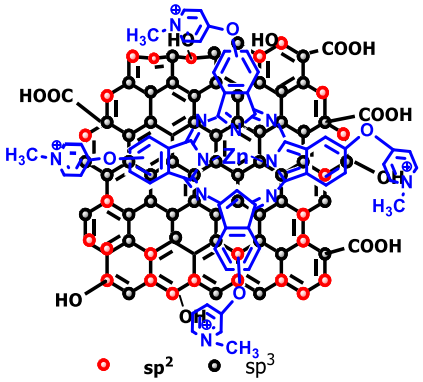	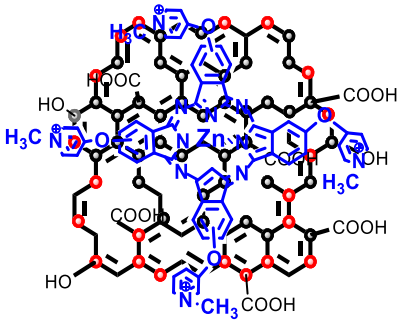
[60, 98, 99]	**New**
3-GQDs (π - π)	**3-CDs (π - π)**
Physicochemical and *In vitro* PDT	Physicochemical and *In vitro* PDT

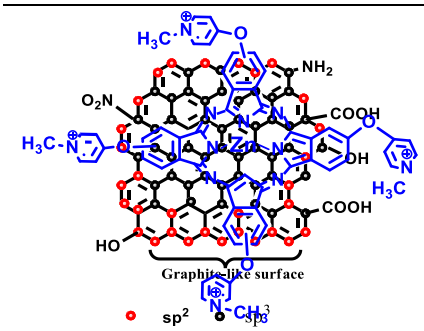

New

3-DNDs (π - π)

Physicochemical and *In vitro* PDT

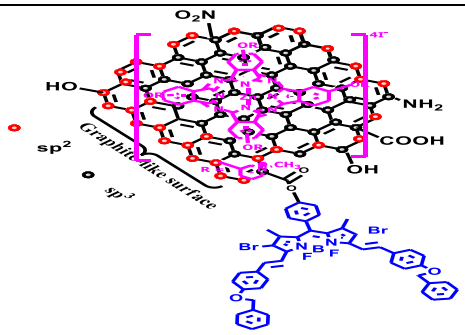

New

3-DNDs@12 (π - π-Pc and ester bond- BODIPY dye)

Physicochemical and *In vitro* PDT

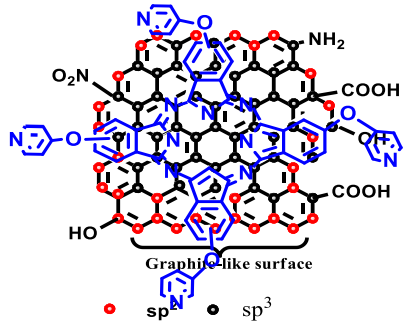

New

4a-DNDs (π - π)

Photophysics and NLO

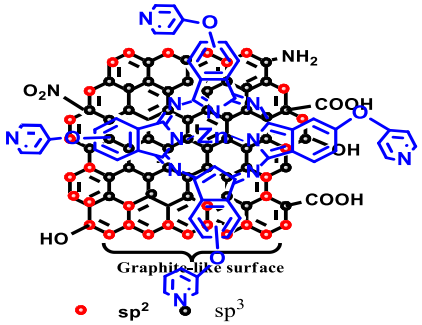

New

4b-DNDs (π - π)

Photophysics and NLO

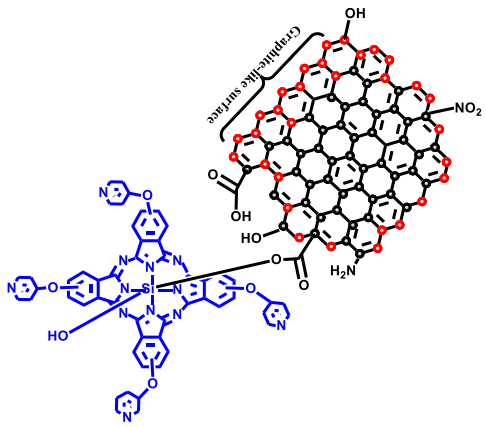

New

4c-DNDs (ester bond)

Photophysics and NLO and Physicochemical and *In vitro* PDT

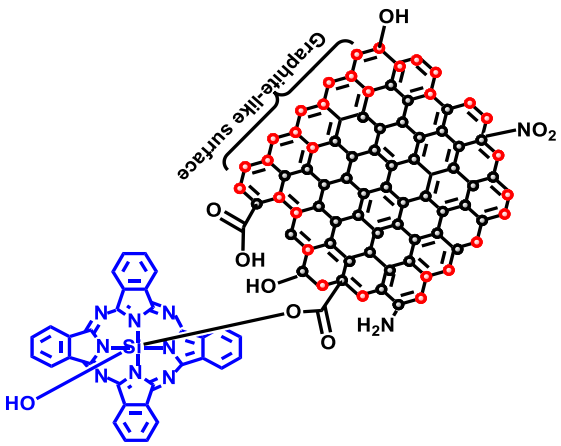

New

5-DNDs (ester bond)

Photophysics and NLO

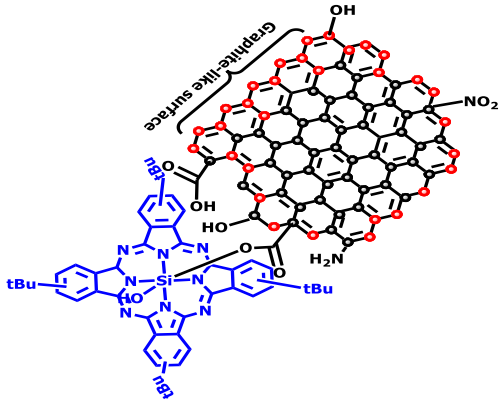

New

6-DNDs (ester bond)

Photophysics and NLO

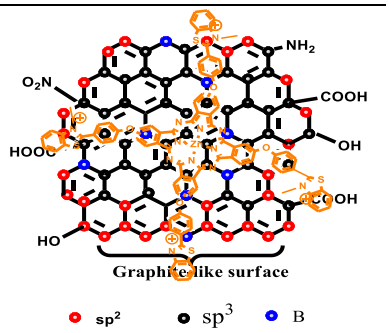

New

9-DNDs@B (π - π)

Physicochemical and *In vitro* PDT

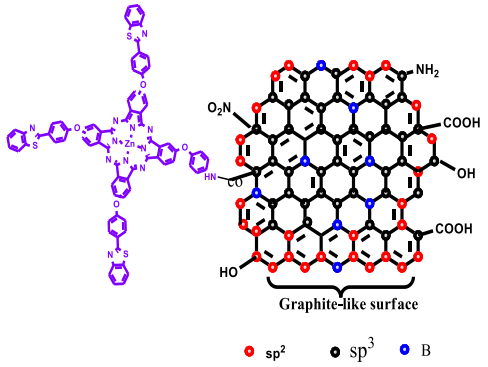

New

10-DNDs@B, P, S, N and S&N (amide bond)

Physicochemical and *In vitro* PDT

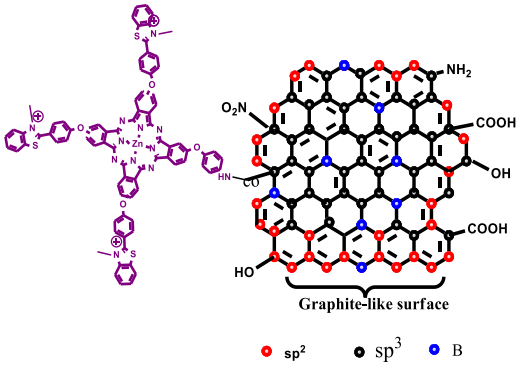

New

11-DNDs@B (amide bond)

Physicochemical and *In vitro* PDT

Table 1.4 shows reported physicochemical parameters such as triplet (Φ_T) and singlet (Φ_Δ) quantum yields of Pc-carbon nanoparticle hybrids **[48, 100-105]**.

Table 1.4: Physicochemical characteristics of dyed carbon nanohybirds for application in PDT and NLO

Nanohybrid	App	Bond	Φ_τ	Φ_Δ	Ref
Carbon nanodots- poly(ethylene glycol) diamine-folic acid/ZnPc (CD-PEG-FA/ZnPc) 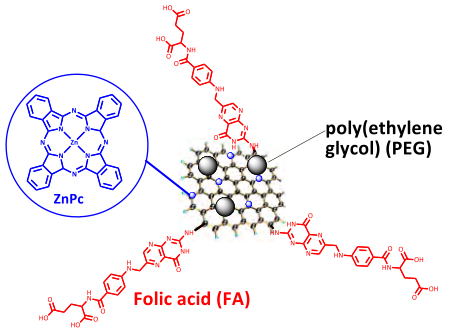	PDT	π - π	-	-	**[105]**
Ascorbic acid doped Graphene quantum dots-tetratrifluoromethyl pyridyloxy ZnPc (GQDs@AA-ZnPc) 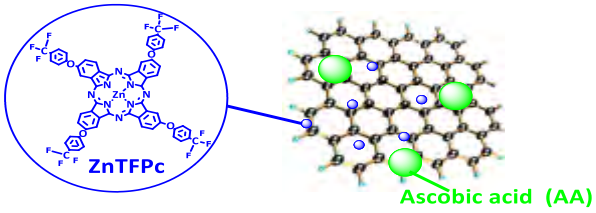	-	π - π	0.96	0.74	**[100]**
Glutathione capped doped Graphene quantum dots-folic acid-aluminium tetrasulfonated Pc (GQD@GSH-FA-AlTSPc), BODIPY dye doped GQDs (BODIPY@GQDs-GSH/ZnPc) 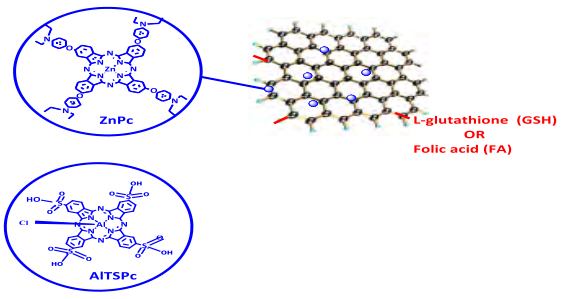	-	π - π	0.73 -	0.54 0.70	**[48, 101]**

GQD@biotin-ZnPc, GQD@biotin-ZnPc(+) 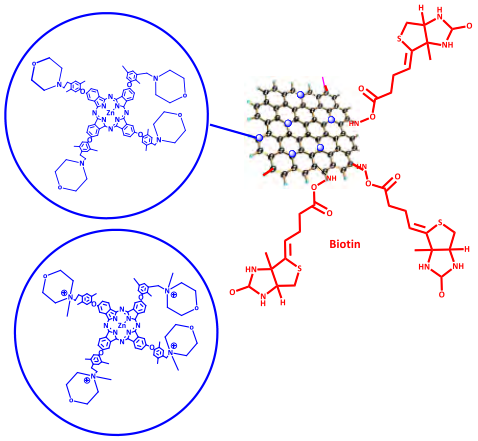	PDT		0.72 0.70	0.47 0.54	**[102]**
Rare-earth functionalised upconversion nanoparticles -GQDs/Tetramethylrhodamine-5-isothiocyanate (UCNPs-GQDs/TRITC) rare-earth doped upconversion nanoparticles (UCNP) with graphene quantum dot (GQD)	PDT	π - π	-	-	**[103]**
GQD-Octa-(3,6-dibromo-9Hcarbazol) ZnPc (GQD-ZnPc) 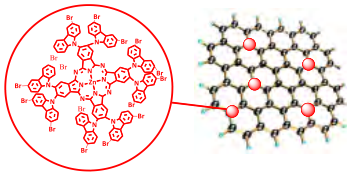	NLO	π - π	0.61	-	**[104]**
Nitrogen (N), sulfur (S) Not@, N,S&N,@GQDs-ZnPc 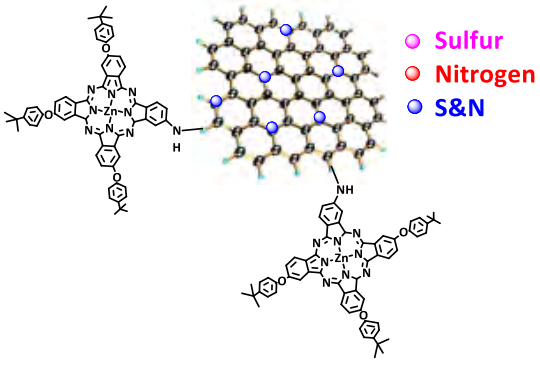	NLO	Amide, π - π	0.74 0.77 0.79	-	**[98, 99]**

Table 1.4 shows that GQDs and CDs have been reported in the presence of Pcs for PDT and nonlinear optics (NLO), DNDs are reported with Pcs for the first time in this thesis. The table shows that only symmetrical Pcs have been used. This thesis reports for the first time asymmetrical Pcs. Asymmetry improves triplet state parameters.

1.5. Molecular modelling

Theoretical calculations require fast, efficient and yet accurate quantum-chemical methods **[106]**. Wave function and density functional theory-based methods reach their limits regarding the feasible system size. Semi-empirical methods utilise approximations to avoid computationally intensive steps, and empirical parameters to obtain the best fit of predicted results **[107]**. Semi-empirical methods are an intermediate between molecular mechanics and ab initio theory. Therefore, the former are considered to be faster than ab initio methods and more versatile than molecular mechanics methods. Semi-empirical quantum mechanical (SQM) methods such as GFNn-xTB (extended tight binding) **[108-110]**, DFTB (density functional tight binding) **[59, 111, 112]**, or PMx **[113, 114]** to name only a few, have established themselves as valuable computational tools. However, in this study visualizations and simulations are conducted in one facet utilising GFN2-xTB as implemented in xTB **[108, 109, 115]** and DFTB+ using the Slater–Koster parameters: 3ob as implemented in Material Studio packages **[116]**.

Molecular structures and stability of phthalocyanines **[112, 117]**, DNDs of various sizes **[59, 72, 75]**, DNDs with functional groups **[71-73, 75]** and dopands **[59, 76]** have been simulated using computational approaches. In this work, molecular structure, stability, reactivity and electronic characteristics of a phthalocyanine in the presence of nanoparticles (using DNDs-Pc and respective doped nanohybrids as examples) are discussed in detail.

1.6. Photodynamic therapy (PDT)

PDT is a selective cancer therapy that utilises specific photosensitisers (dyes, nanomaterials and respective nanocomposites), light of specific wavelength and molecular oxygen to eradicate diseased cancer cells **[118]**. A photosensitiser (PS) in the ground state absorbs light, is electronically excited ($^1PS^*$, PS_n^*) and undergoes intersystem crossing (ISC) to populate the triplet state (**Figure 1.9**). Energy is transferred to ground state molecular oxygen ($^3O_2$) to generate singlet oxygen ($^1O_2$) as illustrated in **Figure 1.9**, also referred to as Type II mechanism. Singlet oxygen is the chief cytotoxic species for PDT and can eradicate diseased cells **[118-121]**.

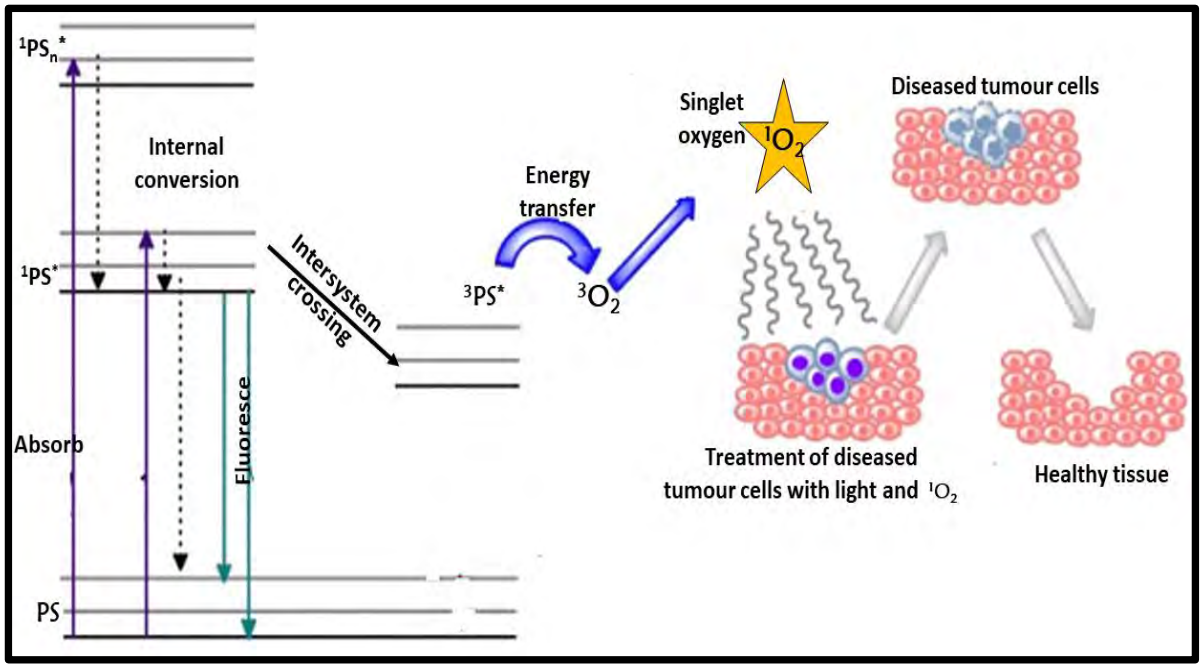

Figure 1.9: Jablonski diagram showing the transitions between ground state (PS) and electronic excited states (^1PS and ^3PS). ^1PS = singlet excited state, ^3PS = first triplet state.

Thus, it is important to study the triplet state population and singlet oxygen generating abilities of potential photosensitizers. In this study, triplet state population and singlet oxygen generating abilities of Pcs are improved in the presence of nanoparticles (GQDs, GQDs, DNDs) and a halogenated styryl-substituted BODIPY dye.

1.7. Nonlinear optics (NLO)

Nonlinear optical limiting material strongly attenuate intense potentially dangerous optical beams, while exhibiting high transmittance for low-intensity ambient light **[33, 34, 99]**. Optical sensors such as human eyes and other optical elements need protection from intense laser pulses. Transmittance of optical limiting material is high at normal light intensity and low under high intensity **[33, 34, 99]**. This is an indication that under linear absorbance **(Figure 1.10)**, output energy linearly depends on input energy until a limiting threshold (I_{lim}) is reached. Under nonlinear absorbing conditions **(Figure 1.10)**, output energy is attenuated to a constant value that causes less damage to the optical sensor. The most important term to note is I_{lim}, it is defined as the input fluence (or energy) at which the transmittance is 50% of the linear transmittance. Therefore, an ideal optical limiting material or device has the characteristic capability to attenuate strongly intense optical beam to a threshold level while maintaining linear transmittance at reduced intensity. In this study, only complexes **4, 5** and **6** are linked to DNDs for enhanced NLO characteristics. Equations for NLO will be discussed in a relevant Chapter. Pcs have been studied in the presence of GQDs for NLO **[99]**. This is the first time DNDs are employed with Pcs for NLO.

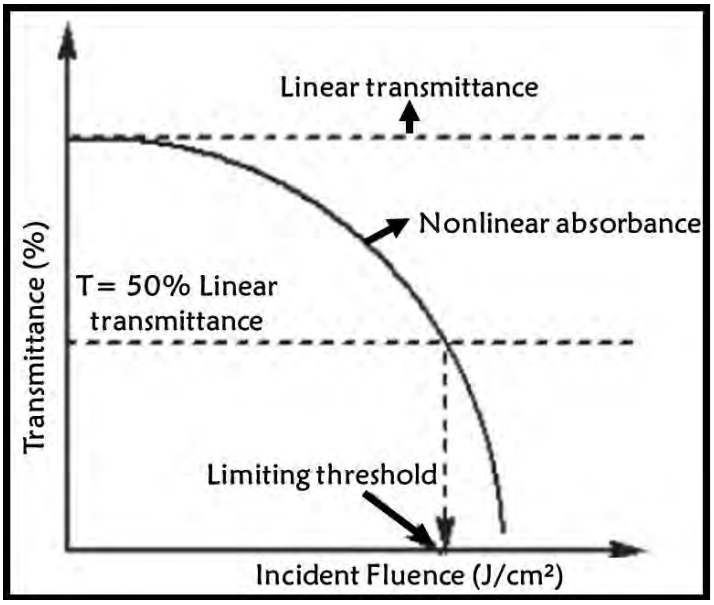

Figure 1.10 Nonlinear optical response of an optical limiter and limitation of output energy to specified value by an ideal optical limiter.

1.8. Physicochemical properties

These parameters include fluorescence quantum yield (Φ_F) and lifetime (τ_F), triplet quantum yield (Φ_T) and lifetime (τ_T) and the singlet oxygen quantum yield (Φ_Δ).

1.8.1. Fluorescence quantum yield (Φ_F) and lifetime (τ_F)

The fluorescence quantum yield (Φ_F) is the ratio of emitted (through fluorescence) relative to absorbed photons. Comparative methods that entail comparison of emission spectrum of a sample with that of a standard when excited at the same wavelength are used to calculate Φ_F using Equation 1.1 **[122, 123]**.

$$\boldsymbol{\Phi_F = \Phi_F^{Std}\ \frac{F\,A_{std}\,n^2}{F_{std}A\,(n_{std})^2}} \qquad \textbf{(1.1)}$$

where n and n_{Std} are the refractive indices of the solvents for sample and standards, respectively; F and $F_{(std)}$ indicate areas under the fluorescence curves for sample and

standards, respectively and Φ_F and $\Phi_{F(Std)}$ are the fluorescence quantum yield of sample and standards, respectively; **[29]**. A and A_{Std} are absorbances of respective sample and standard at the excitation wavelength for sample and standards, respectively. In this study, Φ_F was calculated using unsubstituted ZnPc as a standard in dimethyl sulfoxide (DMSO) (Φ_F = 0.20) **[29]** for the Pcs, quinine sulfate in H_2SO_4 (0.05 M) (Φ_F = 0.52) **[124]** for the GQDs and CDs, and Rhodamine 6G (Φ_F = 0.92) for BODIPY **[124]**. The time a molecule spends in singlet excited state before fluorescing to the ground state is referred to as fluorescence life-time (τ_F) and is quantified with time-correlated single-photon counting (TCSPC) technique in this work **[125]**. Metal centre, substituents, solvents and Förster resonance energy transfer (FRET) are amongst some of the factors that affect Φ_F and τ_F values of Pcs **[122, 126]**.

1.8.2. Triplet quantum yield (Φ_T) and lifetime (τ_T)

Triplet quantum yield (Φ_T) is the ratio of molecules that undergo intersystem crossing (ISC) relative to absorbed photons. Triplet quantum yield values are quantified using comparative methods using Zn phthalocyanine as a standard according to Equation 1.2 **[17, 127, 128]**.

$$\boldsymbol{\Phi_T = \Phi_T^{Std} \frac{\Delta A_T . \varepsilon_T^{Std}}{\varepsilon_T . \Delta A_T^{Std}}} \quad \textbf{(1.2)}$$

where, Φ_T^{Std} is the triplet state quantum yield for the unsubstituted zinc phthalocyanine that is used as a standard in DMSO (Φ_T^{Std} = 0.65) **[128]**. The change in triplet state absorbance of sample and standard are respectively defined by $\Delta \boldsymbol{A_T}$ and $\Delta \boldsymbol{A_T^{Std}}$. $\Delta \boldsymbol{A_s}$ and $\Delta \boldsymbol{A_s^{Std}}$ indicates change in the ground singlet state absorption of samples and respective standard. The molar extinction coefficients of the triplet state of sample and standard ($\boldsymbol{\varepsilon_T}$ and $\boldsymbol{\varepsilon_T^{Std}}$), respectively were determined according to equations 1.3 and 1.4.

$$\boldsymbol{\varepsilon_T = \varepsilon_s . \frac{\Delta A_T}{\Delta A_s}} \quad \textbf{(1.3)}$$

$$\boldsymbol{\varepsilon_T^{Std} = \varepsilon_s^{Std} . \frac{\Delta A_T^{Std}}{\Delta A_S^{Std}}} \quad \textbf{(1.4)}$$

where $\boldsymbol{\varepsilon_s}$ and $\boldsymbol{\varepsilon_s^{Std}}$ are the molar extinction coefficients of the ground singlet state, respectively**.** The duration (μs) for triplet state depopulation is defined as triplet lifetimes. Triplet lifetimes are achieved by using Origin Pro 8 software to fit triplet decay curve obtained from laser flash photolysis instrument.

1.8.3. Singlet oxygen quantum yield (Φ_Δ)

Singlet oxygen quantum yields indicates singlet oxygen species ($^1O_2$), key cytotoxic species in PDT, that results from energy transfer from excited triplet state of the photosensitiser and ground state molecular oxygen ($^3O_2$) illustrated in **Figure 1.9**. Singlet quantum yield values are quantified using comparative chemical methods that utilises singlet oxygen quenchers such as 1,3 diphenylisobenzofuran (DPBF) or anthracene-9,10-bismethylmalonate (ADMA) **[27, 129]**. Respective quenchers react with singlet oxygen generated by the photosensitiser in oxygenated solution (organic solvents and aqueous) and can be spectroscopically monitored over predetermined time intervals to assess the singlet oxygen produced by the photosensitiser (PS). Singlet oxygen quantum yields can be quantified using Equation 1.5.

$$\Phi_\Delta = \Phi_\Delta^{Std} \frac{R \cdot I_{abs}^{Std}}{R^{Std} \cdot I_{abs}} \quad \textbf{(1.5)}$$

where Φ_Δ^{Std} the singlet oxygen quantum yield for the standards; unsubstituted zinc phthalocyanine standard (ZnPc, Φ_{Std} = 0.67) in DMSO **[130]** or aluminium sulfonated phthalocyanine (AlPcSmix (mixture of sulfonated phthalocyanine derivatives) Φ_{Std} = 0.42) in aqueous solutions **[17]** for Pcs and Rose Bengal (Φ_{Std} = 0.76 in DMSO) **[131]** for BODIPY. R *and* R^{Std} are the quenchers photobleaching rate in the presence of the photosensitiser under investigation and the respective standard. I_{abs} *and* I_{abs}^{Std} are the rates of light absorbance respective photosensitiser and standard, respectively equations 1.6 and 1.7 **[132]**.

$$I_{abs} = \frac{\alpha.A.I}{N_A} \quad \textbf{(1.6)}$$

$$I_{abs}^{Std} = \frac{\alpha.A.I}{N_A} \quad \textbf{(1.7)}$$

where $\alpha = 1 - 10^{-A(\lambda)}$, A(λ) is the absorbance of the sensitizer at the illumination wavelength, A is the illuminated cell area (expressed in cm^2), I is the intensity of light (expressed in photons $cm^{-2}s^{-1}$) and N_A is the Avogadro's constant **[17, 132, 133].**

1.8.4. Förster resonance energy transfer (FRET)

Förster resonance energy transfer (FRET) is a non-radiative energy transfer process which occurs between a photoexcited donor fluorophore upon absorption of higher energy photons and an acceptor molecule in close proximity to the donor fluorophore **[134-136]**. The distance (r(Å)) and spectral overlap (J integral) between the donor (GQDs/CDs/DNDs) and acceptor (Pc) indicated in Equations (1.8 - 1.10) are amongst some of the important factors that determine the efficiency of the energy transfer.

$$\boldsymbol{E_{ff} = \frac{R_0^6}{R_0^6 + r^6}} \quad \textbf{(1.8)}$$

$$\boldsymbol{R_0^6 = 8.8 \times 10^{23} k^2 n^{-4} \Phi_{f(donor)} J} \quad \textbf{(1.9)}$$

$$\boldsymbol{J = f_{Donors}(\lambda) \varepsilon_{Pc}(\lambda) \lambda^4 \partial \lambda} \quad \textbf{(1.10)}$$

where r is the centre–to–centre separation distance (in Å) between donor and acceptor, R_0 (the Förster distance, Å) is the critical distance between the donor and the acceptor molecules at which the efficiency of energy transfer is 50%. k^2 is the dipole orientation factor, (the value for the donor-acceptor pairs in a liquid medium is given as 2/3 which are considered to be isotropically oriented during lifetime), n is the solvent's refractive index, $\Phi_{F(Donor)}$ is the fluorescence quantum yield of the donor, f_{Donor} is the normalized donor emission spectrum, ε_{Pc} is the molar extinction coefficient of the MPc $(M^{-1}cm^{-1})$ and λ is the wavelength (nm) at the absorption maximum of the acceptor (Q-band). FRET variables in this study were computed using the PhotochemCAD software **[135]** and the FRET efficiencies (E_{ff}) were determined experimentally from the fluorescence lifetimes or quantum yields of the donor in the absence (τ_A) or ($\Phi_{F(Donor)}$) and presence (τ_p) or ($\Phi_{\mathrm{F(Donors)}}^{conjugate}$) of the acceptor according to equations (1.11, 1.12).

$$E_{ff} = 1 - \frac{\tau_p}{\tau_A} \quad (1.11)$$

$$E_{ff} = 1 - \frac{\phi_{F(Donor)}^{Conjugate}}{\phi_{F(Donor)}} \quad (1.12)$$

1.9. Summary of aims

The aim of this work is to improve physicochemical characteristics of the Pc dyes by constructing carbon nanohybrids with carbon based allotropes (graphene quantum dots, carbon nanodots, detonation nanodiamonds), and BODIPY dye as potential photosensitisers for application in photodynamic therapy and nonlinear optics.

- Synthesis of Pc with different charges, symmetry and central metals.
- Synthesis and characterisation of carbon allotropes: GQDs, CDs and doped DNDs.
- Construction of nanohybrids as indicated in **Table 1.3**.
- Study photophysics and physicochemical characteristics of hybrids.
- PDT of hybrids.
- Study two examples for NLO.

Chapter 2

CHAPTER 2

2. Methodology

This chapter entails details of the materials, equipment and experimental procedures used for the synthesis and characterisation of Pcs, carbon nanoparticles (GQDs, CDs and doped DNDs), and respective nanohybrids (combination of carbon nanoparticle and dye (Pcs and/or BODIPY)), together with applications in PDT and NLO.

2.1. Materials

2.1.1. Solvents

Dimethyl sulfoxide, (DMSO, spectroscopy grade), 1–pentanol, quinoline, DMSO-d_6, $CDCl_3$ and ludox solution were obtained from Sigma Aldrich®. Absolute ethanol (EtOH), methanol (MeOH), acetone, nitric acid (55%), sulphuric acid, tetrahydrofuran (THF) and dimethylformamide (DMF), were obtained from SAARCHEM®. Ultra–pure water was obtained from a Milli–Q Water System (Millipore Corp, Bedford, MA, USA) or Type II water from ELDGA, Veolia water PURELAB, flex system (Marlow, UK).

2.1.2. Chemical reagents

Detonation nanodiamonds (DNDs) were obtained from Nanocarbon Research Institute Ltd. Graphene oxide (GO), quinine sulphate, phosphoric acid, mercaptosuccinic acid, boronic acid, urea, thiourea, zinc (II) acetate dihydrate, 1,8-diazobicylo[5.4.0]undec-7-ene (DBU), unsubstituted zinc phthalocyanine (standard or **2**), methyl iodide, 1,2–dicyanobenzene, N,N'-dicyclohexylcarbodiimide (DCC), N-hydroxysuccinimide (NHS), 1,3-diphenylisobenzofuran (DPBF), anthracene-9,10-bis-methylmalonate (ADMA), Triton X 100, potassium hydroxide pellets, trifluoro acetic acid (TFA), 4-(benzo[d] thiazol-2-yl) phenol **(a)**, and potassium permanganate were purchased from Sigma–Aldrich. The syntheses of 4-nitrophthalonitrile **(c)**

[137], 4-[4-(benzo[d]thiazol-2-yl)phenoxy] phthalonitrile **(e) [34]**, 4-(4-aminophenoxy)phthalonitrile **(f) [138]**, and aluminium sulfonated phthalocyanine (AlPcSmix-mixture of sulfonated phthalocyanine derivatives) **[139]**, 3, 9(10), 16(17), 23(24)-[sulfophthalocyano] zinc (II) **(1) [25-29, 35]**, 3, 9(10), 16(17), 23(24)-[4-(*N*-methylpyridyloxy) phthalocyanato] zinc (II) tetraiodide **(3) [5, 30, 31]**, 3, 9(10), 16(17), 23(24)-[(4-pyridyloxy) phthalocyanato] zinc (II) **(4a) [37]**, 3, 9(10), 16(17), 23(24)-[(4-pyridyloxy) phthalocyanato] zinc (II) **(4b) [5, 37]**, 3, 9(10), 16(17), 23(24)-[(4-pyridyloxy) phthalocyanato] silicon dihydroxide (complex **4c**) **[36]**, 3, 9(10), 16(17), 23(24)- [(4-pyridyloxy) phthalocyanato] silicon dihydroxide **(5) [24]** and 3, 9(10), 16(17), 23(24)-[(butyl) phthalocyanato] silicon dihydroxide **(6) [32]**, 3, 9(10), 16(17), 23(24)-[(4-benzo[d]thiazol-2-ylphenoxy)phthalocyaninato] zinc (II) **(7) [33, 34]** and 3,5-di-p-benzyloxystyryl BODIPY **(12) [54]** have been reported in the literature.

3, 9(10), 16(17), 23(24) [(3-methyl-benzothiazoliumphenoxy) phthalocyaninato] zinc (II) tetraiodide (9)

2.2. Synthesis

2.2.1. Phthalonitriles

2.2.1.1. 3-N-methyl-2-(4-hydroxyphenyl)benzothiazolium iodide (b), Scheme 3.2

A mixture of methyl iodide (1.42 g, 10 mmol) and 4-(benzo[d] thiazol-2-yl) phenol (**a**) (0.8 g, 3.5 mmol) was refluxed at 120^{o} C for 5 h with constant stirring. The reaction mixture was allowed to cool to room temperature and subsequently precipitated using hexane (20 mL). The precipitated solid was isolated by filtering under reduced pressure and washed with hexane (3 x 20 mL). The solid was dried in enclosed fume hood to yield **(b)** 0.92 g (71%) as a light yellow solid. IR(ATR cm^{-1}) ν_{max} 2999.16 (C-H from Ar-H stretch), 1514.54 (C-N stretch), 1448.15 (Ar C-C stretch), 780.21 (CS stretch). ^{1}H NMR (600 MHz, DMSO) δ (ppm) 10.99 (s, 1 H), 8.43 (dd, J = 7.9, 8.1 Hz, 2 H), 8.02 – 7.75 (m, 4 H), 7.13 (d, J = 7.5 Hz, 2 H), 4.25 (s, 3 H)., ^{13}C NMR (75 MHz, $CDCl_3$) δ (ppm) 163.42, 158.41, 140.24, 131.00, 130.41, 129.24, 128.73, 128.04, 125.56, 124.73, 117.55, 116.88, 114.92, 55.01. Elemental Analysis: calculated for $C_{14}H_{12}NOS$, C, 68.70; H, 3.99; N, 6.16; O, 7.04; S, 14.11, Found: C, 68.68; H, 3.97; N, 6.17; S, 14.15.

2.2.1.2. 2-(4-(3,4-dicyanophenoxy)phenyl)-N-methylbenzo[d]thiazolium iodide (d), Scheme 3.2

A mixture of (**b**) (0.6 g, 2.5 mmol) and 4-nitrophthalonitrile (**c**) (0.43 g, 2.5 mmol) in dry DMF (20 mL) was stirred in a 100 mL round bottom flask at 50 °C, under inert atmosphere for 1 h. Dry K_2CO_3 (3 g, 21 mmol) was added and the reaction mixture was allowed to stir undisturbed at ambient temperature for 72 h. The reaction mixture was cooled to room temperature and subsequently precipitated using hexane. The precipitate was filtered under reduced pressure to yield brownish yellow solid. Yield: 0.38 g, (35%), IR (ATR cm^{-1}) ν_{max} 3000.21 (C-H from Ar-H stretch), 2931.21 (C-H from CH_2 stretch) 1561.33 (C-N stretch), 1497.20 (Ar C-C stretch) 778.11 (C-S stretch), ^{1}H NMR (600 MHz, DMSO-d_6) δ (ppm), 8.20 (d, J = 8.0 Hz, 2H, Ar-H), 8.19 – 8.14 (m, 2H, Ar-H), 8.07 (d, J = 8.1 Hz, 1H, Ar-H), 7.96 (s, 1H, Ar-H), 7.56 (t, J = 7.9 Hz, 2H, Ar-H), 7.48 (t, J = 7.6 Hz, 1H, Ar-H), 7.38 (d, J = 8.1 Hz, 2H, Ar-H), 3.85 (s, 3H, CH_3). ^{13}C NMR (75 MHz, $CDCl_3$) δ 179.67, 169.22, 167.08, 153.71, 137.79, 135.34, 134.28, 129.51, 128.98, 127.44, 126.40, 125.43, 122.93, 122.03, 121.56, 50.20, Elemental Analysis: calculated for $C_{22}H_{14}N_3OS^+$ C, 71.72; H, 3.83; N, 11.41; S, 8.70, Found: C, 71.66; H, 3.91; N, 12.09; S, 9.50.

2.2.2. Phthalocyanines

2.2.2.1. 3, 16(17)-(3-methyl-benzothiazoliumphenoxy) 9(10), 23(24)-(benzothiazoliumphenoxy) phthalocyaninato] zinc (II) diiodide (**8**), Scheme 3.1

A solution of methyl iodide (1.42 g, 10 mmol) and complex **7** (0.1 g, 0.07 mmol) in DMF was heated at reflux temperature for 72 h with constant stirring. The reaction mixture was allowed to cool to room temperature and subsequently precipitated using ethanol (20 mL). The precipitated solid was isolated by centrifugation under reduced pressure and washed with ethanol and diethyl ether. Light green solid was dried in enclosed fume hood. Yield: 0.16 g, (40%), IR (ATR cm^{-1}) ν_{max} 3005.52 (C-H from Ar-H stretch), 2931.21 (C-H from CH_2 stretch), 1559.38 (C=N stretch), 1497.20 (Ar C=C stretch) 759.02 (C-S stretch). ^{1}H NMR (600 MHz, DMSO-d_6), (δ, ppm): 8.25-8.17 (m, d, J = 8.2 Hz, 3H, Ar-H), 8.16 – 8.12 (m, 7H, Ar-H), 8.12-8.05 (m, 10H, Ar-H), 7.98-7.87 (m, 7H, Ar-H), 7.64-7.57 (m, 7H, Ar-H), 7.55-7.48 (m, 10H, Ar-H), 4.70 (s, 6H, CH_3). Elemental Analysis: calculated for $C_{86}H_{50}N_{12}O_4S_4Zn^{2+}$: C, 68.45; H, 3.67; N, 10.92;

S, 8.33, Found: C, 67.01; H, 3.52; N, 10.07; S, 9.11. UV-Vis, λ_{max}/nm (log ε): (DMSO), 677(5.03), 614 (4.96), 314 (5.01). MALDI-TOF-MS: Calculated: 1507.13; Found: 1508.72 $[M + 1]^+$

2.2.2.2. 3, 9(10), 16(17), 23(24) [(3-methyl-benzothiazoliumphenoxy) phthalocyaninato] zinc (II) tetraiodide (9), Scheme 3.2

A mixture of zinc acetate (0.20 g, 1.09 mmol), (0.2 g, 0.54 mmol) of **(d)**, DBU (0.2 mL) and 1-pentanol (10 mL) was heated at reflux temperature for 24 h under argon atmosphere. The reaction mixture was precipitated using methanol and collected through centrifugation. The product was washed several times with methanol, ethanol and the light green product was dried under enclosed fumehood. Yield: 0.16 g, (40%), IR (ATR cm^{-1}) ν_{max} 3005.52 (C-H from Ar-H stretch), 2931.21 (C-H from CH_2 stretch), 1559.38 (C=N stretch), 1497.20 (Ar C=C stretch) 759.02 (C-S stretch). ^{1}H NMR (600 MHz, DMSO-d_6), (δ, ppm): 8.25-8.17 (m, d, J = 8.2 Hz, 3H, Ar-H), 8.20 – 8.11 (m, 7H, Ar-H), 8.03-8.00 (m, 10H, Ar-H), 7.98- 7.85 (m, 7H, Ar-H), 7.66-7.56 (m, 7H, Ar-H), 7.49-7.40 (m, 10H, Ar-H), 4.52 (s, 12H, CH_3). Elemental Analysis: calculated for $C_{88}H_{56}N_{12}O_4S_4Zn^{4+}$: C, 68.67; H, 3.67; N, 10.92; S, 8.33, Found: C, 69.32; H, 3.49; N, 11.07; S, 7.89. UV-Vis, λ_{max}/nm (log ε): (DMSO), 679 (5.23), 617 (4.46), 318 (4.97). MALDI-TOF-MS: Calculated: 1536.27; Found: 1537.04 $[M + 1]^{+\cdot}$

2.2.2.3. 9(10), 16(17), 23(24) [(benzo[d]thiazole-2-yl)phenoxy), 3 (aminophenoxyl) phthalocyaninato] zinc (II) (10), Scheme 3.3

A mixture of **(e)** (1 g, 2.83 mmol), 4-(4)-aminophenoxy)phthalonitrile (**f**) (0.22 g, 0.94 mmol), zinc acetate (0.4 g, 2.19 mmol), DBU (3 drops) and 1-pentanol (10 mL) was refluxed at 160 °C for 18 h under nitrogen atmosphere. On cooling, methanol was added and the precipitate was collected through centrifugation. The product was washed with methanol, ethanol and diethyl ether. Column chromatography showed several fractions using tetrahydrofuran and methanol (98:2) as eluents. The desired A_3B product was identified through mass spectrometry and ^{1}H NMR. The purified product was dried in enclosed fume hood. Yield 0.18g (15%).

IR υ_{max} /cm^{-1}]: 1595 (N-H), 2906, 2956 (C–H), 2350 (C=N), 1395 (C-N), 1099 (CS), 938 (Zn-N). ^{1}H NMR (600 MHz, DMSO) δ 8.13 (dd, J = 10.4, 8.8 Hz, 6H, Ar-H), 8.08 – 7.99 (m, 8H, Ar-H), 7.93 (d, J = 2.5 Hz, 4H, Ar-H), 7.91 – 7.82 (m, 3H, Ar-H), 7.63 (dd, J = 9.2, 6.5 Hz, 3H, Ar-H), 7.53 (dd, J = 8.7, 2.6 Hz, 4H, Ar-H), 7.50 – 7.41 (m, 4H, Ar-H), 7.31 – 7.22 (m, 8H, Ar-H), 6.61 (s, 2H, amino-H). Elemental Analysis for $C_{77}H_{42}N_{12}O_4S_3Zn$: calculated: C, 67.98; H, 3.09; N, 12.35; S, 7.07, Found C, 68.72; H, 2.23; N, 11.58, S, 6.77. UV-Vis (DMSO), [λ_{max} (log ε): 681 (6.96), 624 (2.10). MALDI TOF-MS, calc 1358.19, found 1360.32 [M + 2].

2.2.2.4. 9(10), 16(17), 23(24) [(3-methyl-benzothiazoliumphenoxy), 3 (aminophenoxyl) phthalocyaninato] zinc (II) triiodide (11), Scheme 3.3

Positively charged mono substituted Pc (**11**) in **Scheme 3.3** was obtained as follows: (**d**) (1 g, 2.83 mmol), (**f**) (0.22 g, 0.94 mmol), zinc acetate (0.4 g, 2.19 mmol), DBU (3 drops) and 1-pentanol (10 mL) was refluxed at 160 °C for 18 h under nitrogen atmosphere. On cooling, methanol was added, and the precipitate was collected through centrifugation. The product was washed with methanol, ethanol and diethyl ether. Column chromatography showed several fractions using tetrahydrofuran and methanol (98:2) as eluents. The desired A_3B product (**11**) was identified through mass spectrometry and NMR. The purified product of yield: 0.18g (13%) was dried in enclosed fume hood.

IR υ_{max} /cm^{-1}]: 1595 (NH_2), 2916, 2837 (C–H), 1395 (CN), 1099 (CS), 938 (Zn-N). ^{1}H NMR (600 MHz, DMSO) δ 8.25 (dd, J = 10.2, 8.5 Hz, 8H, Ar-H), 8.12 (d, 8.5 Hz, 6H, Ar-H), 8.05 (d, J = 2.7 Hz, 3H, Ar-H), 7.91 – 7.88 (m, 3H, Ar-H), 7.65-7.59 (M, 8H, Ar-H), 7.49 (dd, J = 8.5, 2.8 Hz, 4H, Ar-H), 7.35 – 7.30 (m, 8H, Ar-H), 5.50 (s, 2H, amino-H), 3.60 (s, 6H, N-methyl-H), 3.30 (s, 3H, N-methyl-H). Elemental Analysis: calculated: C, 68.34; H, 3.66; N, 11.96; O, 4.55; S, 6.84; Found C, 68.02; H, 3.99; N, 11.08, S, 5.95 %).UV-Vis (DMSO), λ_{max} (log ε): 682 (5.73), 609 (5.37), 312 (1.35). MALDI TOF-MS, $C_{80}H_{51}N_{12}O_4S_3Zn^{2+}$ calc 1403.26, found 1403.88.

2.2.3. Graphene quantum dots (GQDs) and carbon nanodots (CDs)

GQDs were synthesised following the top-down approach from GO sheet as the source of carbon, and using $KMnO_4$ and H_2SO_4 as oxidative cutting agents. GO (1 g) was suspended in 60 mL (98 %) H_2SO_4 for 2 h in an ice-water bath, and 50 wt% $KMnO_4$ was slowly added with stirring for 0.5 h. The mixture was then heated to 50 °C for 1 h in order to shear the carbon precursor. The reaction mixture was quenched by pouring ice containing small amounts of hydrogen peroxide (H_2O_2), followed by 70 mL millipore water to obtain a yellow transparent solution. The mixture was sonicated for 10 min, then the pH was tuned to basic using 1 mol L^{-1} NaOH solution in an ice bath until black flocculent deposit formed, which was then dialyzed for 72 h using a dialysis membrane (MW 1.5 kDa) to remove excess salts yielding 39.1% GQDs. Different sizes of GQDs were synthesised by increasing the oxidation duration and temperature as follows: (2 h; 50 °C), (6 h, 70 °C) and (10 h; 50 °C) for $GQDs_2$, $GQDs_6$ and $GQDs_{10}$, respectively. Three different batches of GQDs (Batch 1-(B_1), Batch 2-(B_2) and Batch 3 (B_3)) were synthesised under conditions of $GQDs_2$ represented as B1, B2, and B3. Carbon nanodots were synthesised and purified the same way as GQDs, except the amount of $KMnO_4$ was increased to 70% and time in the presence of H_2SO_4 was increased to 12 h.

2.2.4. Doping of nanodiamonds (DNDs)

Boron doped detonation nanodiamonds (B@DNDs) were synthesised with alterations following literature methods as follows **[60]**: boronic acid (0.12 g, 1 mmol) and DNDs (2.4 g) were dissolved in water (100 mL), and stirred to form a clear solution. Then the solution was transferred into a 400 mL Teflon lined stainless autoclave. The sealed autoclave was heated to 160 °C for 4 h. The final product was collected by adding ethanol into the solution and centrifuging at 5000 rpm for 15 min. Similarly, P@DNDs, N@DNDs, S@DNDs and S&N@DNDs: were prepared as described above for B@DNDs, using masses of 0.10 g, 0.06 g, 1.65 g, 0.08 g for phosphoric acid, urea, mercaptosuccinic acid and thiourea, respectively, in place of boronic acid.

2.2.5. Conjugation

Conjugation of nanohybrids between nanoparticle and phthalocyanine/BODIPY occurs following non-covalent (π - π interaction, **Scheme 3.4**) and covalent bond (**Schemes 3.5 –** ester Pc**, 3.6** - ester BODIPY**,** or **3.7 –** amide Pc).

2.2.5.1. π - π Interaction

*Interaction of complexes (**1-3, 4a, 4b**, and **9**),* **Scheme 3.4**

Conjugation of graphene quantum dots (GQDs: $GQDs_2$(B1), $GQDs_2$(B2), $GQDs_2$(B3), $GQDs_6$ and $GQDs_{10}$) for complexes **1-3**, CDs and DNDs to **3** and DNDs to **4a, 4b, 9,** occurs through non-covalent linkage. Complexes **1** (0.01 g, 0.012 mmol) or **2** (0.01 g, 0.002 mmol) or **3** (0.01 g; 0.01 mmol), or **4a** (24 mg, 0.03 mmol) or **4b** (27 mg, 0.05 mmol) or **9** (0.02 g, 9.56 mmol) and were each separately mixed with GQDs (10 mg, for **1-3**) or CDs (20 mg for **3**), or DNDs (20 mg for **3, 4a, 4b, 9**) in 5 mL of DMSO and sonicated for 4 h, followed by overnight stirring for 48 h. Thereafter, the conjugates were centrifuged at 3000 rpm for 10 min in ethanol to precipitate the conjugate out of the solution and remove unreacted Pc derivatives or GQDs, CDs and DNDs. The resulting nanoconjugates were left to dry in a fume hood for 72 h. Represented as NPs - Pc (π - π)

2.2.5.2. Ester bond, Schemes 3.5, 3.6

Respective phthalocyanines **(4c, 5, 6)** or BODIPY **(12)** were covalently linked to the DNDs surface through ester bond, **Schemes 3.5, 3.6**, as follows: DNDs (20 mg) were dissolved in DMSO (3 mL), followed by addition of DCC (0.02 g, 0.098 mmol) to activate the carboxylic acid moiety. The reaction mixtures were stirred for 48 h and followed by addition of **4c** (25 mg, 0.03 mmol) or **5** (25 mg, 0.04 mol) or **6** (25 mg, 0.03 mol) or **12** (0.008 g, 0.01 mmol) and NHS (0.015 g, 0.13 mmol) and the reaction mixtures were further stirred for 48 h. It is important to note that non-covalent interaction are also possible when covalently linking **4c, 5, 6, 12** and DNDs. Thereafter, the mixtures were centrifuged at 3500 rpm for 5 min in ethanol to

precipitate the DNDs-Pc conjugates out of the solution and remove unreacted Pc derivatives or DNDs. The resulting DNDs-**4a**, DNDs-**5** and DNDs-**6** nanoconjugates were left to dry in a fume hood for 72 h. Note that for complex **12** only, the resulting conjugate (DNDs-**12**) was precipitated out from solution with trifluoroacetic acid (TFA) and ice. The precipitates were washed several times with water, centrifuged, and then dried in the fume hood. Represented as Pc-DNDs ester.

2.2.5.3. Construction of 3-DNDs-12 (Scheme 3.6)

Complex **3** (0.01 g; 0.01 mmol) was adsorbed onto DNDs-**12** (10 mg) or DNDs (10 mg) through π - π stacking in 3 mL DMSO. The resulting mixture was ultrasonicated for 4 h, followed by stirring for 96 h. The resulting conjugates were precipitated out of solution with ethanol to ensure that uncomplexed DNDs-**12**, DNDs and Pc were eliminated. The solid product was then dried under vacuum and are represented as **3**-DNDs-**12**. It should be noted that in the presence of complex **12**, **3** is written before DNDs as **3**–DNDs-**2**. In the absence of complex **12**, DNDs-**3** is used.

2.2.5.4. Amide bond, Scheme 3.7

Covalent linkage of doped DNDs nanoparticles to complex **10,** was carried out from first sonicating 20 mg of heteroatom doped nanodiamonds (DNDs) (S@DNDs, N@DNDs, S&N@DNDs, B@DNDs and P@DNDs) for 4 h and left to stir at room temperature for 72 h in order to activate respective nanoparticles using DCC (0.02g, 0.097 mmol) and NHS (0.015g, 0.130 mmol). This was followed by addition of complex **10** (20 mg, 0.01 mmol, in DMSO) and further stirring for 48 h at room temperature. Thereafter, the mixtures were centrifuged at 3000 rpm for 10 min in ethanol to precipitate respective nanoconjugates (DNDs-**10**, N@DNDs-**10**, S@DNDs-**10**, B@DNDs-**10,** P@DNDs-**10** and S&N@DNDs-**10**) out of the solution and remove unreacted Pc derivatives and DNDs. The resulting nanoconjugates were left to dry in a fume hood for 72 h. Complex **11** was linked similarly to B@DNDs only using the same amounts.

2.3. Equipment

❖ Dynamic light scattering (DLS)

Malvern Zetasizer Nanoseries, Nano-ZS90 particle distribution samples were investigated using dynamic light scattering (DLS) and zeta potential to provide information about the average size distribution and zeta potential of molecules in solution **[140, 141].**

❖ Transmission electron microscope (TEM)

Zeiss Libra 120 model transmission electron microscope (TEM) at 80 kV was used to investigate the morphology of nanoparticles and respective hybrids.

❖ UV-Visible spectroscopy (UV-Vis)

Ground state electronic absorption spectra was recorded with Shimadzu UV-2550 spectrophotometer. Varian Eclipse spectrofluorimeter with 360 – 1100 nm filter was employed for recording excitation and emission spectra.

❖ Time correlated single photon counting (TCSPC)

Fluorescence lifetimes were measured using a time correlated single photon counting (TCSPC) setup (Fluo Time 300, Picoquant GmbH) in **Figure 2.1** with a diode laser as an excitation source: LDH-P-670 driven by PDL 800-B, 670 nm, 20 MHz repetition rate, Picoquant GmbH, for the Pcs; and a diode laser LDH-P-485 with 10 MHz repetition rate, 88 ps pulse width for GQDs and CDs. Thermoelectrically cooled photomultiplier tube (PMT) (PMA-C 192-N-M, Picoquant GmbH) under entrancing angle and integrated electronics (PicoHarp 300E, Picoquant GmbH) were used to detect fluorescence. The specific emission wavelength with spectral width of about 4 nm was selected through a monochromator. Ludox solution (DuPont) standard with full width at half-maximum (FWHM) of about 300 ps was used to calibrate and indicate the response function of the system. All fluorescence decay curves were measured at the wavelength of emission maxima. The data were analysed with the FluoFit

software (Picoquant®). Statistical significance of the results was kept at p = 0.05. The support plane approach was used to estimate the errors of the decay times **[136]**.

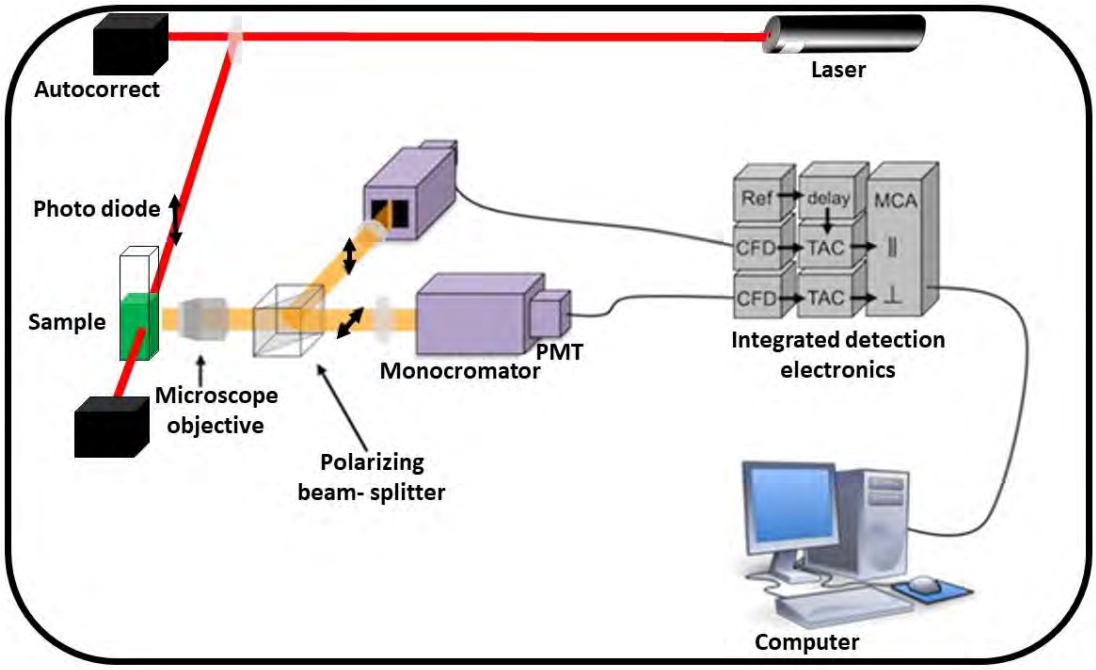

Figure 2.1: Schematic representation of time correlated single photon counting (TCSPC) set–up. PMT = Monochromator Photomultiplier Tube

❖ Matrix-Assisted spectrometry (MS)

Mass spectra data were collected on a Bruker AutoFLEX III Smart-beam TOF/TOF mass spectrometer using α-cyano-4-hydrocinnamic acid as the matrix in the positive ion mode.

❖ Elemental analyses

Elemental analyses of Pcs were analysed using a Vario-Elementar® Microcube ELIII CHNS instrument analyzer.

❖ Nuclear magnetic resonance spectroscopy (NMR)

^{1}H NMR spectra will be recorded on a Bruker AVANCE II 600 MHz NMR spectrometers using tetramethylsilane (TMS) as an internal reference about the structure of novel phthalocyanines synthesised.

❖ X-ray photoelectron spectroscopy (XPS) analysis

X-ray photoelectron spectroscopy (XPS) analysis will be conducted using an AXIS Ultra DLD (supplied by Kratos Analytical) using Al (monochromatic) anode equipped with a charge neutralizer, the following parameters were used: the emission was 10 mA, the anode (HT) was 15 kV and the operating pressure below 5 $\times 10^{-9}$ Torr. A hybrid lens was used and resolution to acquire scans was at 160 eV pass energy in slot mode. The centre used for the scans was at 520 eV (width of 1205 eV) with steps at 1 eV and dwell time at 100 ms **[98]**.

❖ Energy dispersive X-ray spectroscopy (EDX)

Elemental compositions of the NPs and the nanoconjugates were qualitatively determined using energy dispersive X-ray spectroscopy (EDX), INCA PENTA FET coupled to the VAGA TESCAM operated at 20 kV acceleratin voltage.

❖ X-ray diffraction (XRD)

X-ray diffraction (XRD) analysis was performed on a Bruker D8 Discover diffractometer, equipped with a Lynx Eye detector, under Cu-Kα radiation (λ=1.5405 Å). Zero background silicon wafer slide was utilised as a sample holder. The data analysis was carried out using Eva (evaluation curve fitting) software. The XRD patterns were fitted through background subtraction obtained when correcting the baseline of each diffraction pattern and obtaining the full-width at half maximum value from respective spectra.

❖ **Fourier-transform infrared spectroscopy (FT-IR)**

FT-IR spectra were recorded using Bruker alpha model FTIR spectrometer with platinum-ATR.

❖ **Raman spectroscopy**

Raman spectra were recorded with Bruker vertex 70-Ram II Raman spectrometer (1064 nm Nd:YAG laser and liquid nitrogen cooled germanium detector).

❖ **Thermogravimetric characterization technique (TGA)**

Thermogravimetric analysis (TGA) was carried out using a Perkin Elmer TGA 800 thermogravimetric analyser at a heating rate of 20 °C min^{-1} in a high-purity nitrogen and air atmosphere. The resultant data was analysed with Pyris Version 13.1.1 software. The TGA technique is used to calculate the mass loading ratio **[142]**. This involves comparing the mass in the TGA pan after decomposition of the conjugate with that of the Pc before the conjugation. Equal masses (mg) for Pc and respective conjugate were weighed separately in the TGA pan and then heated in argon to 850 °C. This was followed by comparing the masses of the Pc in a conjugate with that of the Pc before the conjugation.

❖ **Laser flash photolysis**

Triplet state quantum yields were determined using a laser flash photolysis system consisting of an LP980 spectrometer with a PMT-LP detector and an ICCD camera (Andor DH320T-25F03). The signal from a PMT detector was recorded on a Tektronix TDS3012C digital storage oscilloscope. The excitation pulses were produced by a tunable laser system consisting of a Nd:YAG laser (355 nm, 135 mJ/4‑6 ns), pumping an optical parametric oscillator (OPO, 30 mJ/3‑5 ns) with a 420 to 2300 nm (NT-342B, Ekspla) wavelength range. Triplet lifetimes were determined by the exponential fitting of the kinetic curves using the ORIGIN 6 Professional software. The absorbance value used for triplet state studies was fixed at 1.5 and the solution degassed by bubbling argon for 30 min prior to measurements.

❖ **Singlet oxygen**

Singlet oxygen quantum yield is determined using chemical methods that utilises indirect methods to determine singlet oxygen quantum yields. The method involves of quenching of the absorption of a molecule sensitive to the singlet oxygen such as DPBF in organic solvents or ADMA in aqueous solution. The amount of quenching is related to the quantity of singlet oxygen species of a sample being analysed. Experimental setup of this is illustrated in **Figure 2.2 [143]**. Photo-irradiations for singlet oxygen studies were done using a General Electric Quartz line lamp (300W). A 600 nm glass cut off filter (Schott) and a water filter were used to filter off ultraviolet and infrared radiations, respectively. An interference filter (Intor, 700 nm with a band width of 40 nm) was additionally placed in the light path before the sample. Light intensities were measured with a POWER MAX5100 (Molelectron detector incorporated) power meter. Light intensity was determined to be 2.87×10^{15} photons s^{-1} cm^{-2}. For singlet oxygen studies, a solution (2 mL) composed of photosensitizer (about 10^{-6} M, based on the Pc) and ADMA or DPBF (10^{-4} M) was irradiated in a 1 cm path length cell.

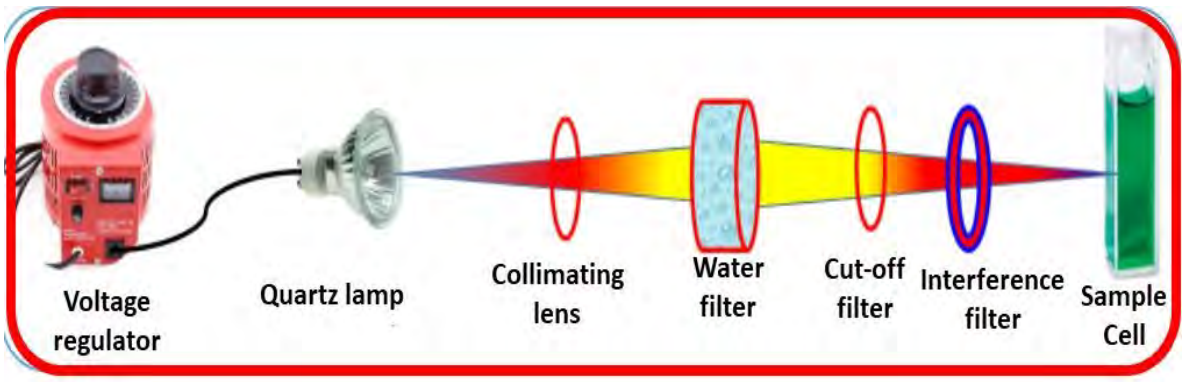

Figure 2.2: Schematic illustration of the set-up of an indirect detection of singlet oxygen

❖ **Theoretical calculations**

Molecular stabilities were determined for structures of complex **10** (alone), 1 nm nanodiamond (core obtained from crystallographic data), and its conjugates were build with

the 3D atomistic document of material studio library **[116]**. The minima used for all structures were obtained from the conformer generation module in material studio **[116]**. Following construction of systems in Materials Studio, geometry optimizations were carried out within extended tight binding (xtb) using GFN2-xTB with an electronic temperature of 300K **[108, 109, 115]**. Highest occupied molecular orbital-lowest unoccupied molecular orbital (HOMO-LUMO) gap values were extracted from the difference between the highest occupied and lowest unoccupied Kohn-Sham orbitals from the xtb output. The molecular orbital densities were visualized using the density functional based tight binding (DFTB+) surfaces **[116]**.

2.4. Photodynamic therapy

2.4.1. Materials for photodynamic therapy (PDT)

Complexes **3,7-12** and conjugates were used as examples for PDT studies. Michigan Cancer Foundation-7 (MCF-7) breast cancer cell lines were obtained from Cellonex. Trypsin ethylenediaminetetraacetic acid (EDTA), trypan blue, Dulbecco's phosphate-buffered saline (DPBS) and Dulbecco's modified Eagle's medium (DMEM) were obtained from Sigma Aldrich. Heat-inactivated fetal calf serum (FCS), neutral red cell proliferation reagent (WST-1), and 100 µg/mL-penicillin-100 unit/mL-streptomycin-amphotericin B mixture were obtained from Lonza (Biowest).

The stock concentrations of each drug was prepared by dissolving each in DMSO (1%) and making the volume up with supplemented media. All nanomaterials and respective conjugates are partially soluble in water but not all Pc complexes are soluble in water. Hence, 1% DMSO in water was used for complete solubility. The cells were incubated for 24 h with 1% (v/v) of DMSO in supplemented media in order to assess the effects of DMSO, at a concentration of 0 µg/mL of the drug (labelled control) in Chapter 6. The surviving cells were subsequently quantified using the WST-1 cell proliferation assay 24 h after the treatment.

2.4.2. Dark and PDT toxicity studies

The MCF-7 cells were cultured in 75 cm^2 vented flasks (Porvair®) in a humidified atmosphere incubator with ~5% CO_2 at 37 ^oC (Heal Force®). A Zeiss® AxioVert. A1 Fluorescence LED (FL-LED) inverted microscope was used for routine microscopy. Photo-irradiations for PDT studies were performed using a General Electric Quartz line projector lamp (300W). A 600 nm glass cut off filter (Schott) and water filter were used to cut off ultraviolet and far infrared radiations, respectively. An interference filter (Intor, 700 nm with a band width of 40 nm) was placed in the light path before the sample. Light intensities were measured with a POWER MAX5100 (Molelectron detector incorporated) power meter and found to be 2.87×10^{15} photons s^{-1} cm^{-2} for PDT studies. An illumination kit, with a capacity to hold a 127.76 x 85.48 mm 96 well tissue culture plate for in vitro PDT studies was used. The cell viability was measured using the WST1 cell proliferation neutral red reagent as described above.

2.4.3. Statistical analysis

The data obtained from the three independent (n=3) triplicate experiments were analysed with a 3-way factorial ANOVA (analysis of variance) to determine the statistical differences between the in vitro cytotoxicity and photodynamic effect of the photosensitizers on MCF-7 cancer cells. p-value of <0.05 was considered significant

2.5. Nonlinear optics

Z-scan analysis were performed using frequency doubled Nd:YAG laser (Quanta-Ray, 1.5 J/10 ns fwhm pulse duration) as the excitation source. The laser was operated in a near Gaussian transverse mode at 532 nm (second harmonic) with low repetition rate of the lasers to prevent cumulative thermal nonlinearities, details have been provided before **[144].** Z-scan profiles were determined at absorbances: 0.1, 02, 0.3, 0.4, 1 and energies 20, 30, 60, and 80 µJ when DNDs were conjugated with complexes **4a, 4b, 4c**, **5** and **6**.

List of Publications Originating from this work

PUBLICATIONS

1. **Matshitse R**. Sekhosana K. Achadu O. Nyokong T. Characterization and physicochemical studies of the conjugates of graphene quantum dots with differently charged zinc phthalocyanines. J. Coord. Chem. 70 (2017) 3308-3324.

2. **Matshitse R.** Nyokong T. Singlet oxygen generating properties of different sizes of charged graphene quantum dot nanoconjugates with a positively charged phthalocyanine, J. Fluoresc. 28 (2018) 827–838.

3. **Matshitse R.** Nwaji N. Mananga M. Prinsloo E. Nyokong T. Effect of number of positive charges on the photophysical and photodynamic therapy activities of quarternary benzothiazole substituted zinc phthalocyanine. J. Photochem. Photobiol. A: 367 (2018) 253-260.

4. **Matshitse R.** Managa M. Nyokong T. The modulation of the photophysical and photodynamic therapy activities of a phthalocyanine by detonation nanodiamonds: Comparison with graphene quantum dots and carbon nanodots. Diam. Relat. Mater. 2020; 101: 10 pages (ID 1077617).

5. **Matshitse R.** Ngoy B.P. Managa M. Mack J Nyokong T. Photophysical properties and photodynamic therapy activities of detonated nanodiamonds-BODIPY-phthalocyanines nanosemblies. Photodiagnosis Photodyn. Ther. 26 (2019) 101–110.

6. **Matshitse R.** Khene S. Nyokong T. Photophysical and nonlinear optical characteristics of pyridyl substituted phthalocyanine - detonation nanodiamond conjugated systems in solution. Diam. Relat. Mater. 94 (2019) 218-232.

7. **Matshitse R.** Nyokong, T. Substituent effect on the photophysical and nonlinear optical characteristics of Si phthalocyanine - detonated nanodiamond conjugated systems in solution. Inorg. Chim. Acta (2020) 504: 119447.

8. **Matshitse R.** Tshiwawa T. Managa M. Nwaji N. Lobb K. Nyokong, T. Theoretical and photodynamic therapy characteristics of heteroatom doped detonation nanodiamonds linked to asymmetrical phthalocyanine for eradication of breast cancer cells. J. Lumin. (2020) 227: 117465.

9. **Matshitse R.** Nwaji N. Managa M. Chen Z-L. Nyokong T. Photodynamic therapy characteristics of phthalocyanine in the presence of boron doped detonation nanodiamonds: Effect of symmetry and charge. Submitted to Diam. Relat. Mater.

Extra Publications

10. Centane S. Sekhosana E.K. **Matshitse R.** Nyokong T. Electrocatalytic activity of a push-pull phthalocyanine in the presence of reduced and amino functionalized graphene quantum dots towards the electrooxidation of hydrazine. Journal of Electroanalytical Chemistry, 820 (2018) 146–160.

11. Openda Y. I. **Matshitse R.** Nyokong T. A search for enhanced photodynamic activity against *Staphylococcus aureus* planktonic cells and biofilms: the evaluation of phthalocyanine–detonation nanodiamond–Ag nanoconjugates. Photochem. Photobiol. Sci. 19 (2020) 1442-1454.

Results and Discussion

Results and Discussion

3. Synthesis and characterization

4. Photophysical and photochemical properties

5. Molecular modelling

6. Photodynamic therapy

7. Nonlinear optical characteristics

8. Conclusion and recommendation

Chapter 3

3. Synthesis and characterization

This chapter entails synthesis and the characterization of phthalocyanines (Pcs), carbon nanomaterials (GQDs, CDs, DNDs, doped DNDs) and respective nanohybrids.

3.1. Phthalocyanines (Pcs)

The syntheses of complexes **1 [25-29, 35]** and **3-7** have been published before **[5, 30-37]** and **2** is purchased. The characterization of new complexes **8-11** will be discussed in detail in the following subsections.

3.1.1. Synthesis of symmetric phthalocyanine complexes 8 and 9

The synthesis of tetrakis[(4-benzo[d]thiazol-2-ylphenoxy)phthalocyaninato] zinc (II) **(7)** has been previously reported **[33, 34]** and was used as the starting material for the synthesis of the quaternary derivative 3, 16(17)-(3-methyl-benzothiazoliumphenoxy) 9(10), 23(24)-(benzothiazoliumphenoxy) phthalocyaninato] zinc (II) diiodide **(8)**. The well-known method of quaternization **[145-147]** was used for the synthesis of complex **8** (**Scheme 3.1**) using methyl iodide as the quaternizing agent.

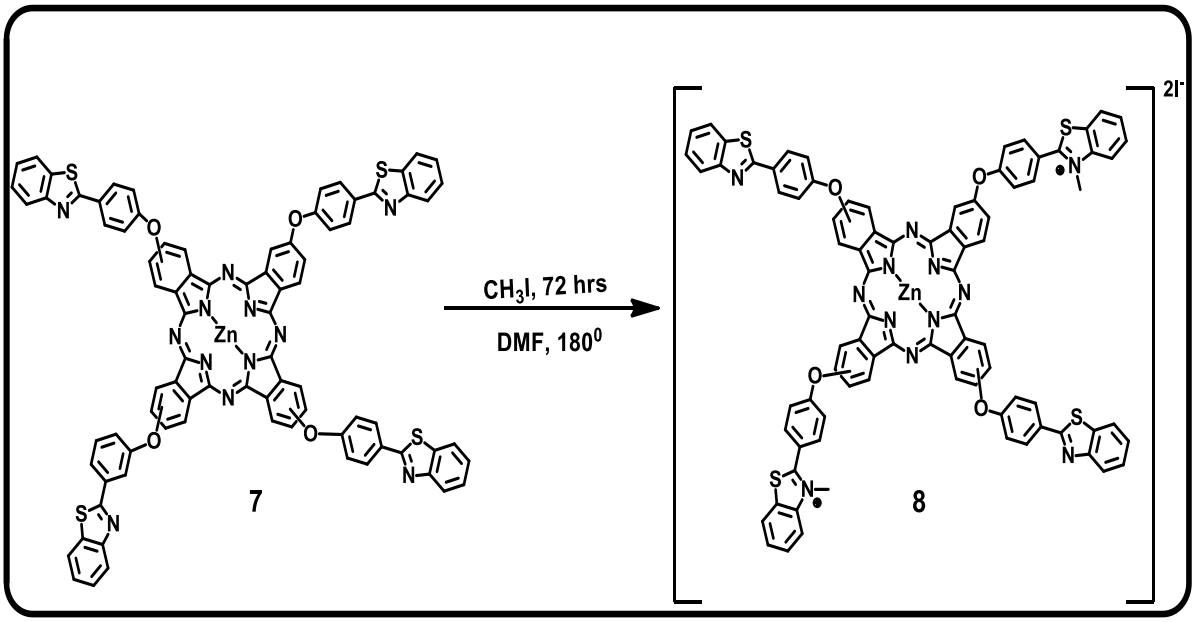

Scheme 3.1: Synthesis of complex **8**

The MALDI-TOF and ^{1}H NMR mass spectra analysis showed that only partial quaternization of complex **(7)** resulted in complex **(8)** (**Figures 3.1, 3.2**). This could be due to either that the quaternary compound precipitates out of the solution or due to evaporation of the methyl iodide (bp = 42 °C) at the high reaction temperatures. Even though the scheme shows a cis arrangement, this is just a representation, the two quaternized groups could be in any other location. To afford a fully quaternized derivative (complex **(9)**), **Scheme 3.2**, a different synthetic route to obtain the quaternary phthalonitrile derivative was followed. This involves the quaternization of 4-(benzo[d] thiazol-2-yl) phenol **(a)** to yield **(b)**, followed by coupling with 4-nitrophthalonitrile **(c)** to result in **(d)**.

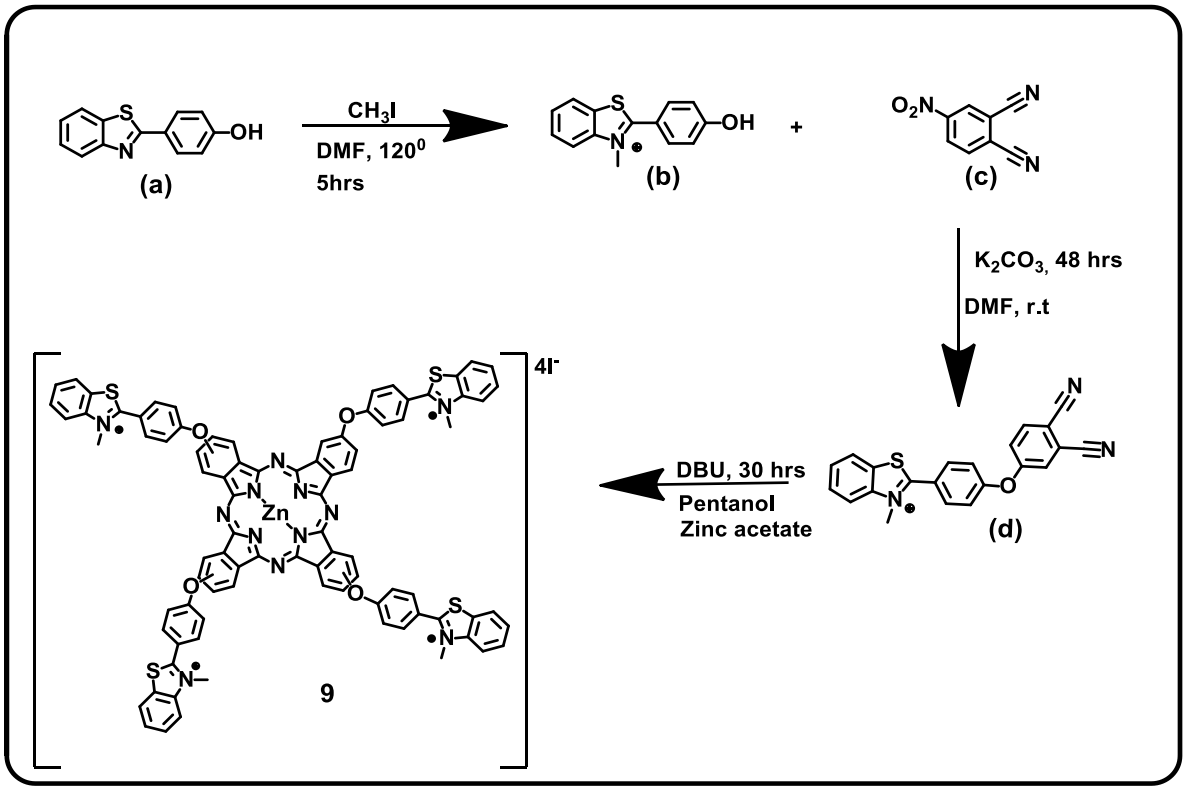

Scheme 3.2: Synthesis of complex **9**

The structure and purity of all the complexes were confirmed using UV-Vis, IR, mass spectra (**Figure 3.1**), ^{1}H NMR (**Figure 3.2**) and elemental analyses, which agreed with the proposed structure as described in experimental section.

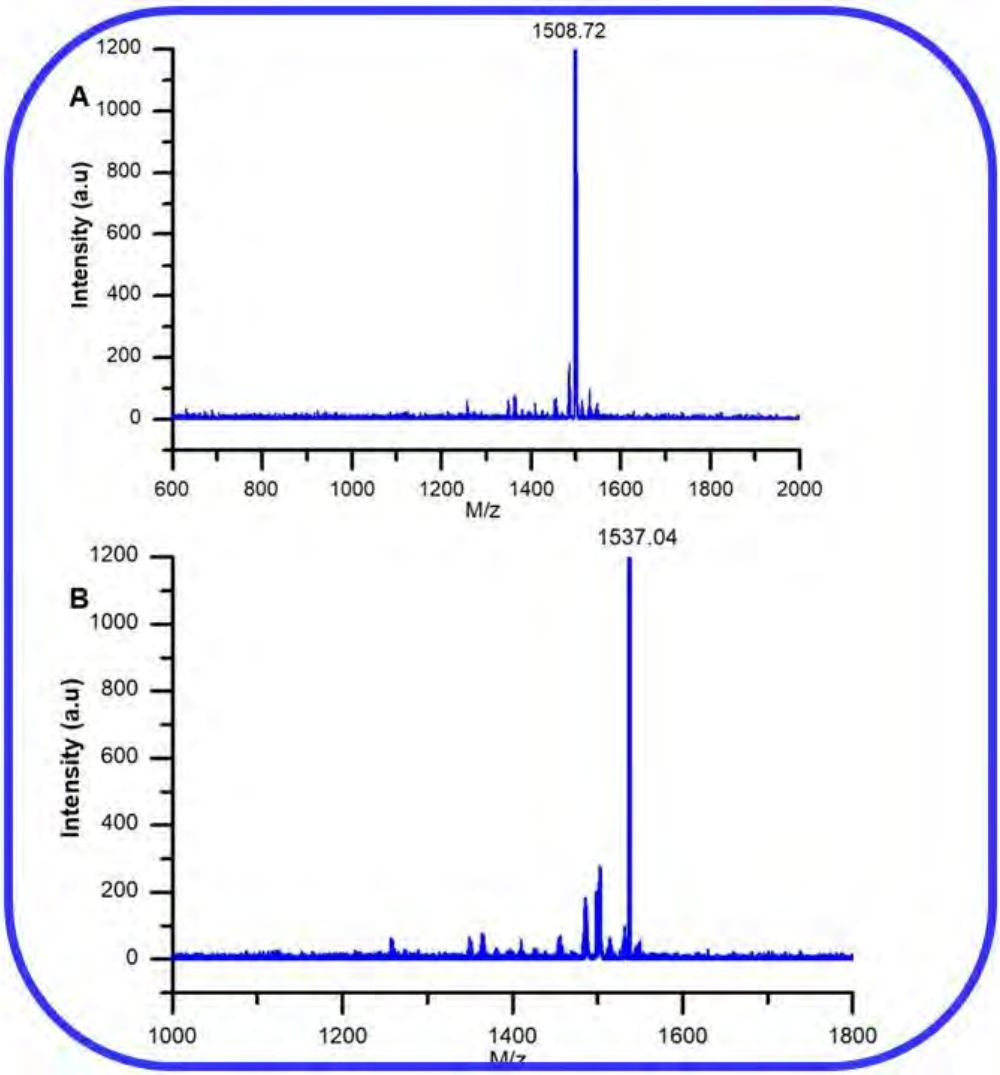

Figure 3.1: MALDI-TOF mass spectra of (A) **8** and (B) **9**

For complex **8**, the aromatic protons of the benzothiazole moiety appeared between 8.25-7.48 ppm and gave 44 protons on integration. Evidence of quaternization was confirmed by the appearance of protons from methyl group around 4.7 ppm which gave 6 protons on integration (**Figure 3.2**)

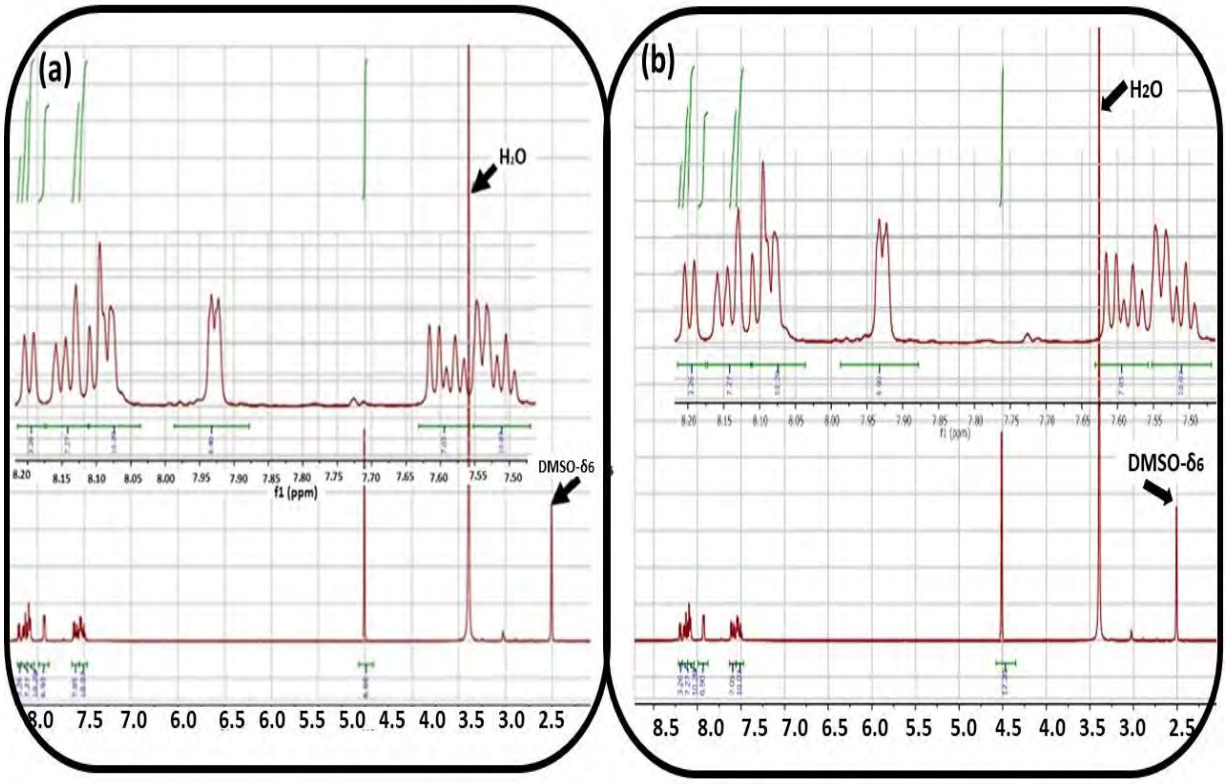

Figure 3.2: ^{1}H NMR of complex **8** (a) and **9** (b) in DMSO-d_6

The ^{1}H NMR spectra of complex **9** is similar to that of **8** with only minor differences in chemical shifts of the aromatic benzothiazole moiety. Full quaternization of complex **9** was confirmed with the appearance of methyl group protons at 4.52 ppm integrated into 12 protons.

3.1.2. Complexes 10 and 11

The synthesis of complex **10** and **11** (**Scheme 3.3**) was accomplished by statistical condensation of 4-[4-(benzo[d]thiazol-2-yl)phenoxy] phthalonitrile **(e)** (for **10**) or phthalonitrile **(d)** (for **11**) with 4-(4-aminophenoxy)phthalonitrile **(f)** in the presence of zinc acetate and 1-pentanol.

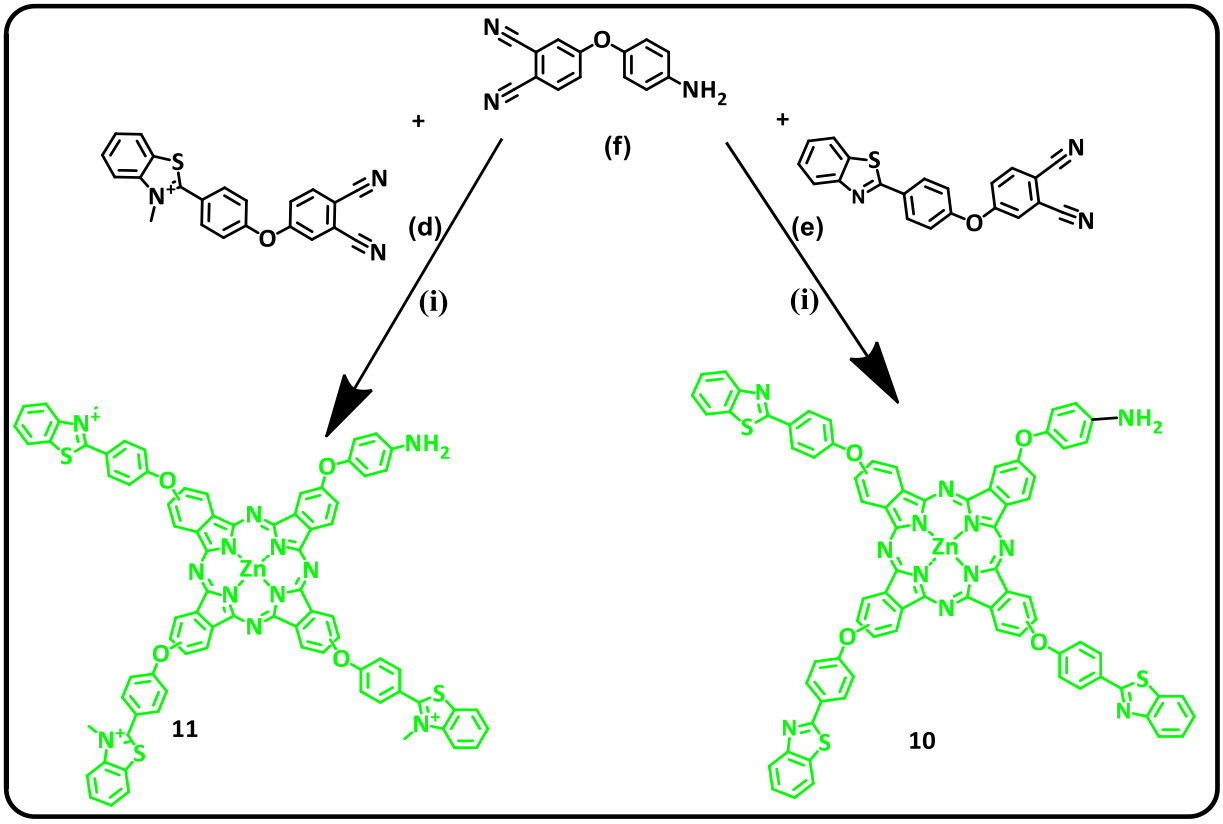

Scheme 3.3: 9(10), 16(17), 23(24) [(benzo[d]thiazole-2-yl)phenoxy) 3 (aminophenoxyl) phthalocyaninato] zinc (II) (**10**) and the corresponding quaternary analogue 9(10), 16(17), 23(24) [(3-methyl-benzothiazoliumphenoxy) 2(3) (aminophenoxyl) phthalocyaninato] zinc (II) triiodide (**11**). (i)=Pentanol, DBU, 160^{o}C, 18 h.

The FTIR, ^{1}H NMR, UV-Vis and elemental analysis data all agreed with the proposed structure in **Scheme 3.3**. The protons of the terminal amino substituent, observed at 6.61 and 5.50 ppm respectively for 9(10), 16(17), 23(24) [(benzothiazoliumphenoxy) 3 (aminophenoxyl) phthalocyaninato] zinc (II) triiodide **(10)** and 9(10), 16(17), 23(24) [(3-methyl-benzothiazoliumphenoxy) 3 (aminophenoxyl) phthalocyaninato] zinc (II) triiodide **(11)**, in the ^{1}H NMR spectra in **Figure 3.3 (a, b**) of complex **10** and **11** integrated into 2 protons. The protons due to methyl group in the quaternary complex **11** resonate at 3.60 ppm and 3.30 ppm integrating to give a total of nine protons. The aromatic protons for the complexes were found between 8.13 – 7.22 ppm for **10** and 8.25-7.30 for **11** and integrated to give anticipated number of protons.

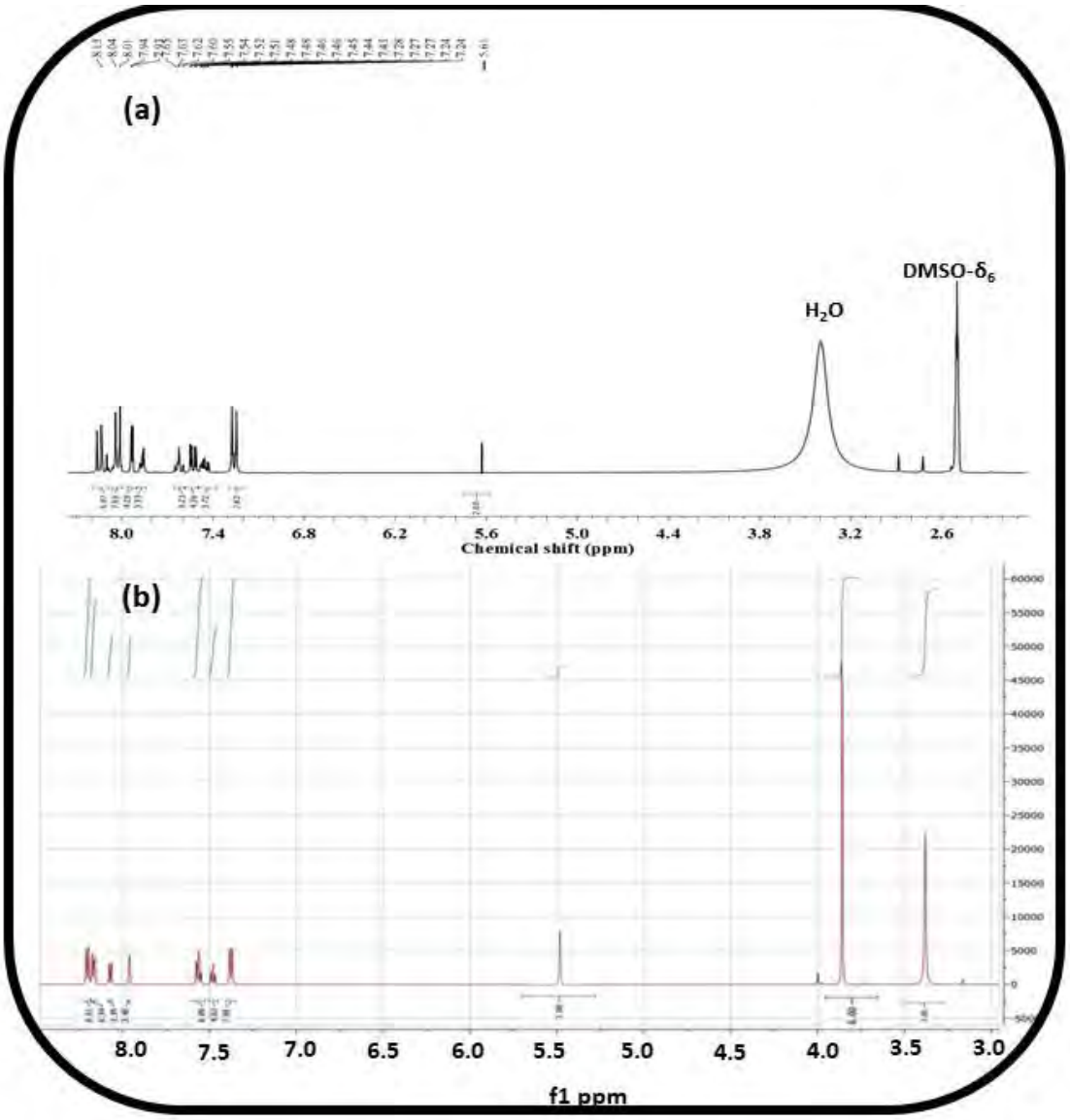

Figure 3.3: ^{1}H NMR for complexes in DMSO-d_6 **(a) 10** and **(b) 11**

The existence of multiple heavy isotopes with an increase in the molecular mass generally leads to a decrease in the relative abundance of the monoisotopic peak; hence the isotopic distribution model has been shown to be the accurate method of assigning molecular mass in large molecules **[148]**. The isotopic mass distribution of complex **10** and **11** was simulated and compared with the experimental MALDI-TOF measured masses. The observed mass of the complexes are in agreement with the calculated values (**Figure 3.4**)

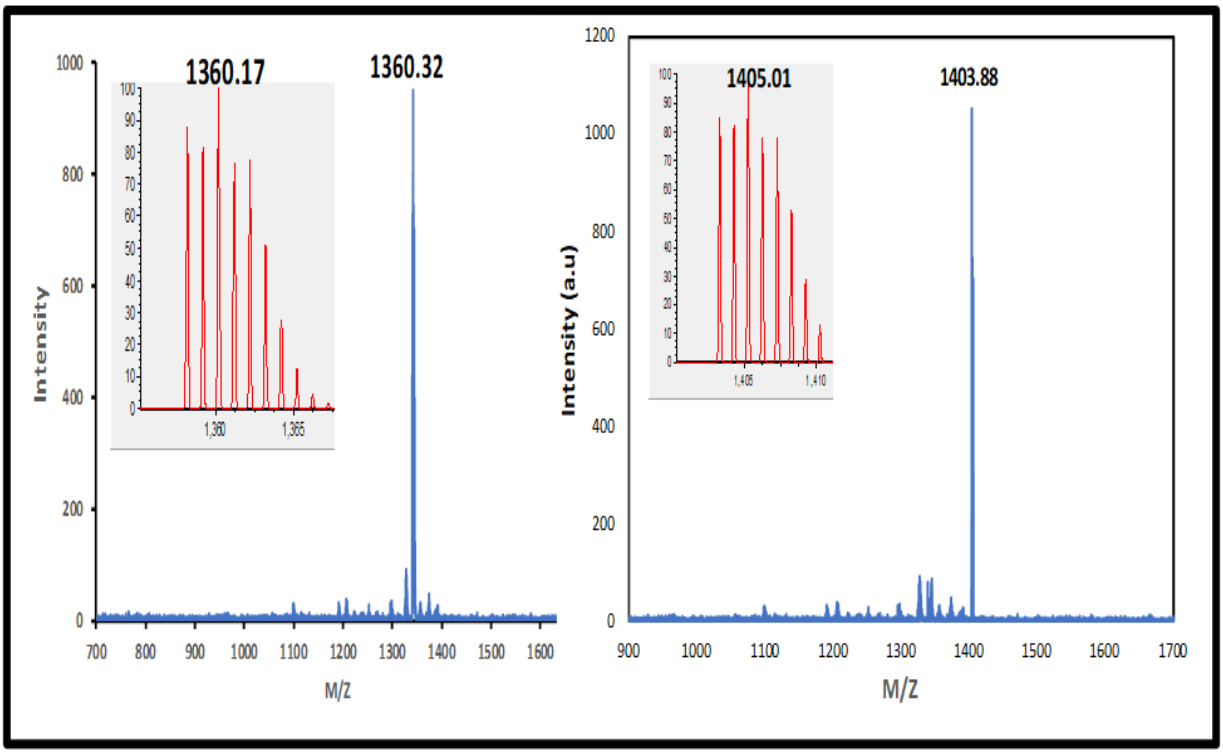

Figure 3.4: MALDI-TOF mass spectra of **10** and **11**

3.1.3. UV-Vis spectra for all Pcs

The UV-Vis absorption spectra of complex **8** and **9** showed the Q band maxima at 677 and 679 nm, which are blue-shifted from 681 nm for complex **7 (Figure 3.5 A)**, **Table 3.1**. The blue-shifting could be attributed to increase in energy gap between the highest occupied molecular orbital (HOMO) and lowest unoccupied molecular orbital (LUMO) because of reduced electron density from the nitrogen of the benzothiazole following quaternization. Similar blue-shifting has been reported **[149]** when 2-morpholinoethoxy phthalocyanine zinc(II) Pc was quarternized. It should be noted that Q band for **4a** show spectra similar to **4b**, and **4c** does not show the normal splitting of the Q band that is typical of free-base phthalocyanines (appendix, **Figure 1A**), showing instead a single sharp Q-band. The lack of splitting of the Q-band in complex **4a (**appendix, **Figure 1A)** is a result of the basicity of the solvents. It has been documented that in basic solvents such as DMSO, the inner pyrrole hydrogens are acidic enough to dissociate and the Pc becomes symmetrical and thus possesses an un-split Q band **[19, 150]**.

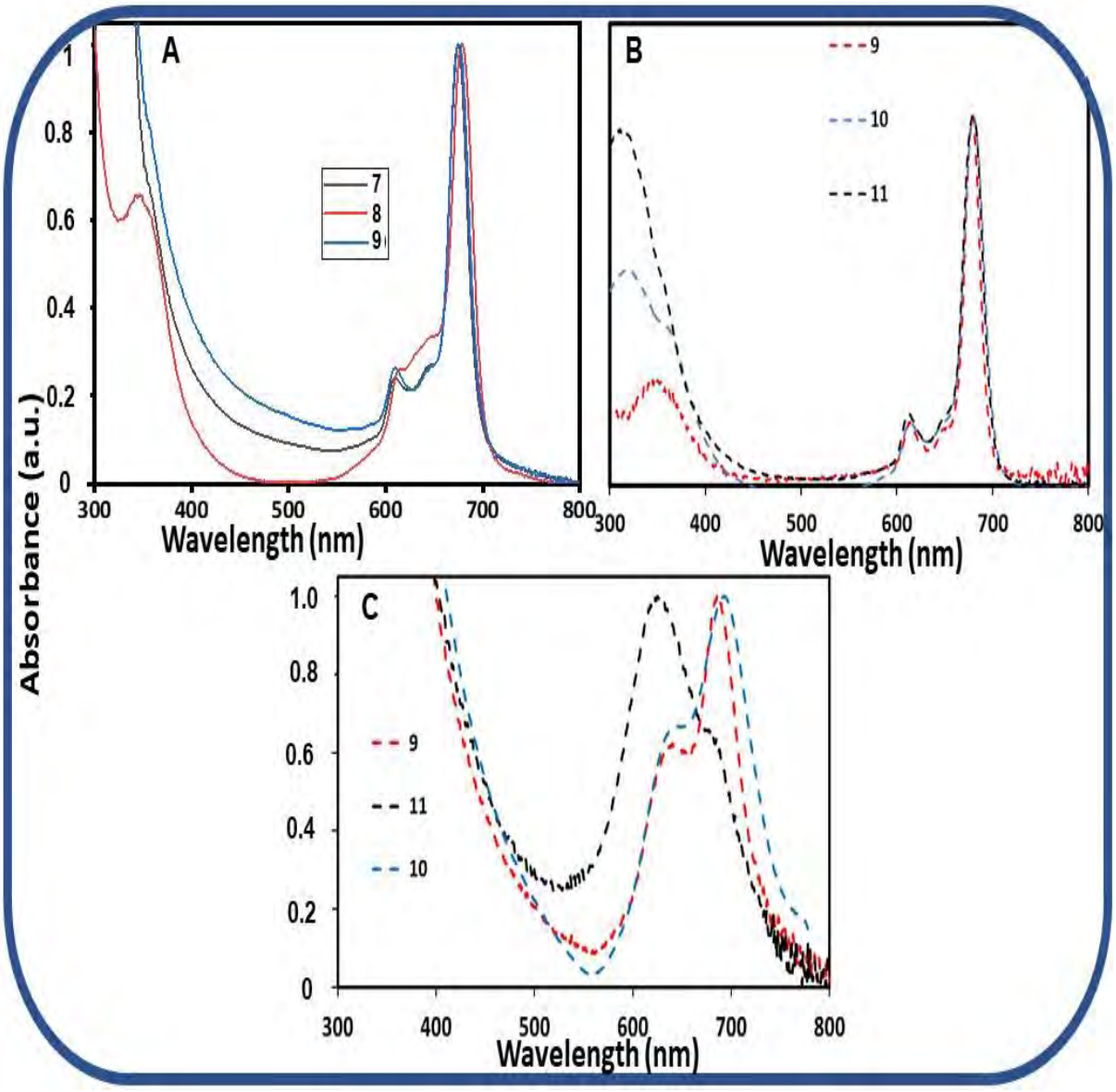

Figure 3.5: Absorption spectra of complexes **(A): 7**, **8**, **9** in DMSO; **(B): 9, 10, 11** in DMSO**;** and **(C): 9, 10, 11** in water containing 1% DMSO.

In water made up of 1% DMSO used for cells, most complexes **9-11** (as examples) are highly aggregated (**Figure 3.5 C**), **Figure 2A in** appendix for **3**. The broad band near 630 nm is due to aggregation. Aggregation in Pcs is due to π–π stacking interaction of the aromatic rings **[19]** resulting in broad or split Q bands, with the low energy band being due to the monomer and the high energy band due to the aggregate. Cofacial stacking mode of Pcs (the so-called H

stacks) give rise to a blue shift of the Q-band (due to the aggregate) relative to the Q-band of the monomer (low energy peak). The other stacking mode (very rare in phthalocyanines) in which the molecules are offset relative to each other leads to slipped stacks (J-stacks) gives rise to a red shifted Q-band **[19]**.

Table 3.1: Absorption spectra of complexes and respective conjugates in DMSO

Complexes and Conjugates	λ_{abs} (nm)[b]
$GQDs_2$(B1)	360
1	679
$GQDs_2$(B1)-**1** (π - π)	672
2	672
$GQDs_2$(B1)-**2** (π - π)	678
3	683
$GQDs_2$(B1)-**3** (π - π)	683
GQD_2(B2)	450
GQD_2(B2)-**3** (π - π)	681
GQD_6	430
GQD_6-**3** (π - π)	682
GQD_{10}	350
GQD_{10}-**3** (π - π)	683
$GQDs_2$(B3)	336
$GQDs_2$(B3)-**3** (π - π)	682
CDs	366
CDs-**3** (π - π)	686
DNDs-**3** (π - π)	686
3-DNDs-**12** (π - π and ester)	683
4a	675
DNDs-**4a** (π - π)	675
4b	675
DNDs-**4b** (π - π)	673
4c	684
DNDs-**4c (**ester)	666 (610)
5	670
DNDs-**5 (**ester)	687
6	677
DNDs-**6 (**ester)	681
7	681
8	677
9	679

B@DNDs-**9**	677
10	678
DNDs-**10** (amide)	690
B@DNDs-**10** (amide)	690
P@DNDs-**10** (amide)	678
N@DNDs-**10** (amide)	688
S@DNDs-**10** (amide)	690
S&N@DNDs-**10** (amide)	688
11	680
B@DNDs-**11** (amide)	682
12	649
DNDs-**12** (ester)	679

3.2. Carbon nanomaterials

Synthesis and characteristics thereof of carbon nanomaterials: graphene quantum dots (GQDs), carbon nanodots (CDs) and heteroatom doped DNDs will be discussed in this section.

3.2.1. GQDs, CDs and DNDs

GQDs synthesised for two hours ($GQDs_2$) consist of three batches: Batch 1 = B1 (used with different Pcs); Batch 2 = B2 (used with different sizes of GQDs); and Batch 3 = B3 (compared with other nanomaterials). The conditions are shown in **Table 3.2.** GQDs size cannot be controlled from batch to batch, hence the different batches with different characteristics. The graphene oxide (GO) sheets were chopped into pieces by $KMnO_4/H_2SO_4$ under various reaction conditions following literature method to form GQDs (various sizes) and CDs containing carboxyl and hydroxyl functionalities **[151]**.

Table 3.2: Synthesis conditions for GQDs

GQDs	Temperature (°C)	$KMnO_4$ (%)	Oxidation time (h)	Application
$GQDs_2$(B1)	50	50	2	Compares Pcs charges: Complexes **1-3**
$GQDs_2$(B2)	50	50	2	Compares GQDs sizes: $GQDs_6$ and $GQDs_{10}$
$GQDs_2$(B3)	50	50	2	Compares types of CNPs: CDs and DNDs
$GQDs_6$	70	60	6	
$GQDs_{10}$	80	80	10	

The synthesised GQDs, CDs and doped DNDs were characterized using TEM, DLS, zetapotential, XPS, FTIR, XRD, UV-Vis, laser Raman and TGA techniques. TEM micrographs showed that carbon nanoparticles alone are monodispersed (**Figure 3.6 (a)-(c)**). Sizes of $GQDs_2$ (B3), CDs and DNDs determined by TEM as indicated by inserts in **Figure 3.6** (3.3, 7.1, 2.3 nm) and DLS (5.1, 7.5 and 2.9 nm), **Figure 3.7,** respectively (**Table 3.3**)

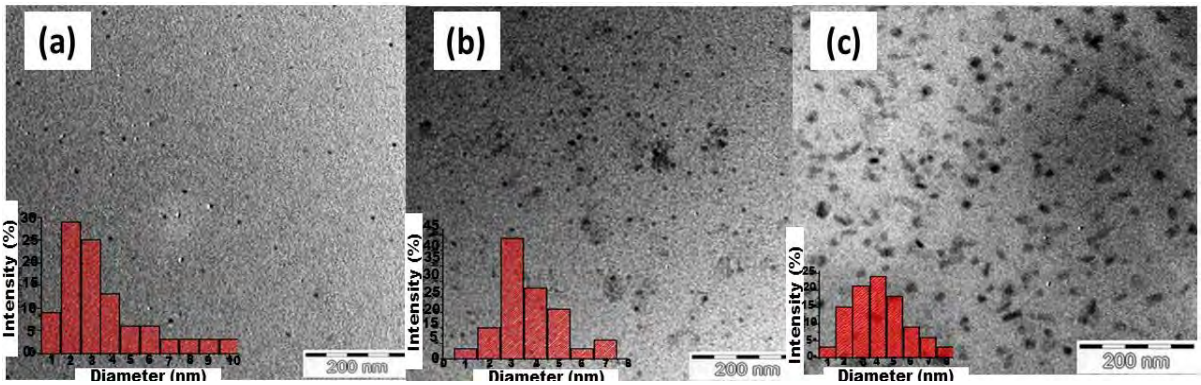

Figure 3.6: TEM micrographs of (a) DNDs, (b) $GQDs_2$ (B3) and (c) CDs

Similar sizes have been previously reported **[151-154]**. Slight discrepancies in particle sizes determined by TEM relative to DLS (**Figure 3.7**) could be attributed to interference of the dispersant into the hydrodynamic diameter, resulting in shifts to higher values **[155]**.

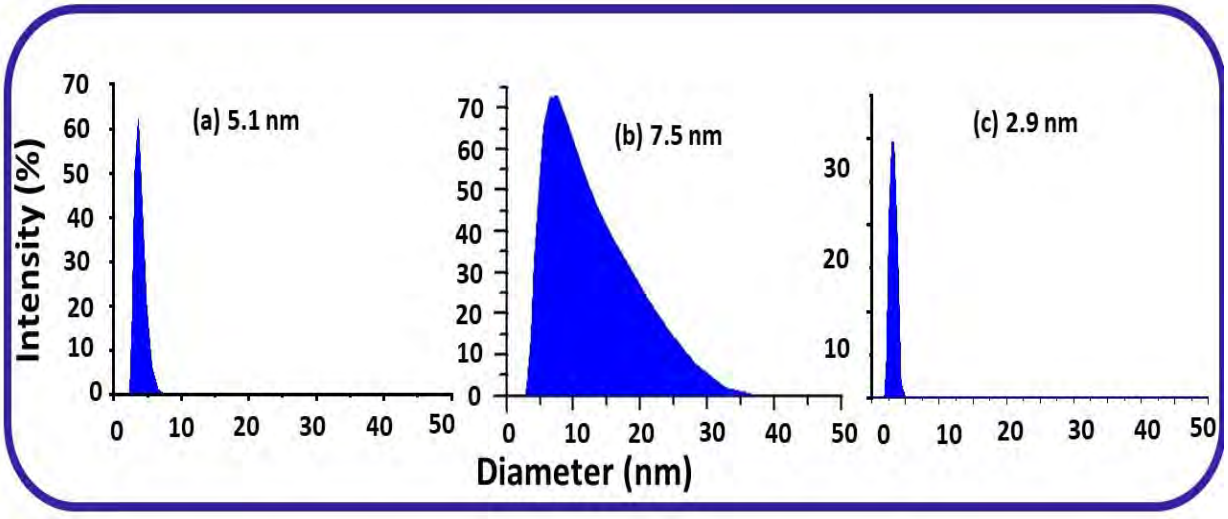

Figure 3.7: DLS size distribution of (a) $GQDs_2$ (B3), (b) CDs and (c) DNDs

Zeta potential is a key indicator of the stability of colloidal dispersions. The magnitude of the zeta potential indicates the degree of electrostatic repulsion between adjacent, similarly charged particles in a dispersion. When the zeta potential is small, attractive forces may exceed repulsion, resulting in aggregation **[156]**. Relative to DNDs, zeta potential of GQDs (B3)and CDs showed negative values as expected due to the predominant carboxylic acid groups in the latter two **[156]**. It has been reported that DNDs from NanoCarbon Research Institute, Japan (where we obtained the DNDs) are positively charged colloidal species **[157]**, also confirmed by zeta potentials in this work.

Table 3.3: Absorption spectra of complexes and respective conjugates in DMSO

Complexes and Conjugates	**DLS (nm)**	**TEM (nm)**	**Loading (μg/mg)**	**Raman ratio I_D:I_G**	**ξ (mV)**
$GQDs_2$ (B1)	2.2	1.5		0.40	-12.5
1					-10.8
$GQDs_2$ (B1)-**1** (π - π)	3.8		3	1.30	-23.6
2					-11.6
$GQDs_2$ (B1)-**2** (π - π)	10.2		4	0.87	-2.9
3					21.6
$GQDs_2$ (B1)-**3** (π - π)	14.2	10.5	14	1.60	0.33
$GQDs_2$ (B2)	2.6			0.40	-5.8
GQD_2(B2)-**3** (π - π)	14.2		10	1.60	99.2
$GQDs_6$	3.3			0.45	-131.1
GQD_6-**3** (π - π)	18.2		5	3.36	163.1
$GQDs_{10}$	5.1			1.09	-7.7
GQD_{10}-**3** (π - π)	25.5		3	0.43	-4.2
$GQDs_2$ (B3)	5.1	3.3		0.18	-12.5
$GQDs_2$ (B3)-**3** (π - π)	16.0		299	0.20	7.8
CDs	7.5	7.1		0.97	-10.4
CDs-**3** (π - π)	65.3		829	0.10	0.6
DNDs	2.9	2.3		0.01	13.0
DNDs-**3** (π - π)	7.2		42	0.22	10.9
3-DNDs(π - π)	3.9		31	0.15	-48.9
3-DNDs-**12** (π - π, ester)	7.5	6.5	334	0.33	-58.3
4a					1.2
DNDs-**4a** (π - π)	7.5		470	0.67	2.02
4b					1.3
DNDs-**4b** (π - π)	28.2		500	0.17	1.8
4c					1.9

DNDs-**4c** (ester)	32.5		800	0.18	2.4
5					
DNDs-**5** (ester)	78.8		38	1.48	10.6
6					
DNDs-**6** (ester)	68.1		3	0.52	17.2
7					-35
8					17.2
9					13.8
B@DNDs	4.8			1.58	4.9
B@DNDs-**9** (π - π)	78.8		887	0.80	17.1
10					-30
DNDs-**10** (amide)	28.2		6	0.43	-13.3
B@DNDs-**10** (amide)	46.5		57	1.82	-3.3
P@DNDs	50.8			0.15	12.9
P@DNDs-**10** (amide)	78.8		814	1.16	-10.6
N@DNDs	3.8			0.63	28.2
N@DNDs-**10** (amide)	54.0		110	1.85	-1.4
S@DNDs	7.8			0.09	9.23
S@DNDs-**10** (amide)	30.8		0.14	0.12	-9.2
S&N@DNDs	37.8			1.62	27.2
S&N@DNDs-**10** (amide)	43.8		11	4.85	-0.5
11					10.6
B@DNDs-**11** (amide)	68.1		792	1.00	12.9
12	1.5				64.7
DNDs-**12** (ester)	4.5	4.1	282	0.25	-48.6

FTIR spectra shows that DNDs have N (**Figure 3.8 (a)**) while GQDs and CDs do not (**Figure 3.8 (b)** and **(c)**). This is because DNDs contain several functional groups present on the surface such as amine, amide in addition to alcohol, carbonyl, and carboxyl **[157]**.

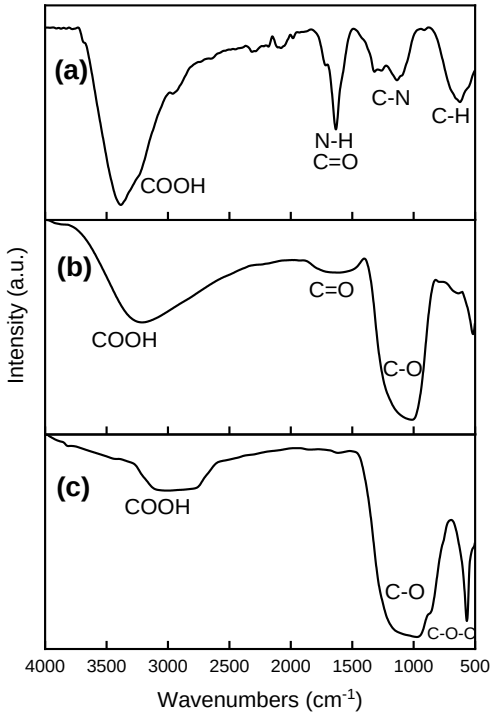

Figure 3.8: FTIR spectra of (a) DNDs (b) $GQDs_2$(B3) (c) CDs

XPS results in **Table 3.4** show that $GQDs_2$(B3) and CDs have high oxygen content, confirming the presence of more oxygen functionalities when compared to DNDs. The larger carbon content and low oxygen content of the DNDs suggest more sp^2 hybridization. CDs and $GQDs_2$(B3) have about the same carbon and oxygen content.

Table 3.4: Apparent XPS surface atomic % composition of carbon, oxygen and nitrogen for GQDs, CDs, and DNDs.

Sample	Atomic concentration (%)		
	C	O	N
$GQDs_2$(B3)	62.09	37.49	
DNDs	95.48	3.04	1.48
CDs	61.41	37.80	

High-resolution C1s spectrum of the DNDs reveals the presence of four components at 282.8, 283.6, 285.8 and 286.9 eV assigned as indicated in **Figure 3.9 (a)**. **Figure 3.9 (b)** showed the following bonds of C=C (284.05 eV), C–O (285.96 eV) and C=O (288.77 eV) typical of GQDs **[100]**. Peaks for $GQDs_2$(B3) and CDs are about the same energies but different intensities.

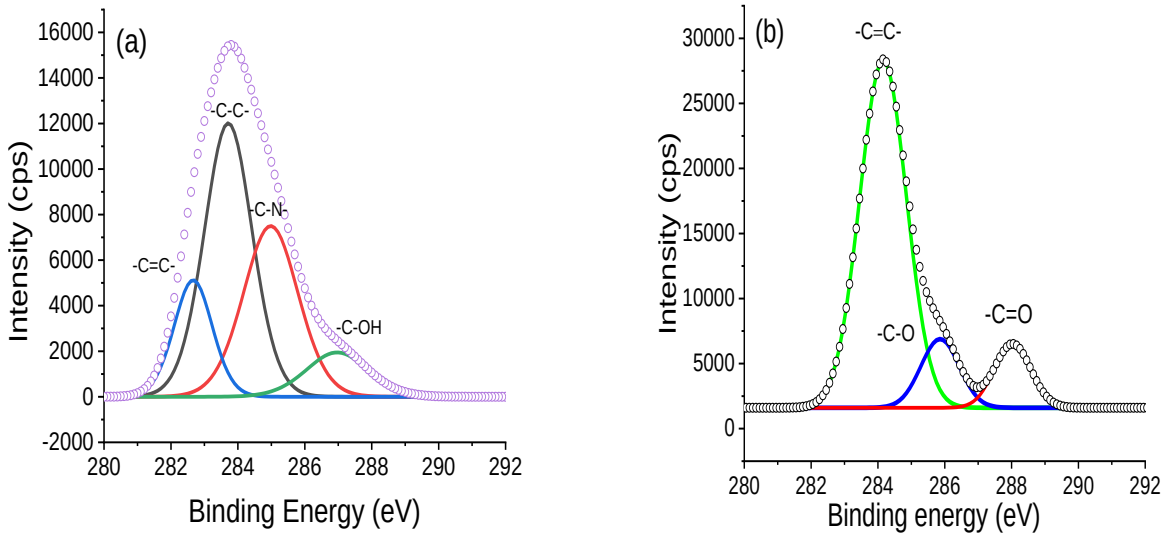

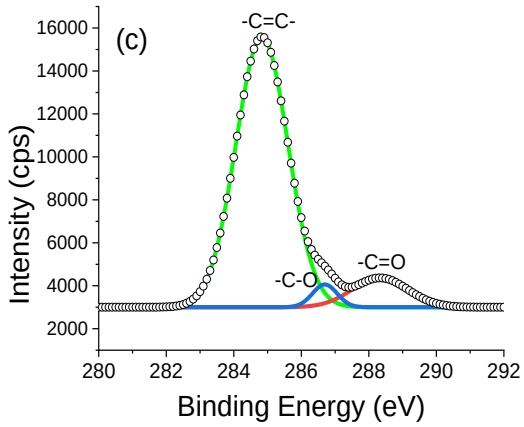

Figure 3.9: XPS High resolution C 1 s spectra of (a) DNDs, (b) $GQDs_2$(B3), (c) CDs

The XRD pattern for DNDs, **Figure 3.10 (a)** showed crystalline phases at (111), (221) and (311) correlating with 45, 73 and 92° (NISTnumberA51588) **[158]**. Broad peaks in **Figure 3.10 (b)** and **(c)** at 2θ≈28° corresponding with (002) for $GQDs_2$(B3) and CDs could be attributed to the amorphous nature and disordered carbons in the materials **[159-161]**. The shifts of XRD peaks for $GQDs_2$(B3) and CDs to a lower 2θ values compared with the DNDs, maybe due to the oxygen-containing groups (including carbonyl, carboxyl, hydroxyl, and epoxy groups) introduced on the edges and basal planes to increase interlayer distance **[86]**.

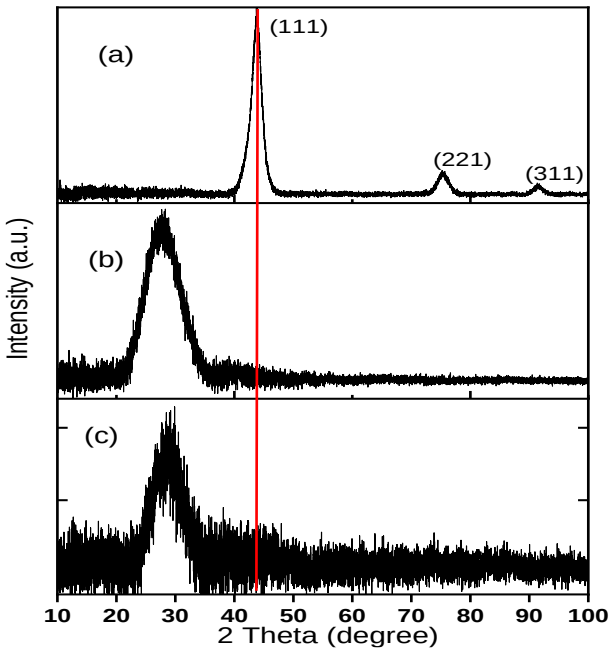

Figure 3.10: XRD pattern of (a) DNDs (b) $GQDs_2$(B3) (c) CDs

Figure 3.11 shows UV-Vis absorption spectra for DNDs, $GQDs_2$ (B3) band CDs dispersed in DMSO. CDs and $GQDs_2$ (B3) showed broad peaks at 366 and 336 nm, respectively in **Figure 3.11**. Similar broad absorption peaks have been previously reported to be due to π–π* transition of aromatic sp^2 domains **[94]**. In addition, previous studies have shown that change in size of nanoparticles results in change in band gap resulting in red or blue shift in absorbance **[95, 162]**.

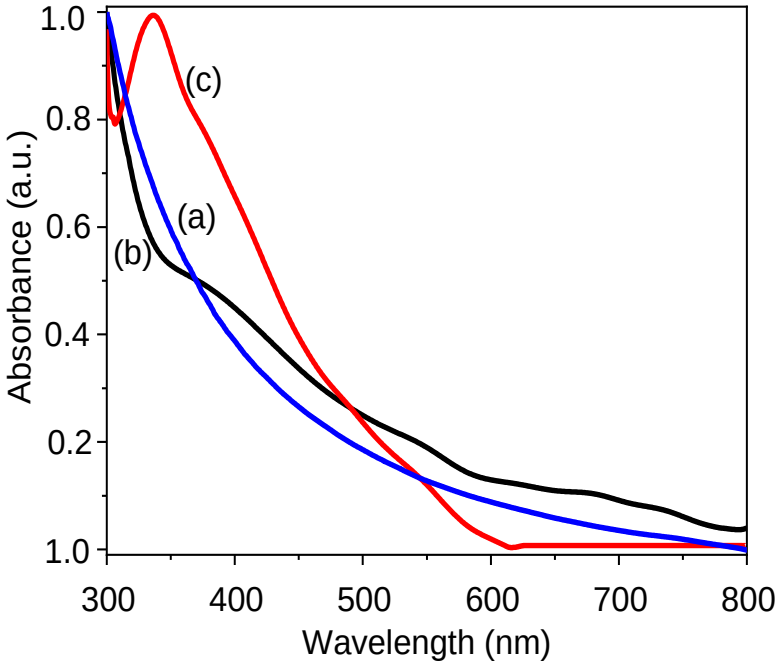

Figure 3.11: Absorbance spectra of (a) DNDs, (b) $GQDs_2$(B3), (c) CDs in DMSO.

Also, larger nanoparticles are usually red-shifted, hence CDs (λ= 366 nm) with a larger size than $GQDs_2$(B3) (λ= 336 nm) shows a red shifted spectrum **(Table 3.1)**. DNDs did not show a clearly defined peak. The absorption spectra of nanoparticles could be attributed to a combination of size, functional groups, degree of surface oxidation and graphitic nature of the nanomaterial (carbon backbone connected to functional groups).

DNDs did not show photoluminescence properties. Emission spectrum of CDs at 587 nm in **Figure 3.12 (b)** was more red shift than $GQDs_2$(B3) (370 nm) in **Figure 3.12 (a)** when both were excited at 310 nm. The mechanism of photoluminescence of carbon nanoparticles could be due to synergistic model which stipulates coexistence of quantum confinement effect; surface traps, type of carbon material and edge states as explained in a review by Gan, et al. **[163]**. Functional groups (such as COOH or OH in $GQDs_2$(B3)) and the quality of carbon nanomaterials (amorphous or graphitic) act as continuous defect states that are responsible for the emissions **[163, 164]**.

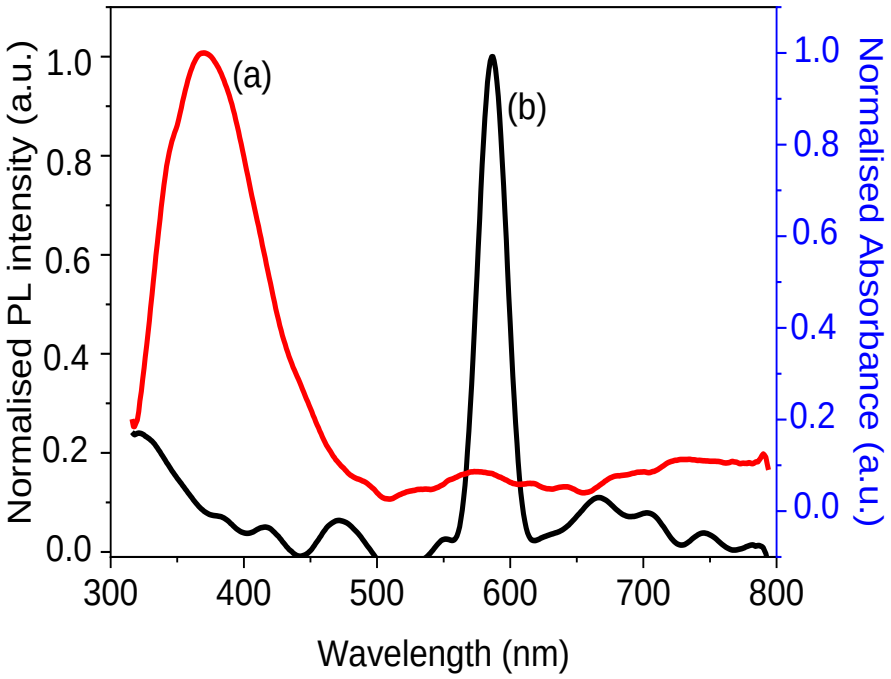

Figure 3.12: Emission spectra of (a) $GQDs_2$(B3), (b) CDs when both NPs are excited at 310 nm in DMSO.

Thermogravimograms of $GQDs_2$(B3), CDs and DNDs conducted in the temperature range of 50–800 °C in air are shown in **Figure 3.13** to indicate thermal stability. In comparison with DNDs (99% mass loss) at 800 °C, the TGA curves of GQDs and CDs revealed a decreased weight loss of 15% and 7%, respectively. Various structural forms of carbon have different oxidation behaviour depending on the available reactive sites **[165-167]**. For instance, amorphous and graphitised carbons tend to be oxidised at different temperatures due to their varying activation energy for oxidation **[168]**. Functional groups with reducing ends are generally known to decrease thermal stability of nanoparticles **[71-73]**. Thus, the loss of mass for DNDs, $GQDs_2$(B3) and CDs observed in **Figure 3.13**, could indicate thermal stability associated with interplay between size and extent of functionalisation of nanoparticles, with the larger CDs showing the largest stability at 7% and the smallest DNDs showing the lowest stability at 99%.

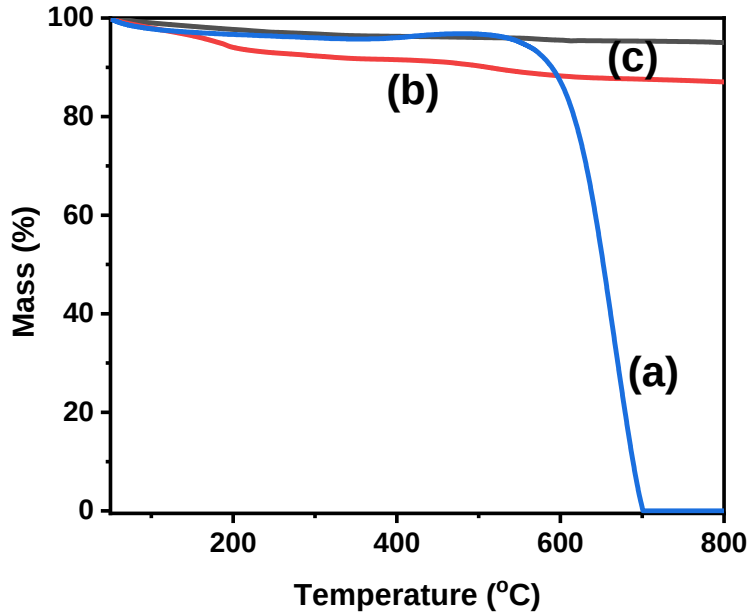

Figure 3.13: Thermogravimetric analysis (TGA) curves for samples (a) DNDs, (b) $GQDs_2$ (B3) and (c) CDs is heated at 20 °C min^{-1} from 50 to 800 °C in air

In this study laser Raman spectral technique (**Figure 3.14**.) was used to determine the quality of as-synthesised DNDs, $GQDs_2$ (B3) and CNDs. The disorder (D) sp^3 defects and graphitic (G) sp^2 peaks from in plane vibrations were observed at approximately (1289; 1595 cm^{-1}) at laser energy of 25 mW, (1280; 1591 cm^{-1}) and (1278; 1627 cm^{-1}) for DNDs, $GQDs_2$ (B3) and CDs alone. Thus, the D bands of the $GQDs_2$ (B3) and CDs alone shift to lower wavenumbers compared to DNDs. The G band for CDs is shifted to higher wavenumbers compared to DNDs, while the G band for $GQDs_2$ (B3) is slightly blue shifted compared to that for DNDs. Raman band shifts have been attributed to factors such as the nature, diameter and strain of nanoparticles **[169, 170]**.

The I_D:I_G (sp^3:sp^2) ratio is generally considered as a quality parameter to determine the extent of functionalization of the carbon nanomaterials. This is because the G-band is not affected by defects, whereas the D-band is enhanced by the presence of sp^3 defects in the sp^2 lattice. CDs have the largest size and defects (0.97) relative to $GQDs_2$(B3) (0.18) and DNDs (0.01) as calculated from the I_D:I_G ratio in **Table 3.3**. The larger carbon composition of 95.48% in DNDs,

compared to 62.09% ($GQDs_2$ (B3)) and 61.41% (CDs) in **Table 3.4** increased defects in the former. Increases or decreases in I_D:I_G ratios of GQDs have been previously reported to be due to size-dependent edge-state variation of GQDs **[171]**. Thus, decrease in I_D:I_G ratio of DNDs, $GQDs_2$ (B3) compared to CDs is associated with increased carbon quantity and decreased nanoparticle sizes.

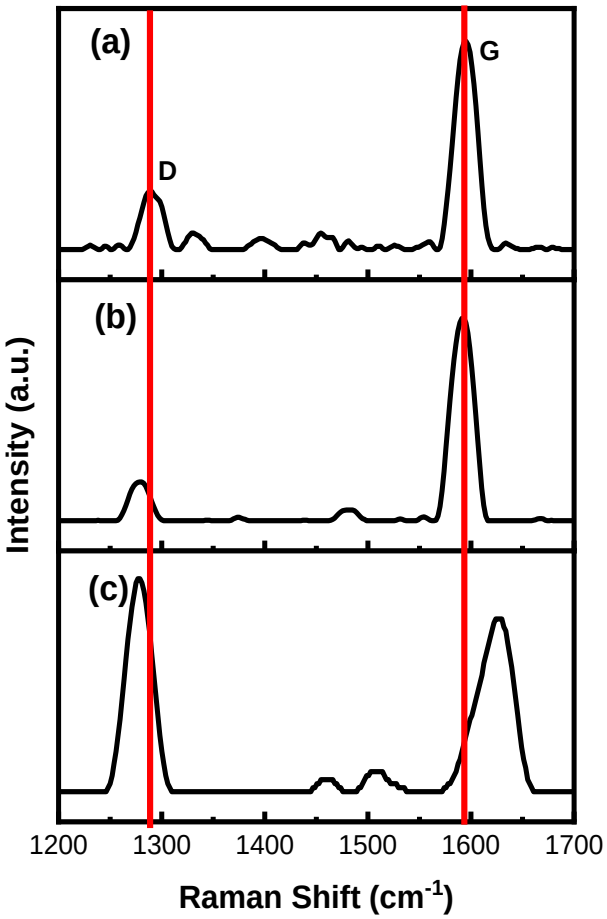

Figure 3.14: Raman spectra at laser power of 25 mW for (a) DNDs, (b)$GQDs_2$ (B3), (c) CDs

3.2.2. Different sizes of GQDs

Three different sizes of GQDs were synthesised (following literature methods **[151]**) depending on the time allowed for the GO cutting process using $KMnO_4/H_2SO_4$. The GQDs are labelled according the oxidizing time in H_2SO_4. **Table 3.2** for $GQDs_2$, 2 h was used at 50% $KMnO_4$**.** In this section, ($GQDs_2$(B2) were employed. The temperature was raised to 70 °C, $KMnO_4$ to 60 wt% and oxidizing time of 6 h was used for $GQDs_6$. For $GQDs_{10}$, temperature was raised to 80 °C, $KMnO_4$ to 80 wt% and oxidation time was 10 h, **Table 3.2**. The increase in the oxidation time, temperature and amounts of the oxidants resulted in increase in the sizes of the GQDs as has been reported before **[172]**.

Table 3.5 shows that the sizes decrease (DLS) as follows: $GQDs_{10}$ > $GQDs_6$> $GQDs_2$(B2). Studies have indicated that changing either concentration of oxidant, time or temperature have effects on any of the following: quality, quantity, morphology, and photoluminescence properties of QDs **[86, 172-174]**. Hence Zhang et. al. **[173]** and Fan et al **[151]** showed that accurate size control of QDs could be obtained when temperature, time and concentration of the oxidant were varied simultaneously. Thus in this work, time, temperature and %$KMnO_4$ were simultaneously varied in order to increase the size of the GQDs.

GQD_6 show relatively higher stability compared to the rest of the GQDs in **Table 3.5,** as judged by larger zeta potential of -131.1 mV compared to $GQDs_2$(B2) at -5.8, $GQDs_{10}$ at -7.7 mV. GQD_{10} which has the largest DLS size and GQD_2(B2) with least DLS size, are both the least stable relative to GQD_6 with moderate size but the largest zeta potential**.** Thus, there is no specific relationship between colloidal stability of GQDs and size of the nanoparticle.

Table 3.5: Physical characteristics of different sizes of GQDs and respective conjugates

Sample[a]	**λ_{abs}** (nm)[b]	**DLS size (nm)**	**Loading (μg)/(mg)**	**ξ (mV)**	**Raman ratio I_D/I_G**
GQD_2(B2)	450	2.6		-5.8	0.40
GQD_2(B2)-**3** (π - π)	681	14.2	10	99.2	1.60
GQD_6	430	3.3		-131.1	0.45
GQD_6-**3** (π - π)	682	18.2	5	163.1	3.36
GQD_{10}	350	5.1		-7.7	1.09
GQD_{10}-**3** (π - π)	683	25.5	3	-4.2	0.43

The XPS wide scan spectra (**Figure 3.15 A: (a) –(c))** showed all the expected elemental compositions of GQDs at respective binding energies with C1s at approximately 284 eV and 530 eV for O1s, for $GQDs_2$ (B2), $GQDs_6$, $GQDs_{10}$ respectively. High-resolution C1s spectrum of the GQDs (**Figure 3.15 B**) indicates the existence of C1s in different chemical environment. Peaks corresponding to GQD_6 in **Figure 3.15 B (b)** were shown at different bonding states of C=C (284.05 eV), C–O (285.96 eV) and C=O (288.77 eV) typical of GQDs **[100]**. Peaks for GQD_2(B2) and GQD_{10} are about the same energies as $GQDs_6$ but different intensities.

A

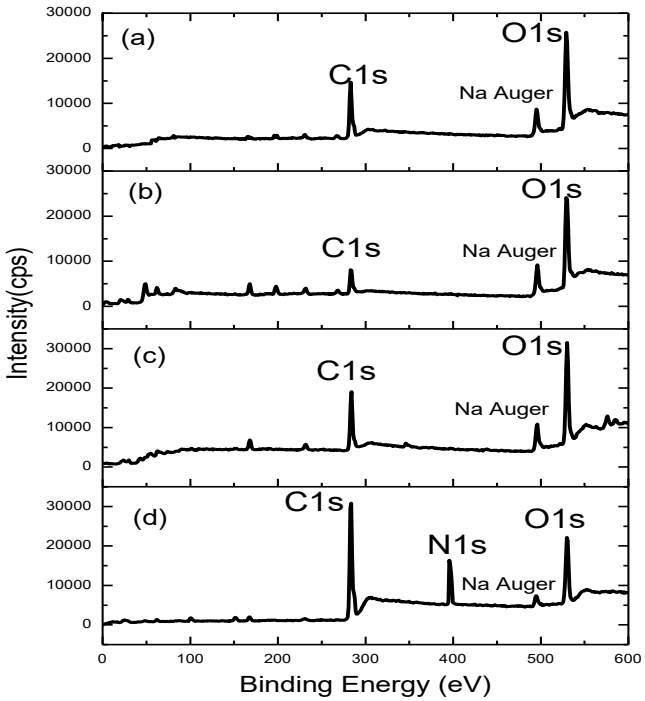
(a)
C1s
O1s
Na Auger
(b)
C1s
O1s
Na Auger
(c)
C1s
O1s
Na Auger
(d)
C1s
N1s
O1s
Na Auger
Intensity(cps)
Binding Energy (eV)

B

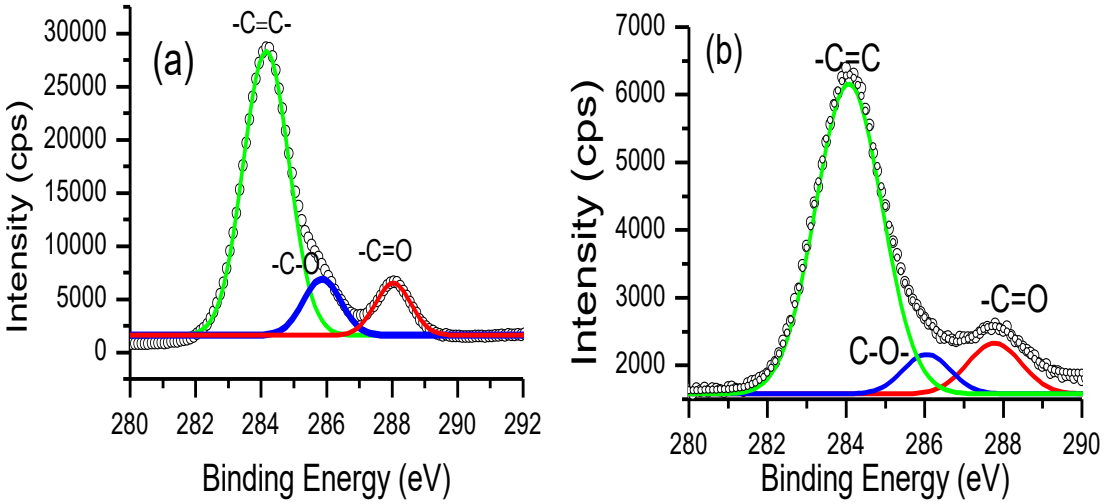
(a)
-C=C-
-C-O-
-C=O
Intensity (cps)
Binding Energy (eV)
(b)
-C=C
C-O-
-C=O
Intensity (cps)
Binding Energy (eV)

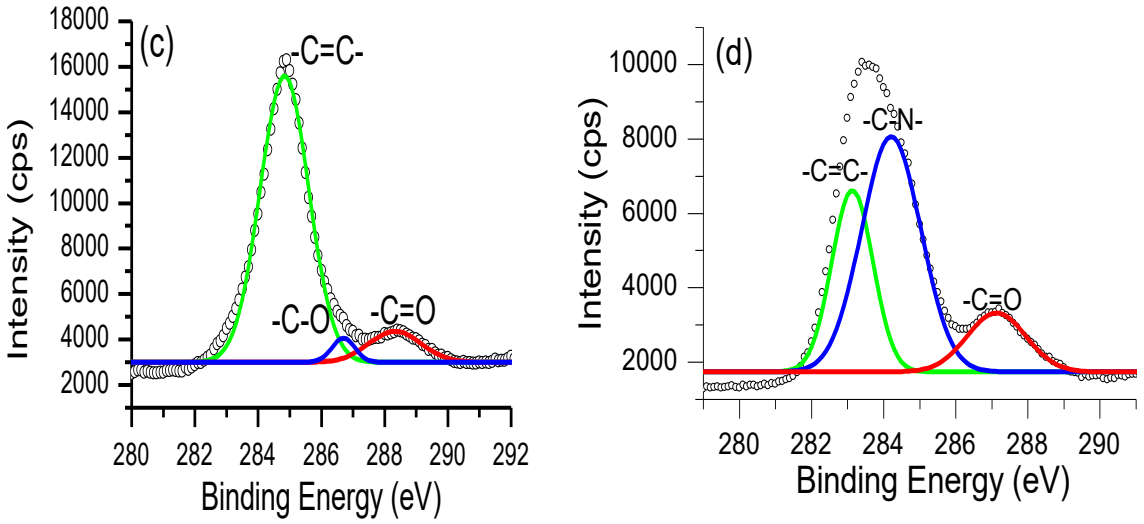

Figure 3.15: (A) Wide scans of (a) GQD_2(B2), (b) GQD_6 (c) GQD_{10} and (d) GQD_6-**3** conjugate, (B)High resolution C1s spectra of (a) GQD_2(B2), (b) GQD_6, (c) GQD_{10}, and (d) GQD_6-**3** (as an example)

Various sizes of graphene quantum dots (GQDs): GQD_2(B2), GQD_6 and GQD_{10} showed that increasing sizes of GQDs decreases the atomic concentrations of oxygen (**Table 3.6**).

Table 3.6: Apparent XPS surface atomic composition and corresponding binding energies of different GQDs sizes

Sample	Atomic concentration (%)		Binding energies (eV)	
	C	O	C1s	O1s
GQD_2(B2)	43.20	56.23	283	529
GQD_6	61.41	37.80	284	530
GQD_{10}	62.09	37.49	285	531

Inserts in **Figure 3.16 (a) – (b)** shows UV-Vis absorption spectrum of GQDs dispersed in water. Broad absorption peaks are observed between 350 nm and 450 nm, inserts in **Figure 3.16 (a-c).** A general blue shift in the absorbance of the GQDs alone from 450 nm to 350 nm, **Figure 3.16 (a-c)**), **Table 3.5** was observed with increase in size. Increase in sizes of semiconductor quantum dots **[173]** and GQDs **[96]** were previously reported to red shift the absorbance. However, it has been suggested that blue shifts in the GQDs absorption spectra are due to a decrease in oxygen functionalities rather than size **[175]**. This could be the case in this work since XPS results (**Table 3.6**) shows less oxygen functionalities for the larger GQDs, with blue shifted absorbance spectra.

Typical excitation-dependent photoluminescence (PL) spectra for $GQDs_2$ and $GQDs_6$ (**Figure 3.16 (a-b)**) showed a decrease in intensity, red shifting and broadening of emission peaks upon increasing the excitation wavelength, consistent with previous reports **[151, 175]**. For GQD_{10} in **Figure 3.16 (c)**, an increase in intensity and red shifting of the emission wavelength upon increasing excitation wavelength was observed. Increase in intensity with red shift of the emission spectra have been reported for GQDs to be due to degree of oxidation **[163]**, a trend consistent with CNDs (carbon nanodots) **[164]**. However, in this work, there is little difference in oxygen content for $GQDs_6$ and $GQDs_{10}$ (**Table 3.6**), yet they show different spectral behaviour. This PL emission behaviour confirms that no individual model can explain the mechanism of excitation-dependency behaviour of synthesised graphene quantum dots. Different emissions have been previously reported to originate from graphite sheets of different size, symmetry, and defects **[176]**. Therefore, synergistic model could be used to explain the mechanism of photoluminescence of GQDs. This model stipulates coexistence of quantum confinement effect; surface traps and edge states as explained in a review by Gan, et al. **[163]**. Following the theory that functional groups (such as COOH or OH in GQDs) and the quality of carbon nanomaterials (amorphous or graphitic) act as continuous defect states that are responsible for the emissions, it is likely that they are also responsible for the excitation-dependent emission behaviour **[151, 163]** observed in this work.

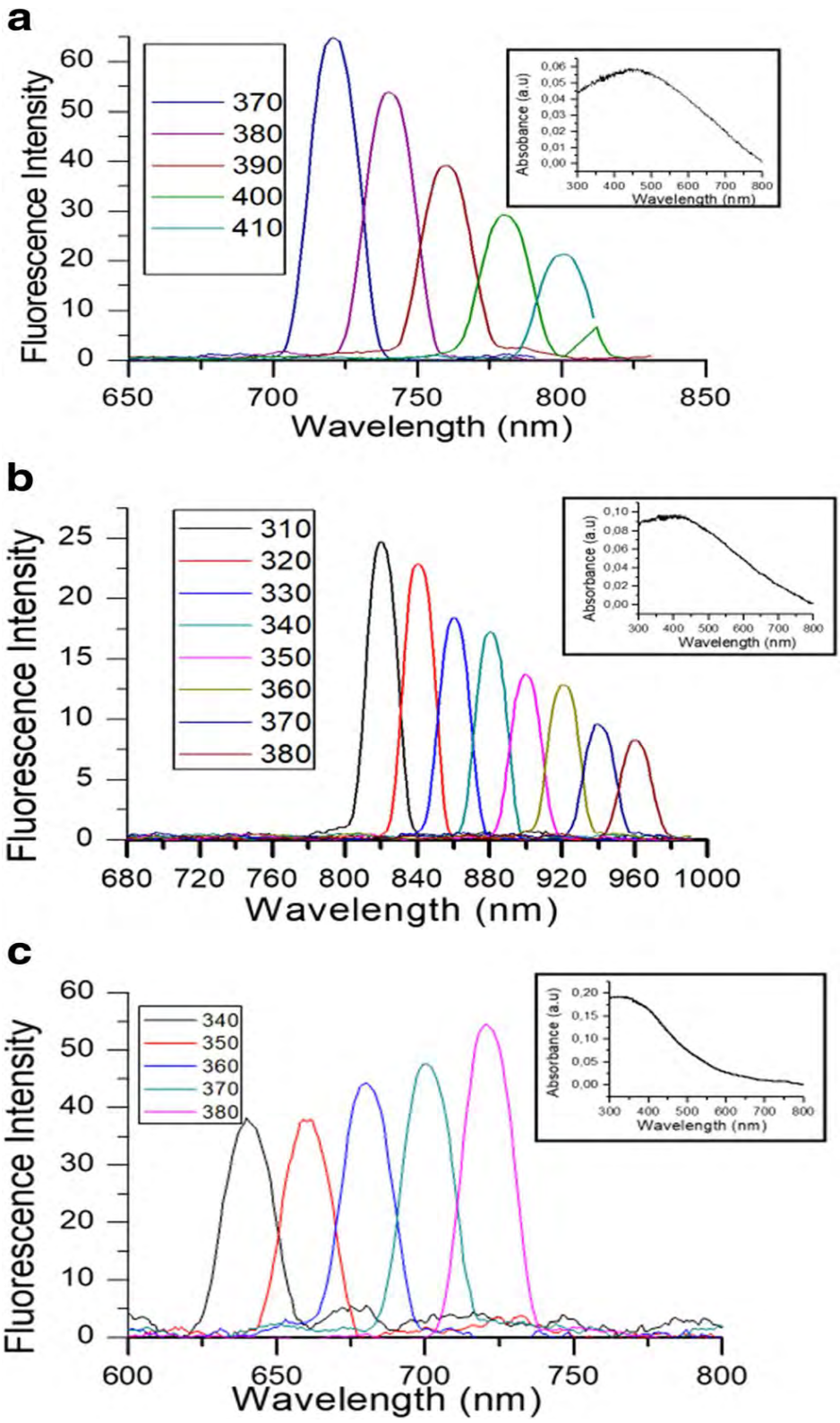

Figure 3.16: PL emission spectra of (a) GQD_2(B2), (b) GQD_6, and (c) GQD_{10}) as the excitation wavelength is increased from 310 nm. Inserts = UV-Vis absorption spectra in DMSO solvent

3.2.3. Heteroatom doped DNDs

Sizes of B, P, N, S and S&N@DNDs alone as determined by dynamic light scattering (DLS) are 4.8, 50.8, 3.8, 7.8, 37.8 nm, respectively (**Figure 3.17 (a)-(e)**), **Table 3.7**. DLS size increases on doping. DLS sizes increases with the atomic radius of respective doped atoms **[177]**.

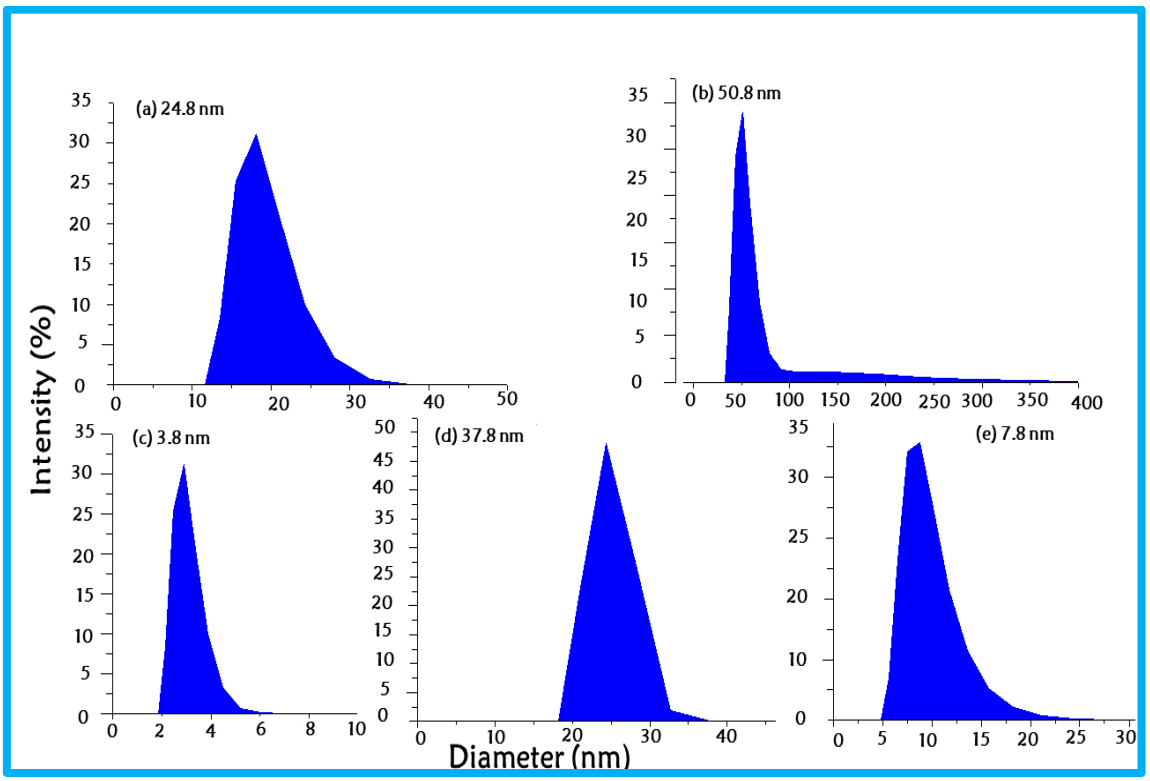

Figure 3.17: DLS of (a) B@DNDs, (b) P@DNDs, (c) N@DNDs, (d) S&N@DNDs (e) S@DNDs

DNDs maintained the positive charge even after doping with various heteroatoms such as B, P, N and S&N, as confirmed by zeta potential values in **Table 3.7**.

Table 3.7: Zeta potential for doped DNDs in water.

Sample	DLS (nm)	Zeta potential (mV)	Raman ratio I_D/I_G
10	-	-30.0	-
DNDs	2.9	43	0.01
B@DNDs	4.8	4.9	1.58
P@DNDs	50.8	12.9	0.15
N@DNDs	3.8	28.2	0.63
S@DNDs	7.8	9.3	0.09
S&N@DNDs	37.9	27.2	0.16

Characteristic FTIR peaks for B@DNDs, P@DNDs, N@DNDs, S&N@DNDs identified by characteristic vibrational bands of B, O=P-OH, –C=N-, S=O and N-H at 1091, 1639, 1632, 1090 and 1472 cm^{-1} respectively **Figure 3.18**. The C=O band at 1732 cm^{-1} is a result of stretching carboxylic group vibrations in the DNDs **[178]**.

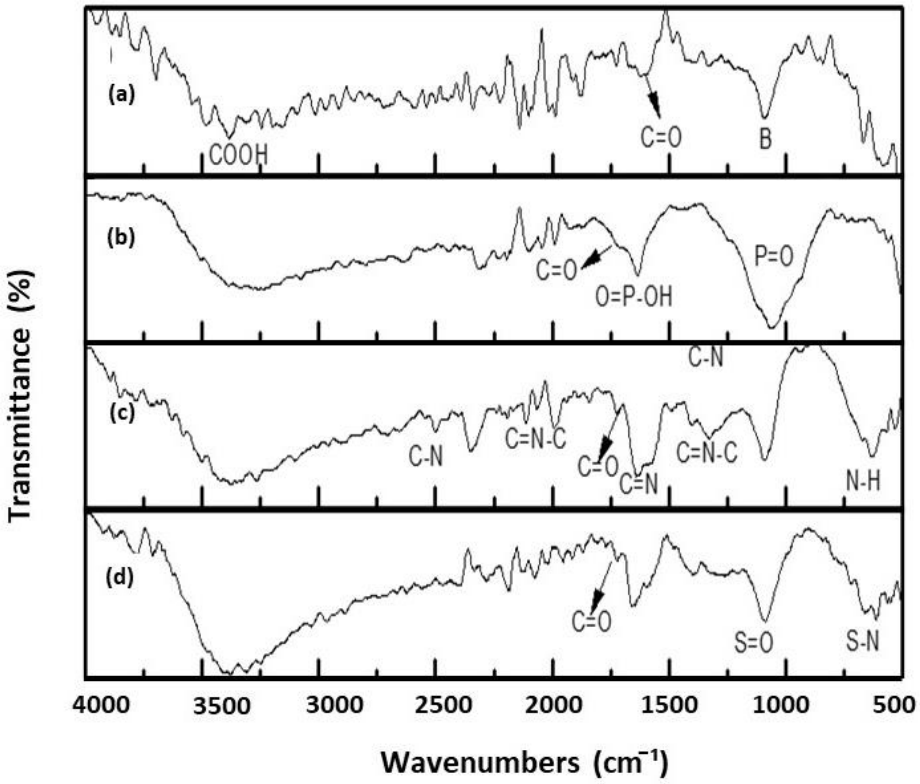

Figure 3.18: FTIR spectra of (a) B@DNDs, (b) P@DNDs, (c) N@DNDs and (d) S&N@DNDs

Figure 3.19 (a) shows UV-Vis absorption spectra of N, and S&N@DNDs (as examples) dispersed in DMSO. DNDs show broad peaks, as stated above while the undoped DNDs did not show peaks. The broad peaks observed for doped DNDs are due to π–π* transition of aromatic sp^2 domains **[179]**. Emission spectra of N and S&N doped DNDs showed peaks at 465 and 434 nm for respective nanoparticles as shown in **Figure 3.19 (b)**. The mechanism of photoluminescence of doped DNDs and respective nanohybrids could be attributed to surface traps as a result of dopant effect on DNDs, which act as continuous defect states that are responsible for the emissions. In addition, previous studies have shown that doping of DNDs alters sizes, molecular structure and band gap that result in changes in optical properties of the material **[180, 181]**. Hence, doped DNDs showed fluorescence characteristics, while undoped did not.

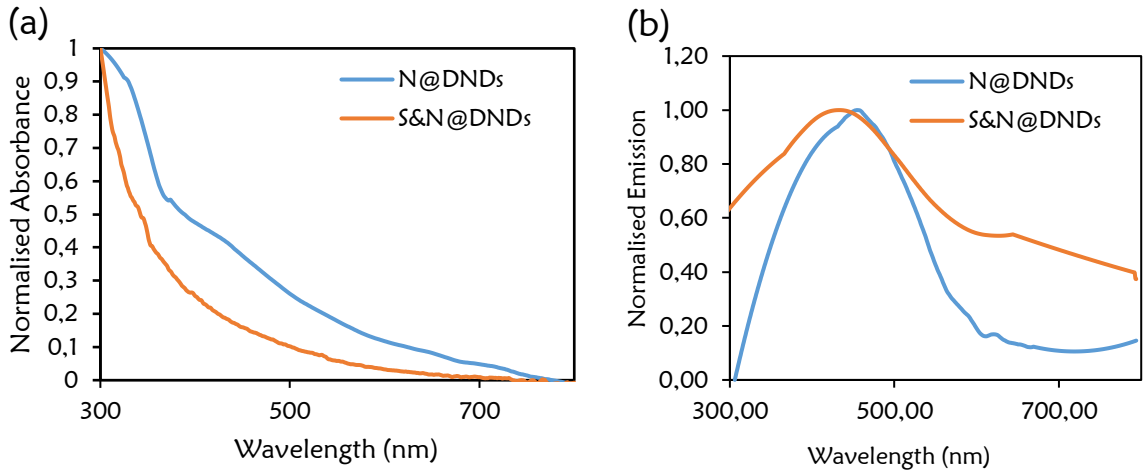

Figure 3.19: (a) Absorbance and (b) photoluminescence emission spectra of N at 465 nm and S&N@DNDs at 434 nm when both were excited at 290 nm in DMSO.

The disorder of (D, sp^3) defects and graphitic (G, sp^2) bands are observed at approximately (1320; 1540 cm^{-1}), (1325; 1596 cm^{-1}), (1275; 1596 cm^{-1}), (1329; 1596 cm^{-1}), (1214; 1596 cm^{-1}) and (1249; 1596 cm^{-1}) in **Figure 3.20** for DNDs, B@DNDs, P@DNDs, N@DNDs, S@DNDs, and S&N@DNDs, respectively. Structural distortion of graphitic carbon due to different bond lengths induced by co-doping are indicated in the Raman spectra by shifts of the G band **[182]**. Shifts in Raman band have been attributed to factors such as nature, diameter and strain of nanoparticles **[169-171]**. Raman bands for DNDs at laser power 30 mW in this section shifted to (1320; 1540 cm^{-1}), relative to (1289; 1595 cm^{-1}) when laser energy was 25 mW in section 3.2.1. Shift to lower frequencies (blue shift) of G bands was observed with increasing laser power **[183]**. The extent of doping and functionalizing DNDs is determined from I_D: I_G (sp^3:sp^2) ratio in **Table 3.7**, because the G-band is not affected by defects, whereas the D-band is, as stated above. Heteroatom doping of DNDs resulted in an increase in I_D:I_G ratio for all the dopands. However, B@DNDs showed the most intense defective peak (D) in **Figure 3.20 (b)**, hence higher I_D:I_G ratio. Doping of boron atoms onto the nanodiamond has been previously reported to increase defects on the nanodiamond surface through residual graphite oxidation **[184]**. Hence the large I_D:I_G ratio for B@DNDs.

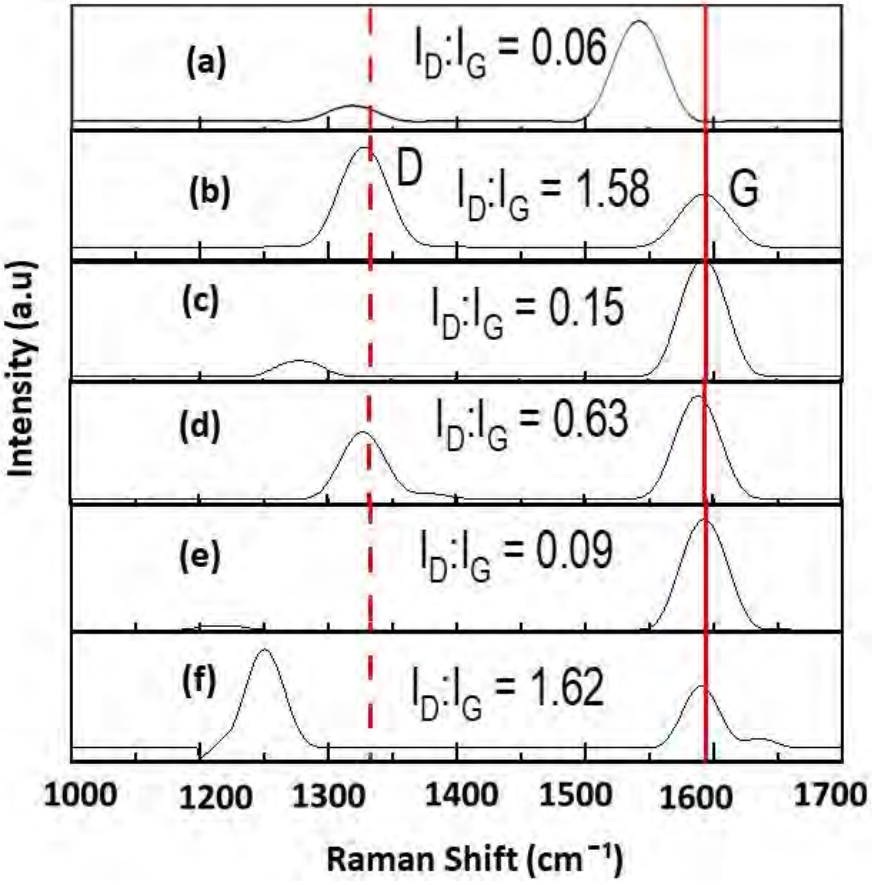

Figure 3.20: Raman spectra for nanoparticles and respective conjugates of (a) DNDs, (b) B@DNDs, (c) P@DNDs, (d) N@DNDs, (e) S@DNDs, and (f) S&N@DNDs.

3.3. Phthalocyanine carbon nanohybrids

3.3.1. $\pi\pi$ Congugates

Conjugates of complexes **1**,**2**,**3** with $GQDs_2$(B1); **3** with CDs, **4a**, **4b** with DNDs and **9** with B@DNDs were studied here for $\pi\pi$ interaction. **Scheme 3.4** shows the noncovalent attachment of complex **3** using different sizes of GQDs as an example. Similar behaviour is observed for all the complexes in this section. **Table 3.3** compares all the data.

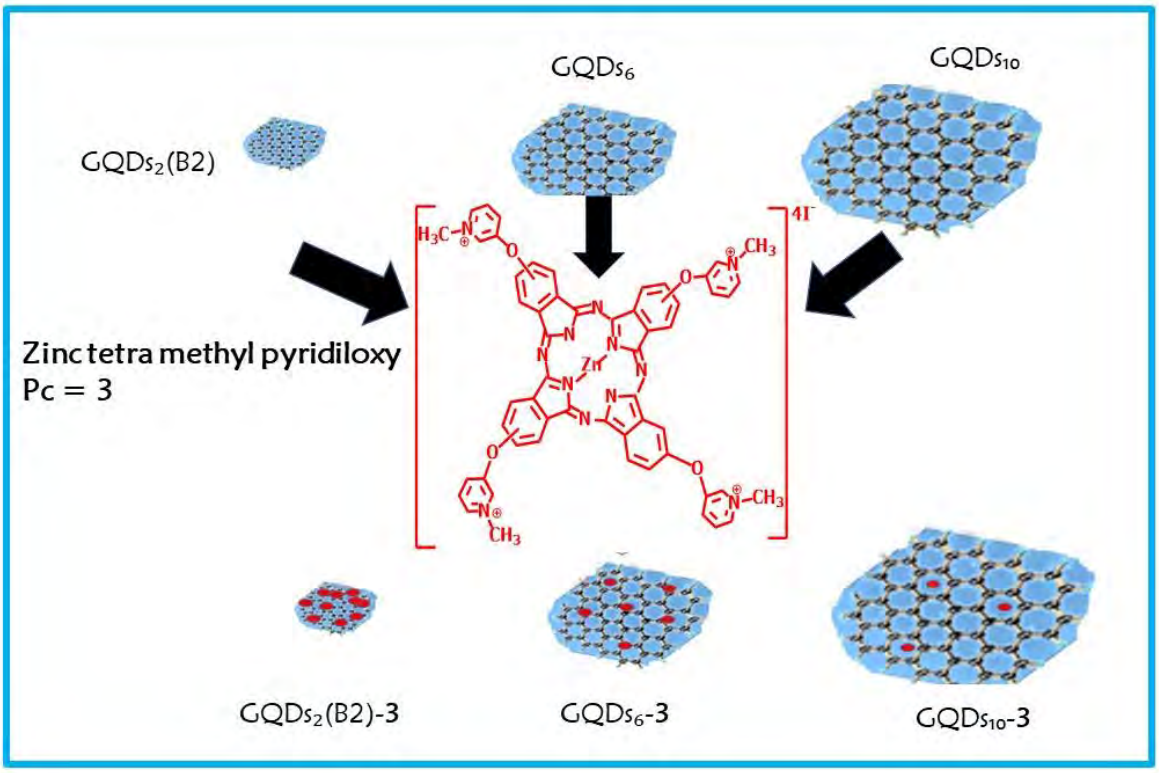

Scheme 3.4: Non-covalent interaction of different sizes of GQDs (GQD_2 (B2), GQD_6 and GQD_{10}) to complex **3.**

3.3.1.1. Fixed size $GQDs_2$(B1)

This section entails a fixed size of graphene quantum dots ($GQDs_2$(B1)) with complexes **1**, **2** and **3**. A general increase in DLS particle size was observed in **Figure 3.21** upon conjugation of $GQDs_2$ (B1) to zinc Pcs complexes **(1**, **2** and **3)** due to aggregation, **Table 3.3**. π–π stacking interaction of the aromatic rings is known for Pcs **[19, 34]**. This could occur between Pcs in neighboring GQDs.

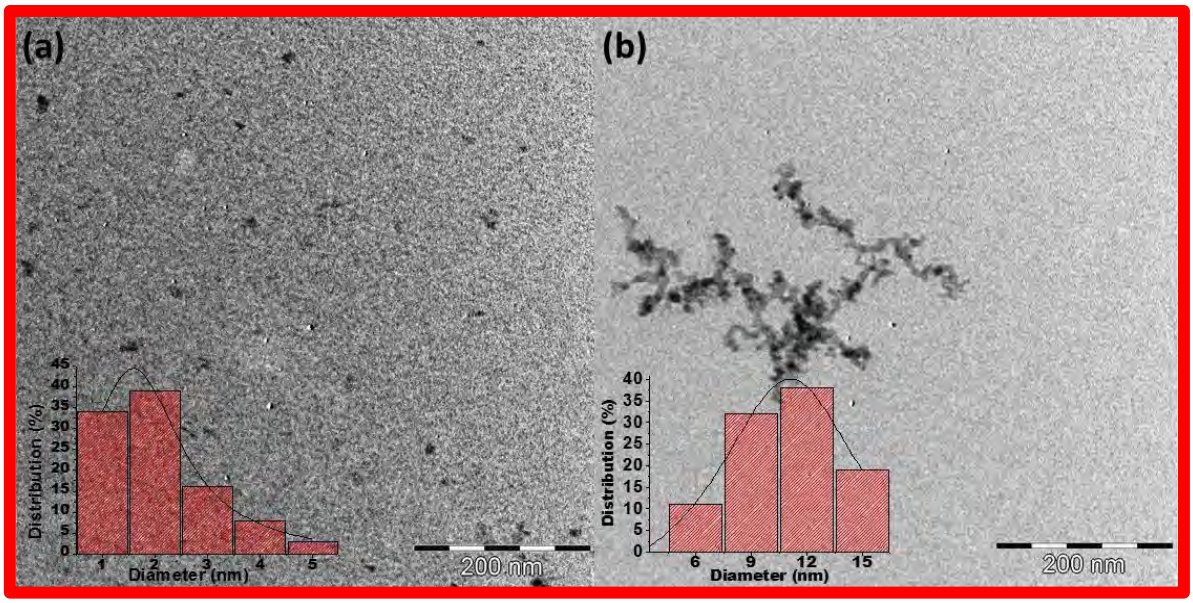

Figure 3.21: Transmission electron microscope (TEM) images of (a) $GQDs_2$(B1) and (b) $GQDs_2$(B1)-**3** and their respective size distribution

The GQDs and Pc nanoconjugates were studied using atomic force microscopy (AFM). In **Figure 3.22 A** and **B (curves (a)** and **(b))** show topological views of the $GQDs_2$(B1) alone and $GQDs_2$(B1)-**3** conjugate (as an example). Respective graphs in **Figure 3.22** (curves **(c)**) are topographic height profiles. The height profile of $GQDs_2$(B1) in **Figure 3.22 A(c)** gives approximately 1.6 nm. This suggests that most GQDs synthesised had single to few layers of graphene sheets, considering the theoretical thickness of graphene layer of 0.34 nm **[151]**. An increase in topographic height to 3.6 nm was observed in **Figure 3.22 B(c)**, indicating conjugation between $GQDs_2$(B1) (negatively charged) and positively charged (**3**). The DLS sizes are slightly larger than the AFM ones. As stated above the sizes determined by DLS have been reported to be larger than those determined by AFM since DLS results tend to be skewed toward larger particles **[155, 185]**.

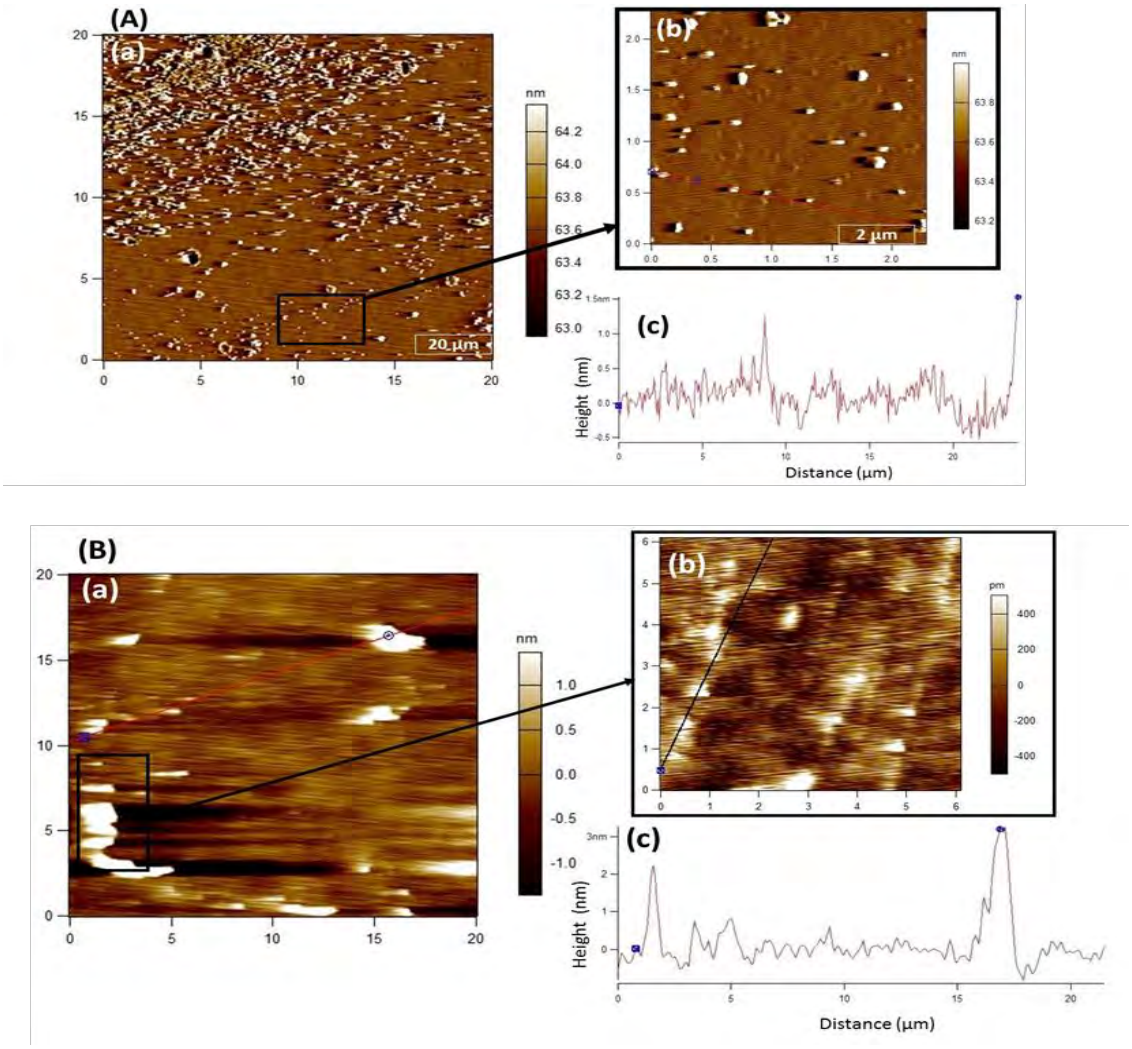

Figure 3.22: Atomic force microscopy (AFM) images showing the morphology and topographic of (A) $GQDs_2$(B1) and (B) $GQDs_2$(B1) -**3 (**as an example). (a) General overview 20 µm (b) closer view at 2 µm, and (c) topographic height graphs.

Table 3.3 shows the zeta potentials of the $GQDs_2$(B1), ZnPc derivatives and their conjugates. It should be noted that zeta potential of complex **2** (neutral) indicates a negative charge however, the complex is not soluble in water. Upon conjugation with GQDs, the conjugate ($GQDs_2$(B1)-**2**) is slightly water-soluble. The conjugate between negatively charged $GQDs_2$(B1) and **1** gave a high zeta potential of -23.6 mV, showing stability (**Table 3.3**). The high zeta potential also means $GQDs_2$(B1)-**1** is the least aggregated. However, there is a possibility of electrostatic repulsion since both $GQDs_2$(B1) and **1** are negatively charged when comparing **1**, **2**, and **3**.

In the presence of $GQDs_2$(B1), there were some blue shift (**1**), no shift (**3**) and red shift (**2**) in Q bands of complexes shown from UV-Vis spectra in **Figure 3.23 (Table 3.1)** as an indication of interaction of Pcs **[186]**. Red shifts and flattening have also been observed in porphyrins-graphene oxide nanoconjugates **[162]**.

The loading of the Pc complexes onto the GQDs was investigated following a literature report **[187-190]** using absorption instead of fluorescence. Similar masses (mg) of Pc and $GQDs_2$(B1)-Pc conjugate were weighed and dissolved in the same volume of the solvent. This was followed by comparing the Q band absorbance intensity of the Pc complex in the conjugate with that of the initial Pc before the conjugation. There was larger Pc loading for $GQDs_2$(B1)-**3** (14 mg) relative to $GQDs_2$(B1)-**2** (4 mg) and $GQDs_2$(B1)-**1 (**3 mg**)**, **Table 3.3**. There is a possibility of Pcs stacking onto each other. π-π stacking of the aromatic ring is known for Pcs **[19, 34]**. The largest Pc loading for GQDs-**3** could be due to the presence of both π-π and electrostatic interactions since GQDs are negatively charged while complex **3** is positively charged.

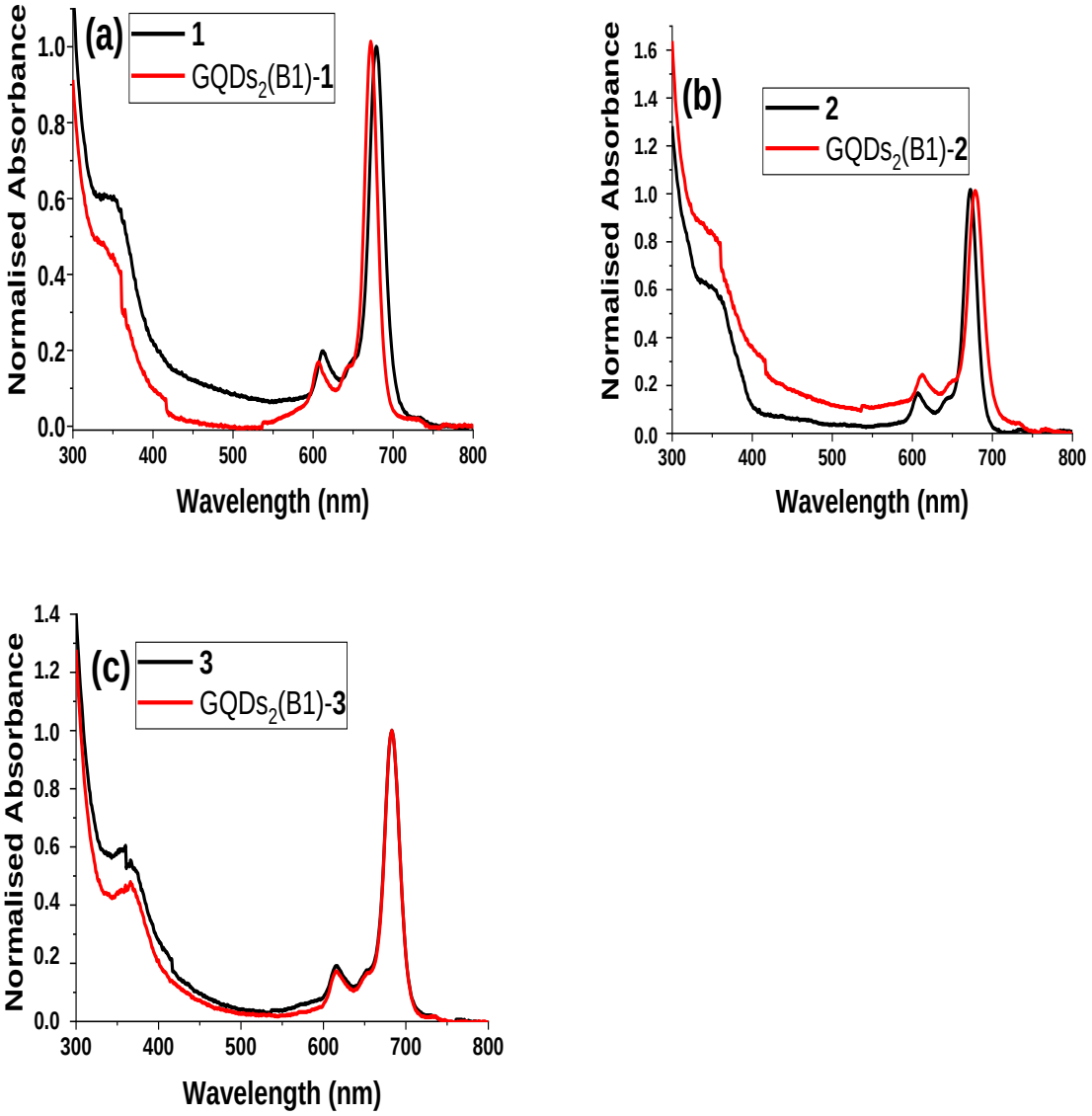

Figure 3.23: UV-Vis spectra of $GQDs_2$ (B1) nanohybrids relative **1**, **2** and **3** alone in DMSO.

3.3.1.2. Different size GQDs

This section discusses different sizes of graphene quantum dots: $GQDs_2$(B2), $GQDs_6$ and $GQDs_{10}$ with complex **3**. XPS spectra showed (N 1s) peak in the wide scan spectra of GQD_6-**3**, (**Figure 3.15 A: (d)** as an example) absent in GQDs alone. The C1s XPS high resolution spectra of the GQD_6-**3** conjugate (**Figure 3.15 B: (d)**) showed subpeaks with corresponding binding energies of C=C (283.17 eV), C-N (284.22 eV) and C=O (287.17 eV). The presence of C-N peak

could be associated with the existence of complex **3** in the conjugate. As stated above **(Table 3.6)** there was a decrease in the % atomic concentration of oxygen as the size of the GQDs increased. The % oxygen for GQD_6 (37.80%) decreased further in the presence of complex **3**. The decrease in % oxygen in the presence of complex **3** may suggest that GQDs are beneath the complex and hence the oxygen functionalities of the GQDs are not exposed and the oxygen on the complex **(3)** is not enough to offset the hidden oxygens of the GQDs.

GQD_6 and respective conjugate (GQD_6-**3**) show relatively high stability compared to the rest of the GQDs and conjugates in **Tables 3.5**. GQD_{10}-**3** which has the largest DLS size, is the least stable as shown in **Tables 3.3** and **3.5** as judged by its low zeta potential. Small particles have high zeta potential and are more stable **[189]**. Hence $GQDs_2$-**3** and $GQDs_6$-**3** are more stable. A positive zeta potential is observed in **Table 3.3** and **3.5** for the conjugates of $GQDs_2$(B2) and GQD_6 with complex **3**. This is important for application of these conjugates in cell studies because positive conjugates are preferred for ease of penetration of the negatively charged cell wall.

The XRD patterns for GQD_6 showed a peak at approximately $2\theta = 28°$, **Figure 3.24 (a)**. Upon conjugation to **3**, only GQD_{10}-**3** had a significant shift in the 2θ value. Shifts to lower 2θ values have been previously reported to be due to increased interlayer spacing from defects that enhance the interlayer distance **[86]**. A shift to higher 2θ values may then imply decreased interlayer spacing.

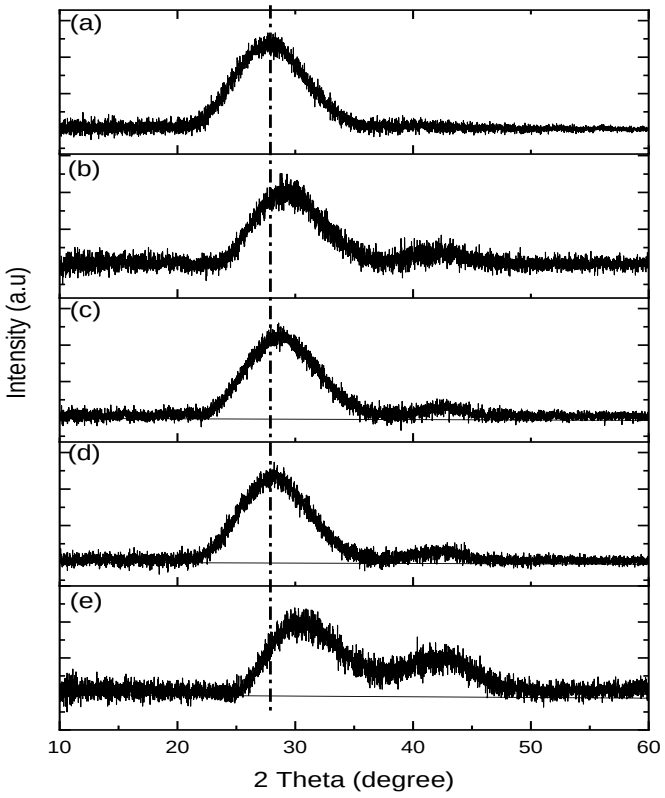

Figure 3.24: XRD spectra of (a) GQD_6 alone, (b) Complex **3** alone, (c) GQD_2-**3**, (d) GQD_6-**3**, and (e) GQD_{10}-**3**.

On conjugation to the Pc, the Raman G bands shift to higher wavenumbers in all cases compared to corresponding GQDs alone. The conjugation also results in the shifting of the D band to higher wavenumbers except for GQD_{10}-**3** which shift to smaller values compared to corresponding GQDs alone. Shifts in the Raman frequencies are often indicative of strong π-electron interactions in hybrid materials **[171]**.

Conjugation of complex **3** to $GQDs_2$(B2) and $GQDs_6$ resulted in increased GQDs defects as judged by increase in I_D:I_G ratio, compared to corresponding unbound, $GQDs_2$(B2) in **Figure 3.25. Table 3.2**, **3.5**. This increase in disorder could have been due to the increased number of Pc molecules loaded onto the small sized GQD nanoparticles, to cause more stress/strain onto the nanoparticle. The increase or decrease in I_D:I_G ratio of GQDs has been previously

reported to be due to size-dependent edge-state variation of GQDs **[190]**. Interestingly, for GQD_{10} there was a decrease in I_D:I_G ratio upon conjugation. A decrease in the I_D:I_G ratio has been reported for graphene oxide in the presence of a phthalocyanines **[190].** Loading was determined from spectra as outlined in section 3.3.1.1. Since GQD_{10} have less Pcs loaded, this indicates that Pcs loaded onto GQDs would have less strain/stress and decreased defects.

Large nanoparticles have less surface coverage than the small nanoparticles because of fewer exposed sites. Hence the decrease in the loading with increase in size, **Table 3.3**, **3.5.**

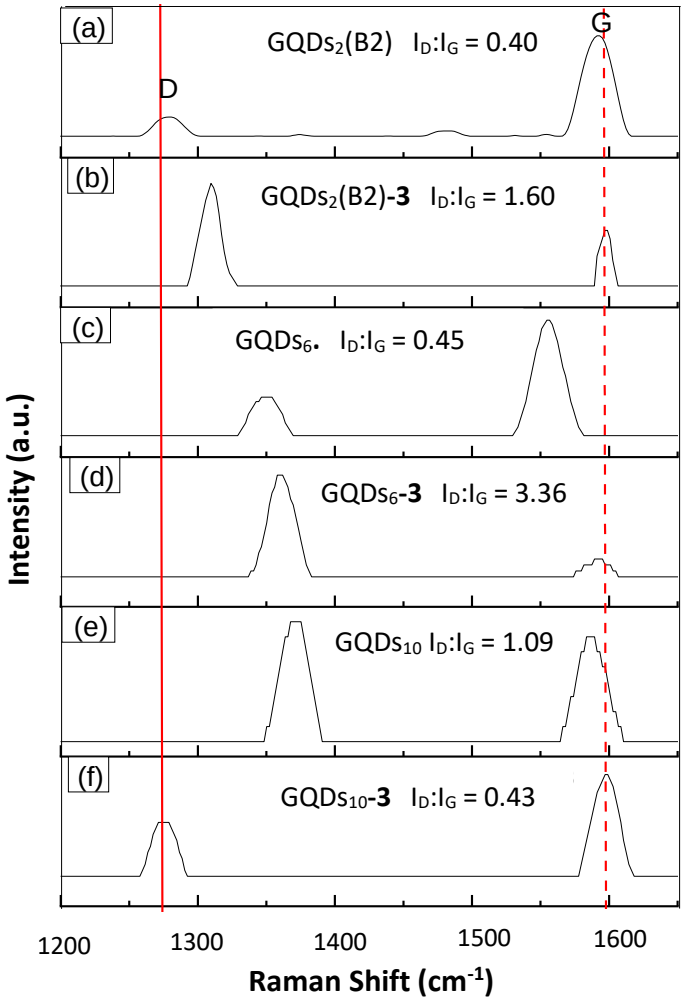

Figure 3.25: Raman spectra for (a) GQD_2, (b) GQD_2-**3**, (c) GQD_6, (d) GQD_6-**3**, (e) GQD_{10} and (f) GQD_{10}-**3**.

3.3.1.3. Types of carbon nanomaterials (GQDs, CDs and DNDs)- π - π conjugates

Complex **3** was non-covalently linked to carbon based nanoparticles: detonation nanodiamonds (DNDs), carbon nanodots (CDs) and graphene quantum dots ($GQDs_2$(B3)) to form nanosembles of DNDs-**3**, $GQDs_2$(B3)-**3** and CDs-**3**, respectively.

There were slight red shifts in the Q band of complex **3** upon conjugation of carbon nanoparticles. CDs: (683 to 686, red shift), $GQDs_2$(B3): (683 to 682, no significant shift) and DNDs: (683 to 686, red shift), **Figure 3.26, Table 3.1**. Red shifts have also been observed in porphyrins-graphene oxide nanoconjugates and were attributed to molecular flattening **[162]**.

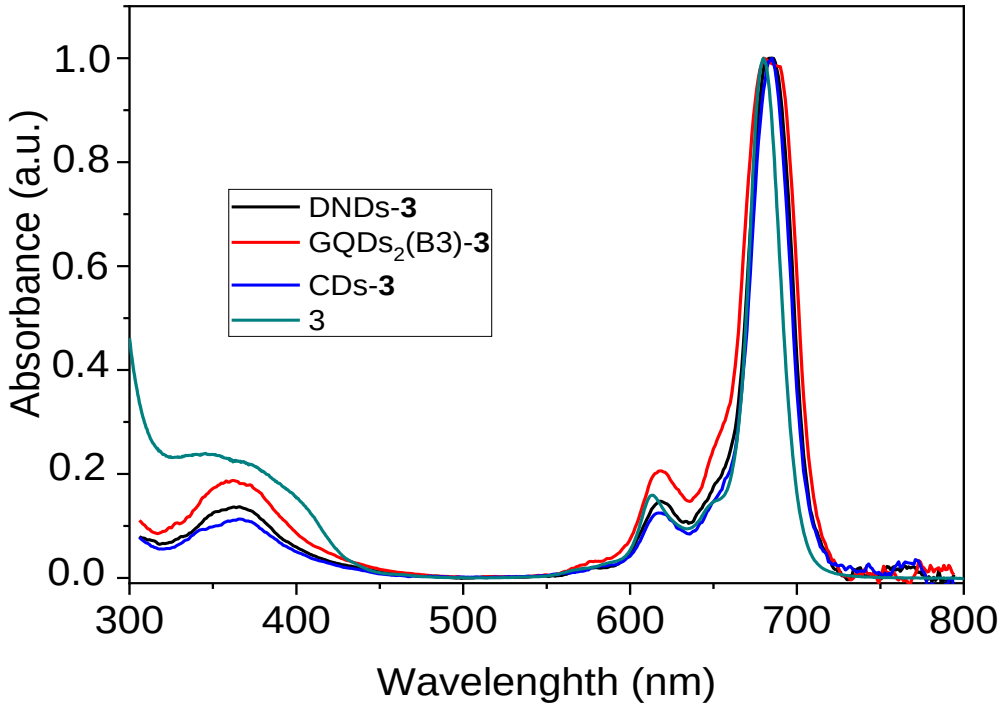

Figure 3.26: Absorbance spectra of complex **3** and its conjugates in DMSO

Thermogravimograms of complex **3**, $GQDs_2$(B3)-**3**, DNDs-**3** and CDs-**3** conducted in the temperature range of 50–1000 °C in air are shown in **Figure 3.27** to indicate thermal stability. Upon grafting complex **3** onto DNDs, less weight loss in the DNDs-**3** nanoconjugate (94%) compared to DNDs alone (99%) at 1000 °C is shown in **Figure 3.27**, thus indicating improvement in thermal stability of nanoparticle (DNDs) associated with adsorption of Pc (complex **3**). Similar improvement in thermal stability of nanoparticle single walled carbon nanotubes (SWCNTs) upon functionalisation of Zn monocarboxy phenoxy phthalocyanine (ZnMCPPc)-spermine has been previously reported **[191]**. However, $GQDs_2$(B3)-**3** (38%) and CDs-**3** (35%) showed an increased weight loss when compared to $GQDs_2$(B3) (15%) and CDs (7%) alone. Similar thermal decomposition behaviour has been previously reported when GO sheets were functionalised with Fe phthalocyanine, with the additional weight loss being associated with the decomposition of the phthalocyanine **[192, 193]**. However, other studies have shown that charge influences both geometry and stability of flat clusters **[194]**. Another possible explanation for this change in thermal stabilities of nanoparticles and respective conjugates might be due to interaction between the carbon network in nanoparticles (consisting of sp^3 and sp^2 bonds) and H and N and embedded metal from Pc which determines the stability of the final system **[94]**. Carbon nanoparticles comprise of a complex interplay of different carbon phases **[156]**. For instance, carbon structure fragments can be surrounded by a shell consisting of graphene-like carbon (sp^2), disordered sp^3 carbon and surface state carbon, as well a number of functional groups on the surface DNDs **[195]**, which will result in differences in stability.

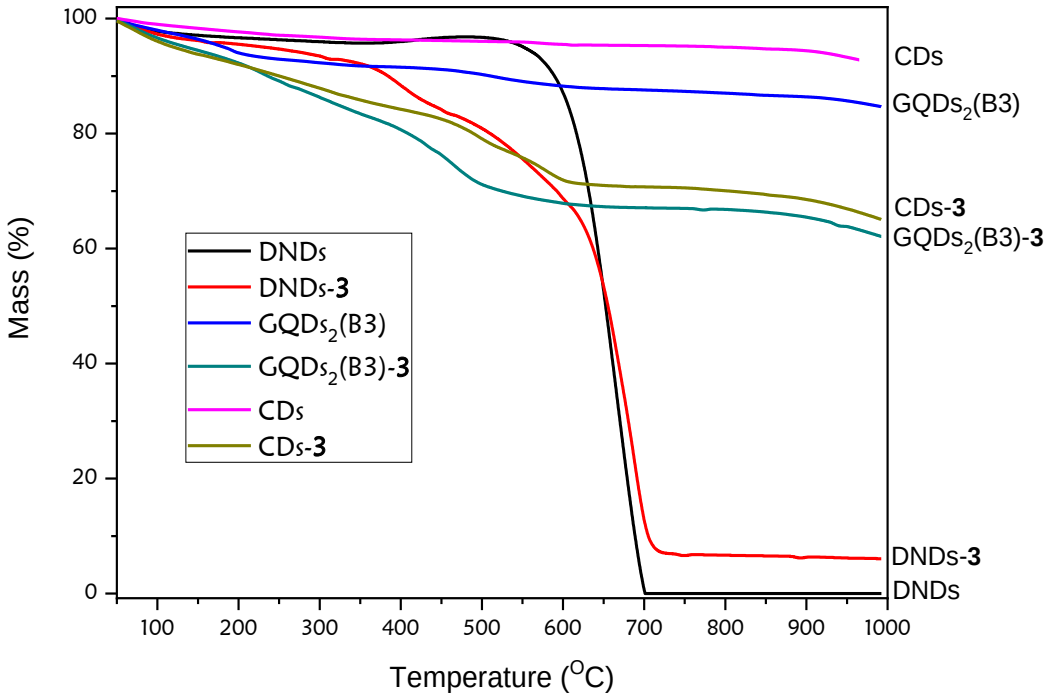

Figure 3.27: Thermogravimetric analysis (TGA) curves for samples heated at 20 °C min^{-1} from 50 to 1000 °C in air

Mass loading ratios were calculated from TGA, using $GQDs_2$(B3), DNDs, and CDs decomposition as a point of reference following previously reported method **[142]**. Mass loading of complex **3** were 299, 829, and 42 μg Pc per mg of the nanoparticle (NP) for $GQDs_2$ (B3)-**3**, CDs- **3**, and DNDs-**3**, respectively. There is a higher mass loading for the larger carbon nanoparticles. However, the nature of the functional groups on the NP may also affect the mass loading in addition to the size.

Raman I_D:I_G ratio in **Table 3.3** decreased for CDs-**3** and increased for DNDs-**3** and $GQDs_2$(B3)-**3** compared to NPs alone**.** Increase in defect is judged by increase in I_D:I_G ratio, compared to corresponding unbound nanoparticles, **Table 3.3**. Increases or decreases in I_D:I_G ratios of GQDs has been previously reported to be due to size-dependent edge-state variation of GQDs **[171]**.

3.3.2. Ester bonds

Complexes **4c**, **5, 6**, **12** were employed since they have OH for linking to COOH of DNDs, as shown in **Schemes 3.5**, **3.6**. Detonation nanodiamonds have been reported to contain carboxyl and hydroxyl moieties on the surface **[70, 178, 196]**. Thus, COOH groups on DNDs were used for covalent linking to complexes **4c**, **5**, **6** and **12** using DCC and NHS as activating and coupling agent, respectively. The ester bond occurred through esterification reaction between the carboxylic moiety on the DNDs and the hydroxyl moieties of complexes. For complex **12,** formation of DNDs-**12** was followed by adsorption of complex **3 (**Pc**)** to form **3**-DNDs-**12** in **Scheme 3.6.**

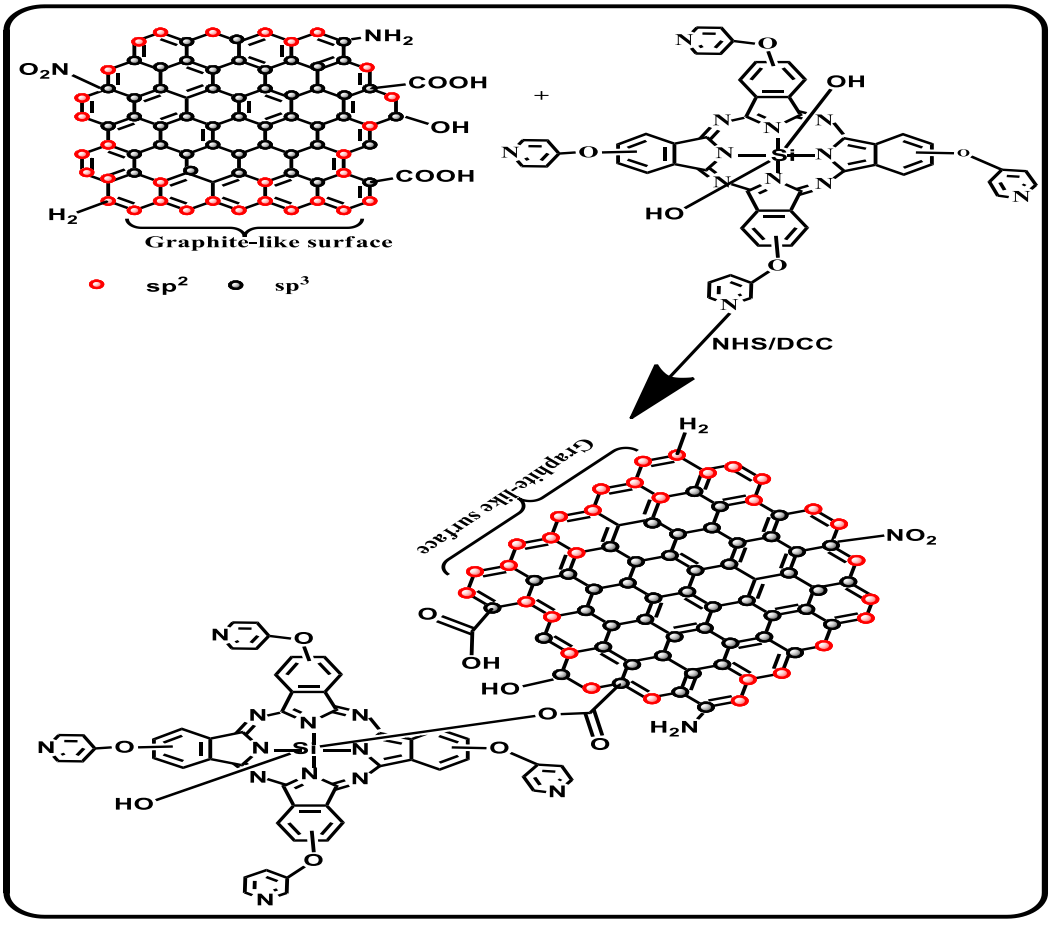

Scheme 3.5: Ester covalent linkage between of complex **5** to DNDs (as an example) resulting in DNDs-5 nanohybrid.

The FTIR spectra following π-π stacking of **4b** as well as covalent linkage of complex **4c** to DNDs are shown in **Figure 3.28**. A slight shift in C=N peak from 1670 cm^{-1} (for Pc alone) to 1656 cm^{-1} (for the conjugate, using complex **4b** and its conjugate as examples in **Figure 3.28A**) is observed. The peak broadening around 3200 cm^{-1} is associated with OH stretching in the DNDs. For complex **4c** (**Figure 3.28 B**) both π-π and ester bond formation are possible. **Figure 3.28 B(c)** shows the FTIR spectrum upon covalent linkage of complex **4c** to DNDs. The DNDs alone showed high intensity OH signal at 3386 cm^{-1}, C=O stretching at ~ 1700 cm^{-1} as a shoulder to the adsorbed water OH bending at 1636 cm^{-1} **[178]**. The C-H peak is observed at 610 cm^{-1}. The OH and C=N signals of **4c** were observed at 3007 and 1510 cm^{-1}. A drastic reduction in intensity and shift to lower wavenumbers for DNDs peaks at 3386 cm^{-1} to 3324 cm^{-1} was observed upon covalent linkage of **4c** to DNDs, suggesting conversion of most OH group in COOH in DNDs to ester bond hence decreasing the OH signal. The splitting of the C=O peak around 1600 cm^{-1} in the conjugate can be associated with the presence of RCOOR' stretch arising from the linkage of **4c** to the DNDs, indicating covalent bonding from hydroxyl group of the Pc to the carboxylic moiety of the DNDs. Moreover, shifts in the C=N peak positions from 1510 cm^{-1} in the Pc to 1438 cm^{-1} in the conjugate (DNDs- **4c**) (**Figure 3.28** (**c**)) also confirms the functionalisation of DNDs by complex **4c**.

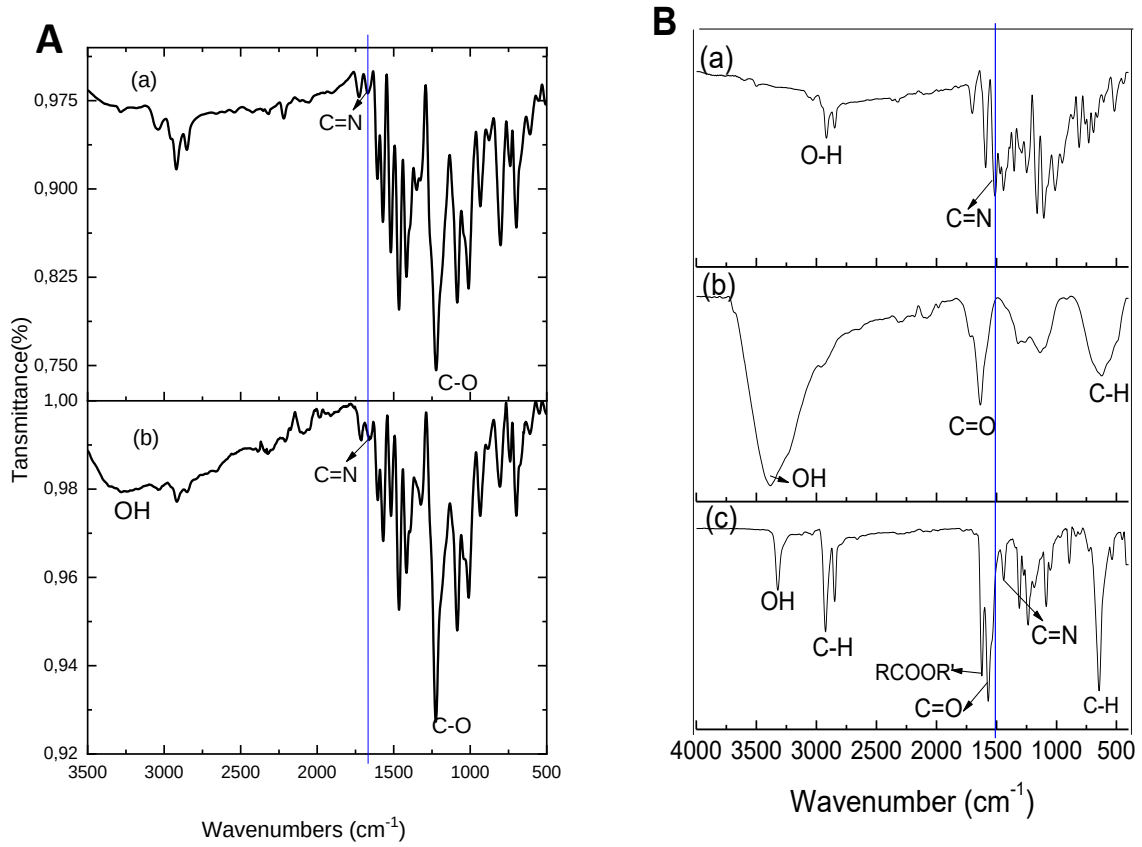

Figure 3.28: FTIR spectra of (A) non-covalent interaction: (a) **4b** and (b) DNDs – **4b** and (B) covalent linkage: (a) **4c** alone, (b) DNDs and (c) DNDs- **4c**.

The XPS wide scan spectra showed all the expected elements for DNDs (**Figure 3.29 A (a))**, **4c** and DNDs- **4c** (**Figure 3.29 A (a)-(b)**) at respective binding energies with C1s (285 eV), N 1s (398 eV) and O1s (530 eV). There are additional Si2p peaks for **4c** (**Figure 3.29 A(b)**) and the conjugate (**Figure 3.29 A (c)**) due to the presence of the central Si atom in the phthalocyanine. **Table 3.4** shows that DNDs consist mainly of C (95.46 %) with some O (3.04%) and N (1.48%). The %O and %N increase in the presence of the Pc since the Pc has both these elements. High resolution spectra obtained for the C1s component are shown in **Figure 3.29B ((a)-(c))** for DNDs, **4c** and respective conjugate. Upon the deconvolution of the C1s spectra, **Figure 3.29B (a)**, the DNDs reveals the presence of four components at 282.8, 283.6, 285.8 and 286.9 eV assigned**.** Pc alone (**Figure 3.29B (b))** also has four components. The C1s spectrum of the

DNDs-**4c** nanohybrid was deconvoluted into five peaks (282.7, 283.7, 285.1, 286.4 and 288.2 eV), **Figure 3.29 B (c)**. The new peak at 288.2 eV is assigned to COOR, due to the ester bond between the hydroxyl moiety of **4c** and carboxyl moiety in DNDs. Hence, XPS proves the formation of the ester bond linkage

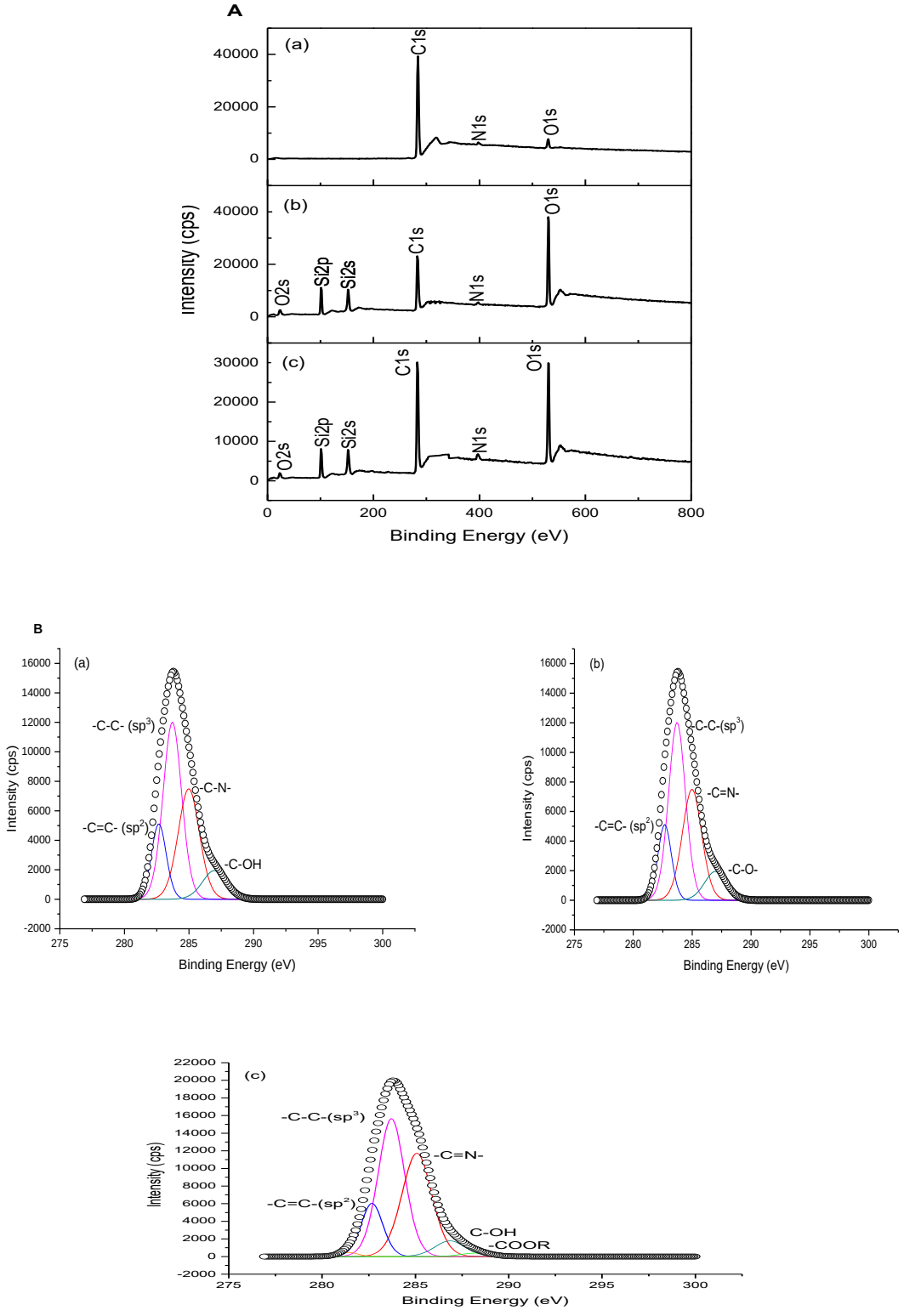

Figure 3.29 A: Wide scans of (a)DNDs, (b) **4c**, (c) DNDs- **4c** conjugate, B High resolution C1s spectra of (a) DNDs, (b) **4c**, and (c) DNDs-**4c**

There was aggregation for DNDs–**4c** and blue shifted peak is observed in **Figure 3.30 A (**Appendix **Figure A1)** which was not observed for **4c** alone, suggests H aggregation. It is most likely that the presence of both the ester and π - π bonds in DNDs–**4c** could have resulted in more association between the Pcs hence resulting in aggregation. Aggregation was confirmed for DNDs–**4c** since there was a decrease in the peak due to the aggregate (high energy peak) as the concentration was decreased, **Figure 3.30 B**, and a slight increase in the peak due to the monomer (low energy peak). There was no aggregation for all the other ester bonded complexes (appendix, **Figure 1A**).

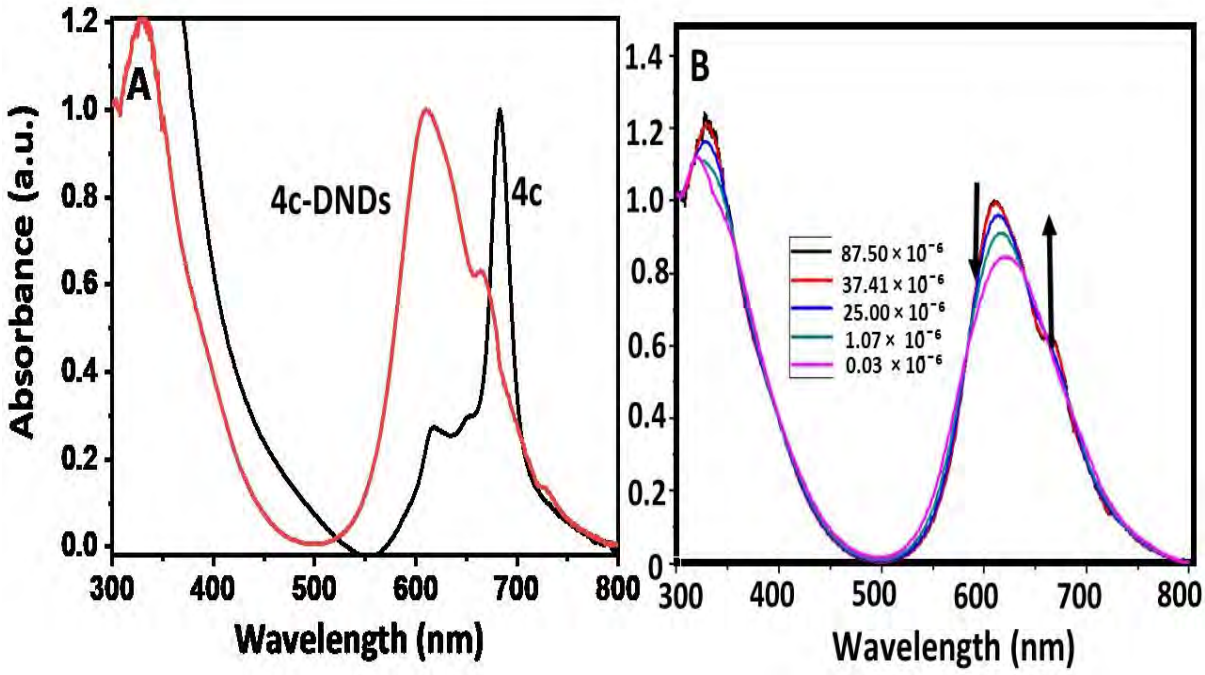

Figure 3.30: Absorbance (A) is for **4c** alone, DNDs-**4c**, (B) Spectral changes for DNDs–**4c** as the concentration was decreased in DMSO.

Qualitative verification of the elemental composition of the DNDs-Pc conjugate was investigated using EDX as shown in **Figure 3.31 (a)-(c).** The EDX spectra of DNDs alone showed the presence of C and O peaks as expected (**Figure 3.31 (a)**). The N peak is not observed for DNDs alone since C and N are next to each other in the periodic table, and presence of major carbon composition in these samples overlaps with the nitrogen peak, which could be found

in small percentages when compared to carbon. However, XPS has proven the presence of N **(Table 3.4)**. DNDs conjugated to complex **4c** showed Si, C, N and O indicative of the presence of SiPc (**Figure 3.31 (b)**). Similarly, nanoconjugates of DNDs-**5** and DNDs-**6** showed the presence of Si, C, N and O peak.

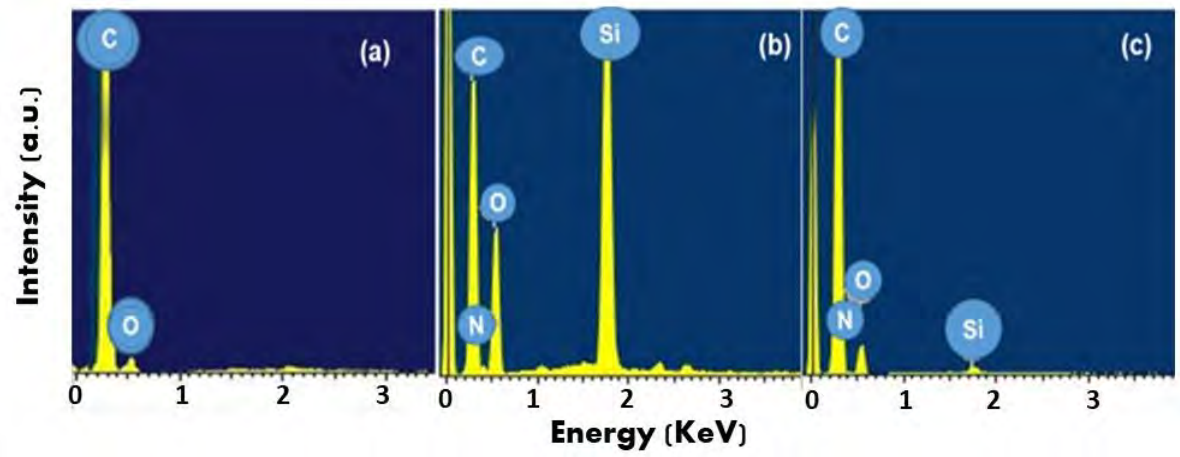

Figure 3.31: EDX spectra for (a) DNDs, (b) **4c**, and (c) DNDs-**4c**

3.3.3. Ester followed by π - π (Pc/BODIPY)

Complex **12** (BODIPY) was linked to DNDs by ester followed by π - π of Pc, (**Scheme 3.6**).

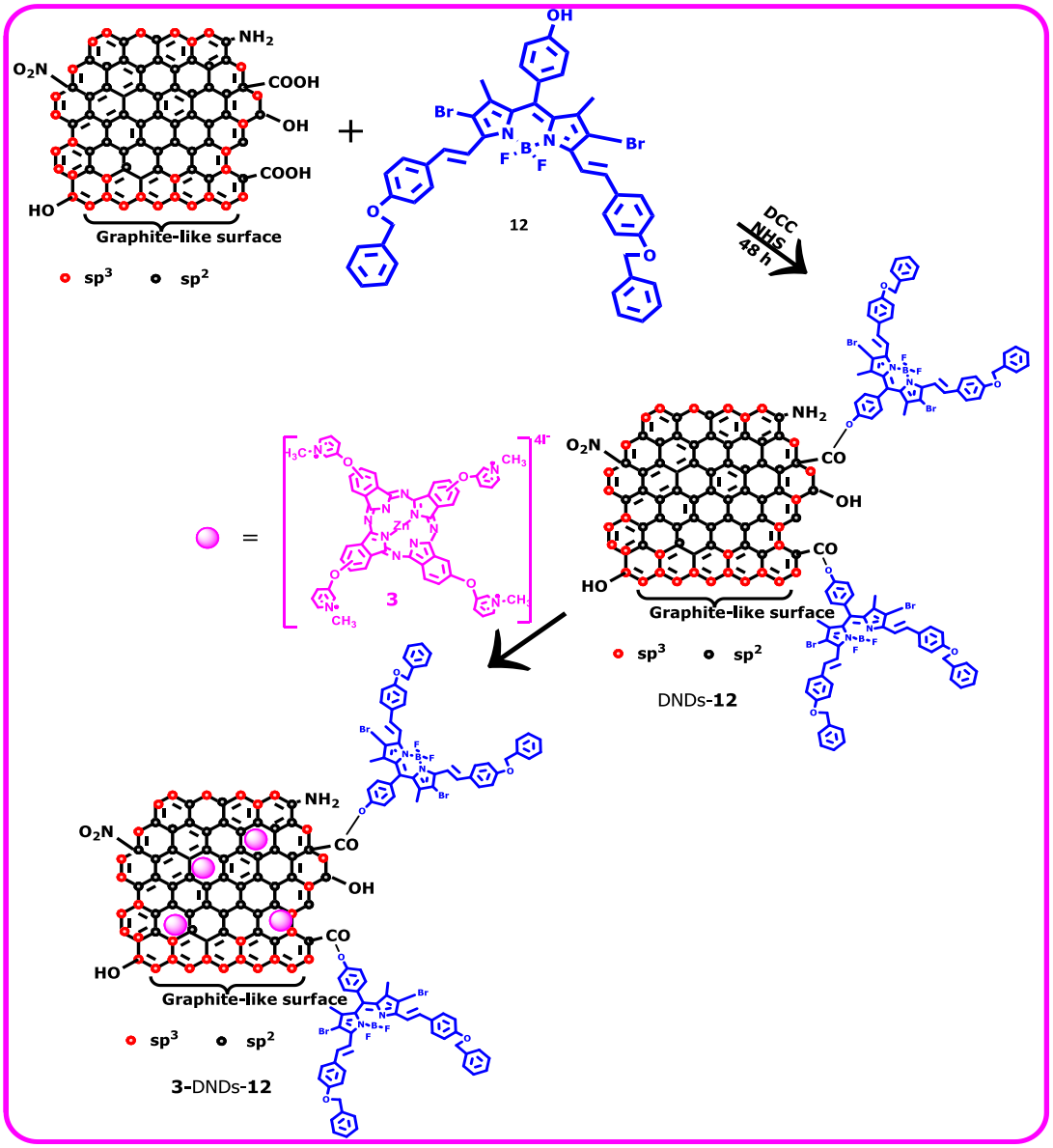

Scheme 3.6: Ester covalent linkage complex **12** and detonated nanodiamonds (DNDs) resulting in DNDs-**12** nanoconjugate systems andπ – π interaction between complex **3** and DNDs-**12** to form **3**-DNDs-**12.**

Ester linkage between DNDs and complex **12** was confirmed using FTIR **(Figure 3.32)**. The covalent linkage between DNDs and BODIPY was confirmed by an emergence of ester bond around 1627 cm^{-1} **(Figure 3.32 (c))**. The FT-IR spectrum of complex **12** in **Figure 3.32 (a)** indicated the presence of ROH and B-N at 2897 and 1440 cm^{-1}. While COOH, C=O and C-H at 3384, 1624 and 625 cm^{-1}, respectively, **Figure 3.32 (b),** were observed for DNDs. Slight shifts of C=O, B-N, ROH and COOH to 1562, 1444, 2922 and 3328 cm^{-1} were observed upon linkage of the BODIPY to the DNDs. Shifts in the IR bands confirm structural change **[197]**.

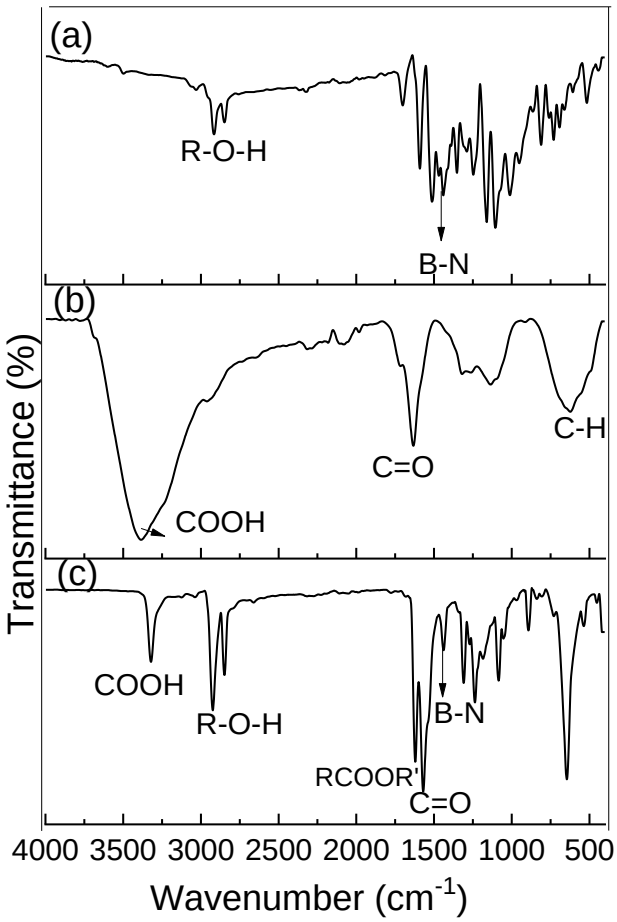

Figure 3.32: FTIR spectra of (a) Complex **12**, (b) DNDs, and (c) DNDs-**12** showing formation of ester bond.

Zeta potential is an important parameter in the fabrication of supramolecular structures as a high zeta potential confers colloidal stability. Therefore, zeta potential values of nanoconjugated assembles intended for biomedical applications gives an indication of aggregation tendencies in aqueous media **[198]**. Previous studies have shown that temperature, pH and sample concentration are amongst other factors that can influence the zeta potential **[199]**. In this study, temperatures (11, 22, 37, 60 and 80 °C), pHs (2, 4, 7, 10 and 13) and concentrations (5, 10, 20, 40 and 50 µg/mL (m/v)) were employed.

Zeta potential was carried out in water instead of cultured medium because previous studies on nanoparticles have shown that cultured media contains albumin protein which is negatively charged in neutral pH and can adsorb to the surface of the nanoparticle to influence their zeta potential **[200, 201]**.

Figure 3.33 (a) illustrates the zeta potential measurement as a function of pH for DNDs nanoparticles with or without complex **12** and/or **3** conjugation. Zeta potential values of DNDs increased (became more positive or more negative) upon conjugation (DNDs-**12**, **3**-DNDs and **3-**DNDs-**12**) for pH = 2, 4 and 7. Similar increases in zeta potential upon functionalisation of the NDs to doxorubicin (DOX) and TAT (HIV trans-activator of transcription protein) have been previously reported **[202]**. High zeta potential values, irrespective of charge, infer stability **[203]**. High zeta potential values following hybrid formation points to improvement in the dispensability of the resulting supramolecular structures, signifying high colloidal stability. When the zeta potential is small, attractive forces may exceed this repulsion, resulting in aggregation **[156]**. Thus, **Figure 3.33 (a)** shows higher stability for **3-**DNDs-**12** when compared to DNDs-**12**, **3**-DNDs and DNDs alone at pHs 2, 4 and 7. To find a suitable concentration of the drug for electrostatic stabilization of the colloids, different concentrations of **3-**DNDs-**12** were investigated in aqueous medium prior to *in vitro* cell studies. Suspensions that have a measured zeta potential above 30 mV or below −30 mV are considered stable because these particles will presumably maintain their repulsive forces while dispersed **[204, 205]**.

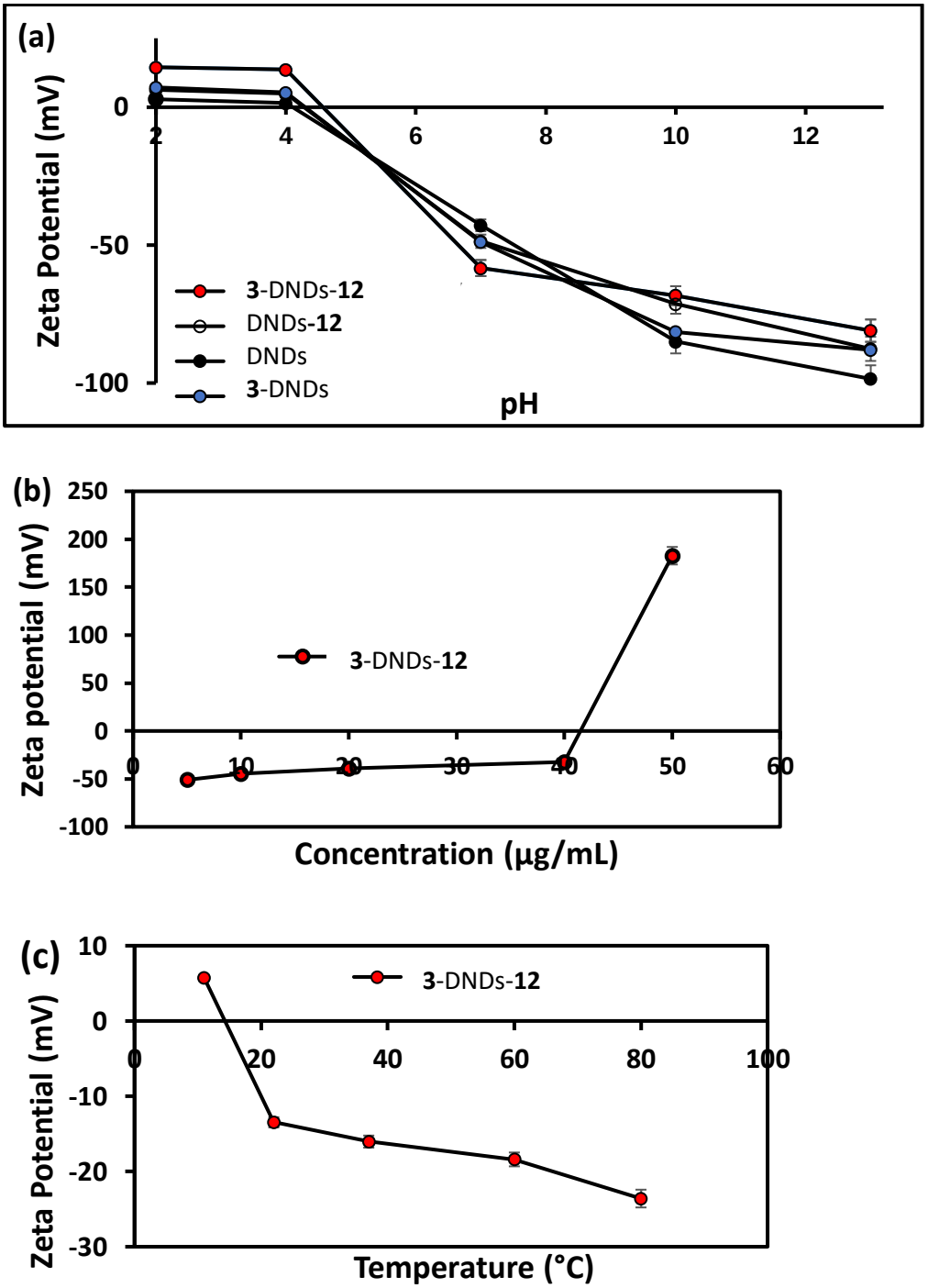

Figure 3.33: Zeta potential of (a) DNDs and conjugates as function of pH when concentration (50 µg/mL) and temperature (27 °C) are kept constant; (b) **3**-DNDs-**12** at different concentrations, but under constant temperature of (37°C) and neutral pH (7), and (c) **3**-DNDs-**12** under constant concentration (50 µg/mL) and neutral pH (7) as the temperature of the aquesous medium changes.

Figure 3.33 (b) shows general stability of **3-**DNDs-**12** (-51, -44, -39, -32 and 183 mV) for various drug concentrations (5, 10, 20, 40 and 50 µg/mL), respectively, in aqueous media. **3-**DNDs-**12** showed the most stability at high concentration of 50 µg/mL when both pH (7) and temperature (37 ˚C) remained constant. Therefore, high concentrations of the nanoconjugate resulted in high zeta potential value. Similar increases due to zeta potential with increase in concentration as obtained in **Figure 3.33 (b)**, have been previously reported as an indication of neutralisation of surface charges in a solution **[199, 203]**

Figure 3.33 (c) shows zeta-potential measurements as a function of the temperature of the solution at approximately 11, 22, 37, 60 and 80 ˚C for 50 µg/mL concentrated solution at pH 7. The behaviour of constructed **3-**DNDs-**12** nanoconjugate system was investigated in order to understand the effect of temperature on the nanohybrid. It is observed that zeta potential increases as the temperature is increased indicating stability of the compound. This behaviour is consistent with experimental results from previous studies **[199]**. Therefore, an increase in body temperature will not compromise the stability of the drug but rather improve it.

Zeta potential values for conjugates (DNDs-**12**, **3**-DNDs and **3-**DNDs-**12**) showed that they are stable because they are > ±30 mV, while DNDs and complex **3** alone are unstable in solution **[205]**.

Figure 3.34 (a) and **(b)** shows UV-Vis absorption spectra of DNDs, Pcs, BODIPY and their conjugates, separately dispersed in DMSO and water, respectively. The broad absorption band of DNDs in both solvents, have been discussed above **[206]**. Absorption maxima for complexes **3** at 683 and **12** at 649 nm has been previously reported **[5, 54].** There was a red shift (and broadening) in the spectrum of BODIPY **(12)** upon conjugation to DNDs. Similar red shifts and peak broadening upon conjugation of complex **12** to nanoparticles has been previously reported **[207].** In water, extensive aggregation occurred as judged by peak broadening shown in **Figure 3.34 (b)** of the dyes, typical of Pcs in aqueous media **[19]**.

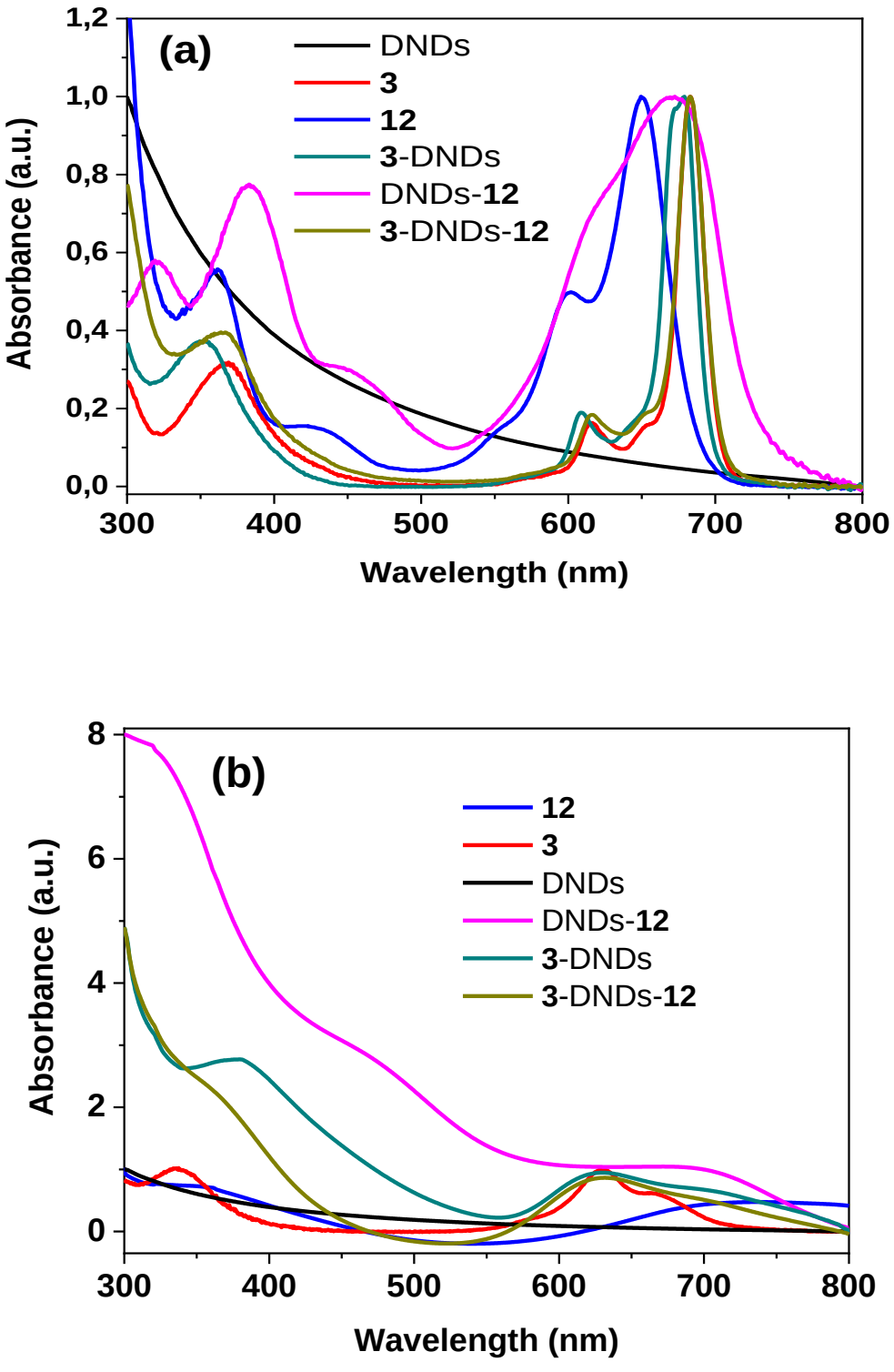

Figure 3.34: UV-Vis spectra of DNDs, **3**, **12**, DNDs-**12**, **3**-DNDs and **3**-DNDs-**12** in (a) DMSO and (b) water (in 1% DMSO).

3.3.4. Amide bond (only asymmetric complex 10 and 11)

Asymmetric complexes (**10** - no positive charge, **11**-three positive charges) are covalently linked to boron doped DNDs to result in B@DNDs-**10** and B@DND-**11**. **Scheme 3.7** shows π - π conjugation is also possible in B@DNDs-**11** as an example. Complexes **10** is linked with different heteroatoms doped DNDs (B@DNDs, P@DNDs, N@DNDs, S@DNDs and S&N@DNDs) through amide bond using B@DNDs as an example in **Scheme 3.7**.

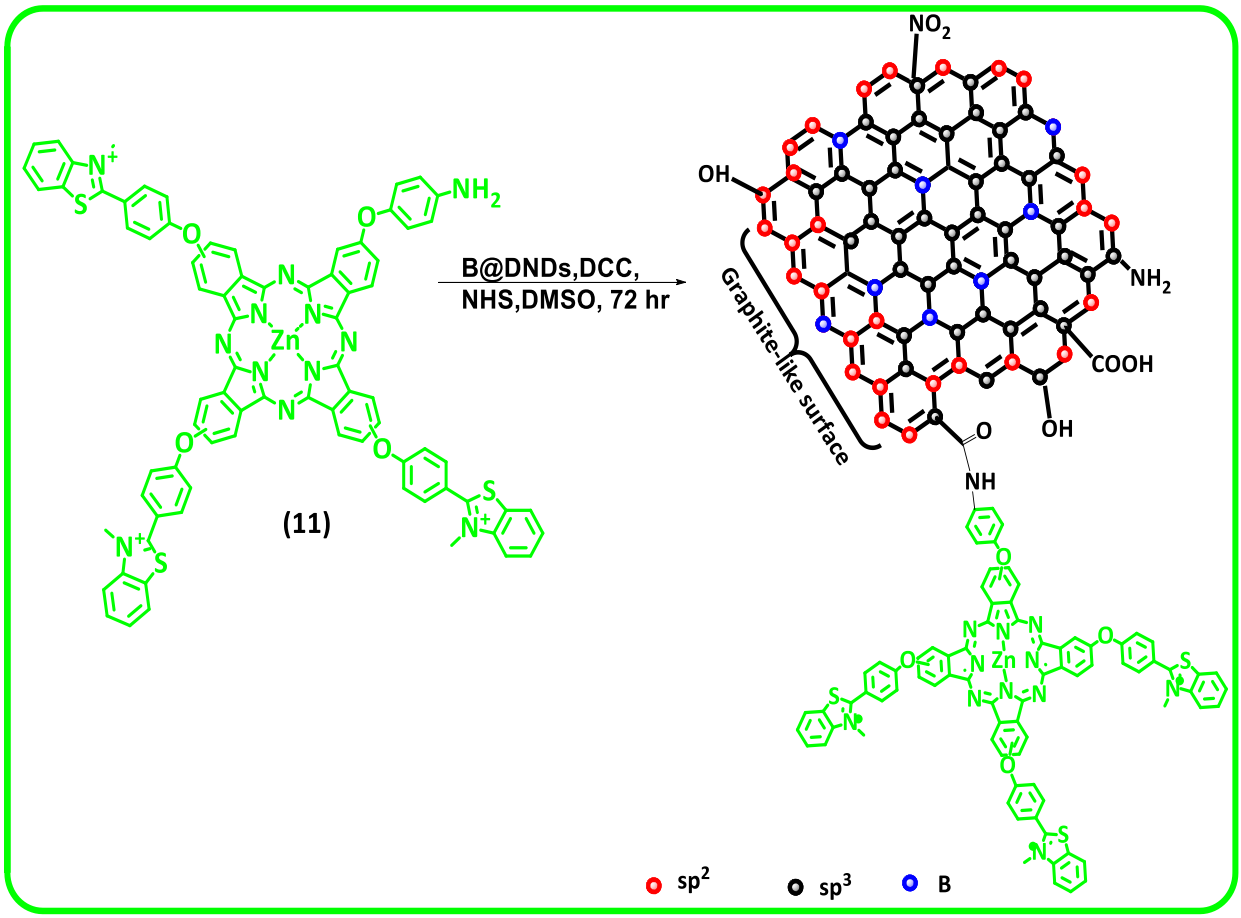

Scheme 3.7: Synthetic route B@DNDs-**11** which also represents B@DNDs-**10**.

TEM micrographs of B@DNDs alone and in the presence of complex **10** as an example is shown **Figure 3.35** due to aggregation following conjugation.

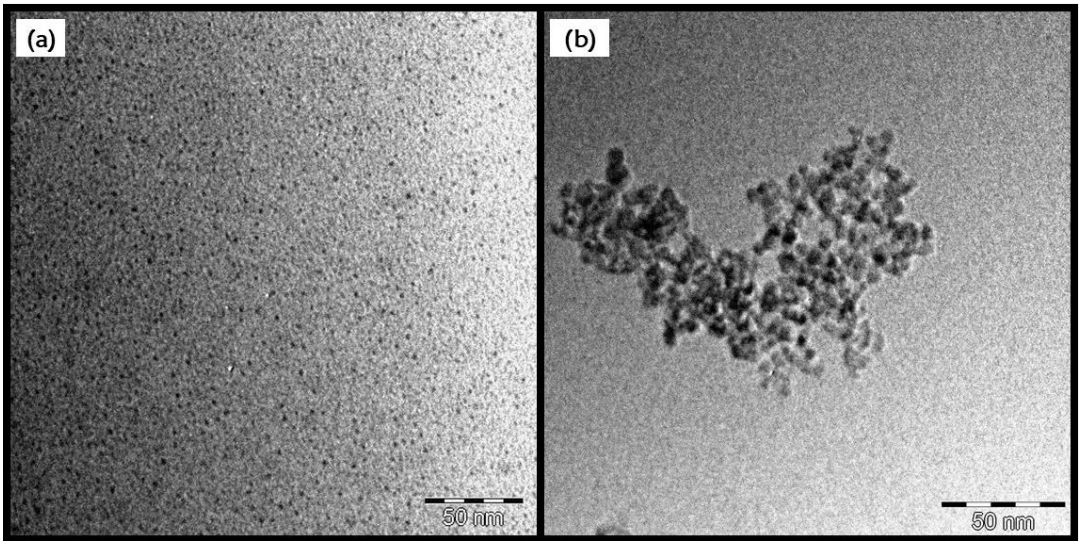

Figure 3.35: TEM micrographs of (a) DNDs alone and (b) DNDs-**10** conjugate (as an example)

There was an increase in DLS size upon conjugation to 28.2, 46.5, 78.78, 54.0, 30.8, and 43.8 nm for DNDs-**10**, B@DNDs-**10**, P@DNDs-**10**, N@DNDs-**10,** S@DNDs-**10** and S&N@DNDs-**10**, respectively, compared to corresponding DNDs in **Table 3.3.** Zeta potential of all conjugates showed negative values as expected due to the presence of the partially electronegative nitrogen from amide groups of the Pc.

Surface functional groups of nanomaterials intended for biomedical application are crucial for their hydrophilicity and dispersibility in water and various bio-fluids. Thus, the chemical groups of the nanoconjugates were determined using FTIR spectroscopy (**Figure 3.36**). The C=O and O-H bands at 1630 and 3377 cm^{-1} are a result of stretching carboxylic and hydroxyl group vibrations in the B@DNDs and are observed in the nanohybrids with Pcs in **Figure 3.36(b, c)**. The vibrational band due to B-C was observed at 1095 cm^{-1} (**Figure 3.36(a)**). Broadening and blue shift in this peak from 1095 to 1018 cm^{-1} is observed for all nanohybrids, **Figure 3.36**(**b, c**), implying formation of new materials **[208]**. The FTIR spectra for Pcs (**10,11**)

showed similar bands: Zn-N **[209]**, C-S, C=N peaks at 938, 1099, and 1395-1500 cm^{-1} are associated with stretching and bending structure of the Pcs (**Figure 3.36(d)**). Upon covalent linkage of complex **10** and **11** to B@DNDs, the primary amine at 1595 cm^{-1} for complexes **10,11** collapsed into a shoulder peak at 1719 cm^{-1} in respective nanohybrids indicative of conversion of primary amine to secondary amine due to formation of amide bond between respective complexes and the B@DNDs (**Figure 3.36**).

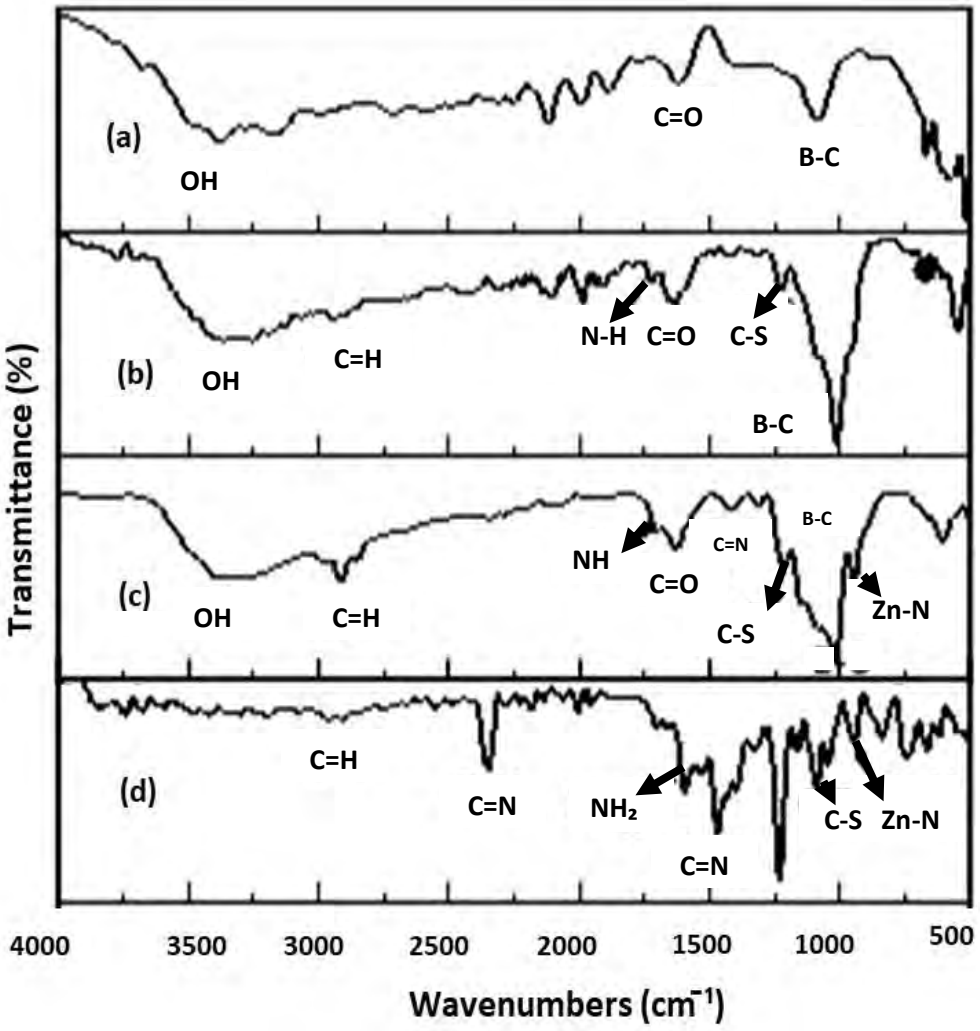

Figure 3.36: FTIR spectra of (a) B@DNDs, (b) B@DNDs-**10,** (c) B@DNDs-**11,** (d) **10**

Figure 3.37shows the X-Ray diffractometer (XRD) patterns for complex **10** and conjugates. Pc (**10**) at 2θ = (15-30)° is typical of Pc alone **[210]**, the peak is broad due to amorphous nature of the Pc. For all the doped DNDs the peaks at 45, 73 and 92° are due to 111, 221 and 311 plane of DNDs **[179]**. **Figures 3.37 (a, c, e, g)** and **(i)** (the latter two planes are very weak), and they showed no significant shift following linking. The broad weak peak for the Pc can be seen in the conjugates.

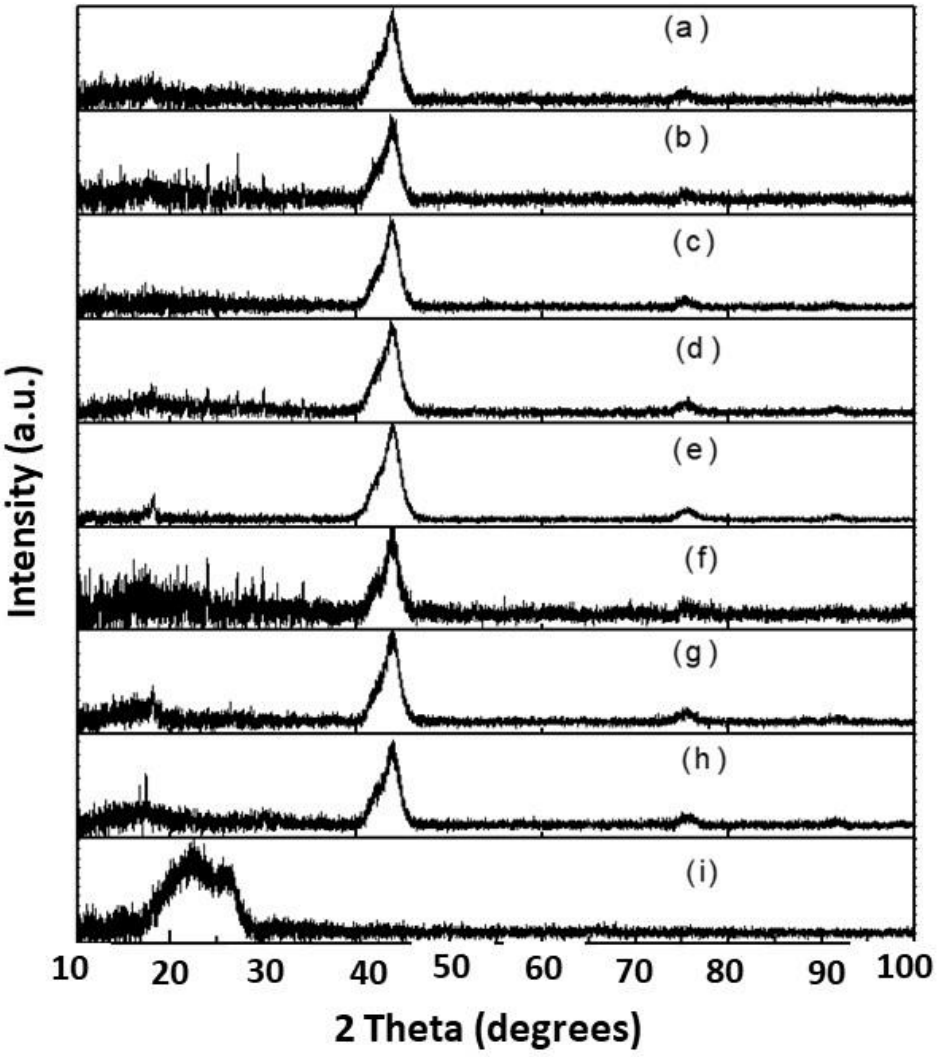

Figure 3.37: XRD spectra (a) B@DNDs alone, (b) B@DNDs–**10**, (c) P@DNDs alone, (d) P@DNDs–**10**, (e) N@DNDs, (f) N@DND-**10**, (g) S&N@DNDs, (h) S&N@DNDs-**10**, and (i) Complex **10** alone.

The increase in absorption above 600 nm to is due to absorption by DNDs, **Figure 3.38**. Broadening and splitting in Q bands shown in **Figure 3.38**, is attributed to aggregation associated with Pcs in the nanoconjugated system, there is more aggregation in water, **Figure 3A** (Appendix)**.** There is more enhancement together with broadening of the Q band for the co-doped S&N@DNDs-**10**. Thus co-doping of DNDs attenuates the Pc spectra. Red shift in Q band of Pc upon linking to respective DNDs was observed for all conjugates, except for P@DNDs. As stated above, red shifts have also been reported for porphyrin-graphene oxide nanoconjugates and were attributed to molecular flattening **[162]**. There was a blue shift in Q-bands of conjugates: P@DNDs-**10**, N@DNDs**10** and S&N@DNDs**10**, relative to undoped DNDs-**10 (Table 3.1)**. A blue-shift in Q band of phthalocyanine doped metal oxide has been previously observed and was said to be dependent on molecular orientation **[211]**. Hence, shift in Q bands of conjugates is associated with the molecular orientation of Pc doped DNDs. Also, it was shown previously that the strong π–π attraction leads to the formation of ground state complexes of Pcs with carbon nanomaterials, resulting in spectral shifts **[212]**. Thus differences in spectral shifts between conjugates of doped compared to undoped DNDs could be a result of differences with interaction, with stronger interaction in the presence of the dopants.

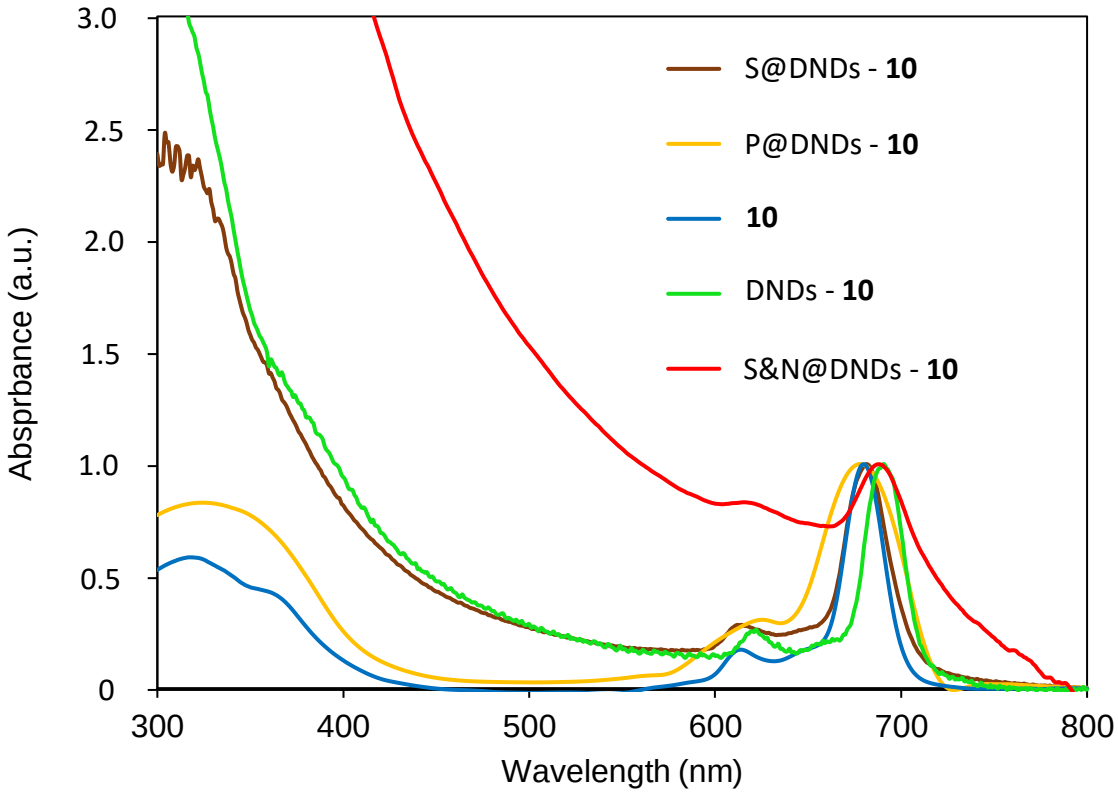

Figure 3.38: Absorbance spectra of a selection of conjugates and complex **10** in DMSO.

When alone, complex **10** starts to decompose at approximately 300˚C, while the DNDs alone and conjugates start at a higher temperature of ~ 500 °C (**Figure 3.39**). Considering the temperature where degradation starts, the conjugates are less stable compared to DNDs alone, except for P@DNDs-**10**. Except for DNDs-**10** and S@DNDs-**10**, the Pc alone is less stable compared to DNDs alone and the conjugates, where degradation starts **Figure 3.39**. The decreased stability of the conjugates compared to DNDs is a result of the low stability of the Pcs at ~ 500 °C. Beyond 650 °C, the Pc is more stable than the conjugates and DNDs alone.

TGA was used to determine the loading as discussed above. Respective masses of Pcs loaded onto B@DNDs constituted 887, 57 and 792 μg Pc per mg of B@DNDs in conjugates of B@DNDs-**9**, B@DNDs-**10**, and B@DNDs-**11 (Table 3.3)**. Positively charged nanohybrid

B@DNDs-**11** with improved colloidal stabilities have higher Pc loading than B@DNDs-**10**. Masses of complex **10** loaded onto DNDs are as follows: 57, 814, 110, 0.14, 11, and 6 μg Pc per mg of the DNDs in respective conjugate: B@DNDs-**10**, P@DNDs-**10**, N@DNDs-**10**, S@DNDs-**10**, S&N@DNDs-**10**, and DNDs-**10**. The largest loading is for P@DNDs-**10** which also has the largest DLS size. An increase in colloidal stability (high zeta potentials) of hybrids can be associated with high drug loading **[209]**. Hence, increase in colloidal stabilities of constructed nanohybrids is associated with the size and Pc loading.

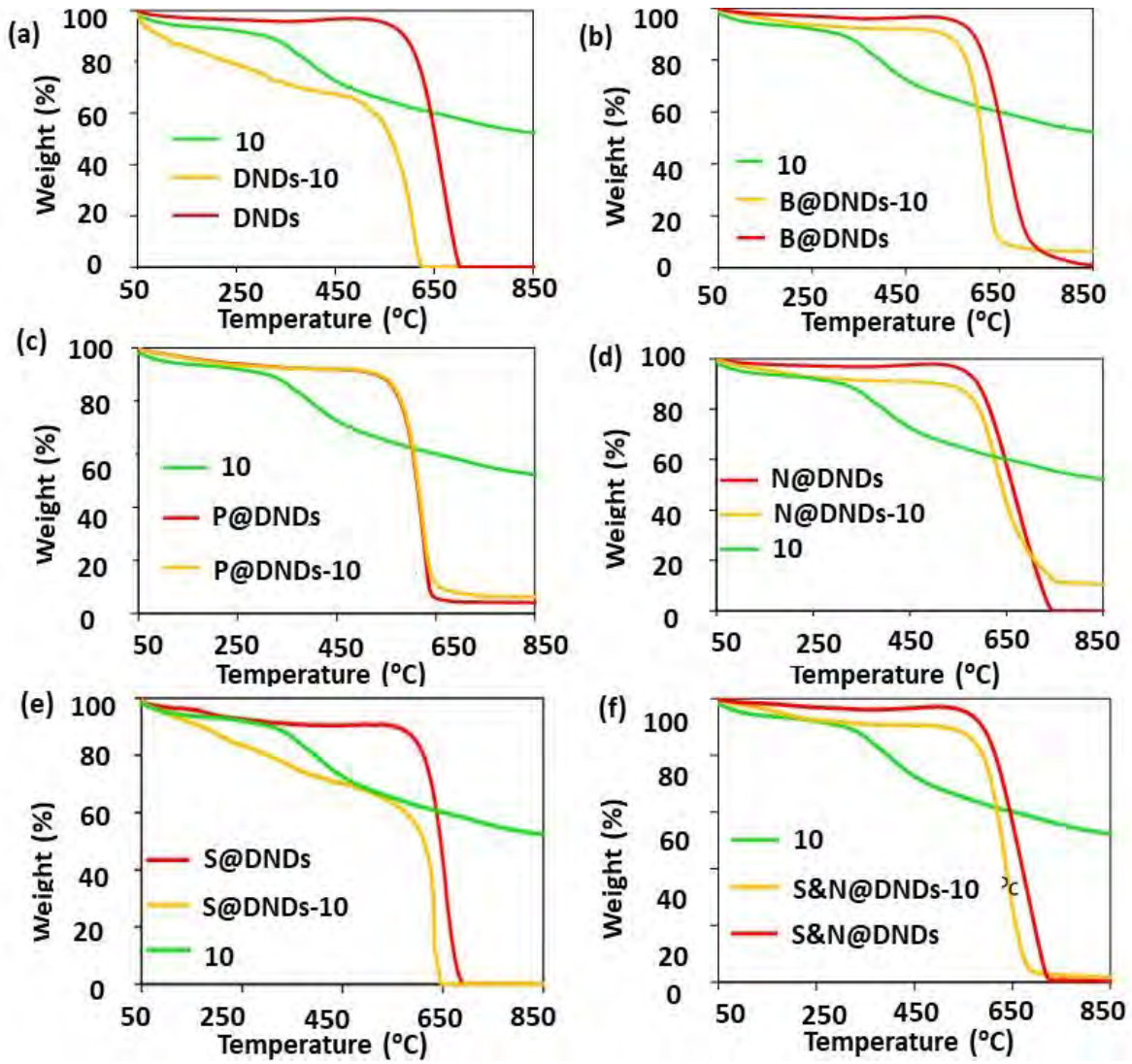

Figure 3.39: Thermogravimetric analysis (TGA) curves for samples thermograms of DNDs, doped DNDs, complex **10** alone and their respective conjugates at 20 °C min^{-1} from 50 to 850 °C in air.

Laser Raman spectral technique was used to determine the effect of DNDs doping by heteroatoms and conjugation to the Pc (**Figure 3.40**). On conjugation to the Pc, the D bands shifted to lower wavenumbers for most of the DNDs. Shifts in the Raman frequencies of DNDs-Pc hybrids have been previously reported to indicate strong π-electron interactions in hybrid materials **[182]** due to change in size **[170]**, structural alterations **[213]** and strain effect on nanoparticles **[170, 214]**. Heteroatom doping and complex **10** conjugation on DNDs in **Figure 3.40** resulted in increased defects as judged by increase in I_D:I_G ratio because the G band is not affected by defects. This increase in disorder could have been due to the Pc causing stress/strain onto the nanoparticles **[171]**.

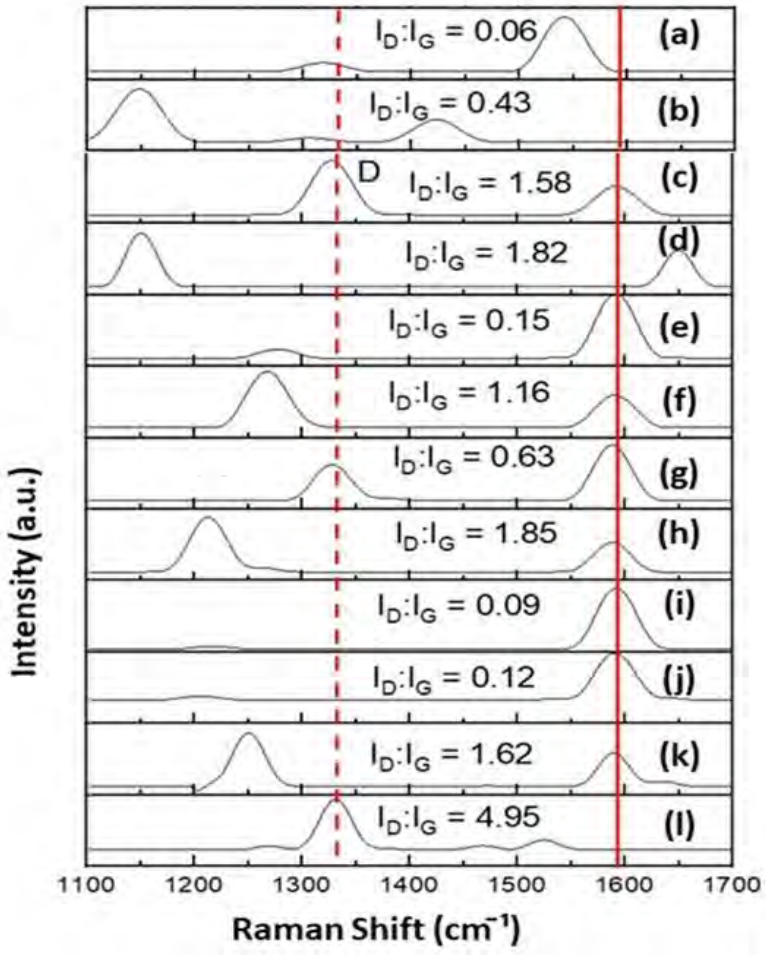

Figure 3.40: Raman spectra for nanoparticles and respective conjugates of (a) DNDs, (b) DNDs-**10**, (c) B@DNDs, (d) B@DNDs-**10**, (e) P@DNDs, (f) P@DNDs-**10**, (g) N@DNDs, (h) N@DNDs-**10**, (i) S@DNDs, (j) S@DNDs-**10**, (k) S&N@DNDs, and (l) S&N @DNDs-**10**

3.4. Summary

The synthesis and characterizations of complexes (**8** - **12**) and conjugates of **(1 - 12)**, carbon nanoparticles (GQDs, CDs and doped DNDs) and the respective conjugates were presented in this chapter. The Pcs were characterized using ^{1}H NMR, mass, UV-Vis, FTIR spectroscopies and elemental analysis to confirm the respective substituted Pcs. Complexes **1 - 12** showed monomeric Q-band in DMSO and broadening of the Q band in water due to aggregation (**Figure 3A,** appendix). Characteristics of complexes and carbon nanoparticles conjugated systems interacting through $\pi - \pi$, ester and amide linkage was characterised using TEM, DLS, zeta-potential, UV-Vis, Laser Raman, AFM, TGA, EDX, XRD and XPS.

Characteristic Q band of complexes alone varied with respect to symmetry, substituent in the macrocycle, central metal, charge and solvent effect. Carbon nanoparticles varied in character depending on the type of nanoparticle, size, functional groups and heteroatoms dopands connected to the carbon frame. Respective nanoconjugate systems possessed increased sizes accompanied with unique characteristics compared to individual components. Nature of interaction between complexes and nanoparticle did not play a major role in altering characteristics of the conjugate. Larger sizes of nanomaterials, such as CDs, had the second largest Pc loading and the least colloidal stability. DNDs with the least size, relative to GQDs and CDs, showed the least complex loading with the most colloidal stability. However, heteroatom doping of DNDs resulted in increased Pc loading accompanied with reduced colloidal stabilities.

Zeta-potential varied with respect to drug concentration, temperature and pH of solution and was used to indicate colloidal stabilities of drugs. No specific trend in colloidal stability could be assigned to the nature of interaction (covalent and noncovalent), loading or I_D:I_G ratio. Zeta potential was used to indicate surface charge of complexes loaded onto the nanoparticle. Loading studies were investigated using thermogravimetric and spectroscopic techniques. TGA was also used to indicate thermal stability. Loading and size, indicated by I_D:I_G ratio, have improving effect on thermal stability of conjugates relative to their individual components.

Chapter 4

Chapter 4

4. Physicochemical characteristics

The chapter discusses the physicochemical characteristics (fluorescence quantum yields, triplet quantum yields, lifetimes and singlet oxygen quantum yields) of phthalocyanines or BODIPY dye when alone and when conjugated to nanoparticles. Fluorescence and triplet quantum yields were determined in DMSO not in water due to aggregation. Aggregates are known to convert electronic excitation energy to vibrational energy, resulting in decrease in fluorescence quantum yield of molecules **[215]**, which will also affect triplet state parameters.

4.1. Fluorescence quantum yields (Φ_F) and lifetimes (τ_F)

Time-resolved emission spectra (decay traces and fits) are shown in **Figure 4.1** for **4c** alone and DNDs-**4c** (as examples). Pc complexes alone showed a mono–exponential decay profiles indicative of one fluorescence lifetime. Biexponential decay profile were obtained when fitting nanoconjugates indicating two lifetimes which could be due to the orientation of the Pc complex around the nanoparticle. Average lifetimes are shown in **Table 4.1.**

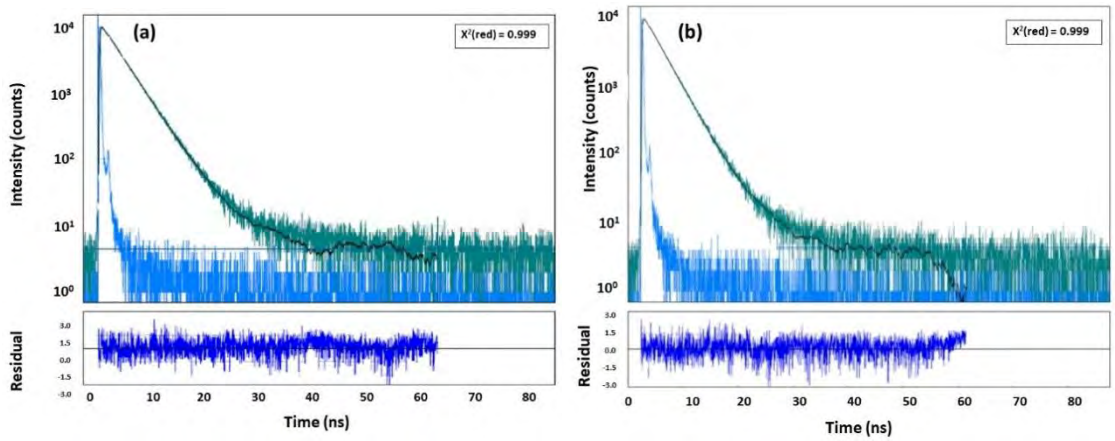

Figure 4.1: Time-resolved emission data (decay traces and fits) for (a) complex **4c** (b) DNDs-**4c** (as example).

Fluorescence quantum yield of CNPs ($\Phi_{F(CNPs)}$) represent quantum yields when exciting where carbon nanoparticles (CNPs) and $\Phi_{F(Pc)}$ where Pc absorb **(Table 4.1)**.

Table 4.1.: Photophysics and photochemistry properties for nanoparticles and its conjugates in DMSO

Sample	λ_{abs} (nm)	$\Phi_{F(CNPs)}$	$\tau_{F(CNPs)}$ (ns)	$\Phi_{F(Pc)}$	$\tau_{F(Pc)}$ (ns)
1	679			0.16	3.28
2	672			0.20	3.44
3	683			0.18	2.74
$GQDs_2$(B1)	360	0.11	5.02		
$GQDs_2$(B1)-**1**	672	0.08	2.72	0.30	3.32
$GQDs_2$(B1)-**2**	678	0.02	3.00	0.25	3.59
$GQDs_2$(B1)-**3**	683	0.02	3.31	0.17	2.70
$GQDs_2$(B2)	450	0.18	4.02		
$GQDs_6$	430	0.24	4.80		
$GQDs_{10}$	350	0.11	2.56		
$GQDs_2$(B2)-**3**	681	0.06	1.00	0.02	0.04
$GQDs_6$-**3**	682	0.08	2.33	0.01	0.02
$GQDs_{10}$-**3**	683	0.09	2.52	0.02	0.03
$GQDs_2$(B3)	336	0.11	5.02		
$GQDs_2$(B3)-**3**	682	0.06	0.04	0.14	1.00
CDs	366	0.10	2.56		
CDs-**3**	686			0.04	0.03
DNDs-**3**	686			0.15	2.69
3-DNDs-**12**	683			0.10	2.61
4a	675			0.57	3.07
4b	675			0.17	2.70

4c	684			0.19	2.77
DNDs- **4a**	675			0.08	2.58
DNDs- **4b**	673			0.08	2.69
DNDs- **4c**	666 (610)			0.02	2.69
5	670			0.67	5.02
6	677			0.38	5.09
DNDs-**5**	687			0.05	5.17
DNDs-**6**	681			0.38	5.09
7	681			0.24	2.86
8	677			0.03	1.85
9	679			0.06	2.83
10	678			0.23	2.74
DNDs-**10**	690			0.16	2.44
B@DNDs		<0.01			
B@DNDs-**10**	690	0.01	0.04	0.11	1.00
P@DNDs		<0.01			
P@DNDs-**10**	678	0.02		0.11	
N@DNDs		<0.01			
N@DNDs-**10**	688	0.02	2.56	0.17	2.56
S@DNDs		<0.01			
S@DNDs-**10**	690	0.01	0.96	0.15	2.12
S&N@DNDs		<0.01			
S&N@DNDs-**10**	688	0.02	2.00	0.17	2.69
11	680			0.10	1.82
B@DNDs-**11**	682			0.08	0.01
12	649			0.53	3.87
DNDs-**12**	675			0.11	2.64

4.1.1. Effect of Pc central metal

Comparison of complexes **4a**, **4b** and **4c** alone, shows that **4a** has the largest Φ_F value of 0.57, while **4b** and **4c** have values of 0.17 and 0.19, respectively in **Table 4.1**. The high value for **4a** is due to the lack of a central metal. Heavy metals such as Zn enhance the intersystem crossing to the triplet state, hence lowering fluorescence **[216]**. The shortening of lifetimes was observed for **4b**, **4c** compared to **4a** corresponding to decrease Φ_F values.

4.1.2. Effect of Substituent

A comparison of SiPcs alone (**4c**, **5** and **6**) in **Table 4.1** showed the highest Φ_F for complex **5** (without substituent) relative to substituted complexes (**4c** and **6**), suggesting that substituents quench Φ_F. Complexes **2**, **4b**, **7** gave Φ_F of 0.20, 0.17 and 0.24, respectively, the lowest being for **4b**. Electron donating characteristics of Pcs are known to encourage intersystem crossing. Sulfur in complex **7** substituent is expected to enhance intersystem crossing to the triplet state. However, it is not clear why complex **7** has a larger fluorescence quantum yield relative to **2**.

4.1.3. Effect of number of charges

The fluorescence quantum yields (Φ_F) for benzathiozole substituted zinc complexes **7, 8,** and **9** were found to be 0.24, 0.03, and 0.06, respectively (**Table 4.1**), suggesting enhancement of intersystem crossing and deactivation of the excited singlet in the quaternary complexes **8** and **9** compared to **7**, τ_F values followed the same trend**.** A further decrease in the Φ_F of asymmetrically charged Pc **(11)** when compared to an uncharged Pc **(10)** is an indication that quartenization reduces Φ_F, with a corresponding shortening of τ_F.

4.1.4. Effect of symmetry on complexes

Complexes **7** and **10** with fluorescence quantum yields of 0.24 and 0.23 in **Table 4.1** did not show any significant effect of symmetry.

4.1.5. Pc versus BODIPY

Relative to the phthalocyanine macrocycle (complex **3** (Φ_F = 0.18)) in **Table 4.1**, complex **12** (0.53) has a high fluorescence quantum yield, typical of BODIPYs **[217] .**

4.1.6. Effect of carbon nanomaterials

4.1.6.1. Size

Fluorescence quantum yields decreased for the largest and smallest GQDs: $GQDs_{10}$-**3** (9%), $GQDs_6$(B2)-**3** (8%), compared to $GQDs_2$(B2)-**3** (6%) when exciting where GQDs absorb **(Table 4.1)**. Fluorescence quantum yields of complex **3** and GQDs alone are quenched when conjugated together due to FRET. When exciting where Pcs absorb, noticeable differences are observed in **Table 4.1.**

4.1.6.2. Type of nanomaterial

Fluorescence quantum yield values for $GQDs_2$(B3) (11%) and CDs (10%) were similar in **Table 4.1**. However, the fluorescence lifetimes were longer for $GQDs_2$(B3) at 5.02 ns compared to CDs at 2.56 ns. Increase or decrease in the fluorescence lifetimes may depend on defects within GQDs and CDs structures. Defects are known to reduce lifetimes by causing disruption in conjugated lattice of the carbon nanomaterials **[218]**. No fluorescence was observed for undoped DNDs. Fluorescence quantum yield values for all the doped DNDs alone

were less than 1%, but insignificantly increased to 1% and 2% for the conjugates, **Table 4.1**, on exciting where DNDs absorb. Fluorescence lifetimes could not be determined for doped DNDs alone due to low fluorescence. Carbon nanomaterials such as GQDs, CDs, and DNDs are electron donating, hence will encourage intersystem crossing to the triplet state, reducing τ_F and Φ_F of the Pc in a conjugated system. Hence the presence of GQDs, CDs and DNDs in complex **3** (as an example) showed less τ_F and Φ_F.

As with fluorescence quantum yields, following conjugation, there was an improvement in the fluorescence lifetimes where DNDs absorb, hence they could be determined except for P@DNDs-**10** conjugate. The increase in Φ_F and τ_F when exciting where DNDs absorb, suggest stabilization of the excited states of DNDs by Pcs **[219]**. Complex **10** alone showed Φ_F of 23% which decreased upon conjugating to DNDs. The τ_F values of the Pc shortened in the presence of DNDs for complex **10.** Increase or decrease in the fluorescence lifetimes may depend on the geometry or distance between nanoparticles and Pcs in conjugates **[219, 220].** Low Φ_F value for DNDs–**4c** is as a result of aggregation.

4.1.6.3 FRET

FRET occurs when there is an efficient overlap between the emission (**Figure 4.2)** spectra of the nanoparticle (donor) and absorption for the Pcs (acceptor). This decrease in fluorescence parameters may be ascribed to quenching between carbon nanomaterials and respective Pcs due to Förster resonance energy transfer (FRET) and other factors that influence the decrease in nanoparticles emission in addition to FRET **[134]**.

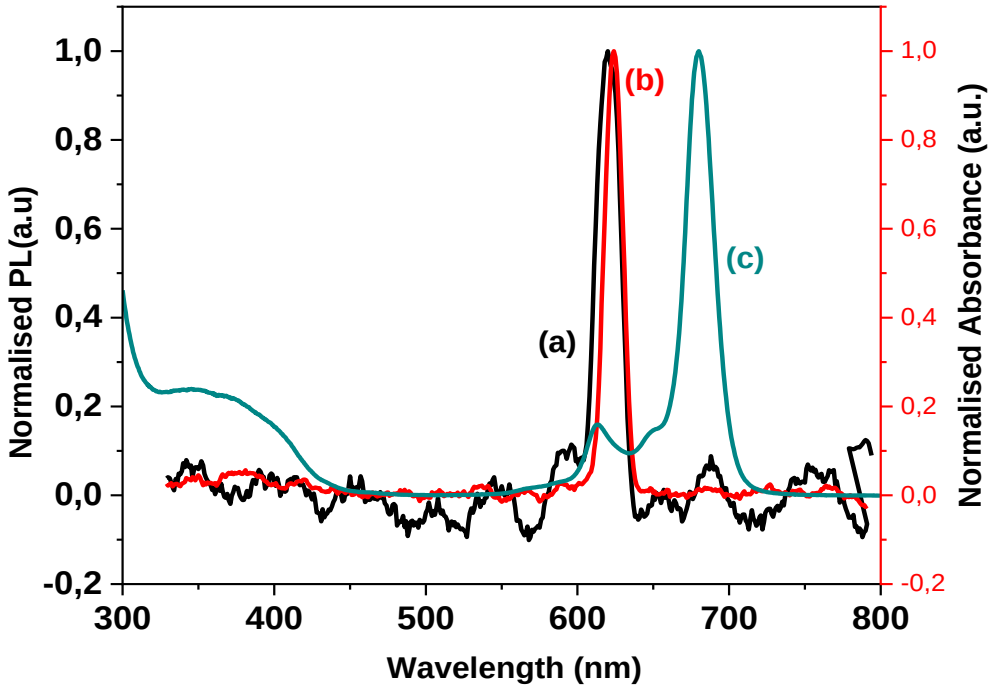

Figure 4.2: Emission spectra of (a) $GQDs_2$(B3), (b) CDs when excited at 310 nm and absorption spectra of (c) complex **3**, respectively, in DMSO.

Photoinduced electron transfer (PET) from a donor and acceptor molecule and inter charge transfer (ICT) between functional groups and GQDs are amongst some of the processes that might induce quenching of GQDs in the constructed GQDs-MPc nanoconjugate systems. FRET efficiencies (E_{ff}) were estimated using fluorescence quantum yields and equation (1.12) to be 0.28, 0.81 and 0.80 for $GQDs_2$(B1)-**1,** $GQDs_2$(B1)-**2** and $GQDs_2$(B1)-**3**, respectively (**Table 4.2 A**). The low FRET efficiency for $GQDs_2$(B1)-**1** could be explained by the fact that similarly charged surfaces are likely to repel each other by increasing the distance between donor (GQDs) and acceptor (complex **1**) molecules. Similarly, oppositely charged surfaces are likely to attract hence the high FRET efficiency for $GQDs_2$(B1)-**3**. A high E_{ff} value was also observed for $GQDs_2$(B1)-**2** even through complex **2** is neutral. FRET efficiencies are 0.22 and 0.43 for $GQDs_2$(B3)-**3** and CDs-**3** respectively **(Table 4.2A)**. The larger values for the latter due to the red shifted emission spectrum, which overlaps better with the absorption spectrum of

complex **3**, **Figure 4.2**. CDs-**3** in **Table 4.2A** also has a larger J integral and a smaller distance between the donor and acceptor, **Table 4.2.**

Table 4.2A: FRET parameters of carbon nanosembles in DMSO

Sample	E_{ff}
$GQDs_2$(B1)-**1**	0.28
$GQDs_2$(B1)-**2**	0.81
$GQDs_2$(B1)-**3**	0.80
$GQDs_2$(B3)-**3**	0.22
$GQDs_6$-**3**	0.24
$GQDs_{10}$-**3**	0.11
CDs-**3**	0.43

Table 4.2B: FRET parameters of carbon nanosembles in DMSO

Sample	E_{ff}	$J(10^{-13}cm^6)$	R(Å)
DNDs-**3**	-	-	-
$GQDs_2$(B3)-**3**	0.22	1.58	38.95
CDs-**3**	0.43	84.5	34.02

4.2. Triplet state quantum yield (Φ_T) and lifetime (τ_T)

The triplet quantum yield (Φ_T) refers to the fraction of molecules that undergo intersystem crossing to the metastable triplet excited state resulting in enhanced triplet state population. Ideally, a high triplet quantum yield will result in a high singlet oxygen quantum yield which is a prerequisite for good photosensitizers intended to be used in PDT applications. The triplet decay curve (**Figure 4.3**) of all complexes (**1-12**) follow a second order decay kinetics which is known for Pcs at high concentration due to triplet-triplet recombination **[221]**.

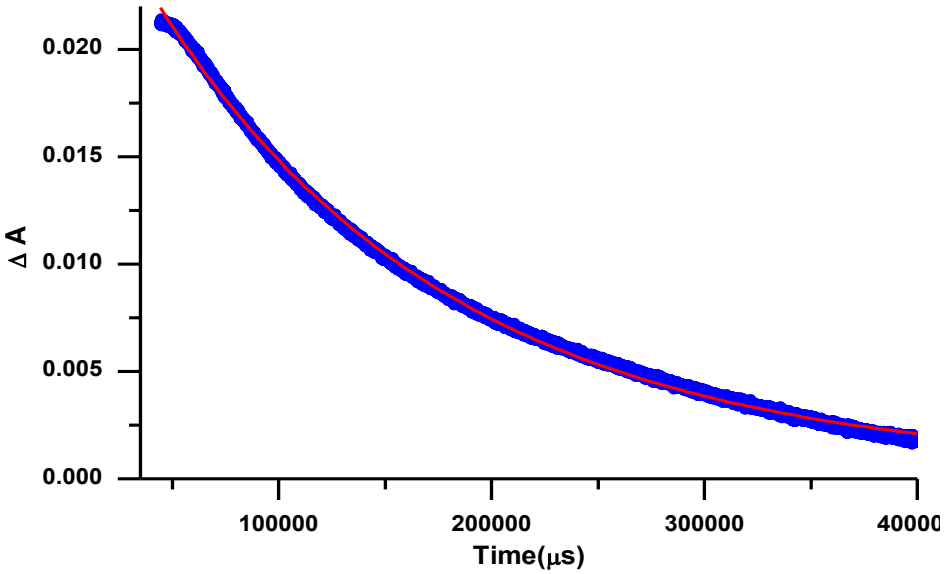

Figure 4.3: Triplet decay curve of complex **8** at 510 nm at A = 1.5 in DMSO (as an example), red solid line indicates theoretical fit.

4.2.1. Effect of Pc central metal

Of the complexes **4a - 4c** alone, complex **4a** gave the lowest Φ_T value of 0.20 corresponding to the high Φ_F values since the two are competing processes. The higher Φ_T values for **4c** and **4b** also correspond to their lower Φ_F values. The highest value of Φ_T is obtained for **4c** at 0.70 in **Table 4.3**.

4.2.2. Effect of Pc substituent

Comparing SiPcs alone in **Table 4.3**, complex **5** gave the lowest Φ_T value of 0.24 corresponding to the high Φ_F, also the shortest τ_T. Φ_F and Φ_T are competing processes, where one is low the other is high. Higher Φ_T values for complex **4c** (0.70) and **6** (0.30) also correspond to their lower Φ_F. Comparing neutral Pc complexes with Zn central metal (**2**, **4b**,**7**), **2** has the largest Φ_T (0.65), followed by **7** (0.56), suggesting quenching by substituents in **4b** at Φ_T = 0.33. Triplet lifetimes (τ_T) is longest for **2**.

4.2.3. Number of charges and quaternization

Following quaternization, significant enhancement in triplet quantum yield was observed from 0.56 in complex **7** to 0.92 and 0.85 in **8** and **9**, indicating efficient intersystem crossing to populate the triplet state for the latter **(Table 4.3).** Triplet lifetimes of 139 and 142 μs for complex **8** and **9**, are longer than 130 μs for complex **7**. High Φ_T for **8** and **9** corresponds to low Φ_F. Therefore, quaternization improves Φ_T but decreases Φ_F. The partially quaternized complex **8** showed higher Φ_T than the fully quaternized **9**. Complex **8** with two quaternized groups will be of lower symmetry than complex **9** with four quaternized groups. Positively charged complex **11** relative to **9** has a much larger triplet quantum yield, showing that a combination of quaternization and asymmetry improves triplet quantum yields. It is known that low symmetry phthalocyanines possess better photophysical behaviour than their corresponding symmetrical analogue **[222]**.

4.2.4. Effect of carbon nanomaterial

Triplet quantum yield (Φ_T) values generated increased with NP conjugation due to increased intersystem crossing. There is a lowering of the Φ_T value for DNDs–**4c** compared to **4c** alone, this could be due to aggregation as shown by the UV-Vis spectra in appendix **(Figure 1A)**. Complexes **5** and **6** showed an increase in Φ_T values in the presence of DNDs, as a result of electron donating ability of DNDs to SiPcs. There is lengthening of triplet lifetimes of Pcs in the presence of NPs in some cases, probably as a result of the protection of the Pcs by the DNDs **[220]**. A decrease in τ_T is usually expected with the increase in Φ_T **[223].**

4.2.5. Type of complexes (Pc and BODIPY)

The triplet quantum yield of BODIPY (**12**) was undeterminable due to its short lived excited state. However, phthalocyanine (complex **3**, as an example) showed (Φ_T = 0.73) in **Table 4.3** and increased slightly in the presence of DNDs for **3**-DNDs (Φ_T = 0.75) and **3**-DNDs-**12** (Φ_T = 0.76).

Table 4.3: Photophysics and photochemistry properties for nanoparticles and its conjugates in DMSO

Sample	**Φ_T**	**τ_T (µs)**
1	0.48	254
2	0.65 [a]	350 [a]
3	0.73	326
$GQDs_2$(B1)-**1**	0.67	531
$GQDs_2$(B1)-**2**	0.73	263
$GQDs_2$(B1)-**3**	0.76	249
$GQDs_2$(B3)-**3**	0.79	386
CDs-**3**	0.79	389
DNDs-**3**	0.75	302
3-DNDs-**12**	0.76	228.9
4a	0.20	119.9
4b	0.33	176.4
4c	0.70	198.7
DNDs- **4a**	0.39	98.9
DNDs- **4b**	0.33	176.4
DNDs- **4c**	0.42	404.5
5	0.24	114.5
6	0.30	372.8
DNDs-**5**	0.37	198.8
DNDs-**6**	0.45	393.8
7	0.56	130
8	0.92	139
9	0.85	142
10	0.73	124
11	0.90	132
DNDs-**12**	0.75	301.5

[a] from reference **[17, 128]**

4.3. Singlet oxygen quantum yields

4.3.1. Spectra and basics

Singlet oxygen species are generated through an energy transfer process between excited triplet state of MPc (^{3}MPc*) and ground state molecular oxygen ($^3O_2$). Complexes **4(a)-(c), 5** and **6** alone and in conjugates with DNDs will be investigated for nonlinear optical limiting characteristics. Hence singlet oxygen will not be determined for these complexes and is not necessary. Singlet oxygen quantum yields were attempted in DMSO and water (1% DMSO) for the complexes **(1, 3, 7, 8, 9, 10** and **11)** and conjugates. Singlet oxygen quantum yield values in water are essential for complexes to use as photosensitizers

Photo-bleaching studies showed change in absorption spectra of DPBF in DMSO (**Figure 4.4 (a)**) and ADMA in water (**Figure 4.4 (b)**) for GQDs$_2$(B1)-**1** (as an example). The decrease in absorption peak at 417 nm indicates quenching of DPBF in the presence of singlet oxygen species. While the decrease in absorption peaks between 350 nm - 410 nm indicated quenching of ADMA. In both cases, there was no change in absorption at the respective Q bands, an indication of stability of as-synthesised GQD-conjugates under photo-irradiation.

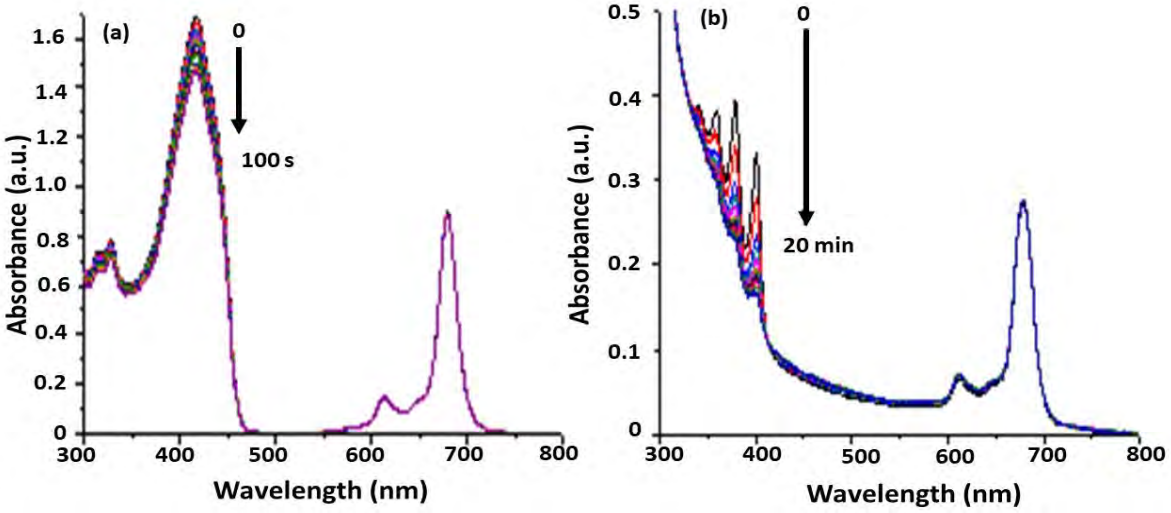

Figure 4.4: Change in absorption spectra of (a) DPBF in DMSO and (b) ADMA in water. (1 % DMSO) Conjugate: GQD$_2$(B1)-**1** (as an example).

4.3.2. Effect of water

A dramatic drop in the Φ_Δ values in water was observed in **Table 4.4**. This could be due to the fact that oxygen has higher solubility in many organic solvents compared to water **[224]**, which could be responsible for low singlet oxygen generation in water. Also in water containing 1% DMSO, the values are low since water is known to quench singlet oxygen **[29].**

4.3.3. Effect of NPs

4.3.3.1. Type of NPs

$GQDs_2$(B3)-**3** and CDs-**3** showed higher Φ_Δ compared to DNDs-**3** in water **(Table 4.4)**. The improved Φ_Δ in $GQDs_2$(B3)-**3** and CDs-**3** could be associated with higher oxygen atomic concentration relative to DNDs-**3** in **Table 3.4** which is known to enhance Φ_Δ **[225]**.

4.3.3.2. Size of GQDs

Nanoconjugate $GQDs_6$-**3** (0.27) showed the largest singlet oxygen quantum yield in water made up of 1% DMSO relative to $GQDs_2$(B2)-**3** (0.17) and $GQDs_{10}$-**3** (0.11). The presence of defects may affect the generation of active oxygen species **[225, 226]**. The most loaded nanoconjugate systems ($GQDs_2$(B2)-**3** in **Table 4.4** was not necessarily the most singlet oxygen species producing.

4.3.3.3. Doping of DNDs

S&N@DNDs-**10** and N@DNDs-**10** gave larger singlet oxygen quantum yield (at 0.66 and 0.55, respectively in DMSO) when compared to B@DNDs-**10** and P@DNDs-**10** (0.52 and 0.44, respectively in DMSO), **Table 4.4**. This is not surprising as it has been previously reported that graphitic carbon nanomaterials with N atoms creates charged sites that enhance the adsorption of O_2 and performance of a photocatalysts **[153]**. The introduction of nitrogen not only increases the charge mobility of the graphitic lattice, but also lowers the energy band

gap **[153]**. Hence, S&N@DNDs-**10** and N@DNDs-**10** showed better singlet oxygen quantum yields. The singlet oxygen quantum yields of the conjugates are however smaller than that for the Pc alone (except for S&N@DNDs-**10** where they are the same with the Pc alone). A very low singlet oxygen quantum yield was obtained for S@DNDs-**10**. The decrease in singlet oxygen quantum yields could be due to the screening effect caused by DNDs which could have prevented the interaction of the excited triplet state of the nanoconjugates and the ground state molecular oxygen discussed above **[227]**.

Table 4.4: Photophysics and photochemistry properties for nanoparticles and its conjugates in DMSO and water (made up of 1% DMSO).

Sample	**Solvent**	**Loading (μg.mg^{-1})**	**Φ_Δ**
1	DMSO		0.32
	H_2O		<0.01
2	DMSO		0.67[d]
3	DMSO		0.41
	H_2O		0.03
$GQDs_2$(B1)-**1**	DMSO	3	0.34
	H_2O		0.05
$GQDs_2$(B1)-**2**	DMSO	4	0.44
	H_2O		0.02
$GQDs_2$(B1)-**3**	DMSO	14	0.41
	H_2O		0.23
$GQDs_2$(B2)-**3**	H_2O	10	0.17
$GQDs_6$(B2)-**3**	H_2O	5	0.27
$GQDs_{10}$(B2)-**3**	H_2O	3	0.11
$GQDs_2$(B3)-**3**	DMSO	299	0.41
	H_2O		0.27
CDs-**3**	DMSO	829	0.42
	H_2O		0.13
DNDs-**3**	DMSO	42	0.62
	H_2O		0.05
3-DNDs-**12**	DMSO	334	0.73
	H_2O		0.50
7	DMSO		0.33
8	DMSO		0.76
	H_2O		0.08

9	DMSO		0.77
	H_2O		0.23
10	DMSO		0.65
	H_2O		0.10
DNDs-**10**	DMSO	6	0.21
	H_2O		<0.01
B@DNDs-**9**	DMSO	887	0.39
	H_2O		0.12
B@DNDs-**10**	DMSO	6	0.21
	H_2O		<0.01
B@DNDs-**10**	DMSO	57	0.52
	H_2O		0.31
P@DNDs-**10**	DMSO	814	0.44
	H_2O		0.25
N@DNDs-**10**	DMSO	110	0.55
	H_2O		0.06
S@DNDs-**10**	DMSO	0.14	0.13
	H_2O		0.02
S&N@DNDs-**10**	DMSO	11	0.66
	H_2O		0.09
11	DMSO		0.80
	H_2O		0.15
B@DNDs-**11**	DMSO	11	0.55
	H_2O		0.18
12	DMSO		0.32
	H_2O		0.24
DNDs-**12**	DMSO	282	0.68
	H_2O		0.36

4.4. Summary

The photophysical properties of the Pc complexes and their conjugates were studied in DMSO. It is only Φ_Δ that was investigated in water made up of 1% DMSO. Fluorescence and triplet quantum yields are competing processes that are affected by substituents, central metal, charge, symmetry of Pc complex and choice of complex (Pc or BODIPY). Carbon nanomaterials utilised their electron donating ability in order to enhance Φ_Δ in water for **3** and **10**. No specific trend in the size, type and doping on the carbon nanomaterial could be deduced in improving characteristics of nanohybrids. Percentage loading of complex onto carbon nanoparticles did not follow any specific pattern to improve characteristics of the nanohybrid.

Chapter 5

Chapter 5

5. Molecular modelling

The chapter utilises theoretical models to calculate molecular stabilities of Pc complex **10** and nanoparticles (DNDs and doped DNDs) alone; and in a conjugate.

5.1. Visualizations and simulations

Figure 5.1 (A-C) is an example of visualized electron density distribution at two different iso values of Pc complex **10** and S&N@DNDs alone and in a conjugated system obtained using visual molecular dynamics (VDM) from the xtb calculation output.

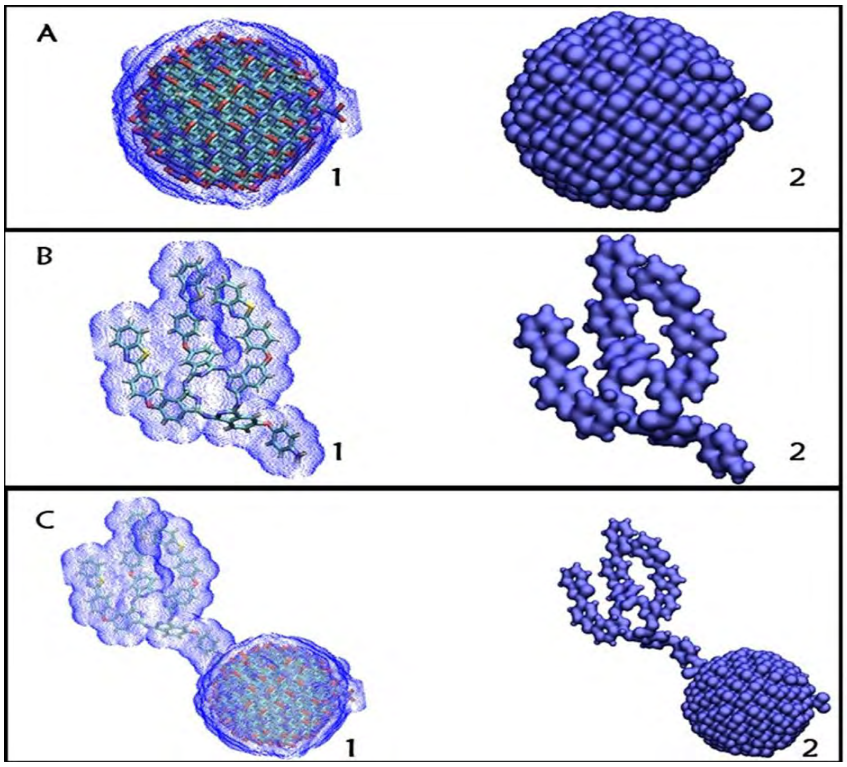

Figure 5.1: **1** is an example of electron density at the first iso value of 0.002 and **2** is second iso value 1 × e^{-5} visualized using visual molecular dynamics (VMD) **[228]** from the xtb calculation output for **(A)** S&N@DNDs, **(B)** Complex **10** alone and **(C)** S&N@NDNs-**10** conjugate**.**

5.2. Molecular stability

Structural stability and electronic properties of Pc complex **10** and doped DNDs (B, P, S, N and S&N) alone and in a respective conjugate are determined by considering molecular energies (Kcal.mol^{-1}) and Highest occupied molecular orbital (HOMO)- Lowest unoccupied (LUMO) gaps (eV) before and after conjugation. The ability of HOMO orbital to donate electrons is an indication of its nucleophilic character and the HOMO energy is related to ionization potential. LUMO is electrophilic because it has the ability to accept electrons. Hence LUMO energy is related to electron affinity. The energy difference between HOMO and LUMO orbitals is referred to as the energy gap. The size of HOMO-LUMO energy gap has considerable chemical effects and gives information on molecular stability and reactivity; the smaller the energy gap, the more unstable (chemically reactive) and the more reactive is the molecular structure with π orbital arrangement **[229, 230]**. Previous theoretical studies using DFT simulation on DNDs have shown that stability upon functionalisation depends on the size, shape, facet and functional group of DNDs **[71-73]**. The major facet for DNDs used in this study shown by XRD in Chapter 3 (**Figure 3.10**) is [111]. DFT simulations on functionalizing DNDs [111] facet with NH_2 functional moieties has been reported to have a stabilizing effect on the energy of DNDs **[72]**. Hence, visualisation and simulation were done on one facet using GFN2-xTB (extended tight binding) as implemented in xtb **[72, 108, 109, 115]** and DFTB+ (density functional tight binding) using the Slater–Koster parameters: 3ob as implemented in Material Studio package **[116]**. Chemical doping, functional groups and increase in size of DNDs are amongst some of the greatest factors that have been reported to affect HOMO-LUMO energy gaps (structural stability) of DNDs **[59, 72, 75, 231]**. **Table 5.1** shows a visual representation and HOMO-LUMO energy gaps of the DNDs, Pc and respective conjugated systems.

Table 5.1: HOMO and LUMO molecular orbitals of complex **10**, (a) N@DNDs, and N@DNDs-**10**, (b) S&N@DNDs and S&N@DNDs-**10**, (c) P@DNDs and P@DNDs-**10** calculated using DFTB+ simulation.

Code	**Molecular structure**	**Highest ocuppied molecular obital (HOMO)**	**Lowest unocuppied molecular obital (LUMO)**
10	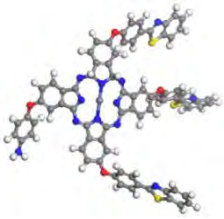 Total Energy: -126 660.98 kcal/mol	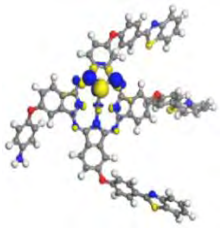 HOMO = -9.17 eV	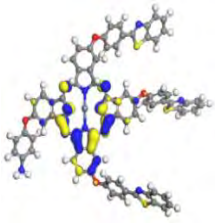 LUMO = -9.05 eV
(a)			
N@DNDs	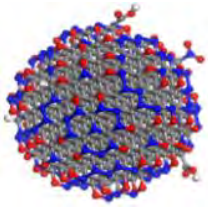 Total Energy: -947 053.51 kcal/mol	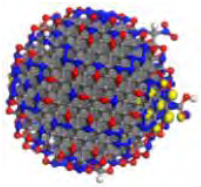 HOMO = -12.99 eV	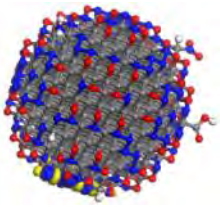 LUMO = -9.87 eV
N@DNDs -**10**	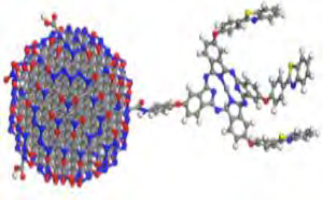 Total Energy: -1 076 494.56 kcal/mol	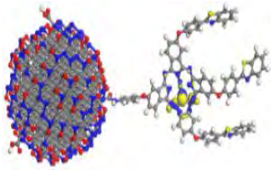 HOMO = -9.51 eV	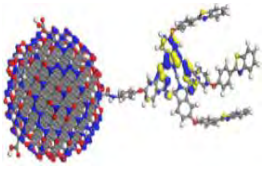 LUMO = -9.37 eV

(b)			
S&N@DNDs	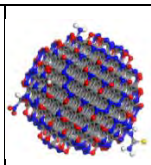 Total Energy: -953 133.46 kcal/mol	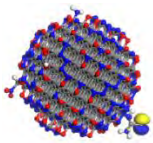 HOMO = -10.22 eV	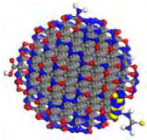 LUMO = -9.89 eV
S&N@DNDs- **10**	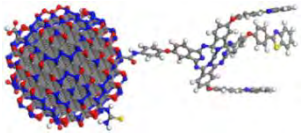 Total Energy: -1 082 462.12 kcal/mol	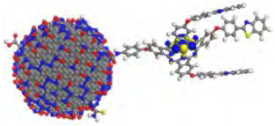 HOMO = -9.50 eV	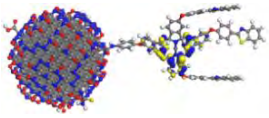 LUMO = -9.37 eV
(c)			
P@DNDs	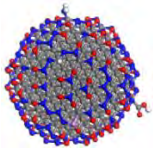 Total Energy: -946 694.96 kcal/mol	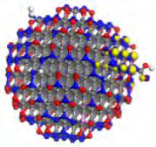 HOMO = -12.98 eV	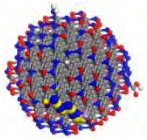 LUMO = -9.87 eV
P@DNDs-**10**	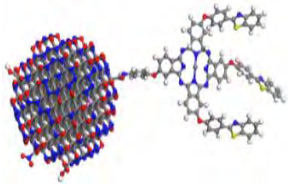 Total Energy: -1 076 230.72 kcal/mol	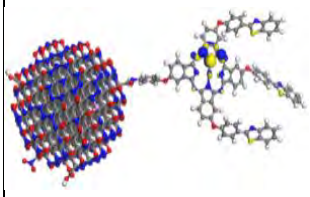 HOMO = -10.83 eV	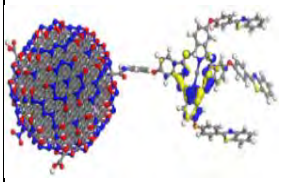 LUMO = -10.76 eV

Pc complex **10** has a decreasing effect on HOMO-LUMO gaps of DNDs, **Table 5.2**. Large HOMO-LUMO gaps of approximately 6.6-7.5 eV have been previously reported to affect the electronic structure of DNDs due to hydrogen ends on the surface of the nanoparticle **[75]**. Hydrogenated DNDs are electron rich because of the sigma-dangling bonds on their surfaces **[74]**. However, carboxyl and nitrogen functional groups have a dramatic decreasing effect on HOMO-LUMO band gap **[75]**. Pc complex **10** is a macrocyclic structure that is comprised of nitrogen (Chapter 1). Hence the decrease in HOMO-LUMO gaps and improved PDT activity in conjugated systems. Nitrogen, oxygen, and sulfur heteroatoms doping on DNDs results in structural changes from the Td to the trigonal C_{3V} point group **[59]**. Reactivity and structural instability as indicated by HOMO-LUMO energy gaps of conjugated systems for DNDs-**10** (0.07 eV), B@DNDs-**10** (0.09 eV) and P@DNDs-**10** (0.07 eV) are smaller than N@DNDs-**10** (0.14 eV), S@DNDs-**10** (0.14 eV)and S&N@DNDs-**10** (0.13 eV). Boron is reported to be the most stable dopant because it undergoes the least change in structural symmetry despite its structural and bond length alterations **[59]**. Hence B@DNDs-**10** conjugated system is a better PDT agent as discussed in the next Chapter.

Table 5.2: Comparison of the electronic properties from xtb of DNDs, Pc, dopands and respective conjugates.

Sample	**Band Gap (eV)**
DNDs	3.02
10	0.12
DNDs-**10**	0.07
B@DNDs	3.12
B@DNDs- **10**	0.09
P@DNDs	3.11
P@DNDs- **10**	0.07
N@DNDs	3.12
N@DNDs- **10**	0.14
S@DNDs	0.35
S@DNDs- **10**	0.14
S&N@DNDs	0.33
S&N@DNDs-**10**	0.13

5.3. Summary

Theoretical calculations and visualization were performed on complex **10**, DNDs and respective dopands alone and when in a conjugate. The HOMO-LUMO gaps were used to indicate molecular reactivity and structural instability of conjugated nanosystems on a molecular level. Conjugating Pc complex **10** to DNDs for all conjugated systems decreased the HOMO-LUMO energy gaps of DNDs. Theoretical calculations have shown that conjugated systems have better reactivity and molecular instability relative eto individual components of the conjugate. The least energy gaps in conjugates of DNDs-**10** (0.07 eV) and P@DNDs-**10** (0.07 eV) is an indication of high molecular instability and reactivity, relative to B@DNDs-**10** (0.09 eV).

APPLICATIONS:

Photodynamic Therapy

Nonlinear Optics

Chapter 6

6. Photodynamic therapy (PDT)

The chapter discusses the effect of Pc complexes (**3**, **7** - **12**) alone, nanoparticles alone (GQDs, CDs, DNDs) and respective conjugates as examples of PDT agents used to eradicate diseased Michigan Cancer Foundation (MCF-7) breast cancer cell lines. In 1% (v/v) DMSO in supplemented media used for PDT study it was observed that approximately 99.3±1% of the cells were still viable, suggesting negligible effect on the cells (**Figures 6.1 - 6.6**).

An efficacious photosensitizer has been previously reported to be sensitive to the cell type, cellular uptake, localization, drug concentration and irradiation time **[232-235]**. Only concentration was changed in this work in order to study the effects of individual photosensitiser when compared to the conjugates. Various concentrations (5-50 μg/mL) of the DNDs, Pc and conjugates were irradiated with 13.5 Jcm^{-2} for the optimized 300 s to evaluate the photodynamic therapy activities **[234]**. The photo-irradiation was done using light from a general electric quartz lamp (following the use of filters) since quartz lamps have been shown to be effective light sources for PDT **[233, 234]**.

6.1. Dark toxicity

Dark toxicity studies of complexes were performed in vitro on MCF-7 cancer cells by quantification of surviving cells using the WST-1 cell proliferation assay 24 h after the treatment with 0–50 μg/mL concentrations **(Figures (6.1 - 6.6)) A**. Toxicity tests confirmed that the conjugates were not toxic up to 50 μg/mL leaving at least 99 ± 3% of cells viable, in appendix **Table A1.** These results confirm what have been previously reported **[191, 236]**. Some Pcs alone (**7**, **8**, **9**) showed dark toxicity. In vitro dark toxicity is not desirable for photosensitizers aimed for use in PDT. There was no statistically significant difference in the percent viability of the cells as the drug concentration increases. Upon analysis of the triplicate replicate data of each concentration, no statistically significant difference was observed as the p-value was found to be greater than 0.05.

6.2. Photodynamic therapy (PDT)

The phototoxicity of complexes, NPs and respective NPs-Pc conjuagates were found to increase with increase in concentration as evidenced by decrease in cell viability in **Figures (6.1 - 6.6) B. Table 6.1** tabulates singlet oxygen quantum yields in water (1% DMSO) and DMSO with percentage of viable MCF-7 breast cancer cell lines at the highest drug dose of 50 μg/mL.

6.2.1. Effect of quaternization and number of charges

Comparing neutral complex **7** with charged complexes **8** and **9**, showed low PDT activity with cell viability of more than 50% at the highest tested concentration for the former (**Figure 6.1 B**). Similarly, complex **11** has better PDT activity than complex **10**. This could be due to low permeability into the cell due to the absence of positive charge in complexes **7** and **10**, positively charged photonsensitizers show higher PDT activity **[237-239]**. Quaternary complexes **8, 9** and **11** showed higher phototoxicity at all concentrations with only 30.74% ± 3, 21.56% ± 3 and 19.48% ± 0.02 cell viability at the highest tested concentration of 50 μg/mL **(Table 6.1)**. Complexes **8**, **9** and **11** have singlet oxygen quantum yields of 0.08, 0.23 and 0.28 respectively in water **(Table 6.1)**. Hence complexes **9** and **11** showed higher photodynamic activity than **8** in terms of percentage viability. A comprehensive analysis of twenty-two cancer cell lines taken from different body parts showed that all the cells specifically bind to positively charged nanoprobes, suggesting that the cancer cells have negative net charge **[239]**. The general enhancement in PDT activity of the quaternary complexes could be attributed to introduction of positively charged sites which specifically bind to cancer cells and increases cell permeability. Thus, the higher PDT activity of **9** and **11** could arise from the increased a combination of positively charged sites and asymmetry in the complexes leading to greater spread of singlet oxygen within the cell. Positively-charged photosensitizers cause more cell damage than neutral or anionic photosensitizers **[240]**, hence **11** and **9** are better than **10**.

Table 6.1: Percentage viability drug toxicity at 50 µg/mL and singlet oxygen quantum yields in water and DMSO.

	Φ_Δ		
PDT drug	**H_2O**	**DMSO**	**% viability at 50 µg/mL**
Complexes			
3	0.03	0.41	34.24
7	-	0.33	55.64
8	0.08	0.76	30.74
9	0.23	0.77	21.56
10	0.10	0.65	25.53
11	0.28	0.80	19.48
12	0.24	0.32	93.20
Carbon nanoparticles (CNPs)			
DNDs		-	31.00
B@DNDs		-	28.89
P@DNDs		-	25.53
N@DNDs		-	29.46
S&N@DNDs		-	33.00
GQDs		-	32.99
CDs		-	32.24
Carbon nanoconjugates (CNPs-Pc)			
$GQDs_2$(B3)-**3** (π - π)	0.27	0.41	31.40
CDs-**3** (π - π)	0.13	0.42	30.11
DNDs-**3** (π - π)	0.05	0.62	29.10
DNDs-**12** (ester)	0.36	0.68	28.22
3-DNDs-**12** (π - π, ester)	0.50	0.73	21.43
B@DNDs-**9** (π - π)	0.12	0.39	6.23
B@DNDs- **10** (amide)	0.21	0.52	6.52
B@DNDs- **11**(amide)	0.35	0.55	5.46
P@DNDs- **10** (amide)	0.25	0.44	7.19
N@DNDs- **10** (amide)	0.06	0.55	22.45
S&N@DNDs-**10** (amide)	0.09	0.66	7.63

The marked increase in PDT activity with increase in concentration indicate probable increase in the cellular uptake of complexes as concentration rises. Indeed, the plot of concentration against cell uptake (**Figure 6.1 C - E**) shows a concentration dependent uptake of the photosensitizer complexes by the cells up to 20 μg/mL for complex **9**, and subsequently followed by a low uptake. For complexes **7** and **8**, the uptake was up ~ 10 μg/mL. Hence, complex **9** shows higher cellular uptake than **7** and **8**. The low uptake has been reported to arise due to an altered transport mechanism(s) at higher concentrations **[241, 242]**.

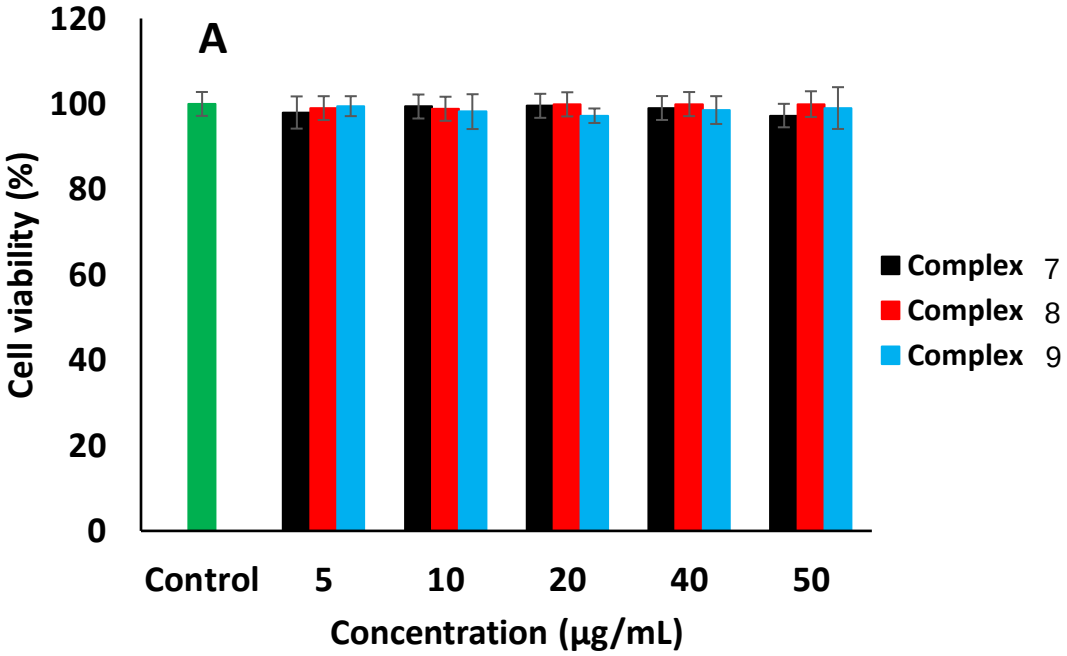
A
120
100
80
60
40
20
0
Cell viability (%)
Control
5
10
20
40
50
Concentration (µg/mL)
Complex 7
Complex 8
Complex 9

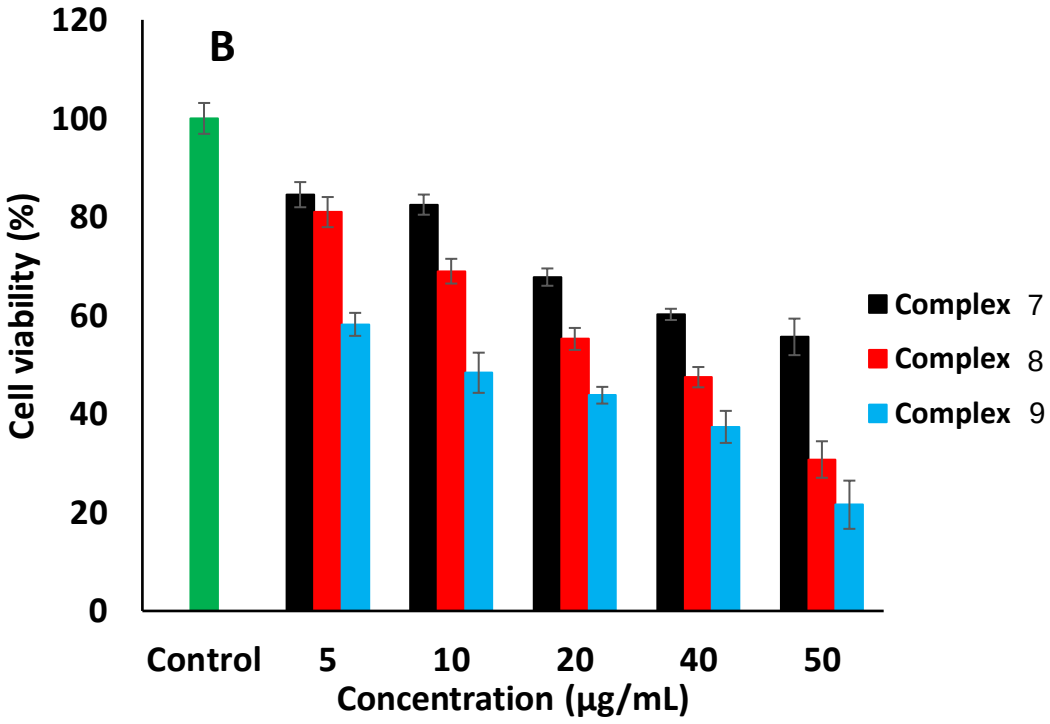
B
120
100
80
60
40
20
0
Cell viability (%)
Control
5
10
20
40
50
Concentration (µg/mL)
Complex 7
Complex 8
Complex 9

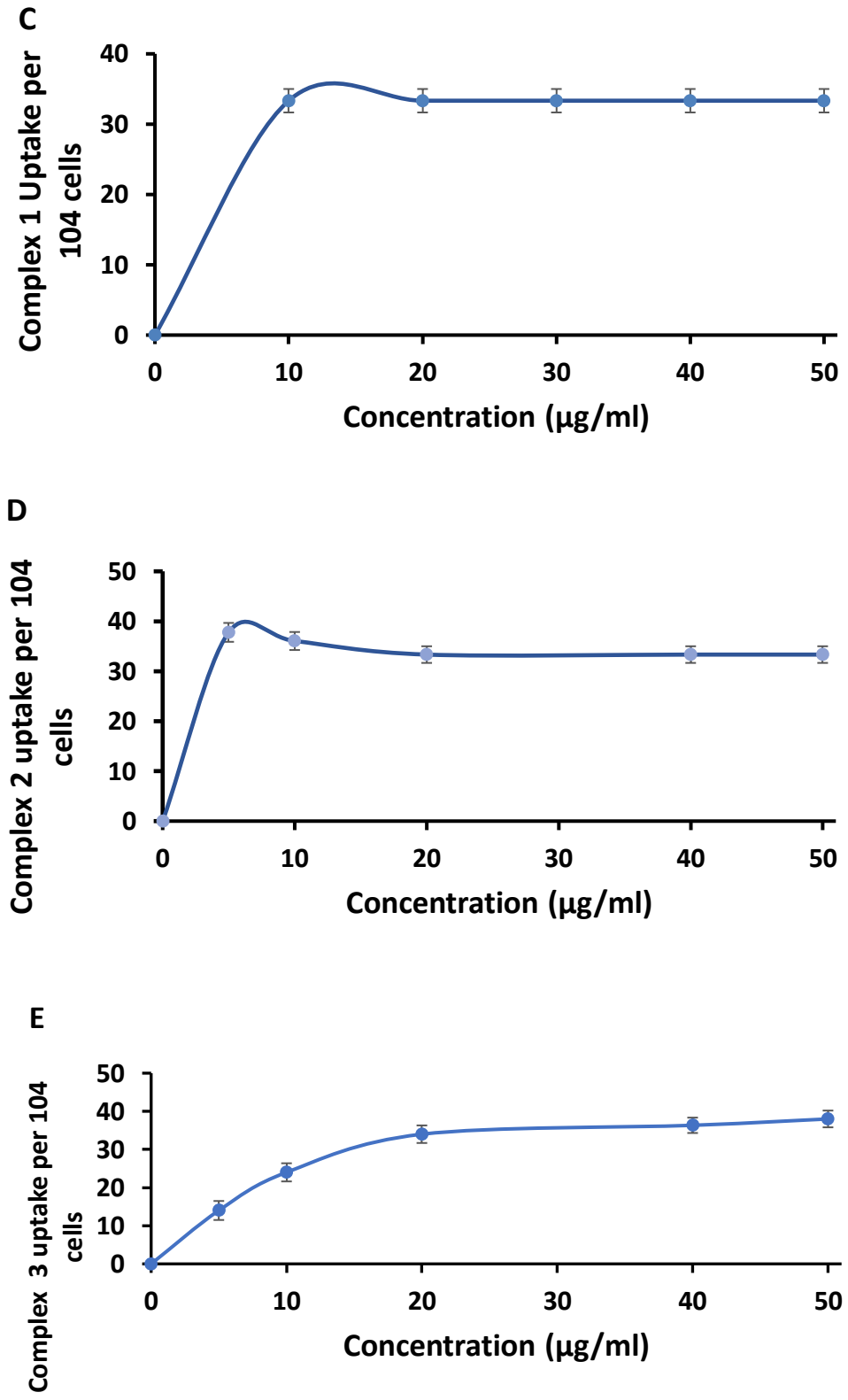

Figure 6.1: (A) Dark toxicit and (B) PDT plots for complex **7**, **8** and **9**. Controls were prepared in 1% DMSO and cultured media. Cellular uptake of complexes: (C) **7**, (D) **8** and (E) **9** as a function of concentration.

6.2.2. Effect of symmetry

Complexes **7** and **10** have percentage cell viability of 55.64% ± 0.3 and 25.53% ± 0.02 **(Figure 6.2 B)**. Showing the importance of low symmetry complexes.

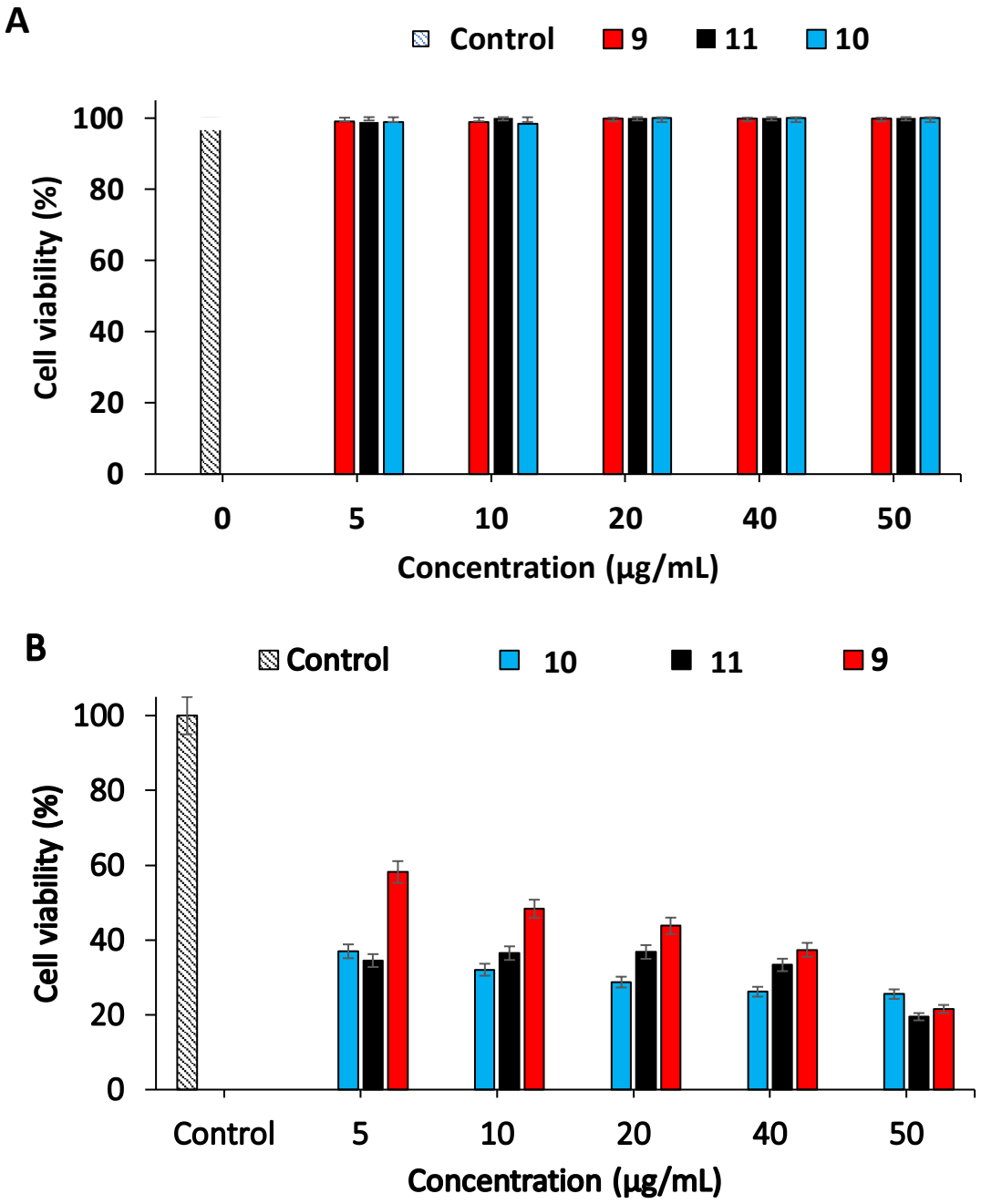

Figure 6.2: (A) Dark toxicity and (B) PDT plots for complexes **9**, **10** and **11**. Control conducted in 1% DMSO in growth media.

6.2.3. Effect of Pc and BODIPY

This section discusses the PDT effect of positively charged Pc complex (**3**), BODIPY (**12**) and the effect of interaction between complexes (**3** and/or **12**) and DNDs in nanohybrids.

Photosensitizers showed significant cytotoxicity on MCF-7 with cell viability at the highest tested concentration (50 μg/mL) for DNDs (31.00% ± 2), **12** (93.20% ± 2), **3** (34.24% ± 7), DNDs-**12** (28.22% ±3), DNDs-**3** (29.10% ± 2) and **3**-DNDs-**12** (21.43% ± 5) in **Figure 6.3 B, D, Table 6.1**. Thus, **3-**DNDs-**12** exhibited the highest phototoxicity towards MCF-7 with only 21 ± 5% cell viability at the highest tested concentration of 50 μg/mL. Complex **3** alone in **Figure 6.3 D** showed low PDT activity with cell viability of ≥34%, while BODIPY **12** showed ≥93% at the highest tested concentration.

For BODIPY **12** (which had a reasonably high singlet oxygen quantum yield (0.24) in water, **(Table 6.1)**, the low PDT activity could be due to low permeability into the cell due to the absence of positive charge on the photosensitiser. As stated above, positively charged photosensitisers show higher PDT activity **[237-239]**. Compared to DNDs-**12,** DNDs-**3** showed relatively low PDT activity, irrespective of the positive charge of complex **3**, due to its low singlet oxygen quantum yield properties in water **(Table 6.1).** The nature of interaction between complex **12**/**3** and the DNDs has an influence in its properties as a conjugate. Covalently linked nanosystems between Pc and carbon nanostructures have been previously reported to show better physicochemical properties when compared to non-covalently linked nanosystems **[62].** This could be attributed to phase separation between non-covalently linked nanosystems due to absence of a covalent bond between DNDs and complex **3.** Enhanced PDT activity of **3-**DNDs-**12** could arise from synergistic effect of positively charged site from Pc **(3)**, BODIPY **(12)** and DNDs from zetapotential in **Table 3.3**, leading to greater spread of singlet oxygen within the cell.

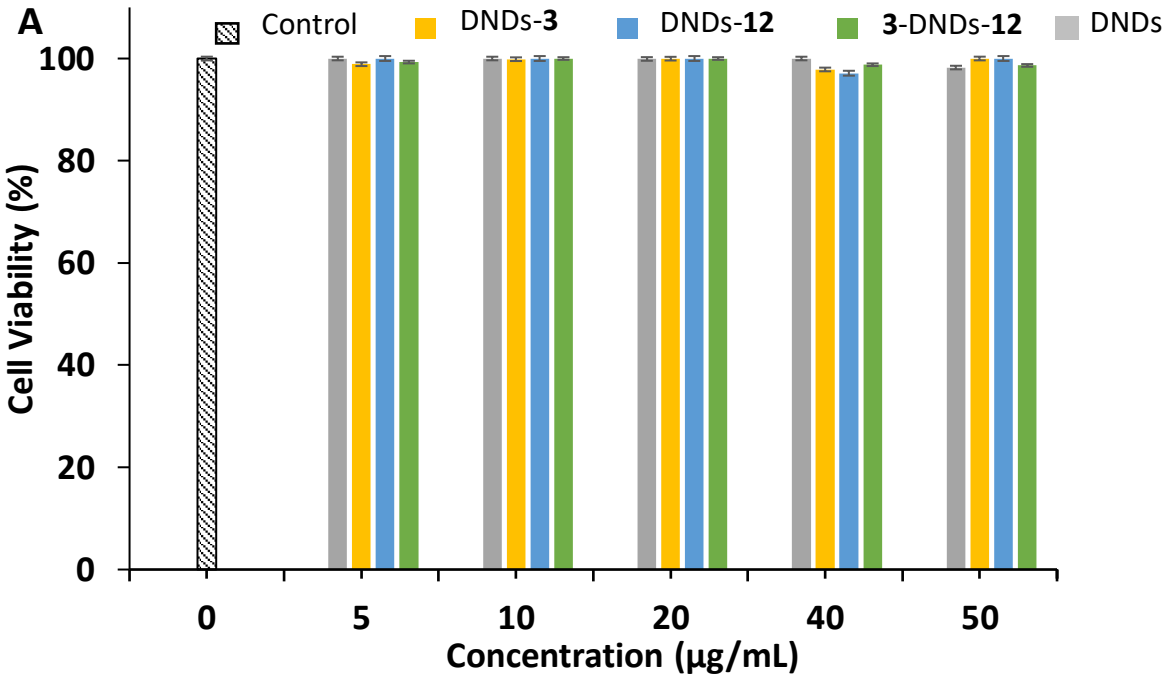
A
Control
DNDs-3
DNDs-12
3-DNDs-12
DNDs
Cell Viability (%)
100
80
60
40
20
0
0
5
10
20
40
50
Concentration (µg/mL)

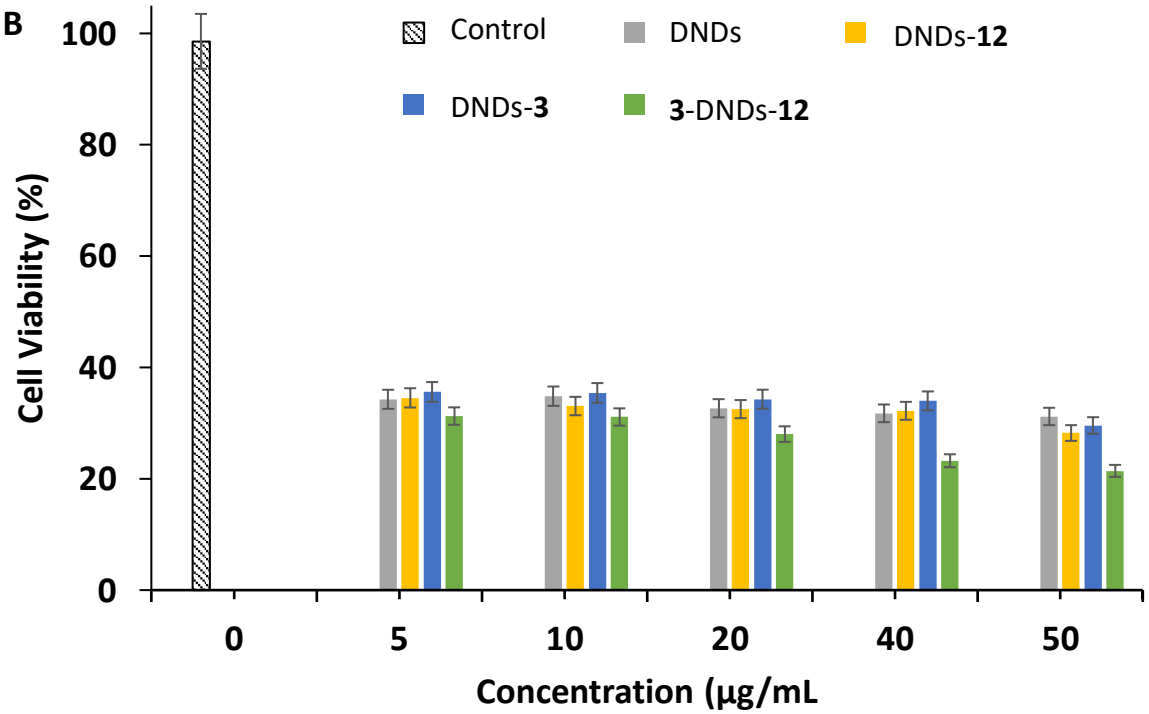
B
Control
DNDs
DNDs-12
DNDs-3
3-DNDs-12
Cell Viability (%)
100
80
60
40
20
0
0
5
10
20
40
50
Concentration (µg/mL

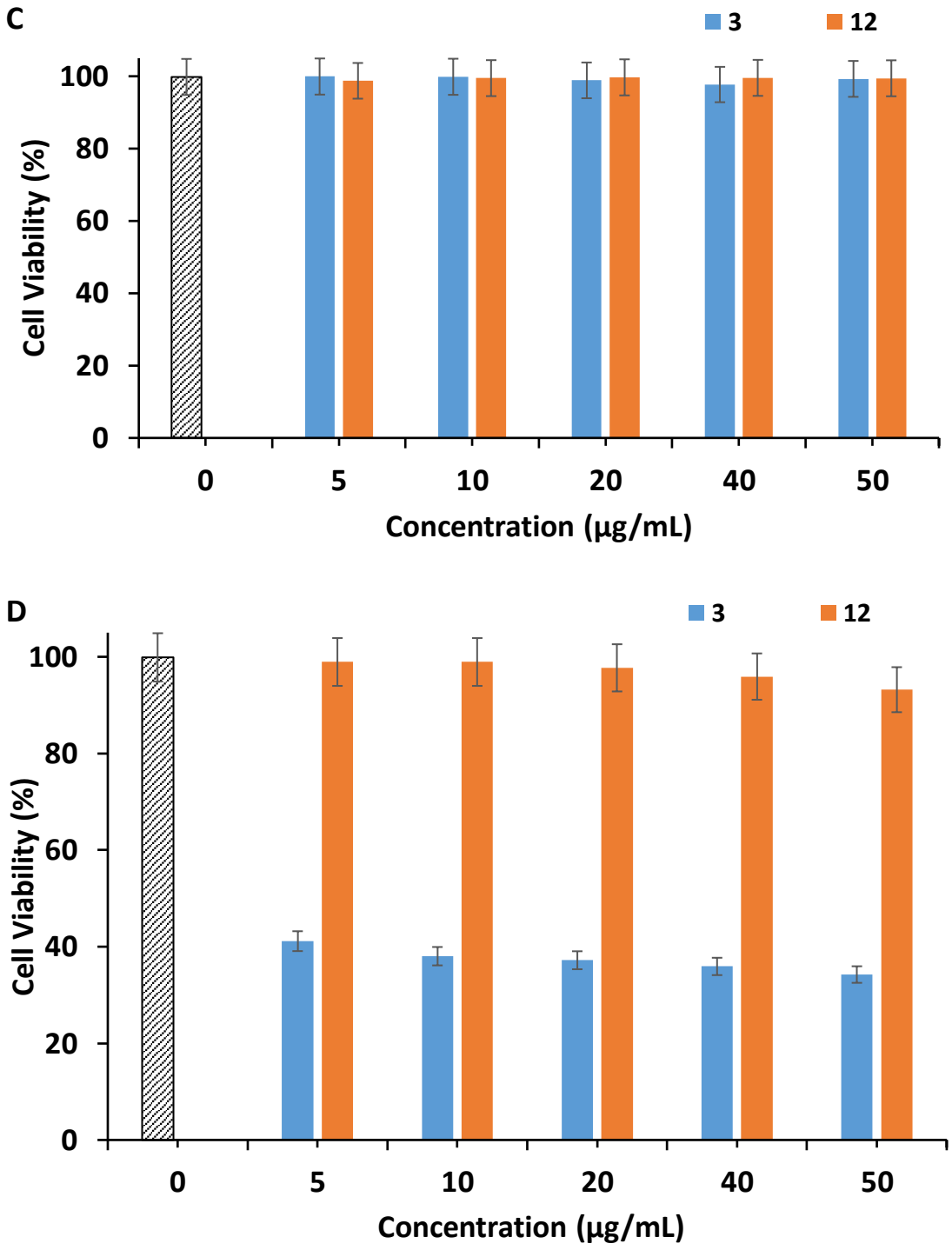

Figure 6.3: (A) Dark toxicity and (B) PDT plots for DNDs, DNDs-**3**, DNDs-**12**, **3**-DNDs-**12**. Controls were prepared in 1% DMSO and cultured media. (C) Dark toxicity and (D) PDT for complexes **3** and **12** alone. Control (0 mg/mL) conducted in 1% DMSO in growth media. Irradiation time 300 s at 13.5 J/cm^2.

6.2.4. Different type of NPs

The MCF-7 cancer cells were treated with different concentrations (5-50 µg/mL) of DNDs, $GQDs_2$(B3), CDs, **3**, DNDs-**3**, $GQDs_2$(B3)-**3** and CDs-**3**. The conjugates: DNDs-**3**, CDs-**3** and $GQDs_2$(B3)-**3**, **Table 6.1**, exhibited higher PDT activity at 29.10% ± 0.02, 30.11% ± 0.02 and 31.40% ± 0.23 cell viability at the highest tested concentration of 50 µg/mL, compared to complex **3** alone at 34 ± 0.55%. Carbon nanoparticles alone (DNDs, CDs and GQDs) showed lower PDT activity as shown by respective cell viability of 31.00% ± 0.17, 32.24% ± 0.01 and 32.99 ± 0.01% when compared to respective conjugates. DNDs-**3** showed the highest PDT activity than the other carbon nanoparticles (CNPs), **Figure. 6.4 B, Table 6.1**. Combining carbon nanoparticles with complex **3** for PDT slightly improved PDT activity. Irrespective of low singlet oxygen quantum yields in water, the slight increase in PDT activity of DNDs-**3** in **Figure 6.4** could be due synergistic effect of positively charged DNDs.

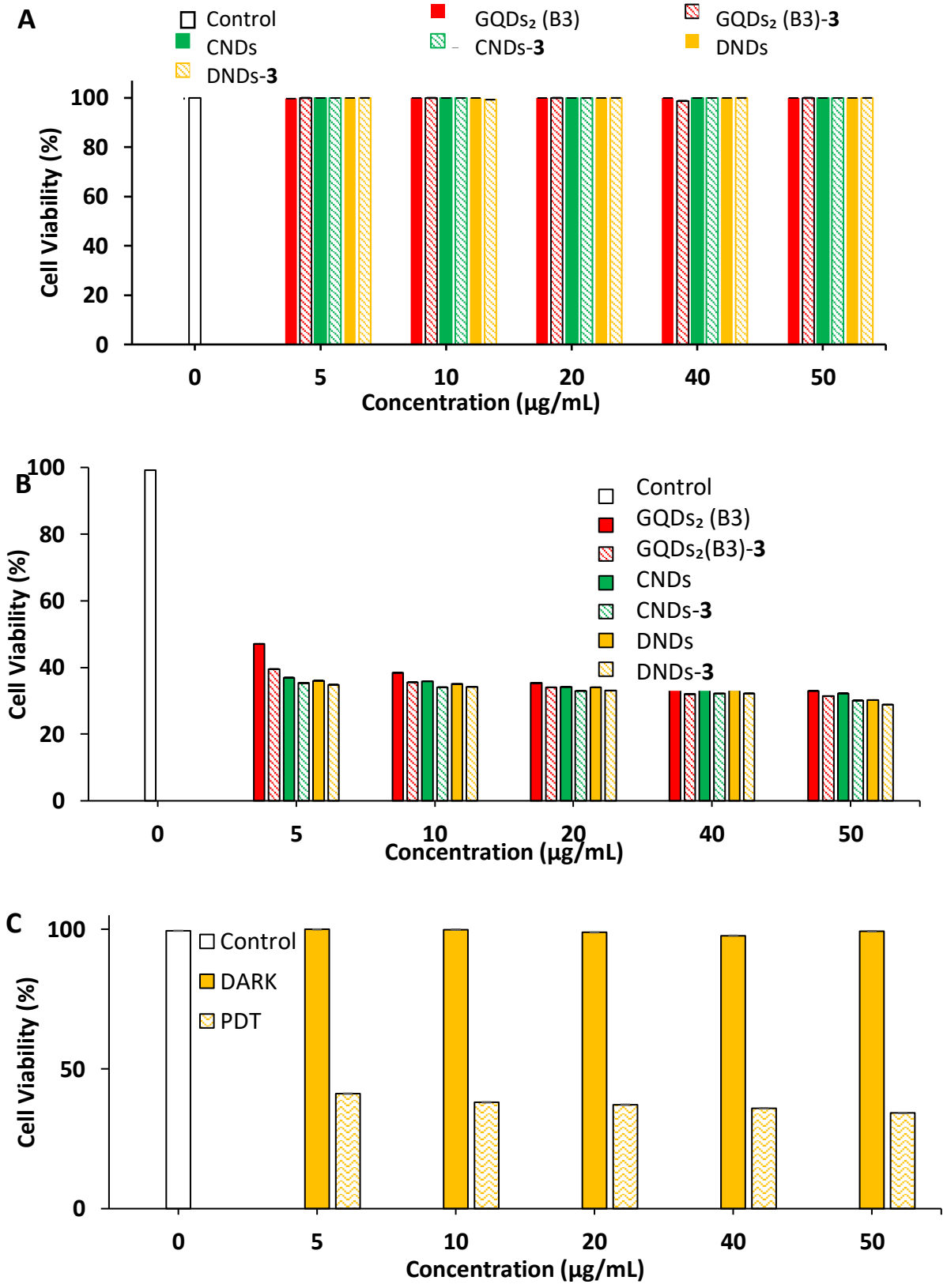

Figure 6.4: (A) Dark toxicity, (B) PDT plots for $GQDs_2$(B3), $GQDs_2$(B3)-**3**, CDs, CDs-**3**, DNDs, DNDs-**3** and (C) Dark, PDT toxicity plots for complex **3** alone

6.2.5. Doped DNDs with complex 10

DNDs-**10** and S@DNDs-**10** in **Table 6.1** were not employed for PDT studies due to the low value of singlet oxygen quantum yield of 0.21, <0.01 and 0.13, 0.02 in DMSO and water, respectively. Photodynamic therapeutic properties and application in MCF-7 breast cancer cell lines of N@DNDs-**10,** S&N@DNDs-**10**, P@DNDs-**10** and B@DNDs-**10** conjugates will be discussed in this section.

The conjugates N@DNDs-**10** exhibited low PDT activity (as % viability) at 22.45% ± 0.56 when compared to S&N@DNDs-**10**, P@DNDs-**10**, B@DNDs-**10** with higher PDT activity of 7.63% ± 0.71, 7.19% ± 0.29, and 6.52% ± 0.76, respectively (**Figure 6.5B, Table 6.1**) at the highest tested concentration of 50 µg/mL. Complex **10** (at 25.53% ± 0.60) and doped DNDs alone (N@DNDs, S&N@DNDs, P@DNDs and B@DNDs) showed the least PDT activities of 29.46% ± 0.19, 33.00% ± 0.09, 25.53% ± 0.60 and 28.89% ± 0.18, respectively, (**Table 6.1**). Upon covalently linking Pcs to doped DNDs, significantly higher PDT activity was observed compared to the Pc complex **10** alone (26 ± 0.60%) with Φ_{Δ} = 0.10 in water. Thus, a combination of doping DNDs with respective heteroatom and loading with complex **10** showed improved PDT activity. Higher PDT activities in B and P@DNDs-**10** could be attributed to combination of Φ_{Δ} and molecular chemical reactivity (structural instability) associated with strain that is relatively reduced upon linking asymmetric Pcs to doped DNDs with relatively small HOMO-LUMO energy gaps (Chapter 5).

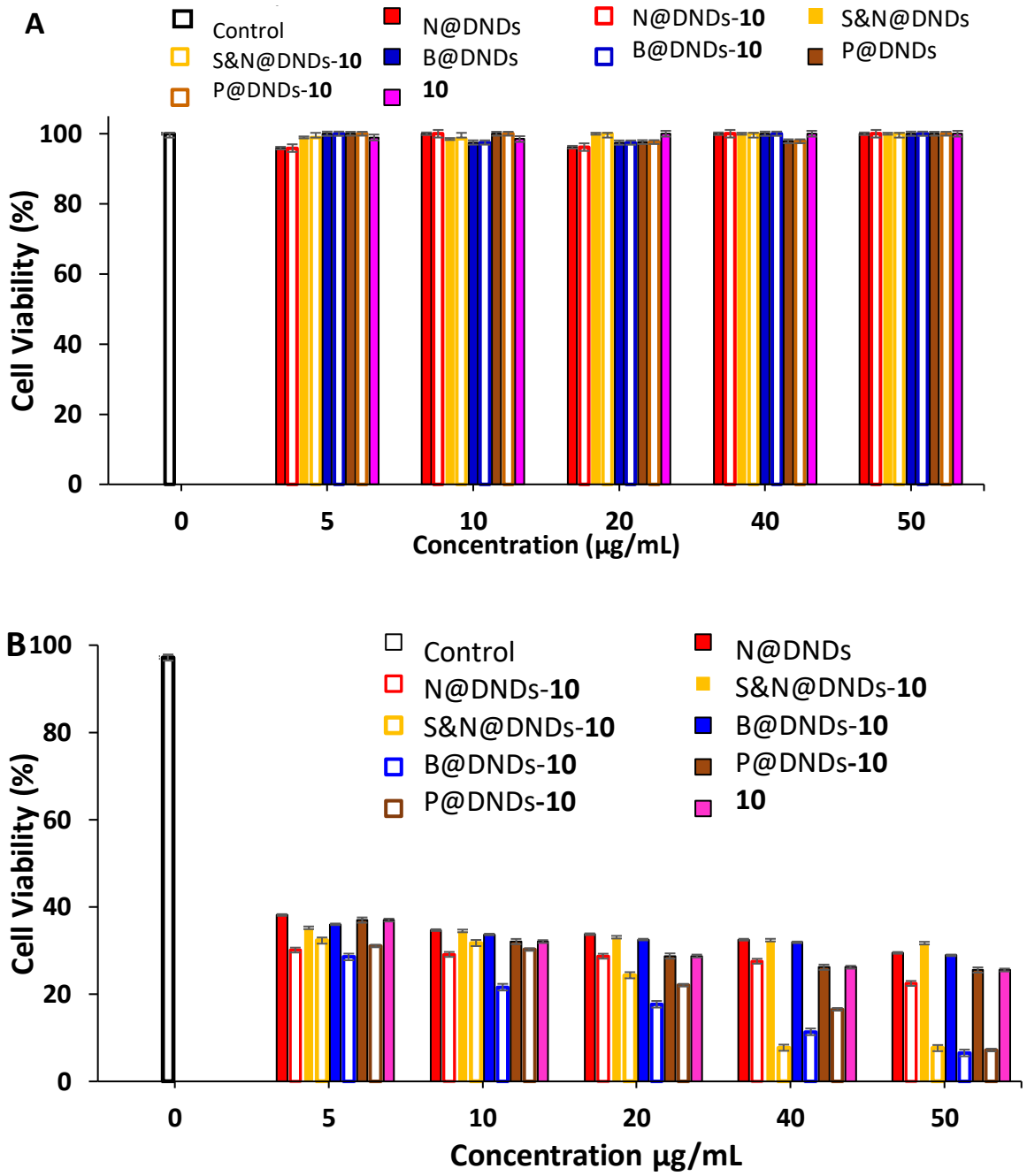

Figure 6.5: (A) Dark toxicity and (B) PDT plots for doped nanodiamonds and respective phthalocyanine conjugated hybrids. Control conducted in 1% DMSO in growth media. Please note that DNDs are filled bars and the corresponding conjugates are empty bars with the same color outline as the DNDs.

6.2.6. B doped

B@DNDs Pc complex hybrids had high Φ_{Δ} in water and good PDT activity. Hence, were employed for PDT studies together with different Pcs (**9, 10, 11**) to obtain respective nanoconjugated systems (B@DNDs-**9**, B@DNDs-**10**, B@DNDs-**11**). B@DNDs were noncovalently (π - π) interacted with symmetric and positively charged complex **9**. Complex **10** is an asymmetric and neutral whereas **11** is asymmetric and positively charged. Complexes **10** and **11** were covalently linked to B@DNDs through amide bond.

Nanohybrids (B@DNDs-**9,** B@DNDs-**10,** and B@DNDs-**11**) showed high PDT activity of 6.23% ± 0.41, 6.52% ± 0.76, and 5.46% ± 0.86 cell viability when compared to B@DNDs (28.89% ± 0.18%) and complexes (**9**, **10**, **11**) alone, 21.56% ± 0.4, 25.53% ± 0.60, and 19.48% ± 0.02 respectively in **Table 6.1** at the highest tested concentration of 50 μgmL^{-1}. B@DNDs-**11** (Φ_{Δ} = 0.35) showed the most PDT activity when compared B@DNDs-**9** (Φ_{Δ} = 0.12) and B@DNDs-**10** (Φ_{Δ} = 0.21) in **Table 6.1**. This can be attributed to a combination of asymmetry, charge and singlet oxygen quantum yields.

Complexes **10** and **11** showed increased singlet oxygen quantum yield in the presence of B@DNDs in water, but decreased Φ_{Δ} in complexes **9.** Thus, the mechanism may not only involve singlet oxygen. In the presence of nanoparticles, intracellular localization of phthalocyanines will improve through the enhanced permeability and retention effect, which is known for nanoparticles **[243]**, resulting in improved PDT activity of the conjugates despite the decrease in singlet oxygen quantum yields compared to Pcs alone. Also, B@DNDs-**11** gave the best PDT results due to combination of charge and asymmetry from of the Pc.

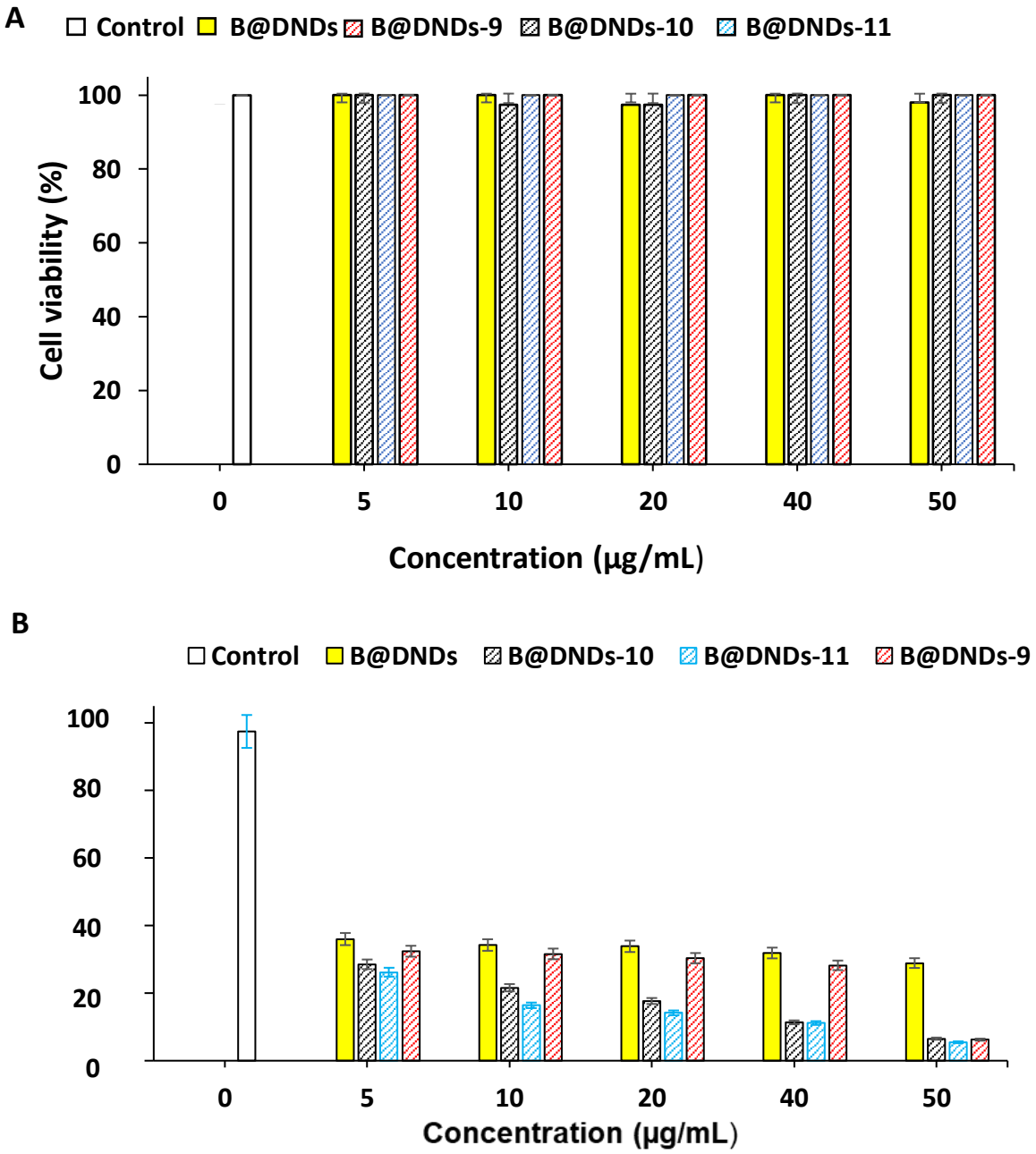

Figure 6.6: (A) Dark toxicity and (B) PDT plots for boron doped nanodiamonds and respective phthalocyanine conjugated hybrids. Control conducted in 1% DMSO in growth media. Please note that B@DNDs are empty bars and the corresponding conjugates are filled bars with the same color outline as the DNDs.

6.3. Summary

Phototoxicity of complexes, NPs and respective nanohybrids increased with increase in concentration from 0 to 50 μg/mL and there was no toxicity in the absence of light, except for some Pcs alone. Positively charged complexes and respective nanohybrids are taken up more readily by MCF-7 breast cancer cell lines. In symmetric complexes (**7**, **8**, **9**), increasing the number of positive charges improves singlet oxygen quantum yields and PDT toxicity of the drug. In conjugated systems, the number of positive charges on symmetric complexes have no specific effect on singlet oxygen quantum yields but rather permeation effect applicable in PDT activity. Conjugated systems possess enhanced PDT activities when compared to their individual components. Furthermore, DNDs have better PDT characteristics relative to CDs and GQDs. An even further enhancement in PDT characteristics upon heteroatom doping of DNDs and conjugating with a Pc complexes (especially asymmetric and positively charged). Therefore, a combination of singlet oxygen quantum yields, asymmetry, positive charge and heteroatom doped DNDs have an enhancing effect on PDT activity of DNDs-Pc conjugate.

Chapter 7

7. Nonlinear optical limiting (NLO)

The chapter discusses the NLO characteristic effect of individual complexes with different central metals, substituent, DNDs and in a conjugated system. Complexes **4a, 4b, 4c**, **5**, **6** and respective conjugates are employed.

7.1. NLO parameters

The major disadvantages of the Z-scan technique is associated with the challenge of separating various nonlinear optical mechanism (excited state absorption (ESA), two photon absorption (TPA), nonlinear scattering and nonlinear refraction) associated with reverse saturable absorption (RSA) or saturable absorption (SA) processes. Suitable equations for analysis of Z-scan data were developed to overcome this challenge. Elaboration of results from such analysis is based on the nature of material and the laser beam (pulse width and rate of repetition) utilized. Optical limiting capability of materials used in this study is measured using nonlinear absorption coefficient (β). Multi-photon absorption is associated with materials that have zero linear absorption at laser wavelength of 532 nm. Effective value (β_{eff}) is determined and indicates the degree of nonlinear absorption and depends on the population of molecules in the first excited triplet state (T_1) because sequential TPA and ESA only occur when a laser with nanosecond pulse is used. The β_{eff} values are calculated by fitting the Z-scan data to the transmittance. Hence, the nonlinear optical behavior of the synthesised complexes were investigated by using the open aperture Z-scan technique and the data were analyzed in the manner reported by Sheik-Bahae *et al* **[244, 245]** using equation (**7.1**):

$$\boldsymbol{T_{(Z)} = \frac{1}{1+\beta_{eff} l_{eff} (I_{00}/(1+(z/z_0)^2))}} \qquad (\mathbf{7.1})$$

where $T_{(Z)}$ is the normalized transmittance of the sample, I_{00} is the intensity of the light on focus, β_{eff} is the two-photon absorption coefficient, z_o is the diffraction length of the beam, z is the sample position with respect to input intensity and l_{eff} is the effective length for two photon absorption in a sample of path length L and is determined using equation (**7.2**).

$$\boldsymbol{l_{eff}} = \frac{\mathbf{1}-\boldsymbol{e}^{-\boldsymbol{\alpha l}}}{\boldsymbol{\alpha}} \quad (\mathbf{7.2})$$

where α is the linear absorption coefficient. Since equation (**7.1**) is not generally suited to directly fit experimental data, a numerical form of equation (**7.1**) which is equation (**7.3**), was employed to fit the experimental data.

$$T_{(z)} = 0.363\boldsymbol{e}^{\left(\frac{-\boldsymbol{q}(\boldsymbol{z})}{5.60}\right)} + 0.286\boldsymbol{e}^{\left(\frac{-\boldsymbol{q}(\boldsymbol{z})}{1.21}\right)} + \mathbf{0.213}\boldsymbol{e}^{\left(\frac{-\boldsymbol{q}(\boldsymbol{z})}{24.62}\right)} + \mathbf{0.096}\boldsymbol{e}^{\left(\frac{-\boldsymbol{q}(\boldsymbol{z})}{115.95}\right)} + \mathbf{0.038}\boldsymbol{e}^{\left(\frac{-\boldsymbol{q}(\boldsymbol{z})}{965.08}\right)} \quad (\mathbf{7.3})$$

The excited state cross-section (δ_{exc}) was obtained by fitting the Z-scan experimental data to equation (**7.4**):

$$\boldsymbol{T_{Norm}} = \frac{\boldsymbol{In}\left(\mathbf{1}+\left(\boldsymbol{q}/\left(\mathbf{1}+\boldsymbol{X}^{\mathbf{2}}\right)\right)\right)}{\boldsymbol{q}/\left(\mathbf{1}+\boldsymbol{X}^{\mathbf{2}}\right)} \quad (\mathbf{7.4})$$

where q is a dimensionless parameter that is given by equation **7.5**:

$$\boldsymbol{q} = \frac{\boldsymbol{\alpha\delta_{exc}}}{\mathbf{2}\boldsymbol{hv}}\boldsymbol{F_0 L_{eff}} \quad (\mathbf{7.5})$$

where T_{Norm} is the normalized transmittance, F_0 (J/cm^2) is the total fluence on axis, h is the Planck's constant, v is the frequency of the laser beam, and $\chi = z/z_0$.

Imaginary third-order susceptibility ($I_m[\chi^{(3)}]$) values were calculated using equation (**7.6**) **[246, 247]**:

$$\boldsymbol{I_m}\lfloor\boldsymbol{\chi}\rfloor^{\mathbf{3}} = \frac{\boldsymbol{n^2\varepsilon_0 C\lambda\beta_{eff}}}{\mathbf{2}\boldsymbol{\pi}} \quad (\mathbf{7.6})$$

where n is the linear refractive index, and c is the speed of light, ε_0 is the permittivity of free space and λ is the wavelength of the laser.

The second order hyperpolarizability (γ), which indicates the nonlinear absorption per mole is related to the imaginary third order susceptibility by equation (**7.7**).

$$\boldsymbol{\gamma} = \frac{\boldsymbol{I_m}[\boldsymbol{\chi}^{\mathbf{3}}]}{\boldsymbol{f}^{\mathbf{4}}\boldsymbol{C_{mol}N_A}} \quad (\mathbf{7.7})$$

where C_{mol} is the molar concentration of the active species in the triplet state, ƒ (the Lorentz local field enhancement factor) = $n^2 + 2)/3$ (where n is the refractive index of the sample), and N_A is the Avogadro's constant.

7.1.1. Effect of central metal

Nonlinear absorption behaviour in this section was investigated using an open aperture Z-scan technique with an excitation pulse of 10 ns at input energy of 30 µJ at 532 nm. Linear absorption coefficient (α_0) for the Pc molecules are presented in **Table 7.1**. The α_0 values of investigated Pcs and respective conjugates in **Table 7.1** show remarkable differences at the same absorbance (A) of 1 in DMSO. Linear absorption (α_0) = A/L where L is the path length of the cuvette. Absorbance depends on the concentration of the material. Hence α_0 will change with material concentration.

Table 7.1: Nonlinear optical properties of DNDs, **4a**, **4b** and **4c** and respective nanoconjugates with DNDs in DMSO (where appropriate) at absorbance of 1 at energy of 30 µJ .

Sample	α_0 (cm^1)	**B_{eff} (cm GW^{-1})**	**$I_m[X^3]$ (esu)**	γ **(esu)**	**k** ($\frac{\delta_{exc}}{\delta_o}$)	**I_{lim} (Jcm^{-2})**	Φ_T **(DMSO)**
DNDs	11.52	22.0	1.43 x 10^{-8}	1.27 x 10^{-28}	-	-	-
4a	13.10	41.0	1.50 x 10^{-8}	1.33 x 10^{-28}	22.3	-	0.20
DNDs-**4a** (π - π)	17.95	58.5	2.04 x 10^{-8}	1.89 x 10^{-28}	55.6	-	0.39
4b	10.43	42.8	1.53 x 10^{-8}	1.82 x 10^{-28}	35.4	-	0.33
DNDs-**4b** (π - π)	31.7	60.9	2.13 x 10^{-8}	2.62 x 10^{-28}	87.0	-	0.49
4c	2.59	136	3.17 x 10^{-8}	4.22x 10^{-28}	342	0.39	0.70
DNDs-**4c** (ester)	1.73	125	2.91 x 10^{-8}	3.88 x 10^{-28}	306	0.47	0.42

α_0 values have been previously reported to be sensitive to structural modification and Pc interactions **[248]**. The average linear transmittances of **4a**, **4b**, **4c** and respective conjugates of **4a** and **4b** is ≈98% (**Figure 7.1**). However, conjugate of DNDs-**4c** showed a lower transmittance of ≈94%.

(a)

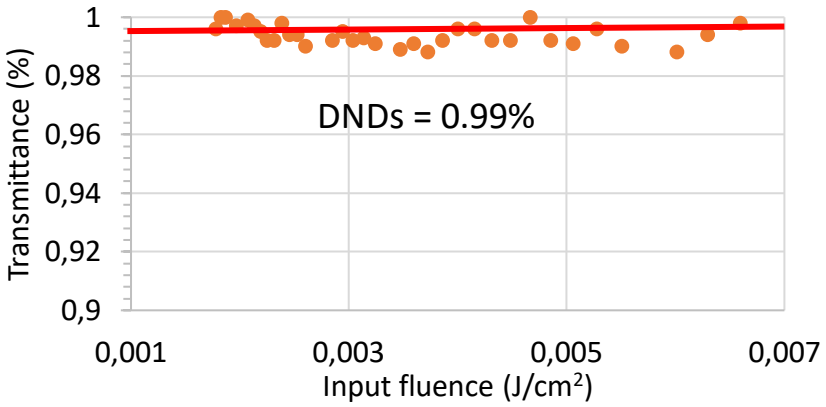

(b)

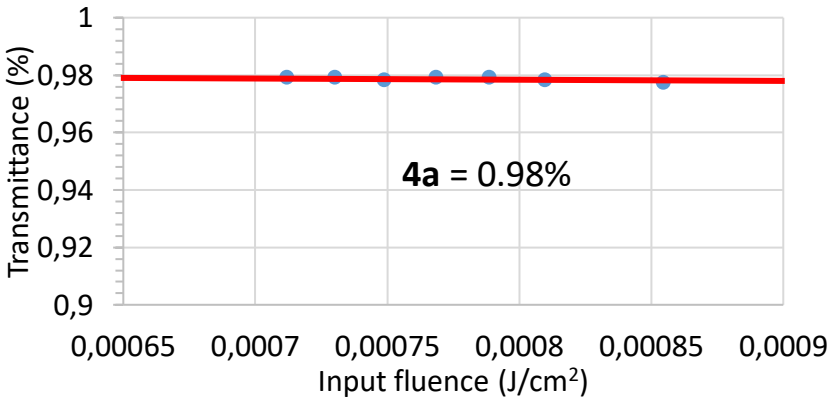

(c)

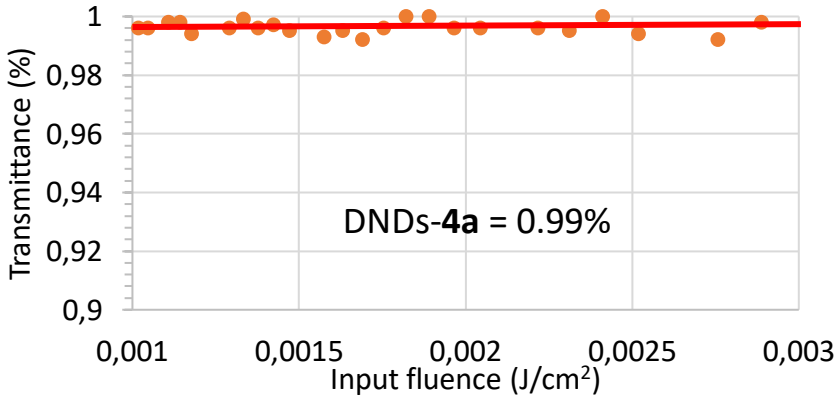

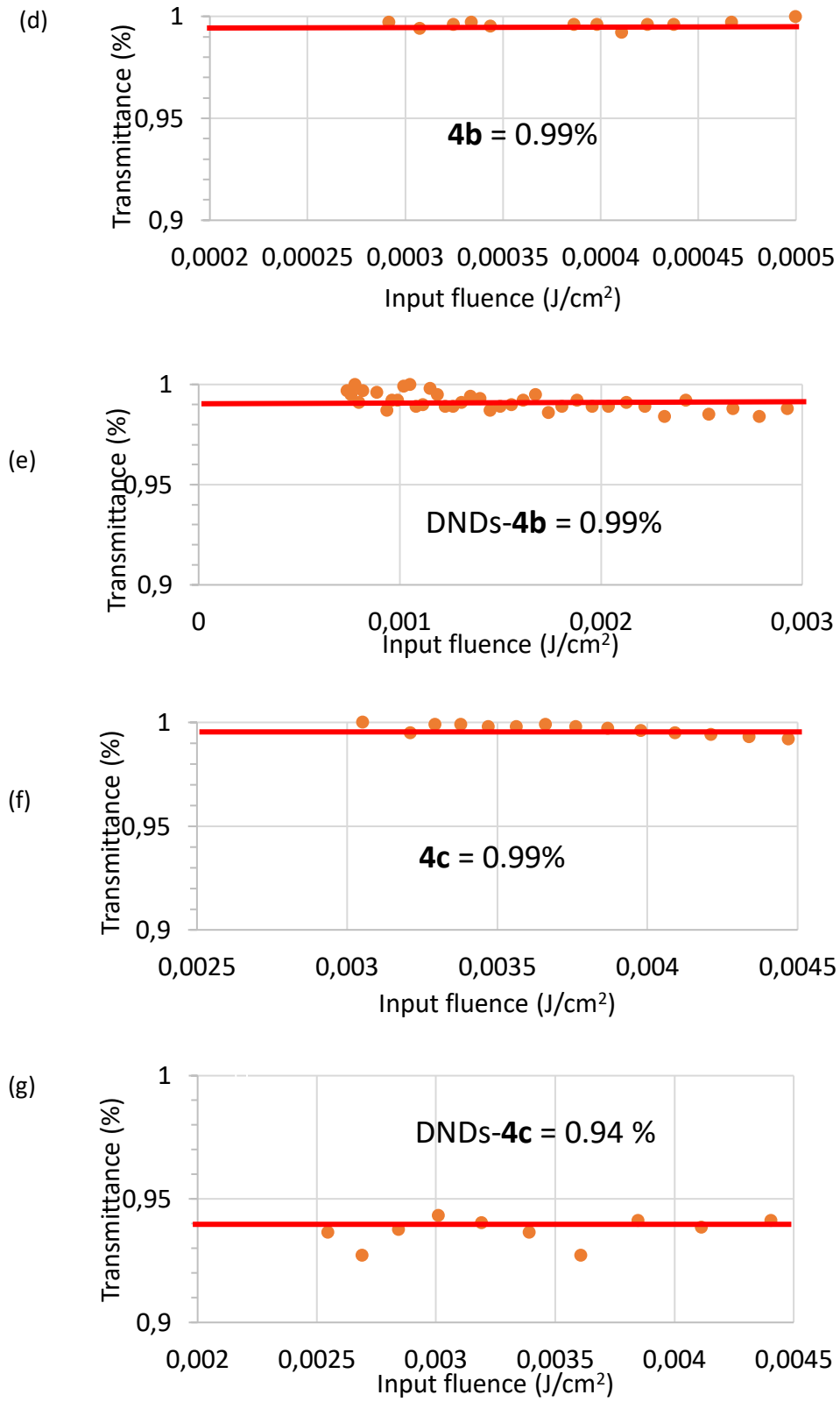

Figure 7.1: Linear transition plots of Pcs and respective conjugates

Z-scan profiles of Pcs alone and nanoconjugate systems (DNDs-**4a**, DNDs-**4b** and DNDs-**4c)** in **Figure 7.2**, show typical RSA characteristics and the measurements showed nonlinear absorption (NLA) behaviours. A higher reduction in transmittance shown by an enhanced dip in RSA profile was observed when **4a** and **4b** were in the presence of DNDs than when alone (only a very small increase for the unmetalated derivative, showing the importance of metalation), suggesting that the nanohybrids could be potential optical limiting materials. The opposite was the case for DNDs–**4c** compared to **4c**, where the latter showed an enhanced dip in transmittance.

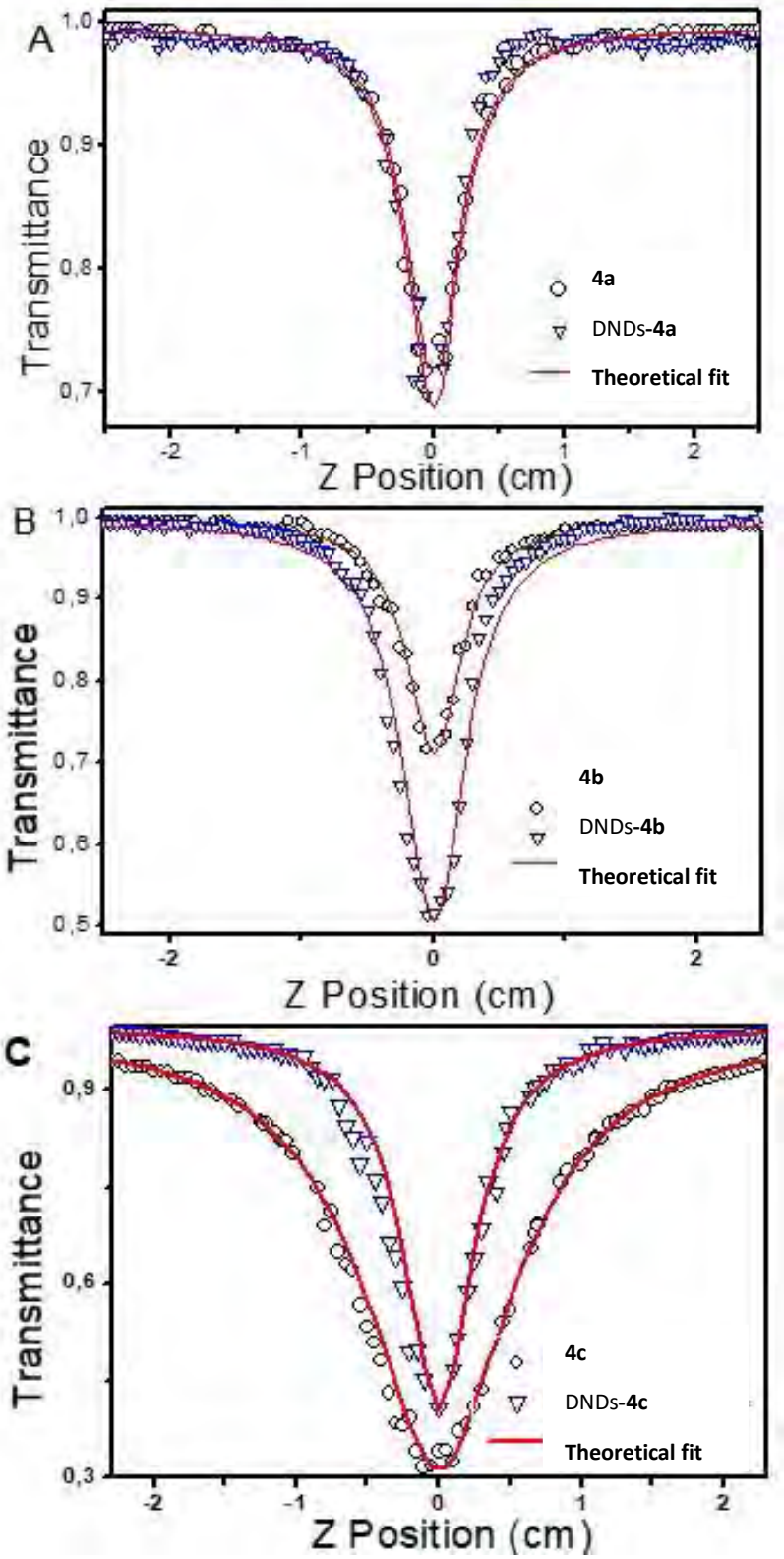

Figure 7.2: Open aperture Z-scan signatures of (A) **4a**, (B) **4b** and (C) **4c** when alone, in the presence of DNDs and respective fittings in DMSO at A=1, energy 30 µJ.

The poor performance of DNDs–**4c** could be due to aggregation discussed in Chapter 3. DNDs alone showed a smaller dip at 82% at 30 µJ (**Figure 7.3**), compared to say DNDs–**4b** at 53%. This suggests that DNDs alone are not as good NLO material as to when combined with Pcs. It has been observed under the laser irradiation with low energy, saturable absorption (SA) occurs for GQDs **[249])** due to ground state bleaching. **Figure 7.3** shows that the Z-scan profiles for DNDs alone at different energies exhibited SA to RSA profiles, which became more defined with decrease in energy. Nonlinear scattering and the nonlinear absorption are the dominant mechanisms of optical limiting DNDs, with the former being observed for larger nanoclusters **[250, 251]**. **Table 7.1** shows the effective nonlinear absorption coefficient values, B_{eff}, obtained for each sample by fitting the experimental data to the transmittance equations reported in previous studies **[252]**, (Eqs. (**7.1**), (**7.2**) and (**7.3**)). The B_{eff} values increased from 41.0 and 42.8 cm/GW in **4a** and **4b** to 58.5 and 60.9 cm/GW for the corresponding nanohybrid conjugates, respectively. Though both **4c** and its conjugate showed RSA behaviour, the Pc alone display enhancement in RSA as well as B_{eff} compared to the conjugate, which could be attributed to effect of aggregation. Aggregation has been known to reduce the excited state lifetime and hence the effective nonlinear optical absorption coefficient **[253]**.

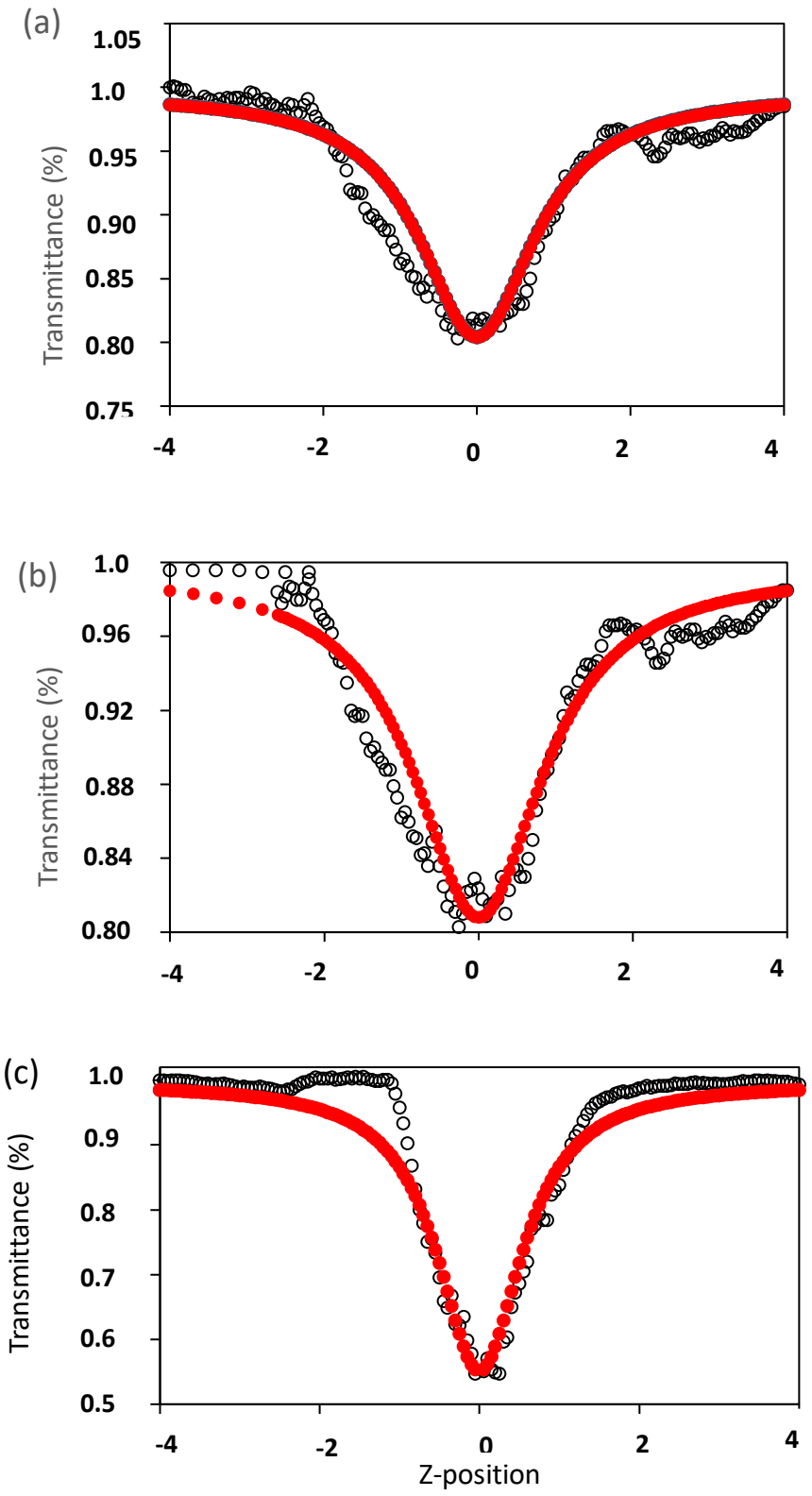

Figure 7.3: Open aperture Z-scan signatures of DNDs alone at energy (a) 30 µJ (b) 21 µJ, and (c) 10 µJ and respective fitting in red

Reverse saturable absorption from nanosecond laser pulses has been previously reported to be due to one-photon, two-photon, three-photon absorption (1PA, 2PA, 3PA) mechanisms, a combination of both or all three **[244, 254, 255]**. It is known that for organic materials, the contribution due to 3PA to the NLO response typically occurs at longer wavelength (using a laser tuned at wavelengths much > 530 nm) **[255]**. The fitting equation used for a 3PA transmittance data, suggests its negligible contribution **[254, 255]**. Laser of 532 nm was used, hence, the contribution of 3PA is expected to be negligible.

Merit coefficient (k) in **Table 7.1** indicates quantitative evaluation of the ratio of the excited and ground state absorption cross-sections **[255, 256]**. The absorption contribution resulting from the excited state was evaluated using Eqs. (**7.4**) and (**7.5**). k values (**Table 7.1**) for the conjugates is larger than the Pcs alone, the opposite is true for **4c** as observed for B_{eff} values above.

The third-order susceptibility ($Im[X^3]$) measures the speed of the response of an optical material to the perturbation initiated by an intense laser beam **[257]** and can be determined using Eq. (**7.6**). The $Im[X^3]$ values for DNDs nanoconjugated systems of 2.04×10^{-8}, 2.13×10^{-8} and 2.91×10^{-8} esu for DNDs-**4a**, DNDs-**4b** and DNDs-**4c**, respectively, **Table 7.1**. DNDs on their own perform the worst, **Table 7.1**. When exposed to light, the permanent dipole of the molecule interacts with light to cause a bias in the average orientation of the molecule, resulting in induced hyperpolarizability (γ). Nonlinear optical properties of a material are directly dependent on the γ value (determined using Eq. (**7.7**)). The values of $Im[X^3]$ and γ for DNDs-**4a** and DNDs-**4b** in **Table 7.1** showed improvement when compared to Pcs alone. For DNDs-**4c**, there is a decrease in $Im[X^3]$ and γ compared to the Pc alone due to aggregation at 30 μJ. However, at low laser energy of 24 μJ shown in **Figure 7.4**, higher difference of the NLO response between the DND-**4c** and **4c** was observed. Previous studies report on a complex dependence on simultaneous action of electronic and secondary vibrational nonlinearities at high intensities **[258]**. Of note however is that at 30 μJ DNDs-**4c** and **4c** have the highest B_{eff}, $Im[X^3]$ and γ in **Table 7.1** compared to the rest of the corresponding conjugates and Pcs despite the aggregated nature of DNDs-**4c**.

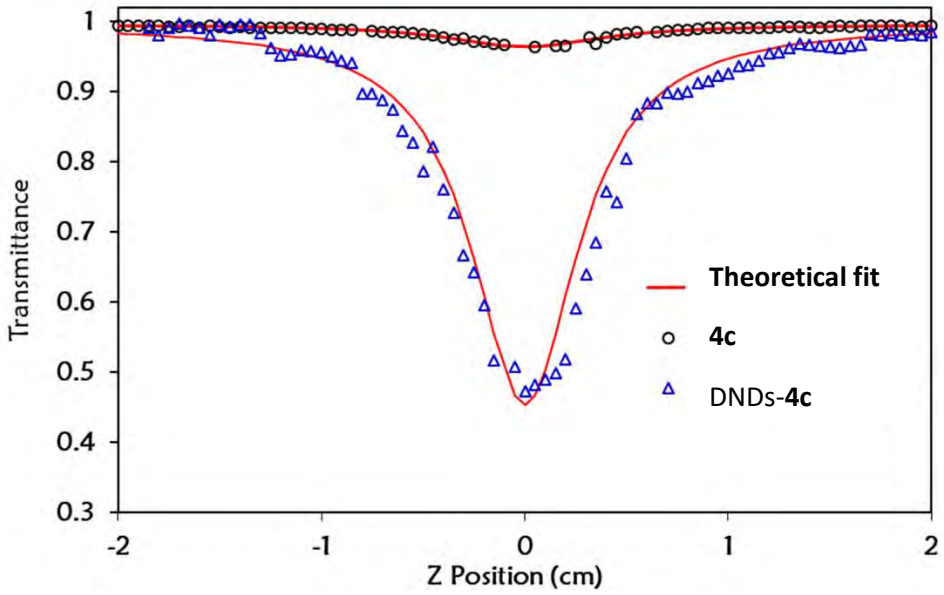

Figure 7.4: Open aperture Z-scan signature of **4c** and DNDs-**4c** at A=1 and energy of 24 µJ.

The γ in this work lie in the range 10^{-28} esu which are much higher than the reported 10^{-29} esu reported for ZnPc derivative on pristine GQDs **[99]**, **Table 7.2**, again showing the superiority of DNDs in improving the NLO behaviour of Pcs. The γ values in this work are in the range of those obtained for doped GQDs **[99]**, **Table 7.2 [99, 254, 259]**.

A good optical limiting (OL) material displays reduced transmittance with increasing incident fluence. This type of device has a linear transmittance at low incident fluence, but abruptly changes at higher incident fluence or there is a threshold at which the output fluence becomes a constant value that should be less than the amount required to damage the optical element **[260]**. This critical point is called the threshold limit intensity or fluence, (I_{lim}) **[261]** which is a very important parameter in optical limiting measurements. The I_{lim} value may be

defined as the input fluence at which the transmittance is 50% of the linear transmittance. While there is currently no defined optimal range for I_{lim} values, it is generally accepted that good nonlinear optical material performs better at a low value of I_{lim}, as this means that the limiting would occur at a lower intensity, allowing for more cautious protection of sensors.

Table 7.2: Comparison of synthesised Pc nanoconjugate systems with the best reported Pc-carbon composites

Sample[a]	**I_{lim} (Jcm^{-2})**	**γ(esu)**	**Reference**
DNDs-**4a** (π - π)	-	1.89×10^{-28}	**This work**
DNDs-**4b** (π - π)	-	2.62×10^{-28}	**This work**
DNDs-**4c** (ester)	0.47	3.88×10^{-28}	**This work**
ZnPc-GQDs	0.61	7.01×10^{-29}	**[99]**
ZnPc-NGQDs	0.58	3.34×10^{-28}	**[99]**
ZnPc-SNGQDs	0.55	5.03×10^{-28}	
CuPc-C_{60}	>200		**[259]**
InPcCl-SWCNT	0.21	5.78×10^{-27}	**[254]**

[a]GQDs = graphene quantum dots, SNGQDs = sulphur/nitrogen doped GQDs
SWCNT= single walled carbon nanotubes.

The values of I_{lim} can be experimentally determined using the plots of transmittance against input fluence **(Figure 7.5 (A–C))**. The I_{lim} values for **4a**, **4b** and their respective nanoconjugates could not be determined since the transmittance did not drop below 50% of the linear transmittance **(Figure 7.5 A and B)**. DNDs-**4c** in **Figure 7.5 C** showed a larger I_{lim} value of 0.47 when compared to **4c** alone (0.39), **Table 7.1** at 30 μJ. The lack of drop below 50% of the linear transmittance for **4a**, **4b** and their respective nanoconjugates could be due to non-covalent interaction of two different molecules with phase separation problems associated with mixtures such as DNDs-**4a** and DNDs-**4b**. However, covalently linked material function as combined molecules because the working dynamic range is extended through the covalent linkage between Pc and DNDs.

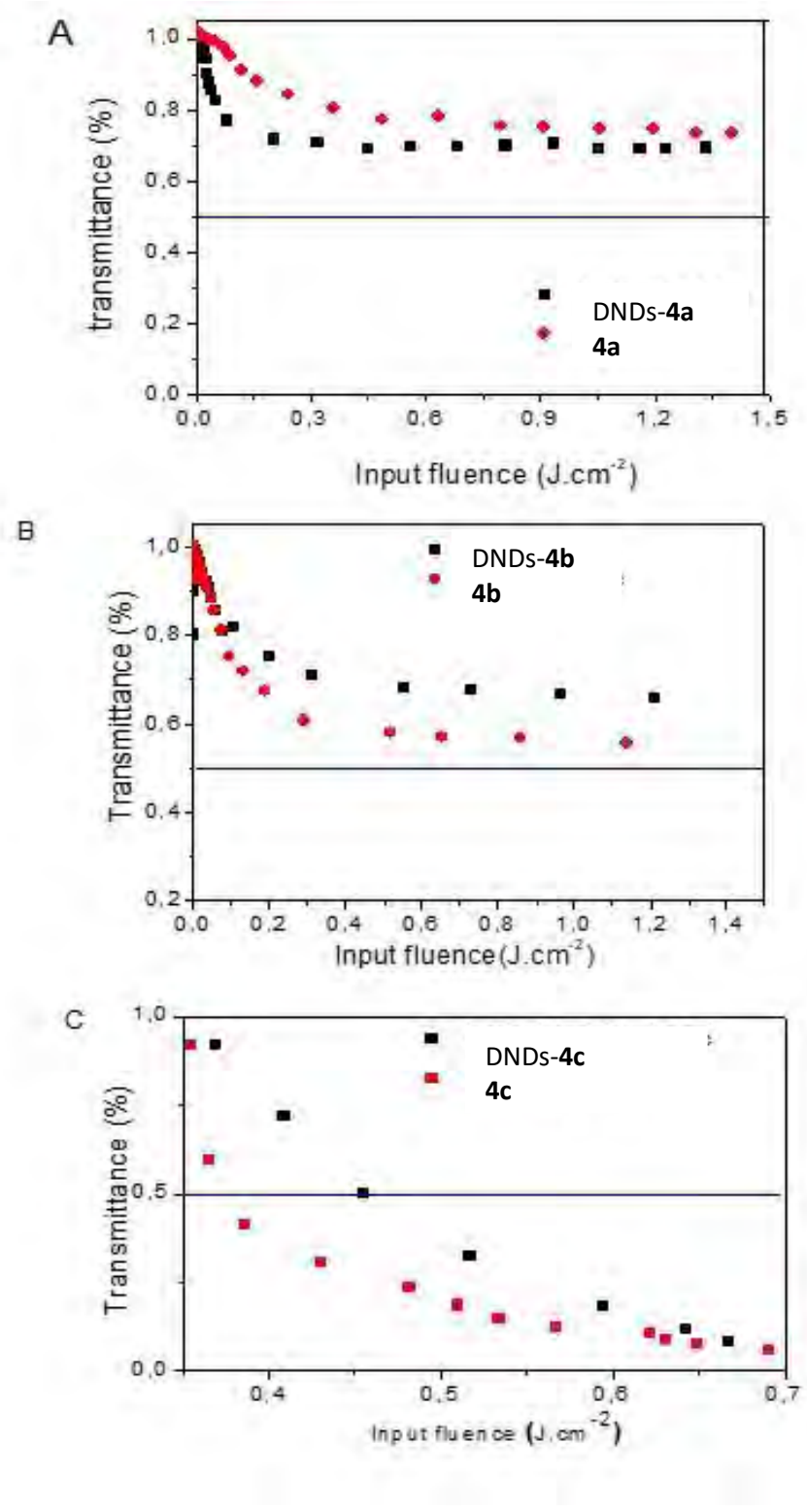

Figure 7.5: Input fluence (I_0) versus transmittance curves of (A) **4a**, DNDs-**4a**; (B) **4b**, DNDs-**4b** and (C) **4c**, DNDs-**4c** nanoconjugate systems in DMSO solvent.

Broadband optical limiting materials are obtained from a combination of individual molecules that possess optical limiting behaviour when linked covalently **[99, 261, 262]**. Such material results in broadened optical limiting band, extended working range and extensively reduced limiting thresholds, that translate to better optical limiting properties. Similar broad band optical limiting materials with phase stability have been previously reported when CuPc was covalently linked to C_{60} and resulted in $I_{lim} > 200$ J/cm^2 **[259]** (**Table 7.2**). This I_{lim} value is much larger than reported in this work showing the importance of DNDs when compared to C_{60}. Physical and photophysical properties of a material system, such as: absorption band, particle size, and aggregation state have been reported to strongly influence optical limiting performance **[263]**.

7.1.2. Substituent effect

Nonlinear absorption behaviour of SiPcs with different substituents (complexes **4c**, **5** and **6**) and respective nanoconjugates were investigated using an open aperture z-scan technique at 532 nm with an excitation pulse of 7 ns at different input energies (20, 30, 60 and 80 μJ) and absorbances (0.1, 0.2, 0.3 and 0.4). Lower absorbances are employed in this section since **4c** behaves better. All measurements reveal nonlinear absorption (NLA) behaviour with reverse saturable absorption (RSA) profiles (appendix (**Figures 4A-10A**). The transmittance values vary with sample absorbance and the input energy. A higher reduction in transmittance shown by an enhanced dip in RSA profile was observed when SiPcs were in the presence of DNDs than when SiPcs were alone, suggesting that the nanoconjugated systems could be potential optical limiting materials. Under optimal conditions, nanoconjugates (DNDs–**4c**, DNDs–**5** and DNDs–**6**), showed a dip in transmittance at 43, 68 and 14%, respectively. Respective SiPcs alone (**4c**, **5** and **6**) showed a dip at (49, 89 and 83)% (**Figure 7.6 (a)-(c)**).

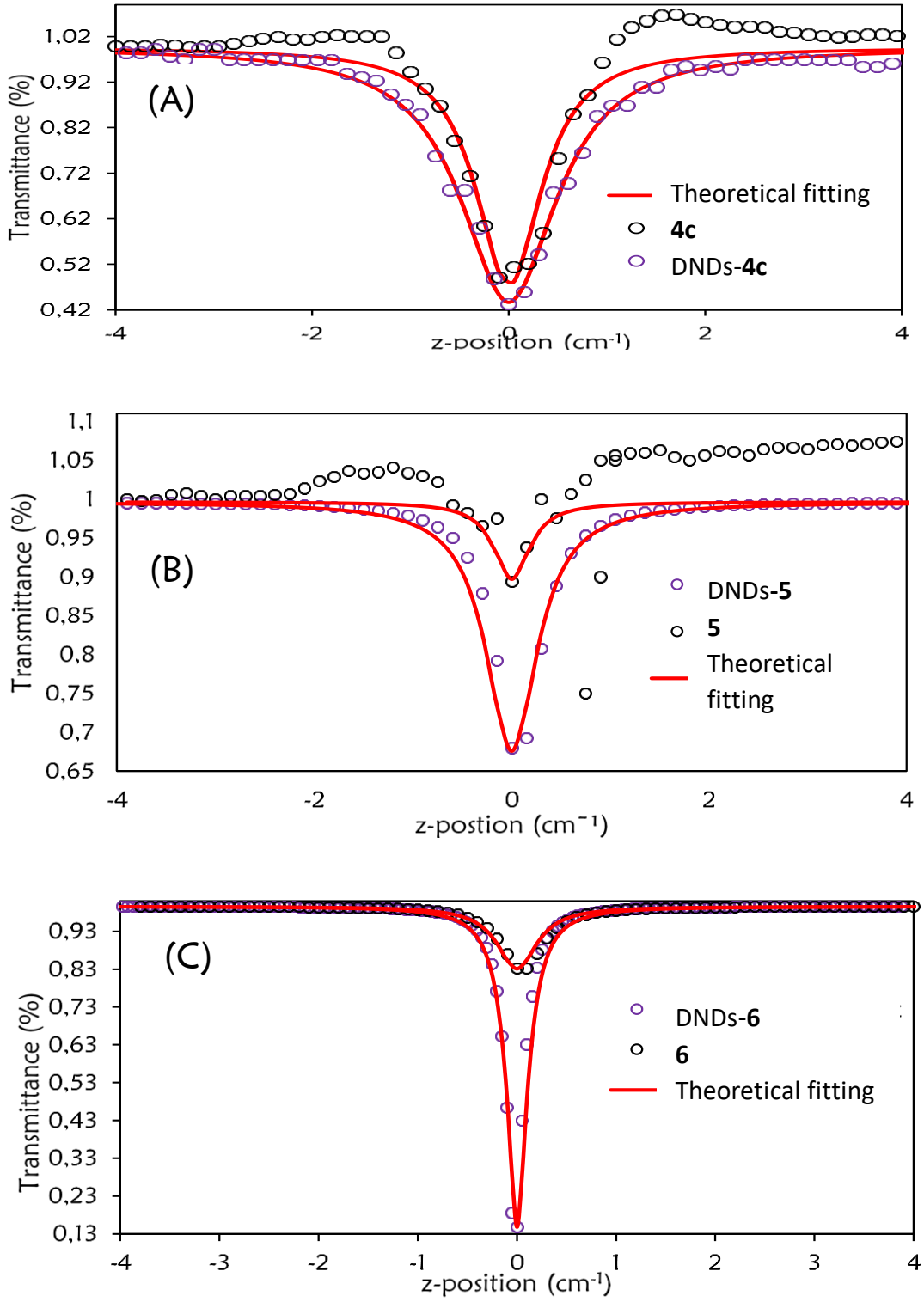

Figure 7.6: Open aperture Z-scan signatures of SiPcs: (A) **4c**, (B) **5** and (C) **6**, respective conjugates at absorbance of 0.1 and energy of 80 µJ and respective fittings in DMSO.

Table 7.3 shows that B_{eff} values increased for the nanohybrid conjugates compared to Pcs alone. The π-network from DNDs combined with SiPcs showed better characteristics relative to individual SiPcs, maybe due to the good NLO of DNDs alone. Nonlinear absorption properties of DND-H and the DND-NH_2 systems have been previously reported to be due to their negative electron affinity (NEA) character, associated with H and N electron donor ability, alternating the band gap to adequate surface dipoles **[264]**. Electron donating groups on the periphery of Pcs have the ability to improve OL effect through an increase in transition dipole moment between the excited states involved in the electronic transition **[33]**. Hence, **4c** and **6** show better NLO behaviour when compared to unsubstituted complex **5**.

Table 7.3: Nonlinear optical properties of DNDs, **4c**, **5**, **6** and respective nanoconjugates with DNDs in DMSO at absorbances and energy of 0.1 and 80 μJ, respectively.

Sample	α_0 (cm^{-1})	**B_{eff} (cm GW^{-1})**	**$I_m[X^3]$ x10^{-8} (esu)**	**γ x10^{-27} (esu)**	**k** $(\frac{\delta_{exc}}{\delta_o})$	**I_{lim} (Jcm^{-2})**
DNDs	0.046	239	5.57	28.5	-	-
4c	0.063	19.99	2.46	1.26	150	0.13
DNDs-**4c**	0.544	30.53	5.19	2.66	177	0.09
5	0.001	4.12	0.005	0.002	1.1	-
DNDs-**5**	0.912	9.77	0.96	0.49	55	-
6	0.010	16.5	2.28	1.17	55	-
DNDs-**6**	0.659	20.50	3.85	1.97	231	0.01

A plot of input energy versus β_{eff} generally showed decreasing β_{eff} as input energy increases, **Figure 7.7A**, for nanoconjugates. Decreases in β_{eff} as input energy increases indicate sequential two photon absorption (2PA) **[265-267]**. In **Figure 7.7B**, it is evident that increasing absorbance of nanoconjugates results in an increase in the B_{eff} of optical limiting materials (see also in appendix **(Figures 11A (a)-(e)),** suggesting that the β_{eff} depends strongly on the number of statistically available 2PA absorbers. Similar linear trends for concentration/absorbance and B_{eff} have been previously reported when Leishman dye **[268]**, and when phthalocyanine dye were separately conjugated to CdSe/ZnS quatum dots **[254]** as optical limiting materials.

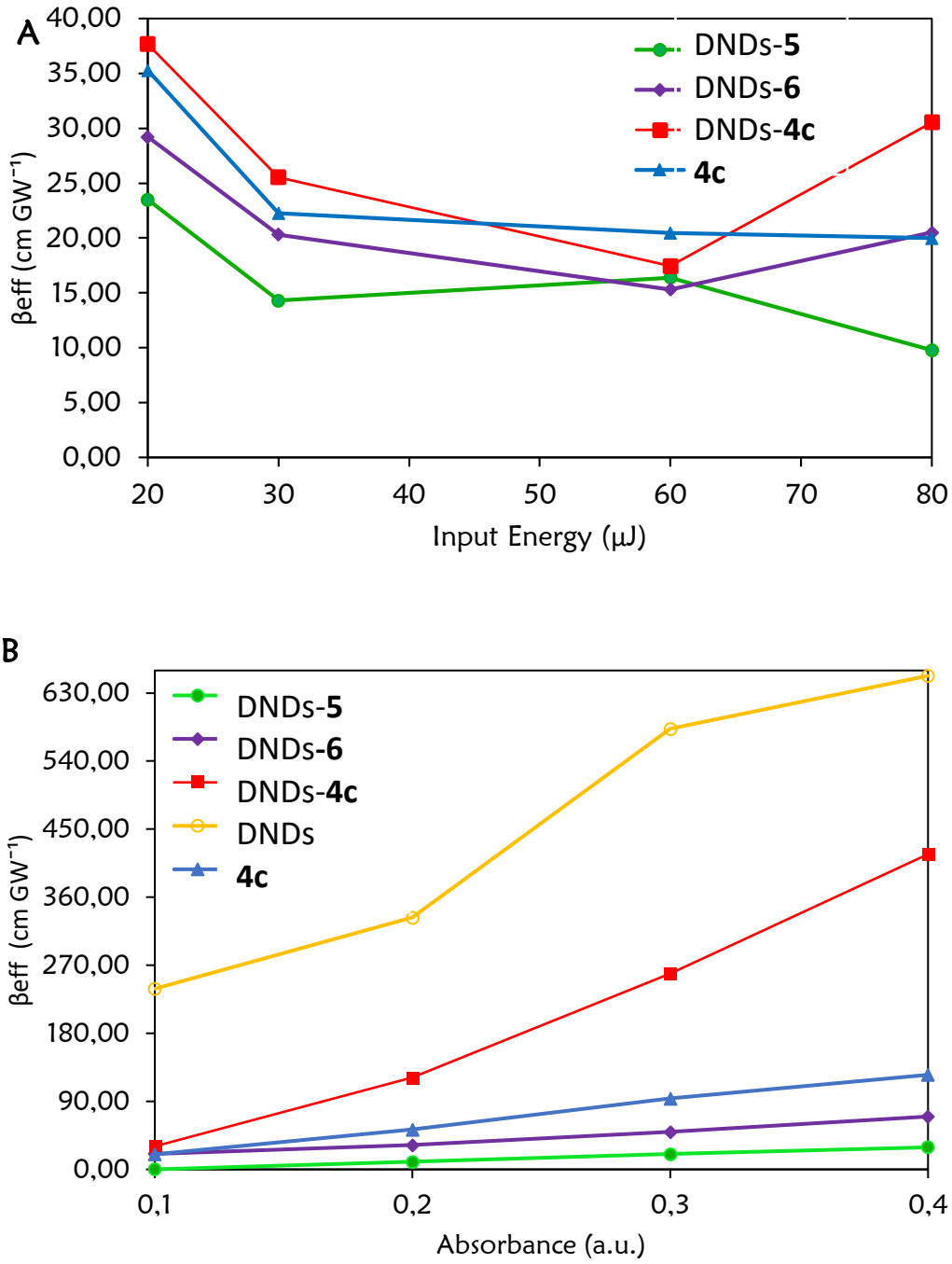

Figure 7.7: Plots showing (A) input energy (20, 30, 60,80) μJ) and (B) absorbance (0.2, 0.2, 0.3 and 0.4) vs β_{eff}. Each data point for each sample represents an independent Z-scan measurement.

Similar to section 7.1.1, k values shown in **Table 7.3** for the Pcs and conjugates indicate the existence of an excited state (δ_{exc}) with higher absorption cross-section than the ground state. Similarly, conjugates in this section have larger k values than the Pcs alone. α_0 values of investigated Pcs and respective conjugates show remarkable differences at the same absorbance of 0.1 in DMSO in appendix (**Figure 12A**). The average linear transmittances of **4c**, **5**, **6** and DNDs at energy and absorbance of 0.1 and 80 µJ is ≈ 93%. Conjugating respective SiPcs to DNDs resulted in a higher transmittance of ≈ 99% shown in appendix (**Figure 12A)**. Good optical limiting materials are generally known to have linear transmittance that exceed 40% **[269]**. Hence, SiPcs when conjugated to DNDs have better optical limiting properties. The Im[X^3] values for DNDs nanoconjugated systems of 5.19 x 10^{-8}, 0.96 x 10^{-8} and 3.85 x 10^{-8} esu for DNDs-**4c**, DNDs-**5** and DNDs-**6**, respectively, **Table 7.3**, and are an improvement compared to the corresponding Pcs alone. In this section, DNDs on their own perform the best, 5.57 x 10^{-8}. Note different values for DNDs alone and **4c (Table 7.1)** due to different energies and absorbance.

The γ in this section lie in the range 10^{-27} esu and are greatly enhanced when compared to section 7.1.1, **Table 7.3**, showing the importance of low absorbance values in **Table 7.3**. The values of γ for DNDs-**4c**, DNDs-**6** and DNDs-**5** in **Table 7.3** showed improvement when compared to SiPcs alone as is the case with $\mathbf{I}_m[X^3]$. The values of I_{lim} are experimentally determined using the plots of transmittance against input fluence (**Figure 7.8(A-C).** I_{lim} values for **4c**, DNDs-**4c,** and DNDs-**6** were determined to be 0.13, 0.09 and 0.01 Jcm^{-2}, respectively. The transmittances for **5**, DNDs-**5** and **6** did not drop below 50%, hence there are no values in **Table 7.3**. DNDs-**4c** gave a lower I_{lim} value of 0.09 when compared to **4c** alone (0.13), **Table 7.3**. A better I_{lim} value of 0.01 was obtained for DNDs-**6**.

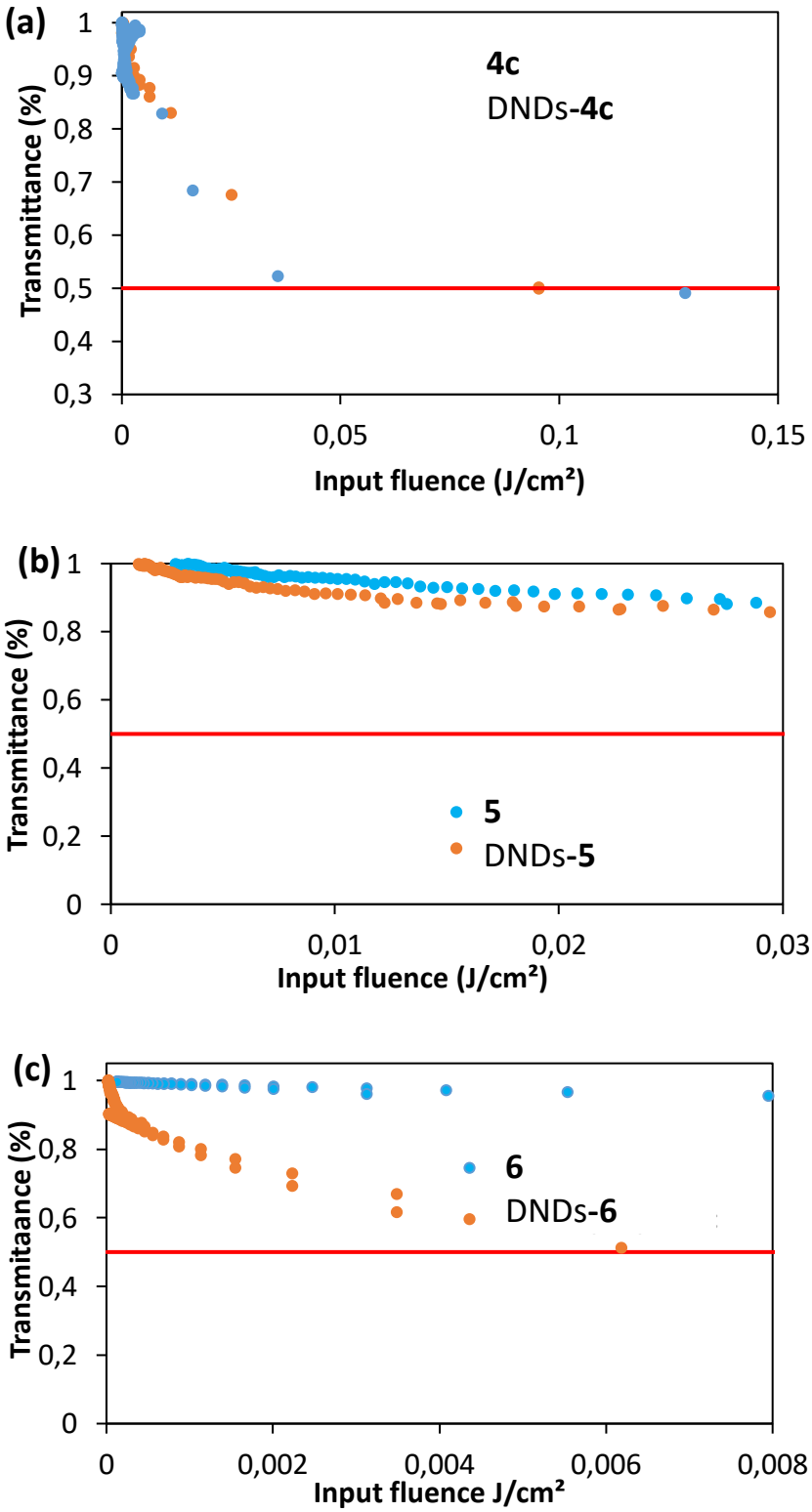

Figure 7.8: Plots of transmittance versus input fluence for (a) **4c**, (b) **5**, and (c) **6** and their conjugates in DMSO.

7.1.3. Mechanism

The most logical mechanism which explains observed RSA observed in phthalocyanines and conjugates when using the nanosecond laser is based on a five-level model, **Figure 7.9.** Irradiation at 532 nm excites molecules from S_0 to either S_1 or S_2 (the latter with excited state absorption cross-section δ_1). The S_2 state is short-lived, hence relaxation to S_1 almost occurs immediately. Since the triplet lifetime of the Pcs and conjugates are much longer than the intersystem crossing lifetime **[270]**, there will be more transfer of molecules from S_1 to the T_1. Subsequent absorption of laser radiation will result in further excitation of molecules in T_1 to T_2 with an excited absorption cross section of δ_2. Similar mechanism has been previously reported in phthalocyanines and carbon based nanomaterials alone and in a conjugate **[99, 144]**. The DNDs absorb at 532 nm, their contribution towards RSA is in the improvement of triplet quantum yields which in turn improves NLO behaviour **[271]**. The contribution of DNDs could also be due to nonlinear scattering as stated above **[250, 251]**. DNDs are also expected to contribute to NLO behaviour of Pcs due to the free-carrier absorption (FCA) mechanism **[254, 271, 272]**. FCA is usually produced when excitation takes place at the wavelengths where there is linear absorption.

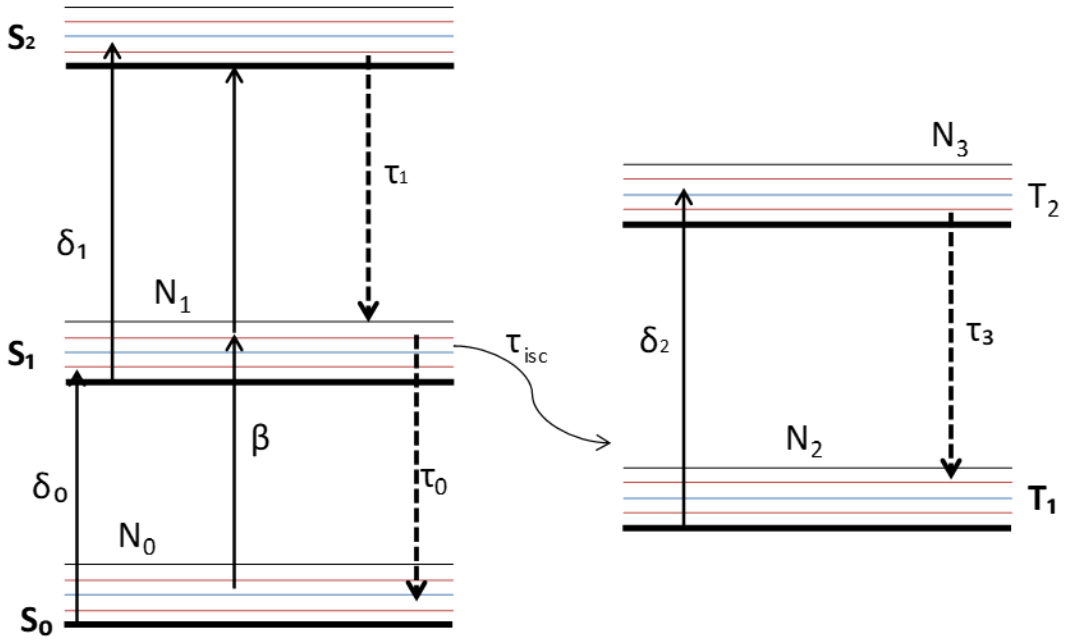

Figure 7.9: Five level energy diagram explaining the dynamics of the excited state population (upward arrows), non-radiative relaxation (dashed arrows) in the studied complexes.

7.2. Summary

All the DNDs-nanoconjugated systems and the corresponding Pcs followed reverse saturable absorption through two photon absorption mechanism at the excitation wavelength of 532 nm. Electron donating properties of DNDs and presence of a central metal with axial ligand for DNDs-**4c** and corresponding Pc showed improvement NLO properties when compared to conjugates of DNDs-**4a** and DNDs-**4b** and respective Pcs. Limiting threshold (I_{lim}) values for DNDs-**4a**, DNDs-**4b,** DNDs-**5** and DNDs-**6** were undeterminable because the input fluence at which the transmittance is 50% of the linear transmittance was < 50%. DNDs-**4c** conjugate showed enhanced NLO characteristics at absorbance of 1 relative to the other conjugates irrespective of its aggregation. The limiting threshold for DNDs-**4c** was shown to be 0.47 and 0.39 for **4c**. However, when NLO properties of DNDs-**4c** were investigated at low absorbance of 0.1, $I_{lim} \approx 0.01$ (**4c**) relative to 0.09 (DNDs-**4c**) were obtained. DNDs-**4c** conjugate showed better NLO characteristics than the Pc complex **4c** at low absorbances. A combination of central metal with axial ligands and bulky donating substituted Pc complexes have the ability to improve NLO characteristics of DNDs-Pc conjugated systems, particularly under dilute concentrations.

Chapter 8

Chapter 8

8. Conclusions and recommendations

This chapter summarizes the results obtained for the studies conducted and reported in this thesis and recommendations.

In this work, a successful synthesis and characterization of new symmetric and asymmetric cationic Pcs functionalized at the peripheral position is presented. The Pcs were characterised using FTIR, UV-Vis, ^{1}HNMR, MALDI-TOF mass spectroscopy and elemental analyses. The prepared Pcs were soluble in DMSO and exhibited monomeric behaviour in solution. These were further linked to DNDs through either π - π interaction or amide, or ester bond from heteroatom doped DNDs. FT–IR spectroscopy were used to confirm the successful formation of the amide, ester bond and was used to confirm the π - π interaction.

Central metal, substituents, charge and symmetry of Pcs alone, alterations of the type of carbon nanomaterial, size of GQDs and heteroatom doping of DNDs alone and in a conjugate of both Pc (or BODIPY) and nanoparticle with the intention to improve photochemical and photophysical behaviour of Pcs. Heavy atoms as metal centres, axial ligation, substituents with extra aromatic rings and asymmetry of Pcs were shown to sometimes promote intersystem crossing to result in high triplet and singlet oxygen quantum yields. In some instances, low triplet and singlet quantum yields were attributed to aggregation.

The presence of aromatic rings from carbon nanoparticles (GQDs, CDs and DNDs) enhanced the triplet and screening effect in most cases of Pcs and this was attributed to the π - π * transition of aromatic sp^2 domains of nanoparticles. The decrease in singlet oxygen quantum yields was attributed to the screening effect caused by DNDs which prevent the interaction of the excited triplet state of the nanoconjugates and the ground state molecular oxygen. The nanoparticle type, size and heteroatom doping was also shown to influence the

photochemical and photophysical behaviour of Pcs studied. Combination of graphitic nature, functional groups, degree of surface oxidation and DNDs nanomaterials doping afforded high loading of Pcs due to increased activation site. Hence physicochemical characteristics of nanoconjugated systems: DNDs-Pc nanoconjugated systems afforded high singlet oxygen quantum yields than GQDs-Pc and CDs-Pc nanohybrids. However, heteroatom doped DNDs-Pc nanohybrids showed even better singlet oxygen quantum yields due to molecular instability (chemical reactivity) associated with strain that is relatively reduced upon linking Pcs to DNDs.

Furthermore, *in vitro* dark cytotoxicity and photodynamic therapy of complexes **3, 7, 8, 9, 10, 11,** GQDs-**3,** CDs-**3,** DNDs-**3** and heteroatom doped DNDs-**10,** and B@DNDs-**9, 10 and 11** against MCF-7 cells were tested. Not all Pc complexes alone and respective nanoconjugated system showed minimum dark toxicity. All Pc complexes displayed poor phototoxicity with > 22% cell viability at concentrations ≤ 50 µg/mL, however the conjugates showed < 22% cell viability at concentrations ≤ 50 µg/mL probably due to aromatic rings in the NPs. Although a decrease in singlet oxygen yield of the Pc was observed in the presence of some heteroatom doped DNDs-Pc conjugates, there was improvement in PDT activity. Thus, the mechanism may not only involve singlet oxygen. The Pc can serve as antenna that harvest energy from the photons during irradiation and transfer this energy to nano-diamonds resulting in some photothermal effect. Higher PDT activities in B and P@DNDs-**10** is due to molecular instability (chemical reactivity) associated with strain that is relatively reduced upon linking Pcs to DNDs with relatively small HOMO-LUMO energy gaps in respective DNDs.

Nonlinear optical characteristics on central metal and substituent of complexes and DNDs alone relative to respective nanoconjugated systems depend on absorbance, input energy, percentage loading, central metal, substituent of Pc and nature of interaction (covalent, noncovalent) in nanohybrids. All materials followed reverse saturable absorption through two photon absorption mechanism at the excitation wavelength of 532 nm. DNDs-SiPc at high concentrations/absorbances aggregate, resulting in reduced excited state lifetime and B_{eff}.

However, at low concentration, a direct relationship between absorbance and B_{eff} of DNDs nanoconjugated systems result in increased optical limiting characteristics of materials.

The electron donating nature of Pc and DNDs has a great influence on the electron distribution of broadband optical limiting materials.

Further studies in improving selectivity of doped DNDs-Pc hybrids for application in PDT needs to follow in order to overcome the current challenge associated with selectivity of phthalocyanines.

References

[1] R. Bonnett In, Chemical Aspects of Photodynamic Therapy, Gordon and Breach Science Publishers, Amsterdam, 2000.

[2] C.M. Allen, W.M. Sharman, J.E. Van Lier, Current Status of Phthalocyanines in the Photodynamic Therapy of Cancer, J. Porphyr. Phthalocyanines, 5 (2001) 161-169.

[3] E.T. Saka, M. Durmuş, H. Kantekin, Solvent and Central Metal Effects on the Photophysical and Photochemical Properties of 4-Benzyloxybenzoxy Substituted Phthalocyanines, J. Organomet. Chem., 696 (2011) 913-924.

[4] T. Nyokong, Effects of Substituents on the Photochemical and Photophysical Properties of Main Group Metal Phthalocyanines, Coord. Chem. Rev., 251 (2007) 1707-1722.

[5] I. Scalise, E.N. Durantini, Synthesis, Properties, and Photodynamic Inactivation of Escherichia Coli Using a Cationic and a Noncharged Zn (II) Pyridyloxyphthalocyanine Derivatives, Bioorg. Med. Chem., 13 (2005) 3037-3045.

[6] R.D. George, A.W. Snow, J.S. Shirk, W. Barger, The Alpha Substitution Effect on Phthalocyanine Aggregation, J. Porphyr. Phthalocyanines, 2 (1998) 110-117.

[7] V.N. Nemykin, E.A. Lukyanets, Synthesis of Substituted Phthalocyanines, Arkivoc, i (2010) 136-208.

[8] A.B. Sorokin, Phthalocyanine Metal Complexes in Catalysis, Chem. Rev., 113 (2013) 8152-8191.

[9] J. Mack, N. Kobayashi, Low Symmetry Phthalocyanines and their Analogues, Chem. Rev., 111 (2011) 281-321.

[10] G. De La Torre, M. Nicolau, T. Torres, Phthalocyanines: Synthesis, Supramolecular Organization, and Physical Properties, Chem. Commun., 20 (2007) 2000-2015.

[11] K.A. Bello, I. Bello, Some Observations on the Visible Absorption Spectra and Stability Properties of the Silicon Phthalocyanine System, Dyes Pigm., 35 (1997) 261-267.

[12] M.K. Lowery, A.J. Starshak, J.N. Esposito, P.C. Krueger, M.E. Kenney, Dichloro (phthalocyanino) Silicon, Inorg. Chem., 4 (1965) 128-128.

[13] H. Tomoda, S. Saito, S. Ogawa, S. Shiraishi, Synthesis of Phthalocyanines from Phthalonitrile with Organic Strong Bases, Chem. Lett., 9 (1980) 1277-1280.

[14] M. Gouterman In, Optical Spectra and Electronic Structure of Porphyrins and Related Rings, The porphyrins, Academic Press, New York, 1978, pp. 17 - 22.

[15] L. Edwards, M. Gouterman, Porphyrins: XV. Vapor Absorption Spectra and Stability: Phthalocyanines, J. Mol. Spectrosc., 33 (1970) 292-310.

[16] T. Fukuda, K. Ono, S. Homma, N. Kobayashi, A Phthalocyanine Producing Green, Ocher, and Red Colors Depending on the Central Metals, Chem. Lett., 32 (2003) 736-737.

[17] T. Nyokong, E. Antunes, In: (K.M. Kadish, K. Smith, R. Guilard, (Eds.)), The Handbook of Porphyrin Science, World Scientific Press, Academic Press, New York, 2010, 7 (Chapter 34), pp. 247–349.

[18] N. Kobayashi, H. Ogata, N. Nonaka, E.A. Luk'yanets, Effect of Peripheral Substitution on the Electronic Absorption and Fluorescence Spectra of Metal-Free and Zinc Phthalocyanines, Chem. Eur. J., 9 (2003) 5123-5134.

[19] M.J. Stillman, T. Nyokong, In: (C.C. Leznoff, A.B.P. Lever, (Eds.)), Phthalocyanines, Properties and Application, VCH Publishers, New York, 1989, pp. 133-289.

[20] T. Nyokong, Z. Gasyna, M.J. Stillman, Analysis of the Absorption and Magnetic Circular Dichroism Spectra of Zinc Phthalocyanine and the. pi.-cation-radical Species [ZnPc (1-)]. cntdot.+, Inorg. Chem., 26 (1987) 1087-1095.

[21] N. Kobayashi, H. Konami, In: (C.C. Leznoff, A.B.P. Lever (Eds.)), Phthalocyanines, Properties and Applications, New York, 1996, pp. 343–404.

[22] A. Günsel, A.T. Bilgiçli, M. Kandaz, E.B. Orman, A.R. Özkaya, Ag (I) and Pd (II) Sensing, H- or J-Aggregation and Redox Properties of Metal-Free, Manganase (III) and Gallium (III) Phthalocyanines, Dyes Pigm., 102 (2014) 169-179.

[23] T. Nyokong, The Nature of the Oxidation Products of Dicyanoruthenium Phthalocyanine in Aqueous and Non-Aqueous Solvents, Polyhedron, 12 (1993) 375-381.

[24] A. Tedesco, F. Primo, M. Beltrame, Phthalocyanines: Synthesis, Characterization and Biological Applications of Photodynamic Therapy (PDT), Nanobiotechnology, Magnetohyperthermia and Photodiagnosis (Theranostics), Reference Module in Materials Science and Materials Engineering, Elsevier, 2016, pp. (6 pages) 7332968693.

[25] F. Dumoulin, M. Durmuş, V. Ahsen, T. Nyokong, Synthetic Pathways to Water-Soluble Phthalocyanines and Close Analogs, Coord. Chem. Rev., 254 (2010) 2792-2847.

[26] J.H. Weber, D.H. Busch, Complexes Derived from Strong Field Ligands. XIX. Magnetic Properties of Transition Metal Derivatives of 4, 4', 4", 4'''-Tetrasulfophthalocyanine, Inorg. Chem., 4 (1965) 469-471.

[27] N.A. Kuznetsova, N.S. Gretsova, V.M. Derkacheva, O.L. Kaliya, E.A. Lukyanets, Sulfonated Phthalocyanines: Aggregation and Singlet Oxygen Quantum Yield in Aqueous Solutions, J. Porphyr. Phthalocyanines, 7 (2003) 147-154.

[28] H. Ali, R. Langlois, J.R. Wagner, N. Brasseur, B. Paquette, J.E. Van lier, Biological Activities of Phthalocyanines-X. Syntheses and Analyses of Sulfonated Phthalocyanines, Photochem. Photobiol., 47 (1988) 713-717.

[29] A. Ogunsipe, J.-Y. Chen, T. Nyokong, Photophysical and Photochemical Studies of Zinc (II) Phthalocyanine Derivatives—Effects of Substituents and Solvents, New J. Chem., 28 (2004) 822-827.

[30] S. Moeno, R. Krause, E. Ermilov, W. Kuzyniak, M. Höpfner, Synthesis and Characterization of Novel Zinc Phthalocyanines as Potential Photosensitizers for Photodynamic Therapy of Cancers, Photochem. Photobio. Sci., 13 (2014) 963-970.

[31] T.T. Tasso, Y. Yamasaki, T. Furuyama, N. Kobayashi, An Exemplary Relationship Between the Extent of Cofacial Aggregation and Fluorescence Quantum Yield as Exhibited by Quaternized Amphiphilic Phthalocyanines, Dalton Trans., 43 (2014) 5886-5892.

[32] A.-A. Soreacu, R.-M. Ion, A. Nuta, Spectral and Photodynamic Properties of a Silicon (Tert-Butil) Phthalocyanine, Mater. Phys. Mech., 12 (2014) 29-33.

[33] N. Nwaji, O.M. Bankole, J. Britton, T. Nyokong, Photophysical and Nonlinear Optical Study of Benzothiazole Substituted Phthalocyanines in Solution and Thin Films, J. Porphyr. Phthalocyanines, 21 (2017) 263-272.

[34] N. Nwaji, B. Jones, J. Mack, D.O. Oluwole, T. Nyokong, Nonlinear Optical Dynamics of Benzothiazole Derivatized Phthalocyanines in Solution, Thin Films and when Conjugated to Nanoparticles, J. Photochem. Photobiol. A, 346 (2017) 46-59.

[35] A. Siejak, D. Wróbel, P. Siejak, B. Olejarz, R. Ion, Spectroscopic and Photoelectric Investigations of Resonance Effects in Selected Sulfonated Phthalocyanines, Dyes Pigm., 83 (2009) 281-290.

[36] V. Mantareva, I. Angelov, V. Kussovski, R. Dimitrov, L. Lapok, D. Wöhrle, Photodynamic Efficacy of Water-soluble Si (IV) and Ge (IV) Phthalocyanines Towards Candida Albicans Planktonic and Biofilm Cultures, Eur. J. Med. Chem., 46 (2011) 4430-4440.

[37] K. Sanusi, E. Antunes, T. Nyokong, Optical Nonlinearities in Non-peripherally Substituted Pyridyloxy Phthalocyanines: A Combined Effect of Symmetry, Ring-Strain and Demetallation, Dalton Trans., 43 (2014) 999-1010.

[38] A. Kamkaew, S.H. Lim, H.B. Lee, L.V. Kiew, L.Y. Chung, K. Burgess, BODIPY Dyes in Photodynamic Therapy, Chem. Soc. Rev., 42 (2013) 77-88.

[39] B.M. Squeo, M. Pasini, BODIPY Platform: a Tunable Tool for Green to NIR OLEDs, Supramol. Chem., 32 (2020) 56-70.

[40] B. Matarranz, A. Sampedro, C. G Daniliuc, G. Fernández, Self-Assembly of a Carboxyl-Functionalized BODIPY Dye via Hydrogen Bonding, Crystals, 8 (2018) 436-446.

[41] A. Loudet, K. Burgess, BODIPY Dyes and their Derivatives: Syntheses and Spectroscopic Properties, Chem. Rev., 107 (2007) 4891-4932.

[42] A. Schmitt, B. Hinkeldey, M. Wild, G. Jung, Synthesis of the Core Compound of the BODIPY Dye Class: 4, 4'-Difluoro-4-bora-(3a, 4a)-Diaza-s-Indacene, J. Fluoresc., 19 (2009) 755-758.

[43] A. Turksoy, D. Yildiz, E.U. Akkaya, Photosensitization and Controlled Photosensitization with BODIPY Dyes, Coord. Chem. Rev., 379 (2019) 47-64.

[44] C.S. Kue, S.Y. Ng, S.H. Voon, A. Kamkaew, L.Y. Chung, L.V. Kiew, H.B. Lee, Recent Strategies to Improve Boron Dipyrromethene (BODIPY) for Photodynamic Cancer Therapy: An Updated Review, Photochem. Photobiol. Sci., 17 (2018) 1691-1708.

[45] S. Kusaka, R. Sakamoto, Y. Kitagawa, M. Okumura, H. Nishihara, Meso-Alkynyl BODIPYs: Structure, Photoproperties, Pi-Extension, and Manipulation of Frontier Orbitals, Chem.: Asian J., 8 (2013) 723-727.

[46] B.P. Ngoy, N. Molupe, J. Harris, G. Fomo, J. Mack, T. Nyokong, Photophysical Studies of 2, 6-Dibrominated BODIPY Dyes Substituted with 4-Benzyloxystyryl Substituents, J. Porphyr. Phthalocyanines, 21 (2017) 431-438.

[47] H. Lu, J. Mack, Y. Yang, Z. Shen, Structural Modification Strategies for the Rational Design of Red/NIR Region BODIPYs, Chem. Soc. Rev., 43 (2014) 4778-4823.

[48] N. Nwahara, R. Nkhahle, B.P. Ngoy, J. Mack, T. Nyokong, Synthesis and Photophysical Properties of BODIPY-Decorated Graphene Quantum Dot–Phthalocyanine Conjugates, New J. Chem., 42 (2018) 6051-6061.

[49] S. Osati, H. Ali, J.E. van Lier, Synthesis and Spectral Properties of Phthalocyanine–BODIPY Conjugates, Tetrahedron Lett., 56 (2015) 2049-2053.

[50] H. Yanık, M. Göksel, S. Yeşilot, M. Durmuş, Novel Phthalocyanine–BODIPY Conjugates and their Photophysical and Photochemical Properties, Tetrahedron Lett., 57 (2016) 2922-2926.

[51] C. Göl, M. Malkoç, S. Yeşilot, M. Durmuş, Novel zinc (II) Phthalocyanine Conjugates Bearing Different Numbers of BODIPY and Iodine Groups as Substituents on the Periphery, Dyes Pigm., 111 (2014) 81-90.

[52] Y. Chen, L. Wan, D. Zhang, Y. Bian, J. Jiang, Modulation of the Spectroscopic Property of Bodipy derivates Through Tuning the Molecular Configuration, Photochem. Photobiol. Sci., 10 (2011) 1030-1038.

[53] Y. Rio, W. Seitz, A. Gouloumis, P. Vázquez, J.L. Sessler, D.M. Guldi, T. Torres, A Panchromatic Supramolecular Fullerene-Based Donor–Acceptor Assembly Derived from a Peripherally Substituted Bodipy–Zinc Phthalocyanine Dyad, Chem. Eur. J., 16 (2010) 1929-1940.

[54] B.P. Ngoy, Z. Hlatshwayo, N. Nwaji, G. Fomo, J. Mack, T. Nyokong, Photophysical and Optical Limiting Properties at 532 nm of BODIPY Dyes with p-Benzyloxystyryl Groups at the 3, 5-Positions, J. Porphyr. Phthalocyanines, 22 (2018) 413-422.

[55] M.S. Mauter, M. Elimelech, Environmental Applications of Carbon-Based Nanomaterials, Environ. Sci. Technol., 42 (2008) 5843-5859.

[56] P. Karthik, A. Himaja, S.P. Singh, Carbon-Allotropes: Synthesis Methods, Applications and Future Perspectives, Carbon Lett., 15 (2014) 219-237.

[57] V. Georgakilas, J.A. Perman, J. Tucek, R. Zboril, Broad Family of Carbon Nanoallotropes: Classification, Chemistry, and Applications of Fullerenes, Carbon Dots, Nanotubes, Graphene, Nanodiamonds, and Combined Superstructures, Chem. Rev., 115 (2015) 4744-4822.

[58] Y. Liu, H. Huang, W. Cao, B. Mao, Y. Liu, Z. Kang, Advances in Carbon Dots: from the Perspective of Traditional Quantum Dots, Mater. Chem. Front., (2020) 1586-1613.

[59] A.S. Barnard, S.P. Russo, I.K. Snook, First-Principles Modeling of Dopants in C_{29} and $C_{29}H_{24}$ Nanodiamonds, J. Phys. Chem., 109 (2005) 11991-11995.

[60] O.J. Achadu, T. Nyokong, Interaction of Graphene Quantum Dots with 4-Acetamido-2,2,6,6-Tetramethylpiperidine-Oxyl Free Radicals: A Spectroscopic and Fluorimetric Study, J. Fluoresc., 26 (2016) 283-295.

[61] Y. Li, Y. Zhao, H. Cheng, Y. Hu, G. Shi, L. Dai, L. Qu, Nitrogen-Doped Graphene Quantum Dots with Oxygen-Rich Functional Groups, J. Am. Chem. Soc., 134 (2012) 15-18.

[62] N.G. Sahoo, H. Bao, Y. Pan, M. Pal, M. Kakran, H.K.F. Cheng, L. Li, L.P. Tan, Functionalized Carbon Nanomaterials as Nanocarriers for Loading and Delivery of a Poorly Water-Soluble Anticancer Drug: A Comparative Study, Chem. Commun., 47 (2011) 5235-5237.

[63] L. Yan, F. Zhao, S. Li, Z. Hu, Y. Zhao, LowToxic and Safe Nanomaterials by Surface-Chemical Design, Carbon Nanotubes, Fullerenes, Metallofullerenes, and Graphenes, Nanoscale, 3 (2011) 362-382.

[64] S. Zhu, Y. Song, X. Zhao, J. Shao, J. Zhang, B. Yang, The Photoluminescence Mechanism in Carbon Dots (Graphene Quantum Dots, Carbon Nanodots, and Polymer Dots): Current State and Future Perspective, Nano Res., 8 (2015) 355-381.

[65] H. Li, Z. Kang, Y. Liu, S.-T. Lee, Carbon Nanodots: Synthesis, Properties and Applications, J. Mater. Chem., 22 (2012) 24230-24253.

[66] T.J. Pillar-Little, N. Wanninayake, L. Nease, D.K. Heidary, E.C. Glazer, D.Y. Kim, Superior Photodynamic Effect of Carbon Quantum Dots Through Both Type I and Type II pathways: Detailed Comparison Study of Top-Down-Synthesized and Bottom-Up-Synthesized Carbon Quantum Dots, Carbon, 140 (2018) 616-623.

[67] H. Sun, L. Wu, W. Wei, X. Qu, Recent Advances in Graphene Quantum Dots for Sensing, Mater. Today, 16 (2013) 433-442.

[68] C. Desai, K. Chen, S. Mitra, Aggregation Behavior of Nanodiamonds and their Functionalized Analogs in an Aqueous Environment, Environ. Sci.: Process. Impacts, 16 (2014) 518-523.

[69] Y. Astuti, F.D. Saputra, S. Wuning, Arnelli, G. Bhaduri, Enrichment of Nanodiamond Surfaces with Carboxyl Groups for Doxorubicin Loading and Release, IOP Conf. Ser. Mater. Sci. Eng., 172 (2017) (8 pages) 012066.

[70] S. Osswald, G. Yushin, V. Mochalin, S.O. Kucheyev, Y. Gogotsi, Control of sp^2/sp^3 Carbon Ratio and Surface Chemistry of Nanodiamond Powders by Selective Oxidation in Air, J. Am. Chem. Soc., 128 (2006) 11635-11642.

[71] L. Lai, A.S. Barnard, Modeling the Thermostability of Surface Functionalisation by Oxygen, Hydroxyl, and Water on Nanodiamonds, Nanoscale, 3 (2011) 2566-2575.

[72] L. Lai, A.S. Barnard, Stability of Nanodiamond Surfaces Exposed to N, NH, and NH_2, J. Phys. Chem. C, 115 (2011) 6218-6228.

[73] L. Lai, A.S. Barnard, Surface Phase Diagram and Thermodynamic Stability of Functionalisation of Nanodiamonds, J. Mater. Chem., 22 (2012) 16774-16780.

[74] T. Enoki, K. Takai, V. Osipov, M. Baidakova, A. Vul, Nanographene and Nanodiamond; New Members in the Nanocarbon Family, Chem. Asian J., 4 (2009) 796-804.

[75] N. Brown, O. Hod, Controlling the Electronic Properties of Nanodiamonds Via Surface Chemical Functionalization: A DFT Study, J. Phys. Chem. C, 118 (2014) 5530-5537.

[76] A.S. Barnard, M. Sternberg, Substitutional Boron in Nanodiamond, Bucky-Diamond, and Nanocrystalline Diamond Grain Boundaries, J. Phys. Chem. B, 110 (2006) 19307-19314.

[77] A. Ambrosi, C.K. Chua, A. Bonanni, M. Pumera, Electrochemistry of Graphene and Related Materials, Chem. Rev., 114 (2014) 7150-7188.

[78] B. Luo, S. Liu, L. Zhi, Chemical Approaches Toward Graphene-Based Nanomaterials and their Applications in Energy-Related Areas, Small, 8 (2012) 630-646.

[79] J. Shen, Y. Zhu, X. Yang, C. Li, Graphene Quantum Dots: Emergent Nanolights for Bioimaging, Sensors, Catalysis and Photovoltaic Devices, Chem. Commun., 48 (2012) 3686-3699.

[80] A. Ananthanarayanan, X. Wang, P. Routh, B. Sana, S. Lim, D.H. Kim, K.H. Lim, J. Li, P. Chen, Facile Synthesis of Graphene Quantum Dots from 3D Graphene and their Application for Fe^{3+} Sensing, Adv. Funct. Mater., 24 (2014) 3021-3026.

[81] S. Chen, J.W. Liu, M.L. Chen, X.W. Chen, J.H. Wang, Unusual Emission Transformation of Graphene Quantum Dots Induced by Self-Assembled Aggregation, Chem. Commun., 48 (2012) 7637-7639.

[82] Y. Zhang, H. Gao, J. Niu, B. Liu, Facile Synthesis and Photoluminescence of Graphene Oxide Quantum Dots and their Reduction Products, New J. Chem., 38 (2014) 4970-4974.

[83] L.L. Li, J. Ji, R. Fei, C.Z. Wang, Q. Lu, J.R. Zhang, L.P. Jiang, J.J. Zhu, A Facile Microwave Avenue to Electrochemiluminescent Two-Color Graphene Quantum Dots, Adv. Funct. Mater., 22 (2012) 2971-2979.

[84] Y. Dong, H. Pang, S. Ren, C. Chen, Y. Chi, T. Yu, Etching Single-Wall Carbon Nanotubes Into Green and Yellow Single-Layer Graphene Quantum Dots, Carbon, 64 (2013) 245-251.

[85] D.B. Shinde, V.K. Pillai, Electrochemical Preparation of Luminescent Graphene Quantum Dots from Multiwalled Carbon Nanotubes, Chem. Eur. J., 18 (2012) 12522-12528.

[86] J. Peng, W. Gao, B.K. Gupta, Z. Liu, R. Romero-Aburto, L. Ge, L. Song, L.B. Alemany, X. Zhan, G. Gao, S.A. Vithayathil, B.A. Kaipparettu, A.A. Marti, T. Hayashi, J.J. Zhu, P.M. Ajayan, Graphene Quantum Dots Derived from Carbon Fibers, Nano Lett., 12 (2012) 844-849.

[87] R. Ye, C. Xiang, J. Lin, Z. Peng, K. Huang, Z. Yan, N.P. Cook, E.L. Samuel, C.-C. Hwang, G. Ruan, G. Ceriotti, A.-R.O. Raji, A.A. Martí, J.M. Tour, Coal as an Abundant Source of Graphene Quantum Dots, Nat. Commun., 4 (2013) (6 pages) 2943.

[88] Y. Dong, C. Chen, X. Zheng, L. Gao, Z. Cui, H. Yang, C. Guo, Y. Chi, C.M. Li, One-step and High Yield Simultaneous Preparation of Single-and Multi-layer Graphene Quantum Dots from CX-72 Carbon Black, J. Mater. Chem., 22 (2012) 8764-8766.

[89] J. Lee, K. Kim, W.I. Park, B.H. Kim, J.H. Park, T.H. Kim, S. Bong, C.H. Kim, G. Chae, M. Jun, Y. Hwang, Y.S. Jung, S. Jeon, Uniform Graphene Quantum Dots Patterned from Self-Assembled Silica Nanodots, Nano Lett., 12 (2012) 6078-6083.

[90] H. Xu, S. Zhou, L. Xiao, H. Wang, S. Li, Q. Yuan, Fabrication of a Nitrogen-Doped Graphene Quantum Dot from MOF-Derived Porous Carbon and its Application for Highly Selective Fluorescence Detection of Fe^{3+}, J. Mater. Chem. C, 3 (2015) 291-297.

[91] Q. Liu, B. Guo, Z. Rao, B. Zhang, J.R. Gong, StrongTwo-Photon-Induced Fluorescence from Photostable, Biocompatible Nitrogen-Doped Gaphene Quantum Dots for Cellular and Deep-Tissue Imaging, Nano Lett., 13 (2013) 2436-2441.

[92] H. Gao, C. Xue, G. Hu, K. Zhu, Production of Graphene Quantum Dots by Ultrasound-Assisted Exfoliation in Supercritical CO_2/H_2O Medium, Ultrason. Sonochem., 37 (2017) 120-127.

[93] P. Namdari, B. Negahdari, A. Eatemadi, Synthesis, Properties and Biomedical Applications of Carbon-Based Quantum Dots: An Updated Review, Biomed. Pharmacother., 87 (2017) 209-222.

[94] C. Charitidis, Nanomechanical and Nanotribological Properties of Carbon-based Thin Films: A Review, Int. J. Refract. Hard Met., 28 (2010) 51-70.

[95] P. Gupta, M. Ramrakhiani, Influence of the Particle Size on the Optical Properties of CdSe Nanoparticles, The Open Nanoscience Journal, 3 (2009) 15-19.

[96] X. Yan, X. Cui, L.S. Li, Synthesis of Large, Stable Colloidal Gaphene Quantum Dots with Tunable size, J. Am. Chem. Soc., 132 (2010) 5944-5945.

[97] X. Miao, D. Qu, D. Yang, B. Nie, Y. Zhao, H. Fan, Z. Sun, Synthesis of Carbon Dots with Multiple Color Emission by Controlled Graphitization and Surface Functionalization, Adv. Mater., 30 (2018) 1704740-1704748.

[98] O.J. Achadu, I. Uddin, T. Nyokong, Fluorescence Behavior of Nanoconjugates of Gaphene Quantum Dots and Zinc Phthalocyanines, J. Photochem. Photobio. A, 317 (2016) 12-25.

[99] O.M. Bankole, O.J. Achadu, T. Nyokong, Nonlinear Interactions of Zinc Phthalocyanine-Graphene Quantum Dots Nanocomposites: Investigation of Effects of Surface Functionalization with Heteroatoms, J. Fluoresc., 27 (2017) 755-766.

[100] G. Fomo, O.J. Achadu, T. Nyokong, One-Pot Synthesis of Graphene Quantum Dots–Phthalocyanines Supramolecular Hybrid and the Investigation of their Photophysical Properties, J. Mater. Sci., 53 (2018) 538-548.

[101] N. Nwahara, J. Britton, T. Nyokong, Improving Singlet Oxygen Generating Abilities of Phthalocyanines: Aluminum Tetrasulfonated Phthalocyanine in the Presence of Graphene Quantum Dots and Folic Acid, J. Coord. Chem., 70 (2017) 1601-1616.

[102] L.C. Nene, M. Managa, T. Nyokong, Photo-Physicochemical Properties and in Vitro Photodynamic Therapy Activity of Morpholine-Substituted Zinc (II)-Phthalocyanines π - π Stacked on Biotinylated Graphene Quantum Dots, Dyes Pigm., 165 (2019) 488-498.

[103] D. Zhang, L. Wen, R. Huang, H. Wang, X. Hu, D. Xing, Mitochondrial Specific Photodynamic Therapy by Rare-Earth Nanoparticles Mediated Near-Infrared Graphene Quantum Dots, Biomaterials, 153 (2018) 14-26.

[104] S.A. Majeed, N. Nwaji, J. Mack, T. Nyokong, S. Makhseed, Nonlinear Optical Responses of Carbazole-Substituted Phthalocyanines Conjugated to Graphene Quantum Dots and in Thin Films, J. Lumin., 213 (2019) 88-97.

[105] Y. Choi, S. Kim, M.H. Choi, S.R. Ryoo, J. Park, D.H. Min, B.S. Kim, Highly Biocompatible Carbon Nanodots for Simultaneous Bioimaging and Targeted Photodynamic Therapy in Vitro and in Vivo, Adv. Funct. Mater., 24 (2014) 5781-5789.

[106] M. Bursch, H. Neugebauer, S. Grimme, Structure Optimisation of Large Transition-Metal Complexes with Extended Tight-Binding Methods, Angew Chem. Int. Ed. Engl., 58 (2019) 11078-11087.

[107] P.W. Atkins, R.S. Friedman, In, Molecular Quantum Mechanics, Oxford University Press Inc., New York, 2011, pp. 258-333.

[108] S. Grimme, C. Bannwarth, P. Shushkov, A Robust and Accurate Tight-Binding Quantum Chemical Method for Structures, Vibrational Frequencies, and Noncovalent Interactions of Large Molecular Systems Parametrized for all spd-Block Elements (Z= 1–86), J. Chem. Theory Comput., 13 (2017) 1989-2009.

[109] C. Bannwarth, S. Ehlert, S. Grimme, GFN2-xTB-An Accurate and Broadly Parametrized Self-Consistent Tight-Binding Quantum Chemical Method with Multipole Electrostatics and Density-Dependent Dispersion Contributions, J. Chem. Theory Comput., 15 (2019) 1652-1671.

[110] G. Zanotti, N. Angelini, G. Mattioli, A.M. Paoletti, G. Pennesi, D. Caschera, A.P. Sobolev, L. Beverina, A.M. Calascibetta, A. Sanzone, A.D. Carlo, B.B. Berna, S. Pescetelli, A. Agresti, [1]Benzothieno [3,2-b][1] Benzothiophene-Phthalocyanine Derivatives: A Subclass of Solution-Processable Electron-Rich Hole Transport Materials, ChemPlusChem, (2020) (12 pages) 21926506.

[111] D. Porezag, T. Frauenheim, T. Kohler, G. Seifert, R. Kaschner, Construction of Tight-Binding-Like Potentials on the Basis of Density-Functional Theory: Application to Carbon, Phys. Rev. B Condens. Matter., 51 (1995) 12947-12957.

[112] V.N. Nemykin, R.G. Hadt, R.V. Belosludov, H. Mizuseki, Y. Kawazoe, Influence of Molecular Geometry, Exchange-Correlation Functional, and Solvent Effects in the Modeling of Vertical Excitation Energies in Phthalocyanines Using Time-Dependent Density Functional Theory (TDDFT) and Polarized Continuum Model TDDFT Methods: Can Modern Computational Chemistry Methods Explain Experimental Controversies?, J. Phys. Chem. A, 111 (2007) 12901-12913.

[113] J.J. Stewart, Optimization of Parameters for Semiempirical Methods II. Applications, J. Comput. Chem., 10 (1989) 221-264.

[114] J.J. Stewart, Optimization of Parameters for Semiempirical Methods VI: more Modifications to the NDDO Approximations and Re-Optimization of Parameters, J. Mol. Model., 19 (2013) (32 pages) 16102940.

[115] P. Pracht, E. Caldeweyher, S. Ehlert, S. Grimme, A Robust Non-Self-Consistent Tight-Binding Quantum Chemistry Method for Large Molecules, ChemRxiv, (2019) (19 pages) doi:10.26434/chemrxiv.8326202.

[116] S. Sharma, Molecular Dynamics Simulation of Nanocomposites Using BIOVIA Materials Studio, Lammps and Gromacs, Matthew Deans, Netherlands, 2019.

[117] T.G. Gantchev, J.E. van Lier, D.J. Hunting, Molecular Models of Zinc Phthalocyanines: Semi-Empirical Molecular Orbital Computations and Physicochemical Properties Studied by Molecular Mechanics Simulations, Radiat. Phys. Chem., 72 (2005) 367-379.

[118] K. Plaetzer, B. Krammer, J. Berlanda, F. Berr, T. Kiesslich, Photophysics and Photochemistry of Photodynamic Therapy: Fundamental Aspects, Lasers Med. Sci., 24 (2009) 259-268.

[119] T. Li, L. Yan, Functional Polymer Nanocarriers for Photodynamic Therapy, Pharmaceuticals, 11 (2018) 1424-8247

[120] A. Juarranz, P. Jaen, F. Sanz-Rodriguez, J. Cuevas, S. Gonzalez, Photodynamic Therapy of Cancer. Basic Principles and Applications, Clin. Transl. Oncol., 10 (2008) 148-154.

[121] A.F. dos Santos, D.R.Q. de Almeida, L.F. Terra, M.S. Baptista, L. Labriola, Photodynamic Therapy in Cancer Treatment - An Update Review, J. Cancer Metastasis Treat., 5 (2019) (20 pages) doi:10.20517/22394-24722.22018.20583.

[122] S. Fery-Forgues, D. Lavabre, Are Fluorescence Quantum Yields so Tricky to Mmeasure? A Demonstration using Familiar Stationery Products, J. Chem. Educ., 76 (1999) 1260-1264.

[123] M.D. Maree, T. Nyokong, K. Suhling, D. Phillips, Effects of Axial Ligands on the Photophysical Properties of Silicon Octaphenoxyphthalocyanine, J. Porphyr. Phthalocyanines, 6 (2002) 373-376.

[124] A.M. Brouwer, Standards for Photoluminescence Quantum Yield Measurements in Solution (IUPAC Technical Report), J. Pure Appl. Chem., 83 (2011) 2213-2228.

[125] Q. Li, T. Ruckstuhl, S. Seeger, Deep-UV Laser-Based Fluorescence Lifetime Imaging Microscopy of Single Molecules, J. Phys. Chem. B, 108 (2004) 8324-8329.

[126] A. Harriman, M.-C. Richoux, Attempted Photoproduction of Hydrogen Using Sulphophthalocyanines as Chromophores for Three-Component Systems, J. Chem. Soc., 76 (1980) 1618-1626.

[127] L. De Boni, E. Piovesan, L. Gaffo, C. Mendonca, Resonant Nonlinear Absorption in Zn-phthalocyanines, J. Phys. Chem. A, 112 (2008) 6803-6807.

[128] T.H. Tran-Thi, C. Desforge, C. Thiec, S. Gaspard, Singlet-Singlet and Triplet-Triplet Intramolecular Transfer Processes in a Covalently Linked Porphyrin-Phthalocyanine Heterodimer, J. Phys. Chem., 93 (1989) 1226-1233.

[129] A.A. Gorman, M.A.J. Rodgers, Singlet Molecular Oxygen, Chem. Soc. Rev., 10 (1981) 205-231.

[130] N.A. Kuznetsova, N.S. Gretsova, E.A. Kalmykova, E.A. Makarova, S.N. Dashkevich, V.M. Negrimovskii, O.L. Kaliya, E.A. Luk'yanets, Relationship Between the Photochemical Properties and Structure of Pophyrins and Related Compounds, Russ. J. Gen. Chem., 70 (2000) 133-140.

[131] P. Murasecco-Suardi, E. Gassmann, A.M. Braun, E. Oliveros, Determination of the Quantum Yield of Intersystem Crossing of Rose Bengal, Helv. Chim. Acta, 70 (1987) 1760-1773.

[132] T. Nyokong, Desired Properties of New Phthalocyanines for Photodynamic Therapy, Pure Appl. Chem., 83 (2011) 1763-1779.

[133] C.S. Foote, In (H.H. Wasserman, R.W. Murray, (Eds.)), Singlet Oxygen, Academic Press, New York, San Francisco, London, 1979.

[134] C. Berney, G. Danuser, FRET or no FRET: A Quantitative Comparison, Biophys. J., 84 (2003) 3992-4010.

[135] H. Du, R.C.A. Fuh, J. Li, L.A. Corkan, J.S. Lindsey, PhotochemCAD‡: A Computer-Aided Design and Research Tool in Photochemistry, Photochem. Photobiol., 68 (1998) 141-142.

[136] J.R. Lakowicz, Principles of Fluorescence Spectroscopy, Kluwer Academic/Plenum Publishers, New York, 1999.

[137] J.G. Young, W. Onyebuagu, Synthesis and Characterization of Di-disubstituted Phthalocyanines, J. Org. Chem., 55 (1990) 2155-2159.

[138] P. Selvakumar, M. Sarojadevi, Development of Oligomeric Phthalonitrile Resins for Advanced Composite Applications, Macromolecular symposia, Wiley Online Library, 2009, pp. 190-200.

[139] M. Ambroz, A. Beeby, A. MacRobert, R. Svensen, D. Phillips, Preparative, Analytical and Fluorescence Spectroscopic Studies of Sulphonated Aluminium Phthalocyanine Photosensitizers, J. Photoch. Photobio. B, 9 (1991) 87-95.

[140] R. Xu, Light Scattering: A Review of Particle Characterization Applications, Particuology, 18 (2015) 11-21.

[141] S.K. Brar, M. Verma, Measurement of Nanoparticles by Light-scattering Techniques, Trends Analyt. Chem., 30 (2011) 4-17.

[142] S. Thomas, R. Thomas, A.K. Zachariah, R.K. Mishra, Thermal and Rheological Measurement Techniques for Nanomaterials Characterization, Elsevier, Netherlands, 2017.

[143] M. Durmus, In: (T. Nyokong, V. Ahsen, (Eds.)), Photosensitizers in Medicine, Environment, and Security, Springer Science & Business Media, 2012, (Chapter 4) pp. 135-266.

[144] K.E. Sekhosana, T. Nyokong, The Nonlinear Absorption in New Lanthanide Double Decker Pyridine-based Phthalocyanines in Solution and Thin Films, Opt. Mater., 47 (2015) 211-218.

[145] D. Çakır, V. Çakır, Z. Bıyıklıoğlu, M. Durmuş, H. Kantekin, New Water Soluble Cationic Zinc Phthalocyanines as Potential for Photodynamic Therapy of Cancer, J. Organomet. Chem., 745 (2013) 423-431.

[146] G.K. Karaoğlan, G. Gümrükçü, A. Koca, A. Gül, U. Avcıata, Synthesis and Characterization of Novel Soluble Phthalocyanines with Fused Conjugated Unsaturated Groups, Dyes Pigm., 90 (2011) 11-20.

[147] H.P. Karaoğlu, A. Gül, M.B. Koçak, Synthesis and Characterization of a New Tetracationic Phthalocyanine, Dyes Pigm., 76 (2008) 231-235.

[148] R.A. Zubarev, P.A. Demirev, Isotope Depletion of Large Biomolecules: Implications for Molecular Mass Measurements, J. Am. Soc. Mass Spectrom., 9 (1998) 149-156.

[149] B.-Y. Zheng, M.-R. Ke, W.-L. Lan, L. Hou, J. Guo, D.-H. Wan, L.-Z. Cheong, J.-D. Huang, Mono-and Tetra-substituted Zinc (II) Phthalocyanines Containing Morpholinyl Moieties: Synthesis, Antifungal Photodynamic Activities, and Structure-activity Relationships, Eur. J. Med. Chem., 114 (2016) 380-389.

[150] T. Nyokong, In: (J. Jiang (eds)) Electronic Spectral and Electrochemical Behavior of Near Infrared Absorbing Metallophthalocyanines, Functional Phthalocyanine Molecular Materials. Structure and Bonding, Springer, Berlin, Heidelberg, 2010, pp. 45-88.

[151] T. Fan, W. Zeng, W. Tang, C. Yuan, S. Tong, K. Cai, Y. Liu, W. Huang, Y. Min, A.J. Epstein, Controllable Size-selective Method to Prepare Graphene Quantum Dots from Graphene Oxide, Nanoscale Res. Lett., 10 (2015) (8 Pages) 19317573.

[152] S. Turner, O.I. Lebedev, O. Shenderova, I.I. Vlasov, J. Verbeeck, G. Van Tendeloo, Determination of Size, Morphology, and Nitrogen Impurity Location in Treated Detonation Nanodiamond by Transmission Electron Microscopy, Adv. Funct. Mater., 19 (2009) 2116-2124.

[153] A. Kelarakis, From Highly Graphitic to Amorphous Carbon Dots: A Critical Review, MRS Energy & Sustainability, 1 (2014) 2329-2229.

[154] B.B. Campos, R. Contreras-Cáceres, T.J. Bandosz, J. Jiménez-Jiménez, E. Rodríguez-Castellón, J.C.E. da Silva, M. Algarra, Carbon Dots as Fluorescent Sensor for Detection of Explosive Nitrocompounds, Carbon, 106 (2016) 171-178.

[155] T.G. Souza, V.S. Ciminelli, N.D.S. Mohallem, A Comparison of TEM and DLS Methods to Characterize Size Distribution of Ceramic Nanoparticles, J. Phys. Conf. Ser, (2016), pp. 6-11.

[156] I. Ostolska, M. Wiśniewska, Application of the Zeta Potential Measurements to Explanation of Colloidal Cr 2 O 3 Stability Mechanism in the Presence of the Ionic Polyamino Acids, Colloid. Polym. Sci., 292 (2014) 2453-2464.

[157] Y.V. Butenko, V. Kuznetsov, E. Paukshtis, A. Stadnichenko, I. Mazov, S. Moseenkov, A. Boronin, S. Kosheev, The Thermal Stability of Nanodiamond Surface Groups and Onset of Nanodiamond Graphitization, Fuller. Nanotub. Carbon Nanostructures, 14 (2006) 557-564.

[158] A. Krueger, In: Carbon Materials and Nanotechnology, John Wiley & Sons, Germany, 2010.

[159] J. Zhang, W. Shen, D. Pan, Z. Zhang, Y. Fang, M. Wu, Controlled Synthesis of Green and Blue Luminescent Carbon Nanoparticles with High Yields by the Carbonization of Sucrose, New J. Chem., 34 (2010) 591-593.

[160] N. Puvvada, B.P. Kumar, S. Konar, H. Kalita, M. Mandal, A. Pathak, Synthesis of Biocompatible Multicolor Luminescent Carbon Dots for Bioimaging Applications, Sci. Technol. Adv. Mater., 13 (2012) (7 pages) 045008.

[161] H. Teymourinia, M. Salavati-Niasari, O. Amiri, M. Farangi, Facile Synthesis of Graphene Quantum Dots from Corn Powder and their Application as Down Conversion Effect in Quantum Dot-dye-sensitized Solar cell, J. Mol. Liq., 251 (2018) 267-272.

[162] Z. De Liu, H.X. Zhao, C.Z. Huang, Obstruction of Photoinduced Electron Transfer from Excited Porphyrin to Graphene Oxide: A Fluorescence Turn-on Sensing Platform for Iron (III) Ions, PLoS One, 7 (2012) e50367.

[163] Z. Gan, H. Xu, Y. Hao, Mechanism for Excitation-dependent Photoluminescence from Graphene Quantum Dots and other Graphene Oxide Derivates: Consensus, Debates and Challenges, Nanoscale Adv., 8 (2016) 7794-7807.

[164] A. Cayuela, M. Soriano, C. Carrillo-Carrión, M. Valcárcel, Semiconductor and Carbon-based Fluorescent Nanodots: The Need for Consistency, Chem. Commun., 52 (2016) 1311-1326.

[165] V. Danilenko, Phase Diagram of Nanocarbon, Combust. Explos. Shock Waves, 41 (2005) 460-466.

[166] S. Porro, S. Musso, M. Vinante, L. Vanzetti, M. Anderle, F. Trotta, A. Tagliaferro, Purification of Carbon Nanotubes Grown by Thermal CVD, Physica E, 37 (2007) 58-61.

[167] C.E. Banks, T.J. Davies, G.G. Wildgoose, R.G. Compton, Electrocatalysis at Graphite and Carbon Nanotube Modified Electrodes: Edge-plane Sites and Tube Ends are the Reactive Sites, Chem. Commun., (2005) 829-841.

[168] Z. Du, A.F. Sarofim, J.P. Longwell, C.A. Mims, Kinetic Measurement and Modeling of Carbon Oxidation, Energy & Fuels, 5 (1991) 214-221.

[169] T. Batakliev, I. Petrova-Doycheva, V. Angelov, V. Georgiev, E. Ivanov, R. Kotsilkova, M. Casa, C. Cirillo, R. Adami, M. Sarno, Effects of Graphene Nanoplatelets and Multiwall Carbon Nanotubes on the Structure and Mechanical Properties of Poly (lactic acid) Composites: A Comparative Study, Appl. Sci., 9 (2019) (15 pages) 469

[170] D.K. Singh, P. Iyer, P. Giri, Diameter Dependence of Interwall Separation and Strain in Multiwalled Carbon Nanotubes Probed by X-ray Diffraction and Raman Scattering Studies, Diamond Relat. Mater., 19 (2010) 1281-1288.

[171] S. Kim, D. Hee Shin, C. Oh Kim, S. Seok Kang, S. Sin Joo, S.-H. Choi, S. Won Hwang, C. Sone, Size-dependence of Raman Scattering From Graphene Quantum Dots: Interplay Between Shape and Thickness, Appl. Phys. Lett., 102 (2013) (4 pages) 053108.

[172] M.A. Hines, G.D. Scholes, Colloidal PbS Nanocrystals with Size-tunable Near-infrared Emission: Observation of Post-synthesis Self-narrowing of the Particle Size Distribution, Adv. Mater., 15 (2003) 1844-1849.

[173] J. Zhang, R.W. Crisp, J. Gao, D.M. Kroupa, M.C. Beard, J.M. Luther, Synthetic Conditions for High-accuracy Size Control of PbS Quantum Dots, J. Phys. Chem. Lett., 6 (2015) 1830-1833.

[174] M. Bacon, S.J. Bradley, T. Nann., Graphene Quantum Dots., Part. Part. Syst. Char., 31 (2014) 415-428.

[175] X. Xu, F. Gao, X. Bai, F. Liu, W. Kong, M. Li, Tuning the Photoluminescence of Graphene Quantum Dots by Photochemical Doping with Nitrogen, Materials, 10 (2017) (9 pages) 1328.

[176] H. Li, X. He, Z. Kang, H. Huang, Y. Liu, J. Liu, S. Lian, C.H.A. Tsang, X. Yang, S.T. Lee, Water-soluble Fluorescent Carbon Quantum Dots and Photocatalyst Design, Angew. Chem. Int. Ed., 122 (2010) 4532-4536.

[177] W. Qi, M. Wang, Size and Shape Dependent Melting Temperature of Metallic Nanoparticles, Mater. Chem. Phys., 88 (2004) 280-284.

[178] T. Petit, L. Puskar, FTIR Spectroscopy of Nanodiamonds: Methods and Interpretation, Diamond Relat. Mater., 89 (2018) 52-66.

[179] G. Yur'ev, V.Y. Dolmatov, X-ray Diffraction Study of Detonation Nanodiamonds, J. Superhard Mater., 32 (2010) 311-328.

[180] S. Choudhury, B. Kiendl, J. Ren, F. Gao, P. Knittel, C. Nebel, A. Venerosy, H. Girard, J.-C. Arnault, A. Krueger, Combining Nanostructuration with Boron Doping to Alter Sub Band Gap Acceptor States in Diamond Materials, J. Mater. Chem. A, 6 (2018) 16645-16654.

[181] A. Vervald, S. Burikov, I. Vlasov, E. Ekimov, O. Shenderova, T. Dolenko, Boron-doped Nanodiamonds as Possible Agents for Local Hyperthermia, Laser Phys. Lett., 14 (2017) (6 pages) 045702.

[182] W. Liu, C. Li, Y. Ren, X. Sun, W. Pan, Y. Li, J. Wang, W. Wang, Carbon dots: Surface Engineering and Applications, J. Mater. Chem. B, 4 (2016) 5772-5788.

[183] G. Bounos, K.S. Andrikopoulos, T.K. Karachalios, & , G.A. Voyiatzis, Evaluation of Multi-walled Carbon Nanotube Concentrations in Polymer Nanocomposites by Raman Spectroscopy, Carbon, 76 (2014) 301–309.

[184] Y. Xianrong, L. Xiaojie, W. Xiaohong, Y. Honghao, Preparation and Characterization of Boron-doped Nanodiamond, J. Mater. Chem. B, 47 (2018) 3634-3639.

[185] C.M. Hoo, N. Starostin, P. West, M.L. Mecartney, A Comparison of Atomic Force Microscopy (AFM) and Dynamic Light Scattering (DLS) Methods to Characterize Nanoparticle Size Distributions, J. Mater. Chem. B, 10 (2008) 89-96.

[186] A. Centane S., O. J., Nyokong, T., Effects of Substituents on the Electrocatalytic Activity of Cobalt Phthalocyanines when Conjugated to Graphene Quantum Dots, Electroanalysis, 29 (2017) 2470–2482.

[187] L. Li, J.-F. Zhao, N. Won, H. Jin, S. Kim, J.-Y. Chen, Quantum Dot-aluminum Phthalocyanine Conjugates Perform Photodynamic Reactions to Kill Cancer Cells Via Fluorescence Resonance Energy Transfer, Nanoscale Res. Lett., 7 (2012) 1-8.

[188] A.V. Zasedatelev, T.V. Dubinina, D.M. Krichevsky, V.I. Krasovskii, V.Y. Gak, V.E. Pushkarev, L.G. Tomilova, A.A. Chistyakov, Plasmon-induced Light Absorption of Phthalocyanine Layer in Hybrid Nanoparticles: Enhancement Factor and Effective Spectra, J. Phys. Chem. C, 120 (2016) 1816-1823.

[189] Z.-J. Zhu, Y.-C. Yeh, R. Tang, B. Yan, J. Tamayo, R.W. Vachet, V.M. Rotello, Stability of Quantum Dots in Live Cells, Nat. Chem., 3 (2011) 963-968.

[190] Z. Li, C. He, Z. Wang, Y. Gao, Y. Dong, C. Zhao, Z. Chen, Y. Wu, W. Song, Ethylenediamine-modified Graphene Oxide Covalently Functionalized with a Tetracarboxylic Zn (ii) Phthalocyanine Hybrid for Enhanced Nonlinear Optical Properties, Photochem. Photobiol. Sci., 15 (2016) 910-919.

[191] R.O. Ogbodu, J.L. Limson, E. Prinsloo, T. Nyokong, Photophysical Properties and Photodynamic Therapy Effect of Zinc Phthalocyanine-spermine-single Walled Carbon Nanotube Conjugate on MCF-7 Breast Cancer Cell Line, Synth. Met., 204 (2015) 122-132.

[192] M. Mahyari, A. Shaabani, Graphene Oxide-iron Phthalocyanine Catalyzed Aerobic Oxidation of Alcohols, Appl. Catal. A, 469 (2014) 524-531.

[193] M.E. Ragoussi, J. Malig, G. Katsukis, B. Butz, E. Spiecker, G. de la Torre, T. Torres, D.M. Guldi, Linking Photo-and Redoxactive Phthalocyanines Covalently to Graphene, Angew. Chem. Int. Ed., 124 (2012) 6527-6531.

[194] M. Salazar-Villanueva, P.H. Hernández Tejeda, U. Pal, J.F. Rivas-Silva, J.I. Rodríguez Mora, J.A. Ascencio, Stable Ti n (n= 2− 15) Clusters and their Geometries: DFT Calculations, J. Phys. Chem. A, 110 (2006) 10274-10278.

[195] A.C. Ferrari, J. Robertson, Raman Spectroscopy of Amorphous, Nanostructured, Diamond–like Carbon, and Nanodiamond, Phil. Trans. R. Soc. Lond. A, 362 (2004) 2477-2512.

[196] T. Jiang, K. Xu, S. Ji, FTIR Studies on the Spectral Changes of the Surface Functional Groups of Ultradispersed Diamond Powder Synthesized by Explosive Detonation After Treatment in Hydrogen, Nitrogen, Methane and Air at Different Temperatures, J. Chem. Soc., Faraday Trans., 92 (1996) 3401-3406.

[197] B.C. Smith, Infrared Spectral Interpretation: A Systematic Approach, CRC press, Florida, 1999.

[198] G.W. Lu, P. Gao, In: V.S. Kulkarni (Eds), Handbook of Non-Invasive Drug Delivery Systems: Science and Technology, Elsevier, Burlington, 2010, pp. 66-67.

[199] R.N. Wijesena, N.D. Tissera, V. Rathnayaka, R.M. de Silva, K.N. de Silva, Colloidal Stability of Chitin Nanofibers in Aqueous Systems: Effect of pH, Ionic Strength, Temperature & Concentration, Carbohydr. Polym., 235 (2020) (8 pages) 116024.

[200] M. Horie, K. Fujita, In: (J. C. Fishbein (Eds)) Toxicity of Metal Oxides Nanoparticles, Advances in molecular toxicology, Elsevier, Amsterdam, 2011, pp. 145-178.

[201] L.K. Limbach, Y. Li, R.N. Grass, T.J. Brunner, M.A. Hintermann, M. Muller, D. Gunther, W.J. Stark, Oxide Nanoparticle Uptake in Human Lung Fibroblasts: Effects of Particle Size, Agglomeration, and Diffusion at Low Concentrations, Environ. Sci. Technol., 39 (2005) 9370-9376.

[202] X. Li, J. Shao, Y. Qin, C. Shao, T. Zheng, L. Ye, TAT-conjugated Nanodiamond for the Enhanced Delivery of Doxorubicin, J. Mater. Chem., 21 (2011) 7966-7973.

[203] J.-G. Park, S.-H. Lee, J.-S. Ryu, Y.-K. Hong, T.-G. Kim, A.A. Busnaina, Interfacial and Electrokinetic Characterization of IPA Solutions Related to Semiconductor Wafer Drying and Cleaning, J. Electrochem. Soc., 153 (2006) G811-G814.

[204] N. Gibson, O. Shenderova, T. Luo, S. Moseenkov, V. Bondar, A. Puzyr, K. Purtov, Z. Fitzgerald, D. Brenner, Colloidal Stability of Modified Nanodiamond Particles, Diamond Relat. Mater., 18 (2009) 620-626.

[205] H.D. Silva, M.Â. Cerqueira, A.A. Vicente, Nanoemulsions for Food Applications: Development and Characterization, Food Bioprocess Technol., 5 (2012) 854-867.

[206] G.S. Yurjev, V. Yu, Dolmatov, J. Superhard, Nanophase and Nanocomposite Materials II, Mater. Res. Soc. Symp. Proc., 435 (2010) 311–1328.

[207] J.H. Gibbs, Z. Zhou, D. Kessel, F.R. Fronczek, S. Pakhomova, M.G.H. Vicente, Synthesis, Spectroscopic, and in Vitro Investigations of 2, 6-diiodo-BODIPYs with PDT and Bioimaging Applications, J. Photochem. Photobiol. B, 145 (2015) 35-47.

[208] J. Romanos, M. Beckner, D. Stalla, A. Tekeei, G. Suppes, S. Jalisatgi, M. Lee, F. Hawthorne, J. Robertson, L. Firlej, Infrared Study of Boron–carbon Chemical Bonds in Boron-doped Activated Carbon, Carbon, 54 (2013) 208-214.

[209] S.L. Gawali, B. Barick, K. Barick, P. Hassan, Effect of Sugar Alcohol on Colloidal Stabilization of Magnetic Nanoparticles for Hyperthermia and Drug Delivery Applications, J. Alloys Compd., 725 (2017) 800-806.

[210] R. Prabakaran, R. Kesavamoorthy, G. Reddy, F.P. Xavier, Structural Investigation of Copper Phthalocyanine Thin Films Using X-Ray Diffraction, Raman Scattering and Optical Absorption Measurements, Phys. Status Solidi B, 229 (2002) 1175-1186.

[211] N.G. Mphuthi, A.S. Adekunle, O.E. Fayemi, L.O. Olasunkanmi, E.E. Ebenso, Phthalocyanine Doped Metal Oxide Nanoparticles on Multiwalled Carbon Nanotubes Platform for the Detection of Dopamine, Sci. Rep., 7 (2017) (23 Pages) 43181.

[212] X.-F. Zhang, X. Shao, π–π Binding Ability of Different Carbon Nano-materials With Aromatic Phthalocyanine Molecules: Comparison Between Graphene, Graphene Oxide and Carbon Nanotubes, J. Photochem. Photobiol. A, 278 (2014) 69-74.

[213] A.V. Gubarevich, J. Kitamura, S. Usuba, H. Yokoi, Y. Kakudate, O. Odawara, Onion-like Carbon Deposition by Plasma Spraying of Nanodiamonds, Carbon, 41 (2003) 2601-2606.

[214] J.-B. Wu, M.-L. Lin, X. Cong, H.-N. Liu, P.-H. Tan, Raman Spectroscopy of Graphene-based Materials and its Applications in Related Devices, Chem. Soc. Rev., 47 (2018) 1822-1873.

[215] Y. Shimizu, T. Azumi, Mechanism of External Heavy Atom Effect on Intersystem Crossing in Fluid Solutions. Analysis Based on Fluorescence Decay Data, J. Phys. Chem., 86 (1982) 22-26.

[216] R.D. James, Peter Douglas, Anthony Harriman, George Porter, M.-C. Richoux, Metal Phthalocyanines and Porphyrins and Photosensitizers for Reduction of Water to Hydrogen, Coord. Chem. Rev., 44 (1982) 83- 126.

[217] R. Moriarty, A. Martin, K. Adamson, E. O'reilly, P. Mollard, R. Forster, T. Keyes, The Application of Water Soluble, Mega-Stokes-shifted BODIPY Fluorophores to Cell and Tissue Imaging, J. Microsc., 253 (2014) 204-218.

[218] S.J. Bradley, R. Kroon, G. Laufersky, M. Rödin, R.V. Goreham, T. Gschneidtner, K. Schroeder, K. Moth-Poulsen, M. Andersson, T. Nan, Heterogeneity in the Fluorescence of Graphene and Graphene Oxide Quantum Dots, Microchim. Acta, 184 (2017) 871–878.

[219] M. Vieweger, X. Jiang, Y.-K. Lim, J. Jo, D. Lee, B. Dragnea, Conformationally Dynamic π-Conjugation: Probing Structure–Property Relationships of Fluorescent Tris (N-salicylideneaniline)s, J. Phys. Chem. A, 115 (2011) 13298-13308.

[220] J.R. Lakowicz, Y. Shen, S. D'Auria, J. Malicka, J. Fang, Z. Gryczynski, I. Gryczynski, Radiative Decay Engineering: 2. Effects of Silver Island Films on Fluorescence Intensity, Lifetimes, and Resonance Energy Transfer, Anal. Biochem., 301 (2002) 261-277.

[221] M. Debacker, O. Deleplanque, B. Van Vlierberge, F. Sauvage, A Laser Photolysis Study of Triplet Lifetimes and of Triplet–Triplet Annihilation Reactions of Phthalocyanins in DMSO Solutions (Etude des Durées de Vie du Triplet et des Réactions d'Annihilation Triplet–Triplet de Phthalocyanines dans le DMSO par Photolyse Laser), Laser Chem., 8 (1988) 1-11.

[222] S.V. Rao, P. Anusha, L. Giribabu, S.P. Tewari, Picosecond Optical Nonlinearities in Symmetrical and Unsymmetrical Phthalocyanines Studied Using the Z-scan Technique, Pramana, 75 (2010) 1017-1023.

[223] J.R. Darwent, P. Douglas, A. Harriman, G. Porter, M.-C. Richoux, Metal Phthalocyanines and Porphyrins as Photosensitizers for Reduction of Water to Hydrogen, Coord. Chem. Rev., 44 (1982) 83-126.

[224] H. Ramesh, T. Mayr, M. Hobisch, S. Borisov, I. Klimant, U. Krühne, J.M. Woodley, Measurement of Oxygen Transfer from Air Into Organic Solvents, J. Chem. Technol. Biotechnol., 91 (2016) 832-836.

[225] A.S. Stasheuski, V.A. Galievsky, A.P. Stupak, B.M. Dzhagarov, M.J. Choi, B.H. Chung, J.Y. Jeong, Photophysical Properties and Singlet Oxygen Generation Efficiencies of Water-Soluble Fullerene Nanoparticles, Photochem. Photobiol., 90 (2014) 997-1003.

[226] Khin K. Chin, Shih-Ching Chuang, Billy Hernandez, Matthias Selke, Christopher S. Foote, M.A. Garcia-Garibay, Photophysical Properties of a 1,2,3,4,5,6-Hexasubstituted Fullerene Derivative, J. Phys. Chem. A, 110 (2006) 13662-13666.

[227] E.I. Sagun, E.I. Zenkevich, V.N. Knyukshto, A.M. Shulga, D.A. Starukhin, C. von Borczyskowski, Interaction of Multiporphyrin Systems with Molecular Oxygen in Liquid Solutions: Extra-ligation and Screening Effects, Chem. Phys., 275 (2002) 211-230.

[228] W. Humphrey, A. Dalke, K. Schulten, VMD: Visual Molecular Dynamics, J. Mol. Graphics, 14 (1996) 33-38.

[229] J. Aihara, Reduced HOMO−LUMO Gap as an Index of Kinetic Stability for Polycyclic Aromatic Hydrocarbons, J. Phys. Chem. A, 103 (1999) 7487–7495.

[230] K. Anand, F.I. Khan, T. Singh, P. Elumalai, C. Balakumar, D. Premnath, D. Lai, A.A. Chuturgoon, M. Saravanan, Green Synthesis, Experimental and Theoretical Studies to Discover Novel Binders of Exosomal Tetraspanin CD81 Protein, ACS omega, 5 (2020) 17973-17982.

[231] A.A. Fokin, P.R. Schreiner, Band Gap Tuning in Nanodiamonds: First Principle Computational Studies, Mol. Phys., 107 (2009) 823-830.

[232] M. Alexiades-Armenakas, Laser-mediated photodynamic therapy, Clin. Dermatol., 24 (2006) 16-25.

[233] D. Atilla, N. Saydan, M. Durmuş, A.G. Gürek, T. Khan, A. Rück, H. Walt, T. Nyokong, V. Ahsen, Synthesis and Photodynamic Potential of Tetra-and Octa-triethyleneoxysulfonyl Substituted Zinc Phthalocyanines, J. Photochem. Photobiol. A, 186 (2007) 298-307.

[234] R. Dondi, E. Yaghini, K. Tewari, L. Wang, F. Giuntini, M. Loizidou, A. MacRobert, I. Eggleston, Flexible Synthesis of Cationic Peptide–porphyrin Derivatives for Light-triggered Drug Delivery and Photodynamic Therapy, Org. Biomol. Chem., 14 (2016) 11488-11501.

[235] C. Fabris, G. Valduga, G. Miotto, L. Borsetto, G. Jori, S. Garbisa, E. Reddi, Photosensitization with Zinc (II) Phthalocyanine as a Switch in the Decision Between Apoptosis and Necrosis, Cancer Res., 61 (2001) 7495-7500.

[236] M. Managa, J. Britton, E. Prinsloo, T. Nyokong, Effects of Pluronic Silica Nanoparticles on the Photophysical and Photodynamic Therapy Behavior of Triphenyl-p-phenoxy Benzoic Acid Metalloporphyrins, J. Coord. Chem., 69 (2016) 3491-3506.

[237] J. Bremner, S. Wood, J. Bradley, J. Griffiths, G. Adams, S. Brown, 31 P Magnetic Resonance Spectroscopy as a Predictor of Efficacy in Photodynamic Therapy Using Differently Charged Zinc Phthalocyanines, Br. J. Cancer, 81 (1999) 616-621.

[238] D. Wöhrle, N. Iskander, G. Graschew, H. Sinn, E. Friedrich, W. Maier-Borst, J. Stern, P. Schlag, Synthesis of Positively Charged Phthalocyanines and their Activity in the Photodynamic Therapy of Cancer Cells, J. Photochem. Photobiol., 51 (1990) 351-356.

[239] B. Chen, W. Le, Y. Wang, Z. Li, D. Wang, L. Ren, L. Lin, S. Cui, J.J. Hu, Y. Hu, Targeting Negative Surface Charges of Cancer Cells by Multifunctional Nanoprobes, Theranostics, 6 (2016) 1887-1898.

[240] L. Costa, M.A.F. Faustino, M.G.P. Neves, Â. Cunha, A. Almeida, Photodynamic inactivation of mammalian viruses and bacteriophages, Viruses, 4 (2012) 1034-1074.

[241] S. Gupta, B.S. Dwarakanath, K. Muralidhar, T. Koru-Sengul, V. Jain, Non-monotonic Changes in Clonogenic Cell Survival Induced by Disulphonated Aluminum Phthalocyanine Photodynamic Treatment in a Human Glioma Cell Line, J. Transl. Med., 8 (2010) 43.

[242] M.M. Qualls, D.H. Thompson, Chloroaluminum Phthalocyanine Tetrasulfonate Delivered Via Acid-labile Diplasmenylcholine-folate liposomes: Intracellular Localization and Synergistic Phototoxicity, Int. J. Cancer, 93 (2001) 384-392.

[243] G. Obaid, I. Chambrier, M.J. Cook, D.A. Russell, Cancer Targeting with Biomolecules: A Comparative Study of Photodynamic Therapy Efficacy Using Antibody or Lectin Conjugated Phthalocyanine-PEG Gold Nanoparticles, Photochem. Photobiol. Sci., 14 (2015) 737-747.

[244] M. Sheik-Bahae, A.A. Said, T.-H. Wei, D.J. Hagan, E.W. Van Stryland, Sensitive Measurement of Optical Nonlinearities Using a Single Beam, IEEE J. Quantum Electron., 26 (1990) 760-769.

[245] M. Sheik-Bahae, A.A. Said, E.W. Van Stryland, High-sensitivity, Single-beam n2 Measurements, Opt. Lett., 14 (1989) 955-957.

[246] E.M. García-Frutos, S.M. O'Flaherty, E.M. Maya, G. de la Torre, W. Blau, P. Vázquez, T. Torres, Alkynyl Substituted Phthalocyanine Derivatives as Targets for Optical Limiting, J. Mater. Chem., 13 (2003) 749-753.

[247] E.W. Van Stryland, M. Sheik-Bahae, Z-scan measurements of optical nonlinearities, Characterization Techniques and Tabulations for Organic Nonlinear Materials, 18 (1998) 655-692.

[248] S.M. O'Flaherty, S.V. Hold, M.J. Cook, T. Torres, Y. Chen, M. Hanack, W.J. Blau, Molecular Engineering of Peripherally and Axially Modified Phthalocyanines for Optical Limiting and Nonlinear Optics, Adv. Mater., 15 (2003) 19–32.

[249] X. Zheng, M. Feng, Z. Li, Y. Song, H. Zhan, Enhanced Nonlinear Optical Properties of Nonzero-bandgap Graphene Materials in Glass Matrices, J. Mater. Chem. C, 2 (2014) 4121-4125.

[250] V. Vanyukov, T. Mogileva, G. Mikheev, A. Puzir, V. Bondar, Y. Svirko, Size Effect on the Optical Limiting in Suspensions of Detonation Nanodiamond Clusters, Appl. Opt., 52 (2013) 4123-4130.

[251] G. Mikheev, V. Vanyukov, K. Purtov, T. Mogileva, Nonlinear Scattering of Light in Nanodiamond Hydrosol, Tech. Phys. Lett., 36 (2010) 358-361.

[252] N. Nwaji, J. Mack, J. Britton, T. Nyokong, Synthesis, Photophysical and Nonlinear Optical Properties of a Series of Ball-type Phthalocyanines in Solution and Thin Films, New J. Chem., 41 (2017) 2020-2028.

[253] E.M. Maya, A.W. Snow, J.S. Shirk, R.G. Pong, S.R. Flom, G.L. Roberts, Synthesis, Aggregation Behavior and Nonlinear Absorption Properties of Lead Phthalocyanines Substituted with Siloxane Chains, J. Mater. Chem., 13 (2003) 1603-1613.

[254] K. Sanusi, S. Khene, T. Nyokong, Enhanced Optical Limiting Performance in Phthalocyanine-quantum Dot Nanocomposites by Free-carrier Absorption Mechanism, Opt. Mater., 37 (2014) 572-582.

[255] S.V. Rao, Phthalocyanines, Porphycenes, and Corroles: Nonlinear Optical Properties and Ultrafast Dynamics, Nonlinear Optics and Applications VI, International Society for Optics and Photonics, 2012, pp. 84341B.

[256] M. Yüksek, A. Elmali, M. Durmuş, H.G. Yaglioglu, H. Ünver, T. Nyokong, Good Optical Limiting Performance of Indium and Gallium Phthalocyanines in a Solution and Co-polymer Host, J. Opt., 12 (2009) (9 Pages) 015208.

[257] R.L. Sutherland, Handbook of Nonlinear Optics, CRC press, Ohio, 2003.

[258] R. Gadonas, K.-H. Feller, A. Pugzlys, Wavelength Dependent Nonlinear Optical Properties of Pseudoisocyanine J-aggregates, Opt. Commun., 112 (1994) 157-162.

[259] P. Zhu, P. Wang, W. Qiu, Y. Liu, C. Ye, G. Fang, Y. Song, Optical Limiting Properties of Phthalocyanine-fullerene Derivatives, Appl. Phys. Lett., 78 (2001) 1319-1321.

[260] M. Hanack, T. Schneider, M. Barthel, J.S. Shirk, S.R. Flom, R.G. Pong, Indium Phthalocyanines and Naphthalocyanines for Optical Llimiting, Coord. Chem. Rev., 219 (2001) 235-258.

[261] E. Ramya, N. Momen, D.N. Rao, Preparation of Multiwall Carbon Nanotubes with Zinc Phthalocyanine Hybrid Materials and their Nonlinear Optical (NLO) Properties, J. Nanosci. Nanotechnol., 17 (2018) 407-414.

[262] M.S. Savelyev, A.Y. Gerasimenko, V.M. Podgaetskii, S.A. Tereshchenko, S.V. Selishchev, A.Y. Tolbin, Conjugates of thermally stable phthalocyanine J-type dimers with single-walled carbon nanotubes for enhanced optical limiting applications, Opt Laser Technol., 117 (2019) 272-279.

[263] J. Wang, W.J. Blau, Inorganic and Hybrid Nanostructures for Optical Limiting, J. Opt. A: Pure Appl. Opt., 11 (2009) (16 Pages) 024001.

[264] O. Muller, V. Pichot, L. Merlat, D. Spitzer, Optical Limiting Properties of Surface Functionalized Nanodiamonds Probed by the Z-scan Method, Sci. Rep., 9 (2019) (11 pages) 519.

[265] S. Couris, E. Koudoumas, A. Ruth, S. Leach, Concentration and Wavelength Dependence of the Effective Third-order Susceptibility and Optical Limiting of C60 in Toluene Solution, J. Phys. B: At. Mol. Opt. Phys, 28 (1995) 4537-4554.

[266] C. Bindhu, S. Harilal, V. Nampoori, C. Vallabhan, Experimental Investigation of Optical Limiting and Thermal Lensing in Toluene Solutions of C70, Appl. Phys. B, 70 (2000) 429-434.

[267] P. Poornesh, G. Umesh, P.K. Hegde, M. Manjunatha, K. Manjunatha, A. Adhikari, Studies on Third-order Nonlinear Optical Properties and Reverse Saturable Absorption in Polythiophene/poly (Methylmethacrylate) Composites, Appl. Phys. B, 97 (2009) 117-124.

[268] I. Al-Saidi, S. Abdulkareem, Nonlinear Optical Properties and Optical Power Limiting of Leishman Dye Using z-scan Technique, J. Mater. Sci.: Mater. Electron., 26 (2015) 2713-2718.

[269] M.J. Miller, A.G. Mott, B.P. Ketchel, General Optical Limiting Requirements, Nonlinear Optical Liquids for Power Limiting and Imaging, Army Research Laboratory, delphi, MD 20783-1197, (1999), pp. 24-29.

[270] N. Nwaji, O.J. Achadu, T. Nyokong, Photo-induced resonance energy transfer and nonlinear optical response in ball-type phthalocyanine conjugated to semiconductor and graphene quantum dots, New J. Chem., 42 (2018) 6040-6050.

[271] I. Papagiannouli, A.B. Bourlinos, A. Bakandritsos, S. Couris, Nonlinear Optical Properties of Colloidal Carbon Nanoparticles: Nanodiamonds and Carbon Dots, RSC Adv., 4 (2014) 40152-40160.

[272] V. Vanyukov, Effects of Nonlinear Light Scattering on Optical Limiting in Nanocarbon Suspensions, Department of Physics and Mathematics University of Eastern Finland, Finland, 2015, pp. 146.

Appendix

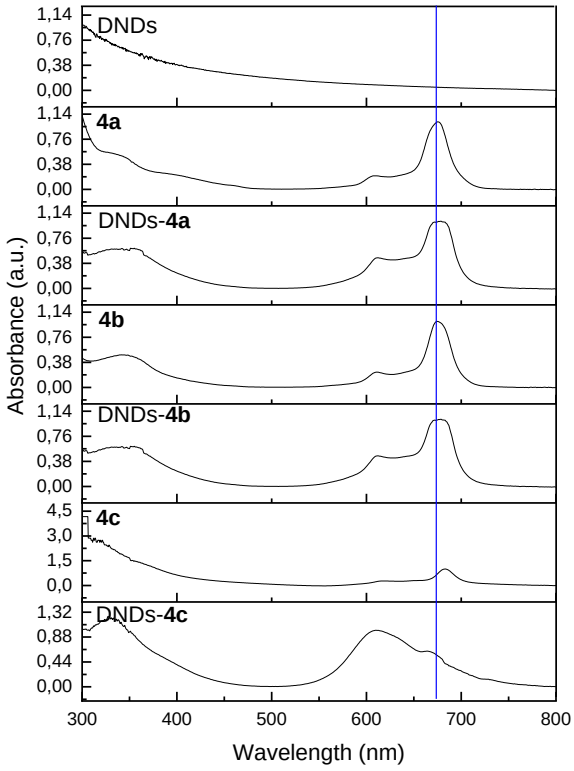

Figure 1A: UV-Vis spectra of DNDs, **4a**, DNDs-**4a, 4b**, DNDs-**4b**, **4c**, and DNDs-**4c** in DMSO.

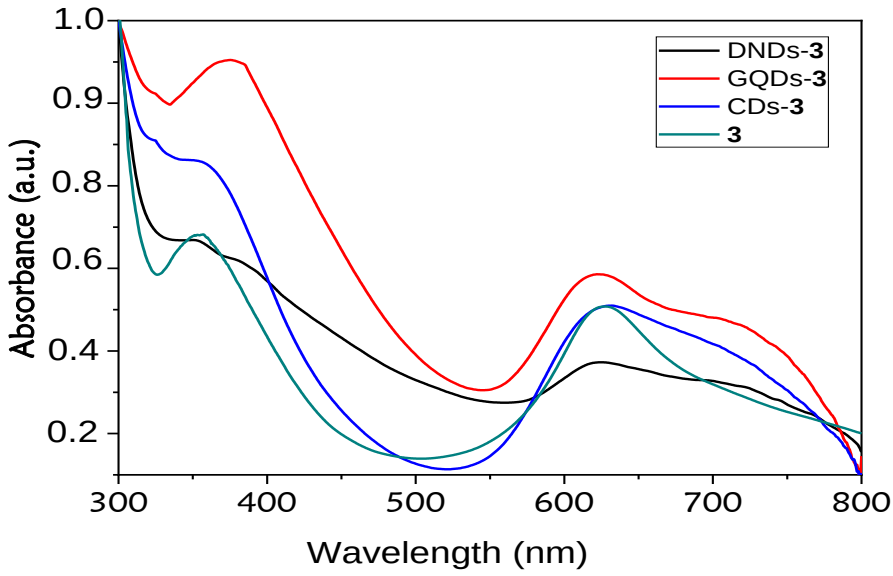

Figure 2A: Absorbance spectra of conjugates and complex **3** in 1% DMSO in water.

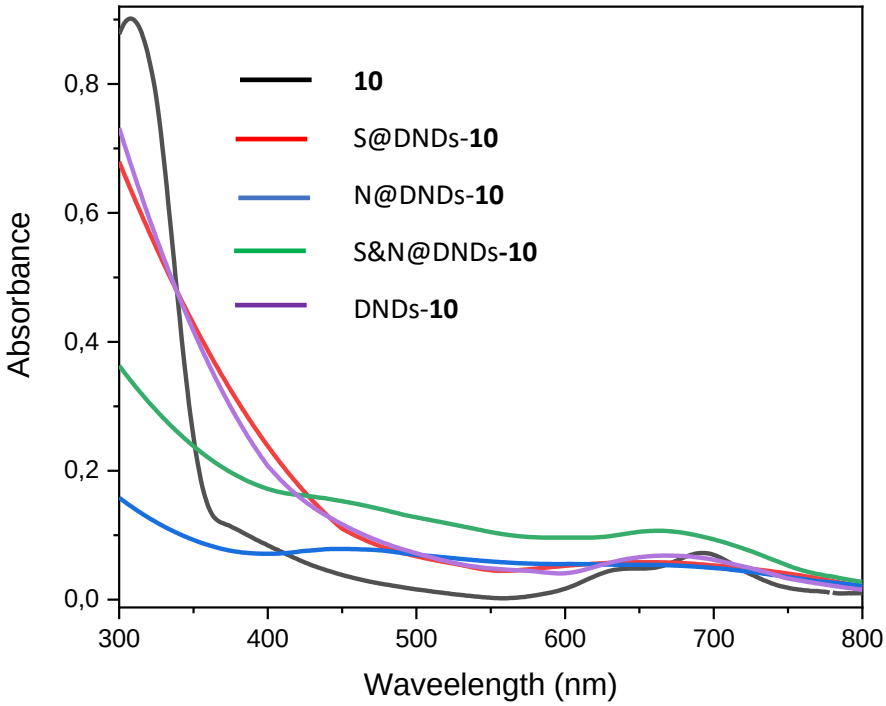

Figure 3A: UV-Vis for conjugates dissolved in 1% DMSO in water

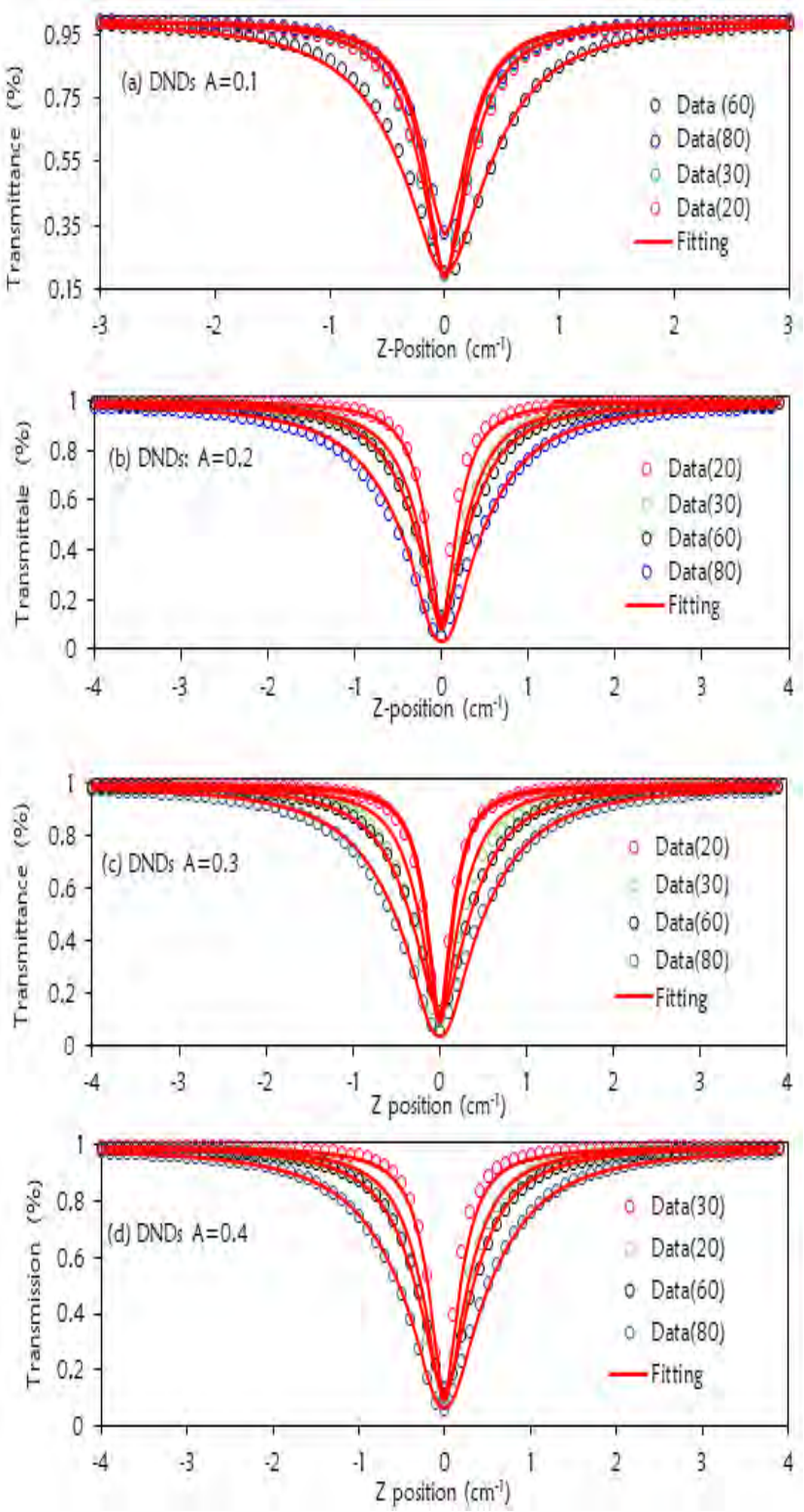

Figure 4A: Open aperture Z-scan signatures of DNDs alone in DMSO at various energies (20, 30, 60 and 80 µJ in brackets) and absorbances (a) 0.1 (b) 0.2 (c) 0.3 (d) 0.4 and respective fitting in red

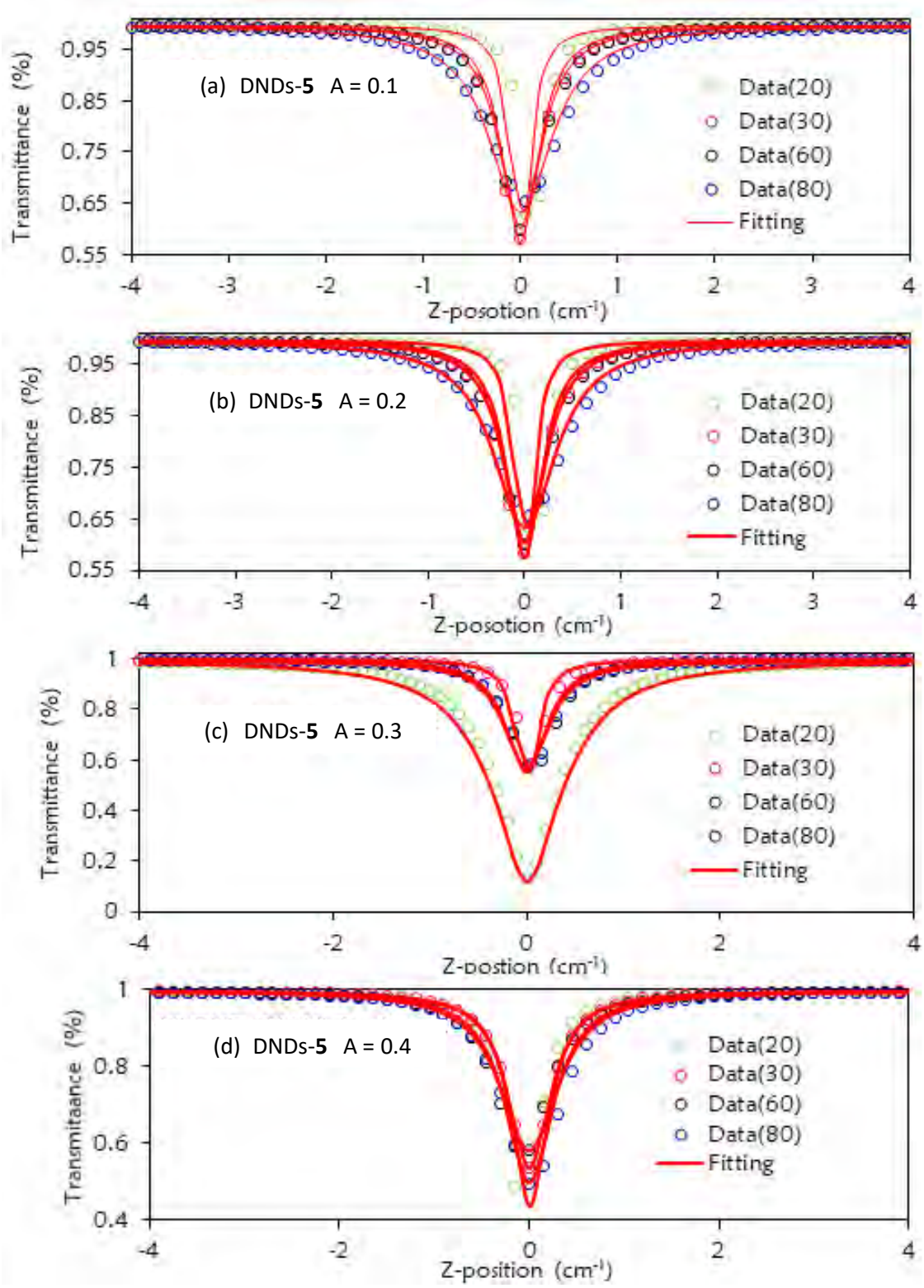

Figure 5A: Open aperture Z-scan signatures of DNDs-**5** in DMSO at various energies (20, 30, 60 and 80 µJ, in brackets) and absorbances (a) 0.1 (b) 0.2 (c) 0.3 (d) 0.4 and respective fitting in red

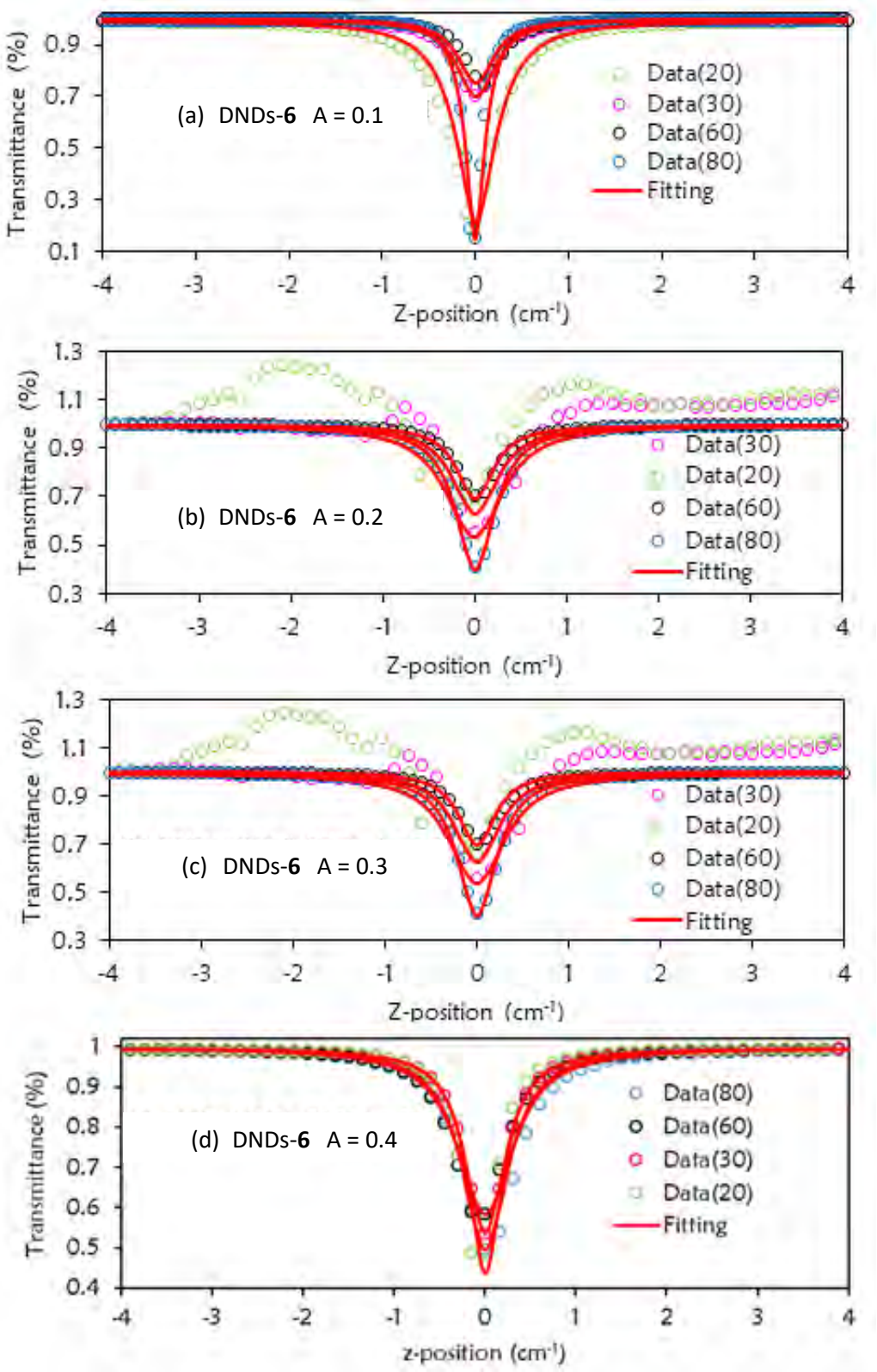

Figure 6A Open aperture Z-scan signatures of DNDs-**6** in DMSO at various energies (20, 30, 60 and 80 µJ, in brackets) and absorbances (a) 0.1 (b) 0.2 (c) 0.3 (d) 0.4 and respective fitting in red

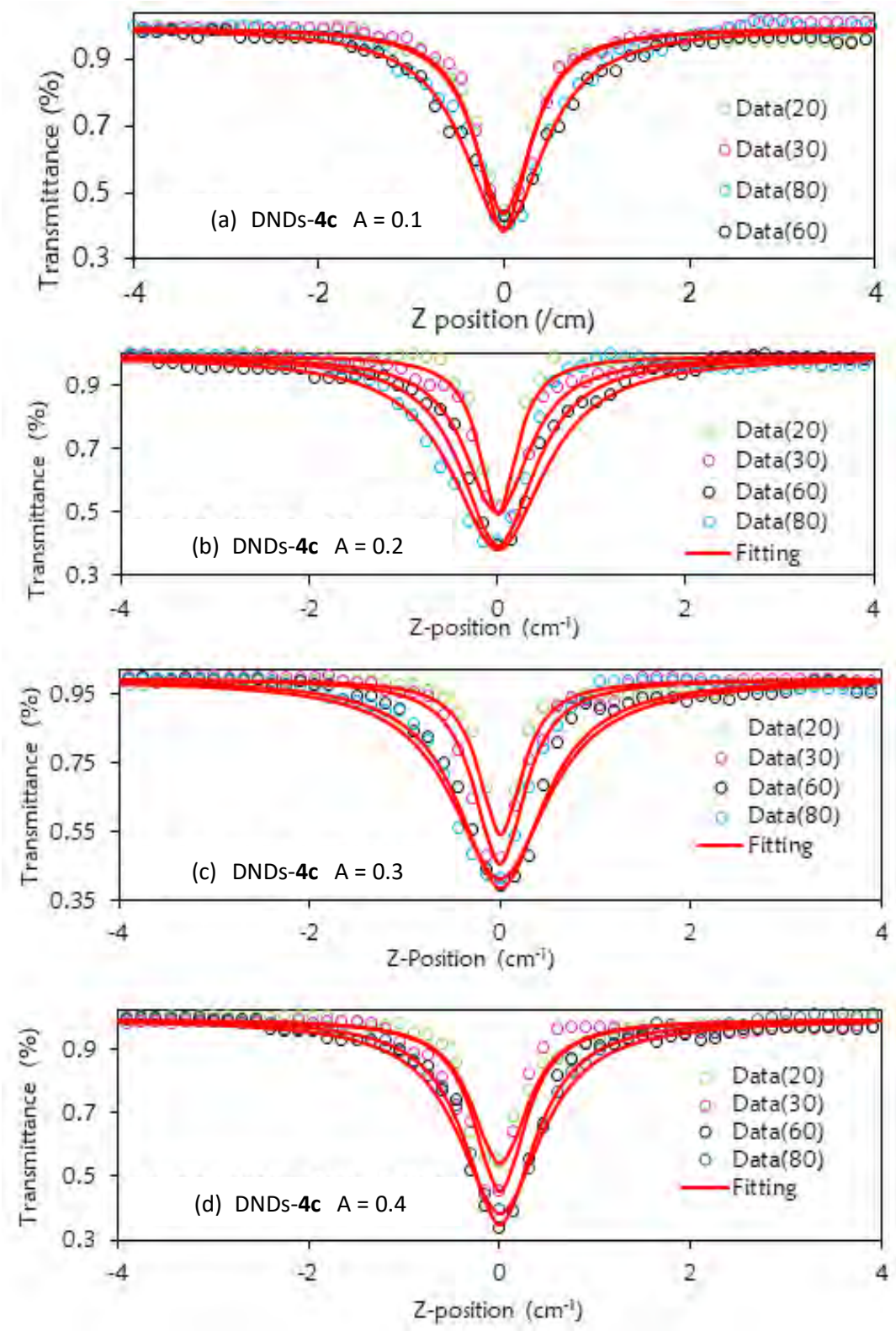

Figure 7A: Open aperture Z-scan signatures of DNDs-**4c** in DMSO at various energies (20, 30, 60 and 80 µJ, in brackets) and absorbances (a) 0.1 (b) 0.2 (c) 0.3 (d) 0.4 and respective fitting in red

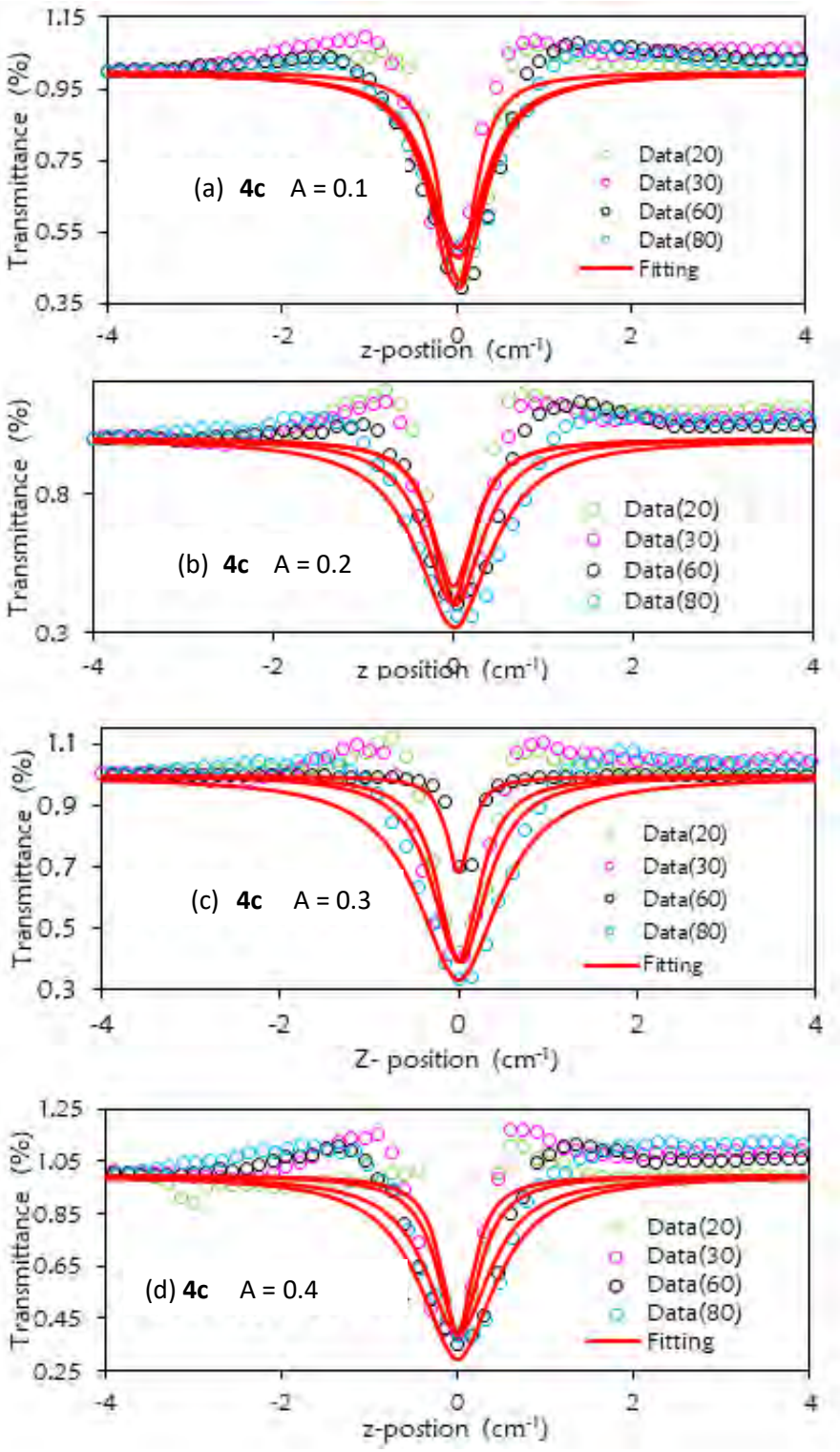

Figure 8A: Open aperture Z-scan signatures of **4c** alone in DMSO at various energies (20, 30, 60 and 80 µJ, in brackets) and absorbances (a) 0.1 (b) 0.2 (c) 0.3 (d) 0.4 and respective fitting in red

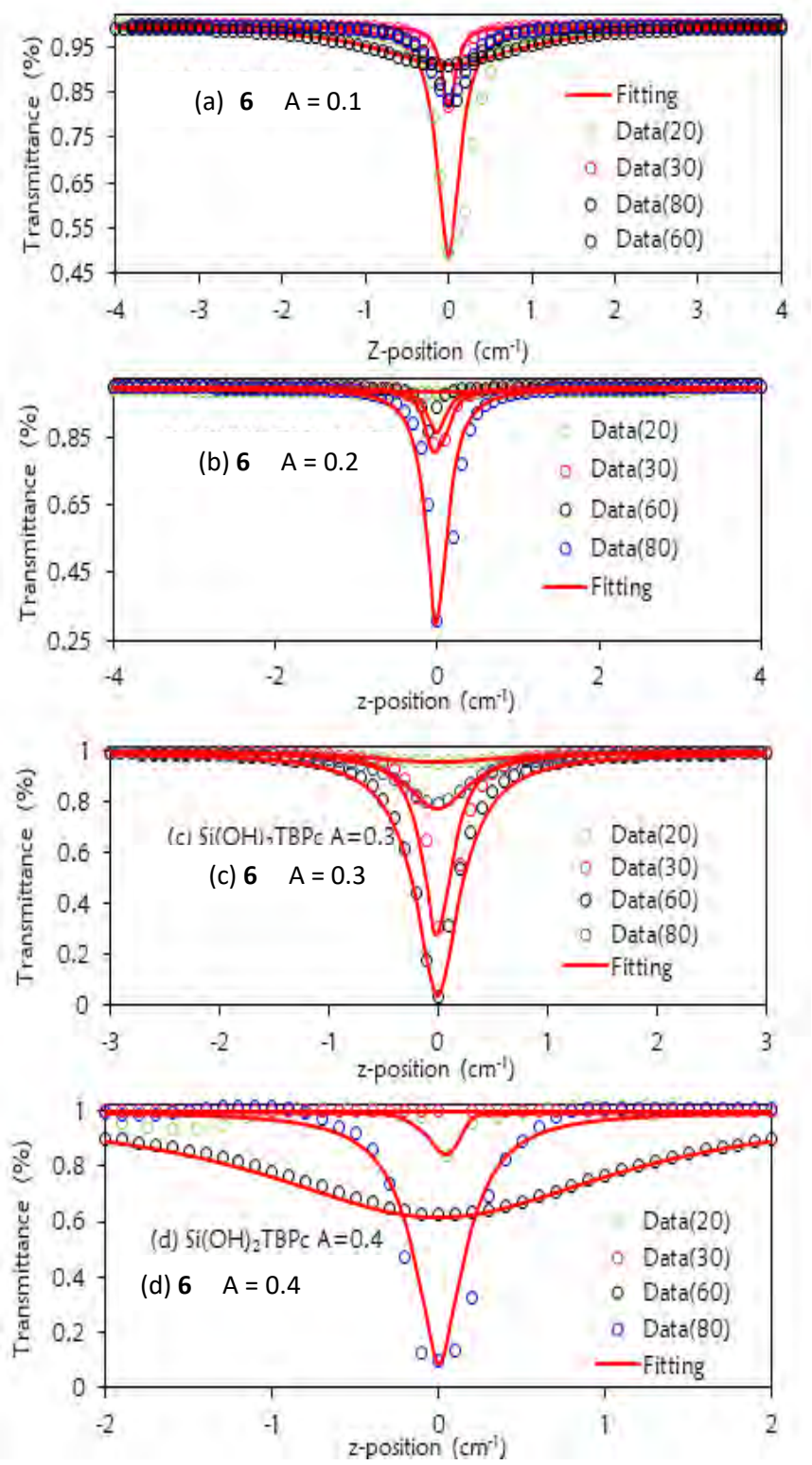

Figure 9A: Open aperture Z-scan signatures of **6** alone in DMSO at various energies (20, 30, 60 and 80 µJ, in brackets) and absorbances (a) 0.1 (b) 0.2 (c) 0.3 (d) 0.4 and respective fitting in red

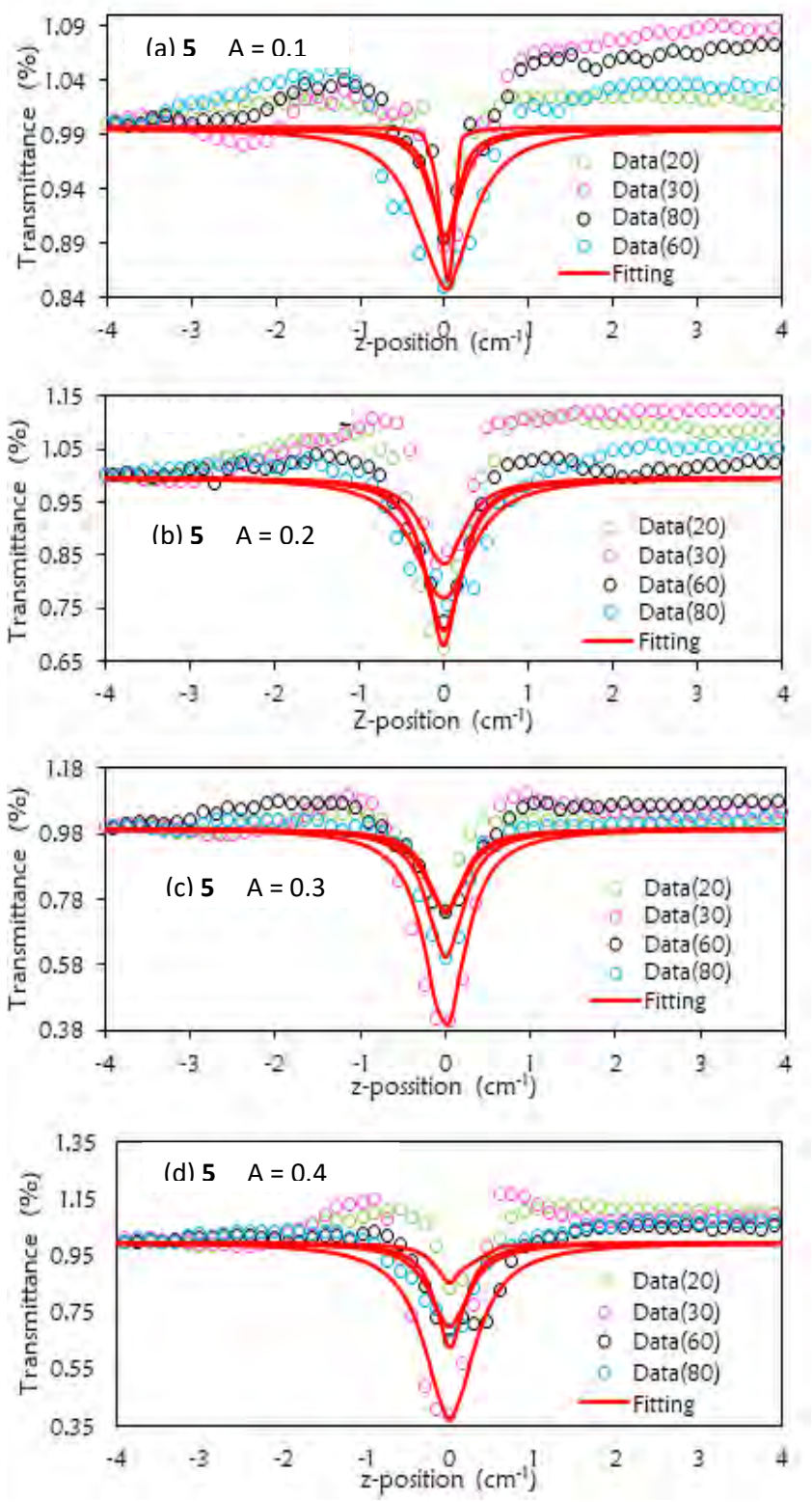

Figure 10A: Open aperture Z-scan signatures of **5** alone in DMSO at various energies (20, 30, 60 and 80 µJ, in brackets) and absorbances (a) 0.1 (b) 0.2 (c) 0.3 (d) 0.4 and respective fitting in red

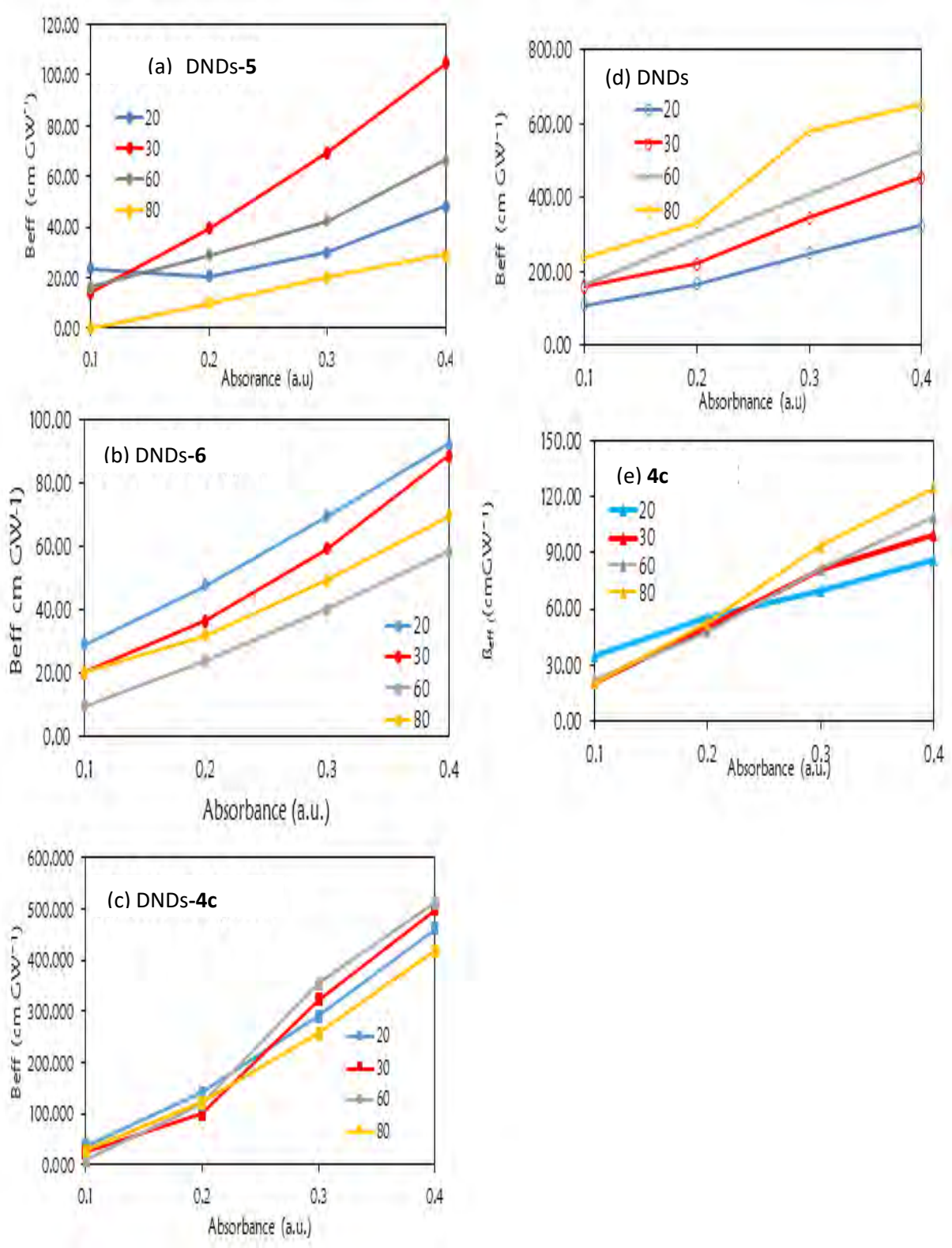

Figure 11A: Plots showing β_{eff} dependence on absorbance for (a) DNDs-**5**, (b) DNDs-**6**, (c) DNDs-**4c**, (d) DNDs, and (e) **4c** at various energies. Each data point for each sample represents an independent Z-scan measurement.

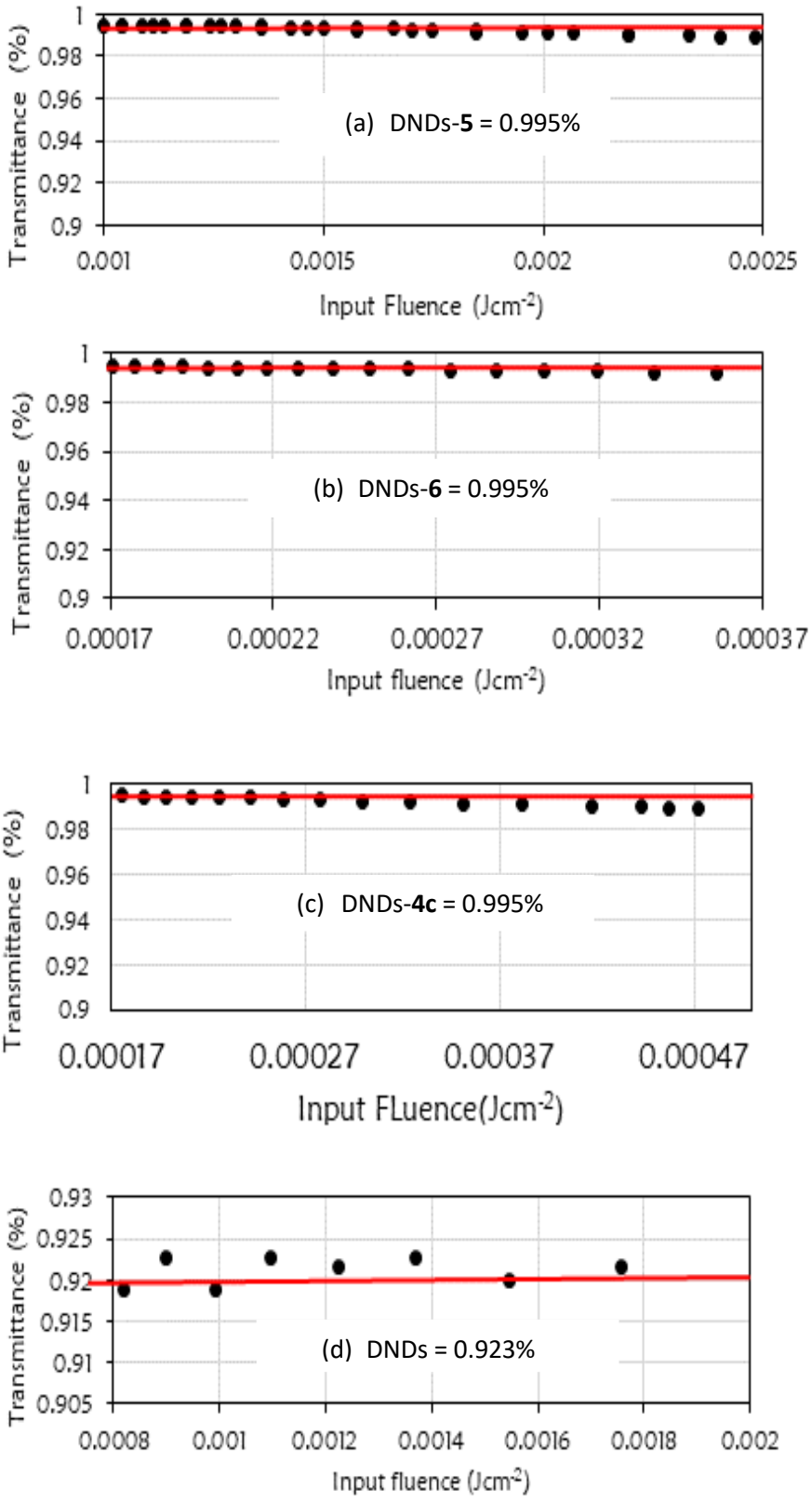

Figure 12A: Linear absorption plots of DNDs and respective conjugates (a) DNDs-**5** (b) DNDs-**6** (c) DNDs-**4c**(d) DNDs at absorbance of 1 and 80 µJ.

Table A1: Drug toxicity in the dark to eradicate MCF7 breast cancer cell lines .

PDT drug	**5**	**10**	**20**	**40**	**50**
			Complexes		
3	99.92	99.85	98.86	97.71	99.27
7	84.51	82.48	67.77	60.20	55.64
8	80.972	68.97	55.22	47.46	30.74
9	58.18	48.36	47.79	37.34	21.56
10	98.95	98.49	99.99	99.99	99.99
11	98.85	99.99	99.99	99.99	99.99
12	98.74	99.48	99.69	99.56	99.44
			Carbon NPs		
DNDs	99.99	99.99	99.91	99.99	98.23
P@DNDs	99.99	99.99	97.62	97.86	99.99
B@DNDs	99.99	97.51	97.48	99.99	99.99
N@DNDs	95.91	99.99	96.18	99.99	99.99
S&N@DNDs	98.95	98.49	99.99	99.99	99.99
GQDs	99.75	99.97	99.96	99.97	99.98
CDs	99.99	99.99	99.99	99.99	99.99
			Carbon nanoconjugates (CNPs-Pc)		
GQDs-**3**	99.99	99.99	99.99	98.77	99.99
CDs-**3**	99.99	99.99	99.99	99.99	99.99
DNDs-**3**	98.89	99.87	99.97	97.86	99.99
DNDs-**12**	99.99	99.99	99.99	97.12	99.99
3-DNDs-**12**	99.30	99.99	99.99	98.78	98.65
B@DNDs- **9**	99.99	99.99	99.99	99.99	99.99
B@DNDs- **10**	99.99	97.51	97.48	99.99	99.99
B@DNDs- **11**	99.99	99.99	99.99	99.99	99.99
P@DNDs- **10**	99.99	99.99	97.62	97.86	99.99
N@DNDs- **10**	95.91	99.99	96.18	99.99	99.99
S&N@DNDs-**10**	98.95	98.49	100	99.99	99.99